

CHARACTERIZATION OF NAVAJO SANDSTONE
HYDROUS FERRIC OXIDE CONCRETIONS

by

Sally Latham Potter

A thesis submitted to the faculty of
The University of Utah
in partial fulfillment of the requirements for the degree of

Master of Science

in

Geology

Department of Geology and Geophysics

The University of Utah

December 2009

Copyright © Sally Latham Potter 2009

All Rights Reserved

THE UNIVERSITY OF UTAH GRADUATE SCHOOL

SUPERVISORY COMMITTEE APPROVAL

of a thesis submitted by

Sally Latham Potter

This thesis has been read by each member of the following supervisory committee and by majority vote has been found to be satisfactory.








Erich U. Petersen

Dec. 3 2009


John Bowman

ABSTRACT

In Utah's Grand Staircase Escalante National Monument (GSENM), abundant spheroidal hydrous ferric oxide (HFO) concretions (cemented mineral masses) of the Jurassic Navajo Sandstone are present both *in situ* and loose in topographic lows. The HFO cement phases are typically amorphous HFO, goethite and hematite. Concretions are a significant record of diagenetic history, iron cycling and precipitation/mobilization events. The physical characterization of the concretions provides data to infer the processes affecting precipitation geometries and timing of precipitation events throughout the diagenetic history of the sandstone reservoir. Physical properties of the concretions also provide data to propose a model for formation of spheroidal HFO concretions.

Three precipitation geometries are present in GSENM: 1. spheroidal (aspect ratio ranges from 1.00 to 1.06) to discoidal (aspect ratio >1.06) macro concretions >5 mm diameter, 2. spheroidal to discoidal micro concretions <5 mm diameter, and 3. HFO-lined joints and related asymmetrical loopy mineralization and banded precipitation patterns (Liesegang bands). Three end members of Utah macro concretions (rind, layered and solid) and two end members of micro concretions (rind and solid) are distinguished by internal structure. Different precipitation geometries result from a combination of diffusive and advective mass transfer.

Multiple generations of cement textures and minerals suggest a pervasive growth model similar to some carbonate concretions where HFO concretions are precipitated with a set radius from multiple nuclei throughout the concretion. Chemical and mineral

phase gradients detected via QEMSCAN and visible to near infrared (Vnir) reflectance spectroscopy suggest that concretions form initially from an amorphous HFO gel that dehydrates with age to more stable phases (goethite, hematite). Some internal structures of concretions are a result of overprinting from late-stage precipitation events.

The Utah concretions interest planetary scientists because similarities with spherules in Meridiani Planum suggest that Mars “blueberries” also form via diffusive reactant transfer during groundwater diagenesis and Mars hematite likely had precursor HFO phases. Multiple mineralization events have probably occurred on Mars although variability of Utah concretions represents a more complex history of diagenesis.

Concretions preserve a record of diagenetic events. Reservoir evolution is better understood by determining how concretions grow and change over time.

TABLE OF CONTENTS

ABSTRACT.....	iv
ACKNOWLEDGEMENTS.....	x
INTRODUCTION.....	1
Background.....	1
Mars Analog.....	2
Purpose of Study.....	4
References.....	5
CHAPTERS	
1. CHARACTERIZATION OF NAVAJO SANSTONE CONCRETIONS: MARS COMPARISON AND CRITERIA FOR DISTINGUISHING DIAGENETIC ORIGINS.....	9
Abstract.....	9
Introduction.....	11
Concretion Growth.....	13
Purpose of Study.....	16
Mars Analog.....	16
Methods.....	17
Field Methods.....	17
Lab Measurements.....	18
Petrographic Microscopy.....	18
QEMSCAN.....	18
Visible to Near Infrared (V _{nir}) Reflectance Spectroscopy.....	20
Mössbauer Spectroscopy.....	22
Textural and Geometric Characterization.....	23
Rind Macro Concretions.....	26
Description.....	26
Interpretation.....	27
Layered Macro Concretions.....	28
Description.....	28

Interpretation.....	28
Solid Macro Concretions.....	30
Description.....	30
Interpretation.....	30
Micro Concretions.....	31
Description.....	31
Interpretation.....	31
Doublets and Triplets.....	33
Description.....	33
Interpretation.....	35
Size Distribution.....	35
Description.....	35
Interpretation.....	38
Analytical Results.....	39
Petrographic Microscopy Results and Interpretation.....	39
QEMSCAN Results and Interpretation.....	40
Vnir Reflectance Spectroscopy Results and Interpretation.....	46
Mössbauer Spectroscopy Results and Interpretation.....	52
Discussion.....	55
Interpretation of Cement Phases.....	56
Pervasive Growth Model.....	56
Mars Spherules and Analog Comparisons.....	58
Burns Formation (Host Rock), Meridiani Planum, Mars.....	58
Mars Spherule Characteristics.....	59
Proposed Terrestrial Analogs to Mars.....	60
Impact Lapilli.....	60
Mauna Kea.....	61
Western Australian Acid Saline Lakes.....	61
Navajo Sandstone HFO Concretions.....	62
Host Rock.....	62
External Structure.....	65
Internal Structure.....	67
Mineralogy and Crystallography.....	67
Size Distribution Comparison.....	70
Strengths and Weaknesses of Utah Analog.....	72
Conclusions.....	72
References.....	76
2. JOINT-CONTROLLED FLUID FLOW PATTERNS IN JURASSIC NAVAJO SANDSTONE: ANALOG IMPLICATIONS FOR MARS HEMATITE.....	83
Abstract.....	83
Introduction.....	84
Purpose of Study.....	85
Terrestrial Analog to Mars.....	87
Methods.....	92

Field Observations.....	94
Precipitation Geometries.....	95
Macro Concretions.....	95
Micro Concretions.....	98
HFO-lined Joints and Asymmetrical Mineralization.....	101
Field Relationships and Relative Timing of Events.....	102
Description.....	102
Interpretation.....	110
Analytical Investigation.....	114
Nearest Neighbor Spacing Description and Interpretation.....	114
Volumetric Density Description and Interpretation.....	116
Whole Rock Analysis Description and Interpretation.....	117
Discussion.....	119
Diffusive Mass Transfer.....	119
Advective Mass Transfer.....	120
Mars Comparison.....	121
Conclusions.....	122
References.....	124

APPENDICES

A. SAMPLES: LOCATION AND ANALYSES.....	129
B. QEMSCAN AREA PERCENT MINERALOGY AND POROSITY.....	136
C. VNIR REFLECTANCE SPECTROSCOPY.....	137
D. MÖSSBAUER SPECTROSCOPY.....	151
E. CONCRETION DIAMETER MEASUREMENTS.....	159
F. NEAREST NEIGHBOR SPACING AND DIAMETER.....	168
G. WHOLE ROCK ANALYSIS OF OXIDES AND TRACE ELEMENTS.....	173

ACKNOWLEDGEMENTS

I wish to thank my committee, Marjorie A. Chan (advisor), Erich U. Petersen, John Bowman and William Parry for their generous guidance, time and effort that they put into this research and into training me to be a scientist. I am forever grateful.

I also wish to acknowledge my fellow students for their encouragement, assistance and support, in particular, Winston Seiler, Greg Nielson, Matt Heumann, Jessica Allen, Henrietta Cathey and Anita Brown.

Special recognition goes to my husband Travis, our children, Hannah, Lillian, Alexis and James, and my mother, Jackie Allen, for their selfless sacrifices so I could have the opportunity to become a geologist. I am a blessed woman to have the support from these amazing people.

Research within Grand Staircase Escalante National Monument (GSENM) was completed on a special scientific research permit (to Chan). I gratefully acknowledge the Bureau of Land Management (BLM) for their logistical support.

Funding for this research was provided by ExxonMobil 2009 Geoscience Grant (to Potter), NASA Mars Fundamental Research grant (NNG06GI10G) and BLM GSENM grant (both to Chan).

INTRODUCTION

Background

The Jurassic Navajo Sandstone is one of the most porous sedimentary units on the Colorado Plateau and is the host rock for the variety of concretions in this study. This formation represents the largest erg to ever have existed in the history of the Earth (Blakey et al., 1988; Blakey, 1994). It is widely exposed throughout southern Utah and northern Arizona and is known for its dramatic coloration patterns and precipitation geometries. One of the most notable features in the Spencer Flat area of Grand Staircase Escalante National Monument (GSENM) is the presence of abundant spheroidal (aspect ratio 1.00-1.06) to discoidal (aspect ratio >1.06) hydrous ferric oxide (HFO) concretions (1mm to 10+ cm diameter).

The Navajo Sandstone is the subject of much research because of the regional coloration patterns created by HFO precipitation (amorphous HFO, goethite and hematite phases) and bleaching of this porous and permeable eolian sandstone. Beitler et al. (2003, 2005) determined that the regional coloration and bleaching occurred during and after the Laramide orogeny when blind thrust structures provided conduits for a reducing fluid to infiltrate the reservoir and mobilize the iron that was present in the unit. Several different diagenetic coloration facies are recognized, including an original red facies, a bleached facies and several different secondary coloration facies.

Chan et al. (2000) formulated a three part model to explain iron cycling in the Navajo Sandstone and this is detailed in subsequent publications (Beitler et al., 2003, 2005; Chan

et al., 2004, 2005, 2006, 2007; Parry et al., 2004) with a summary of the three steps below.

- 1) Source: Early depositional hematite grain coatings precipitate from the breakdown of ferromagnesian minerals upon deposition of the erg.
- 2) Mobilization: A reducing fluid (likely hydrocarbon) infiltrates the reservoir and puts the iron into solution as Fe^{2+} .
- 3) Precipitation: An oxidizing fluid meets and mixes with the reducing fluid and HFO is precipitated.

HFO precipitation likely occurred several times throughout the diagenetic history of the Navajo Sandstone. Although the regional coloration patterns are well-studied, the physical distribution and characterization of the spheroidal concretions have received less attention. These concretions record a story of iron cycling, hydrologic regimes, tectonics and possibly organic influence that have affected diagenesis. The purpose of this study is to provide a detailed characterization of the concretions in order to better understand concretion formation processes, the effect of reactant mass transfer processes on precipitation geometries and to present a relative timing of iron precipitation and mobilization events in the Spencer Flat area (see Chapter 1 for study area location).

Mars Analog

Navajo Sandstone concretions have long been a geologic curiosity to rock collectors, but they became of special interest to the geologic and planetary community with the discovery of similar hematite spherules (“blueberries”) on Mars (Squyres et al., 2004a; Squyres et al., 2004b). In 2004, the Mars Exploration Rover (MER) Opportunity landed in Meridiani Planum. This site was chosen because of an abundance of remotely sensed

hematite (Golombek et al., 2003). Hematite is a mineral that commonly forms in water; thus, the hope was to find evidence of water and perhaps extinct or extant life because water is a requirement for life.

In the Burns formation in Meridiani Planum (Grotzinger et al., 2005), Opportunity imaged eolian and water-laid sedimentary rock outcrops. The stratification shows marked similarities to the depositional environment of the Navajo Sandstone such as eolian cross-stratification, reworking of sediments by a high water table evidenced by ripple marks and distorted bedding (McLennan et al., 2005). Another similarity is the presence of hematite spherules that have been interpreted as diagenetic concretions (McLennan et al., 2005). Chan et al. (2004) and Ormö et al. (2004) first proposed the Navajo Sandstone as a terrestrial analog for the Martian “blueberries” because of many similarities: mineralogy, geometry, weathering resistance, collection in topographic lows, and formation in a porous and permeable media. Similarities between Navajo Sandstone concretions and Mars spherules present compelling evidence for a watery diagenetic history for the Burns formation.

Terrestrial analog study is a useful tool for planetary geology because most planetary geology is currently interpreted from remote sensing. The benefit of being able to physically examine the rocks and subject them to lab analyses is invaluable. Some of the other various proposed analogs (from the literature) for the Martian “blueberries” are evaluated in comparison to the Navajo Sandstone analog.

Purpose of Study

Although some of the diagenetic history of the Navajo Sandstone has been studied and mapped throughout southern Utah and northern Arizona on a regional scale (Beitler et al., 2005; Bowen et al. 2007; Nielson and Chan, 2008; Seiler, 2008), questions still remain about concretion genesis, the relative timing of iron precipitation and mobilization events and how mass transfer of reactants affects precipitation geometry. This research focuses on the Spencer Flat area of the GSENM where the diagenetic history includes a variety of spheroidal HFO concretions and other HFO precipitation geometries. The detailed characterization provides data to interpret the processes of concretion formation both here and in Meridiani Planum, Mars.

This study was undertaken to explore three hypotheses:

1. Concretions can form quickly and grow over time.
2. Micro concretions form by diffusion.
3. Concretions evolve over time via multiple diagenetic stages.

In the first chapter, "Characterization of Navajo Sandstone Concretions: Mars Comparison and Criteria for Distinguishing Diagenetic Origins," a detailed textural, geometric and mineralogical characterization of the spheroidal concretions provides data to understand concretion formation and criteria for distinguishing diagenetic origin. HFO phases, cement textures and chemical gradients are analyzed using an array of traditional methods such as petrographic microscopy, Mössbauer spectroscopy and visible to near infrared (Vnir) reflectance spectroscopy. A new approach using QEMSCAN analysis provides information about chemical/mineralogical gradients and cement textures and proves to be a useful mineralogical tool. The diagnostic characteristics of Utah

concretions are compared to a characterization of Martian spherules (Calvin et al., 2008) and to other proposed genetic models from the literature to determine a diagenetic origin. This first chapter is, in large part, my work with assistance from two members of my graduate committee, Marjorie A. Chan (advisor) and Erich U. Petersen. M. Darby Dyar and Elizabeth Sklute from Mount Holyoke College performed the Mössbauer analysis.

The second chapter, “Joint Controlled Fluid Flow in Jurassic Navajo Sandstone: Analog Implications for Mars Hematite,” provides outcrop-scale field evidence that documents multiple fluid flow events and establishes the relative timing of iron cycling events throughout the diagenetic history of the Navajo Sandstone. Different precipitation geometries are documented and this characterization demonstrates how advective and diffusive mass transfer of reactants affects precipitation geometries in the Spencer Flat area. Statistical analysis of distribution in the host rock, volumetric density and whole rock analysis (WRA) provide insight into formation mechanisms, reaction front geochemistry and the thermodynamics that nucleate concretions. These documented characteristics are compared to Meridiani Planum spherules, and similarities suggest diffusive mass transfer may be responsible for both the Utah micro concretions and the Mars spherules. This second chapter is also, in large part, my own work with assistance from my advisor, Marjorie A. Chan.

References

- Beitler, B., Chan, M.A., Parry, W.T., 2003. Bleaching of Jurassic Navajo Sandstone on Colorado Plateau Laramide highs; evidence of exhumed hydrocarbon supergiants? *Geology*, 31, 1041-1044.
- Beitler, B., Parry, W.T. Chan, M.A., 2005. Fingerprints of fluid flow: chemical diagenetic history of the Jurassic Navajo Sandstone, southern Utah, U.S.A. *JSR*, 75, 547–561.

- Blakey, R.C., Peterson, F., Kocurek, G., 1988. Synthesis of late Paleozoic and Mesozoic eolian deposits of the western interior of the United States. *Sed. Geol.*, 56, 3–125.
- Blakey, R.C., 1994. Paleogeographic and tectonic controls on some lower and middle Jurassic erg deposits, Colorado Plateau. In: Caputo, M.V., Peterson, J.A., and Franczyk, K.J. (Eds.), *Mesozoic Systems of the Rocky Mountain Region, USA* SEPM, Rocky Mountain Section, pp. 273–298.
- Bowen, B.B., Martini, B.A., Chan, M.A., Parry, W.T., 2007. Reflectance spectroscopic mapping of diagenetic heterogeneities and fluid-flow pathways in the Jurassic Navajo Sandstone. *AAPG Bulletin*, 91, 173–190.
- Calvin, W.M., Shoffner, J.D., Johnson, J.R., Knoll, A.H., Pockock, J.M., Squyres, S.W., Weitz, C.M., Arvidson, R.E., Bell J.F., III, Christensen, P.R., de Souza, P.A., Jr., Farrand, W.H., Glotch, T.D., Herkenhoff, K.E., Jolliff, B.L., Knudson, A.T., McLennan, S.M., Rogers, A.D., Thompson, S.D., 2008. Hematite spherules at Meridiani: results from MI, Mini-TES and Pancam. *J. Geophys. Res.*, 113, E12S37.
- Chan, M.A., Parry, W.T., Bowman, J.R., 2000. Diagenetic hematite and manganese oxides and fault-related fluid flow in Jurassic sandstone, southeastern Utah. *AAPG Bulletin*, 84, 1281-1310.
- Chan, M.A., Beitler, B., Parry, W.T., Ormö, J., Komatsu, G., 2004. A possible terrestrial analogue for hematite concretions on Mars. *Nature*, 429, 731-734.
- Chan, M.A., Beitler, B.B., Parry, W.T., Ormö, J., Komatsu, G., 2005. Red rock and red planet diagenesis: comparison of Earth and Mars concretions. *GSA Today*, 15, 4-10.
- Chan, M.A., Johnson, C.M., Beard, B.L., Bowman, J.R., Parry W.T., 2006. Iron isotopes constrain the pathways and formation mechanisms of terrestrial oxide concretions: a tool for tracing iron cycling on Mars? *Geosphere*, 2, 324-332.
- Chan, M.A., Ormö, J., Park, A.J., Stich, M., Souza-Egipsy, V., Komatsu, G., 2007. Models of iron oxide concretion formation: field, numerical, and laboratory comparisons. *Geofluids*, 7, 1–14.
- Golombek, M.P., Grant, J.A., Parker, T.J., Kass, D.M., Crisp, J.A., Squyres, S.W., Haldemann, A.F. C., Adler, M., Lee, W.J., Bridges, N.T., Arvidson, R.E., Carr, M.H., Kirk, R.L., Knocke, P.C., Roncoli, R.B., Weitz, C.M., Schofield, J.T., Zurek, R.W., Christensen, P.R., Fergason, R.L., Anderson, F.S., Rice, J.W., Jr, 2003. Selection of the Mars Exploration Rover landing sites. *JGR*, 108, E12.

- Grotzinger, J.P., Arvidson, R.E., Bell, J.F., III, Calvin, W.M., Clark, B.C., Fike, D.A., Golombek, M.P., Greeley, R., Haldemann, A., Herkenhoff, K.E., Jolliff, B.L., Knoll, A.H., Malin, M.C., McLennan, S.M., Parker, T., Soderblom, L., Sohl-Dickstein, J.N., Squyres, S.W., Tosca, N.J., Watters, W.A., 2005. Stratigraphy and sedimentology of a dry to wet eolian depositional system, Burns Formation, Meridiani Planum, Mars. *EPSL*, 240, 11-72.
- McLennan, S.M., Bell, J.F., III, Calvin, W.M., Christensen, P.R., Clark, B.C., de Souza, P.A., Farmer, J.D., Farrand, W.H., Fike, D.A., Geller, R., Ghosh, A., Glotch, T.D., Grotzinger, J.P., Hahn, B., Herkenhoff, K.E., Hurowitz, J.A., Johnson, J.R., Johnson, S.S., Jolliff, B.J., Klingelhofer, G., Knoww, A.H., Lerner, Z., Malin, M.C., McSween, H.Y., Jr., Pocick, J., Ruff, S.W., Soderblom, L.A., Squyres, S.W., Tosca, N.J., Watter, W.A., Wyatt, M. B., Yen, A., 2005. Provenance and diagenesis of the evaporite-bearing Burns Formation, Meridiani Planum, Mars. *ESPL*, 240, 95-121.
- Nielsen, G.B., Chan, M.A., 2006. Colorful diagenetic facies and fluid-related alteration features of the Jurassic Navajo Sandstone, Snow Canyon State Park, Utah. *GSA Abstracts with Programs*, 38, 518.
- Ormö, J., Komatsu, G., Chan, M.A., Beitler, B., Parry, W.T., 2004. Geological features indicative of processes related to the hematite formation in Meridiani Planum and Aram Chaos, Mars: A comparison with diagenetic hematite deposits in southern Utah, U.S.A. *Icarus*, 171, 295-316.
- Parry, W.T., Chan, M.A., Beitler, B., 2004. Chemical bleaching indicates episodes of fluid flow in deformation bands in sandstone. *AAPG Bulletin*, 88, 175-191.
- Seiler, W.M., 2008. Jurassic Navajo Sandstone of Coyote Buttes, Utah/Arizona: Coloration and diagenetic history, preservation of a dinosaur trample surface, and a terrestrial analog to Mars. M.S. Thesis, University of Utah, Salt Lake City, Utah, U.S.A.
- Squyres, S.W., Arvidson, R.E., Bell, J.F., III, Brueckner, J., Cabrol, N.A., Calvin, W.M., Carr, M.H., Christensen, P.R., Clark, B.C., Crumpler, L., Des Marais, D.J., d'Uston, C., Economou, T., Farmer, J., Farrand, W.H., Folkner, W., Golombek, M.P., Gorevan, S., Grant, J.A., Greeley, R., Grotzinger, J.P., Haskin, L., Herkenhoff, K.E., Hviid, S.F., Johnson, J.R., Klingelhofer, G., Knoll, A.H., Landis, G., Lemmon, M.T., Li, R., Madsen, M.B., Malin, M.C., McLennan, S.M., McSween, H.Y., Ming, D.W., Moersch, J.E., Morris, R.V., Parker, T., Rice, J.W., Richter, L., Rieder, R., Sims, M., Smith, M., Smith, P., Soderblom, L.A., Sullivan, R.J., Waenke, H., Wdowiak, T., Wolff, M.J., Yen, A., 2004a. The Opportunity Rover's Athena science investigation at Meridiani Planum, Mars. *Science*, 306, 1698-1703.

Squyres, S.W., Grotzinger, J.P., Arvidson, R.E., Bell, J.F., III, Calvin, W.M., Christensen, P.R., Clark, B.C., Crisp, J.A., Farrand, W.H., Herkenhoff, K.E., Johnson, J.R., Klingelhofer, G., Knoll, A.H., McLennan, S.M., McSween, H.Y., Morris, R.V., Rice, J.W., Rieder, R., Soderblom, L.A., 2004b. In situ evidence for an ancient aqueous environment at Meridiani Planum, Mars. *Science*, 306, 1709-1714.

CHAPTER 1

CHARACTERIZATION OF NAVAJO SANDSTONE CONCRETIONS: MARS COMPARISON AND CRITERIA FOR DISTINGUISHING DIAGENETIC ORIGINS

Sally L Potter¹, Marjorie A. Chan¹, Erich U. Petersen¹, M. Darby Dyar², and
Elizabeth Sklute²

¹University of Utah, Department of Geology and Geophysics, 115S. 1460E. Rm. 383,
Salt Lake City, UT 84112; ²Mount Holyoke College, Department of Geology and
Geography, 50 College Street, South Hadley, MA 01075
contact e-mail: sally.potter@utah.edu

Abstract

The Jurassic Navajo Sandstone is host to dramatic, regional precipitation patterns and geometries including spheroidal (aspect ratio 1.00 to 1.06) to discoidal (aspect ratio >1.06) hydrous ferric oxide (HFO) concretions. Concretions are characterized by physical properties of size, shape, *in situ* distribution, mineralogy and microscopic textural relationships. They are divided by size into macro (>5 mm diameter) and micro (<5 mm diameter) concretions. Three end members of macro concretions are identified based on interior structure: rind, layered and solid. Two end members of micro concretions are rind and solid.

Three HFO phases are identified using visible to near infrared (Vnir) reflectance spectroscopy: an amorphous HFO (typically located in the rinds), goethite (along interior

edges of rinds and throughout layered and solid concretions) and hematite (in the centers of rind concretions). Multiple generations of cement are identified with QEMSCAN, petrographic microscopy and Mössbauer spectroscopy. Chemical and mineralogical gradients (μm - to mm -scale) are identified with QEMSCAN and Vnir reflectance spectroscopy. Statistical methods differentiate different size populations and reaction fronts.

Multiple generations of cement suggest that concretions form initially as an amorphous HFO gel that sets the radius and retains some original porosity. Subsequent precipitation events infill remaining pore space with both younger HFO and manganese oxide (MnO) phases such that concretions grow pervasively (as opposed to radially expanding). Both macroscopic and microscopic inward digitate cement crystal growth indicates concretions grow from a set radius toward the centers. Late-stage precipitation events overprint the internal structure of the concretions. The characteristics of the concretions provide proxy data to infer the processes and timing of formation.

Concretions comprise valuable diagenetic records that may preserve multiple fluid events of diffusive and advective mass transfer. Under the right conditions, concretions likely grow quickly (1000 year scale) but may be modified by dehydration and/or by addition of diffusive Liesegang bands. These records of iron cycling are important to understanding precipitation and preferential pathways of fluid flow in a subsurface reservoir.

Physical characterization of textures and minerals provide comparative data for understanding how similar concretions (“blueberries”) form on Mars. The terrestrial analogs of the eolian Navajo Sandstone show similar characteristics of self-organized

spacing, spheroidal geometries, internal structures, conjoined forms, and precursor HFO phases that dehydrate to goethite or hematite mineralogies. These characteristics indicate a similar origin of groundwater diagenesis and diffusive mass transfer of iron oxides in a homogeneous, porous sulfate-rich host rock in the Burns formation in Meridiani Planum.

Introduction

The Jurassic Navajo Sandstone is widely exposed throughout southern Utah and northern Arizona. The Spencer Flat study area located in Grand Staircase Escalante National Monument (GSENM; Fig. 1.1) hosts a variety of hydrous ferric oxide (HFO) mineralogies and precipitation geometries (including spheroidal concretions) from different generations of chemical reaction fronts. Spheroidal (aspect ratio 1.00 to 1.06) to discoidal (aspect ratio ranges >1.06) HFO concretions are cemented mineral masses that form due to the porous and permeable nature of the host rock and a complex diagenetic history of iron cycling (Chan et al., 2000, 2004, 2005; Beitler et al, 2003, 2005 ; Parry et al. 2004; Bowen et al., 2007; Seiler, 2008).

The Navajo Sandstone is known throughout southern Utah and northern Arizona for its dramatic coloration patterns. Much of this coloration occurs in reaction fronts of banded precipitation patterns known as Liesegang bands (Liesegang, 1896). Liesegang bands are self-organized, macroscopic bands of precipitated cement that form via diffusion of reactants through the host rock. Formation of these bands requires either two unequal concentrations of reactants (in this study, iron and oxygen) or unequal mobility of reactants (Hedges and Meyers, 1926; Stern, 1954; Sultan et al., 1990). Ostwald (1925) suggested that these bands form by a supersaturation, nucleation and depletion cycle that begins when the two reactants meet. The result is a cyclic, banded pattern that forms

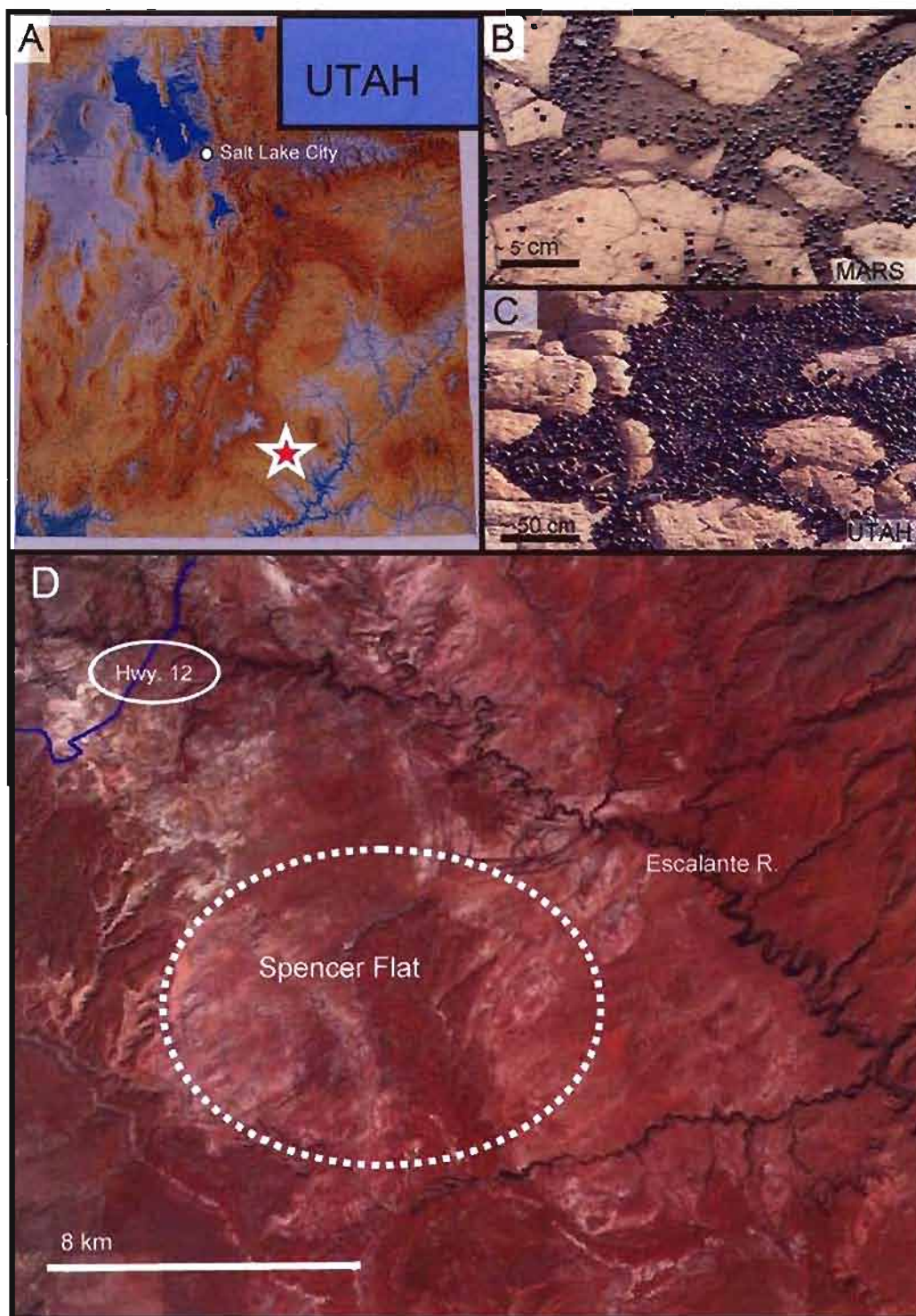


Fig. 1.1. Study area. A. State of Utah, USA with Spencer Flat, Grand Staircase Escalante National Monument (GSENM) study area (star). B. Mars Exploration Rover (MER) Opportunity image of loose hematite concretions in Meridiani Planum (NASA/JPL/Cornell) C. Loose and weathered HFO concretions in GSENM. D. Aerial Photo of Spencer Flat area within the GSENM (dotted circle). Spencer Flat is located at $\sim 37^{\circ}40'$ N. and $111^{\circ}18'$ W.

perpendicular to the direction of diffusive movement.

A tripartite geochemical fluid flow model (Chan et al., 2000, 2005) explains iron cycling that is reflected in the diagenetic facies and precipitation patterns. 1. Iron source: The iron precipitates as early diagenetic grain coatings (Fe^{3+}) formed via the breakdown of ferromagnesian minerals upon deposition of the erg. 2. Iron mobilization: Infiltration of a reducing fluid mobilizes the iron into solution as ferrous iron (Fe^{2+}). 3. Iron precipitation: When this iron-bearing, reducing fluid meets and mixes with an oxidizing fluid, HFOs (Fe^{3+}) precipitate as a cement to form concretions.

Concretion Growth

Concretions are cemented mineral masses. The most common and best studied type of concretions are carbonate concretions (e.g., Clifton, 1957; Raiswell, 1976; Coleman and Raiswell, 1981, 1995; Raiswell and Fisher, 2000; Seilacher, 2001; Mozley and Davis, 2005; Lyons et al., 2007). Concretions form in a variety of geologic settings and by different processes. They can form during burial diagenesis like calcareous concretions in sandstones, limestones or shales. They can also form during late diagenesis like most siderite concretions (Seilacher, 2001). Ooids are morphologically similar to concretions and grow radially like most calcareous concretions, but are accretionary primary precipitates (versus diagenetic cemented mineral masses).

Two end member models for carbonate concretion formation proposed by Raiswell and Fisher (2000) are concentric growth and pervasive growth (Fig. 1.2). Their end member terminology is used in this paper, although it should be noted that the exact growth mechanisms for carbonate concretions in mudrocks may not be directly

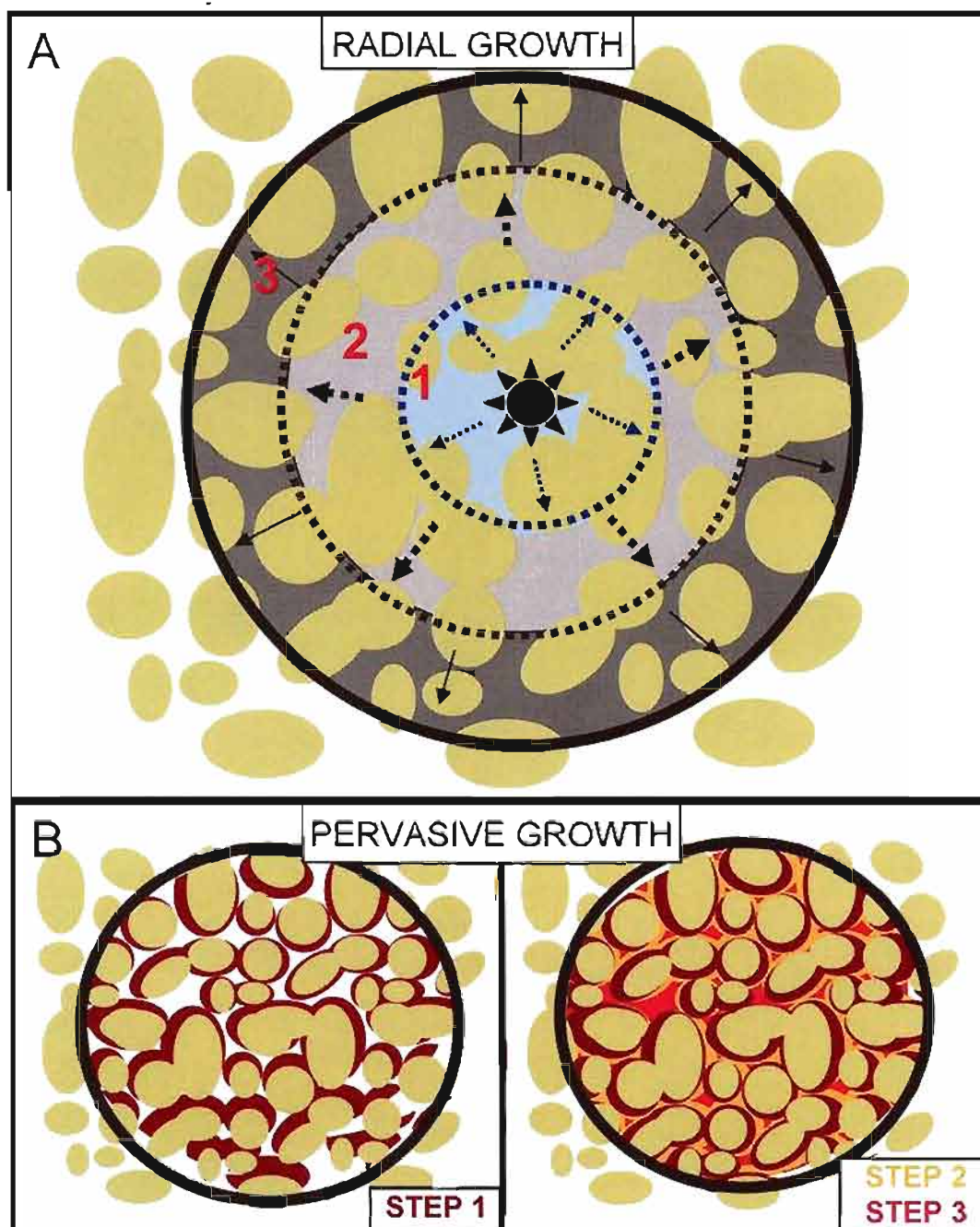


Fig. 1.2. End member carbonate concretion growth models after Raiswell and Fisher (2000). A. Radial growth where a concretion nucleates biogenically on some organic matter and grows with an expanding radius. B. Pervasive growth where (Step 1) crystals nucleate concomitantly throughout the concretion, setting up a plastic body with some retained porosity, then (Step 2, 3) subsequent precipitation events infill remaining pore space with younger cements.

applicable to iron oxide concretions in sandstones. Concentric growth occurs when a small piece of organic matter biogenically nucleates the precipitation reaction and the concretions grow radially (with an increasing radius). Pervasive growth occurs as the crystals nucleate due to thermodynamically favorable conditions and grow concomitantly throughout the body of the concretion. Pervasive growth is particularly common in siderite (iron carbonate) concretions (Mozley, 1996; Fisher et al., 1998; Raiswell and Fisher, 2000).

In carbonates, cement textures are diagnostic of the type of concretion growth. Where multiple generations of cements are present (early- and late-stage cements within pore spaces), growth is not radial, but pervasive (Feistner, 1989; Mozley, 1989; Fisher et al., 1998; Raiswell and Fisher, 2000). In these pervasive growth concretions, early cementation forms a framework with some small, retained porosity so that late-stage infilling can occur (Dickson and Barber, 1976; Hudson 1978; Jordan et al., 1992; Huggett, 1994; Raiswell and Fisher, 2000).

Pervasive growth concretions initially develop as plastic, porous, weakly cemented masses that become more rigid with further cementation (Raiswell and Fisher, 2000). This is especially well-studied in carbonate concretions (Bjølykke, 1973; Hesselbo and Palmer, 1992; Criss et al., 1988, Raiswell and Fisher, 2000). HFO can also precipitate as a primary concretion cement that may initially be an amorphous gel that dehydrates over time to more stable phases such as goethite and hematite (Klein and Bricker, 1977).

The rate of concretion formation is difficult to determine. Estimates range from 65 million years in pyrite concretions (Prosser et al., 1994) to between 140,000 and 65 million years in septarian calcite nodules (Boles et al., 1985) to 7500-20,000 years in

Quaternary calcareous concretions (Pantin, 1958). Research on modern iron oxide concretions in acid saline lakes (Western Australia) suggest concretions can form within hundreds of years at low temperature in acidic conditions (Bowen et al., 2008). Lab experiments in agarose gels with concentrated chemicals nucleate concretions within a matter of days at room temperature (Barge and Petruska, 2007). Other modeling experiments of diffusion rates based on early Mars conditions suggest that concretion growth occurs on the scale of 1000s of years (Sefton-Nash and Catling, 2008).

Purpose of Study

The purpose of this study is to characterize concretions with respect to physical and chemical attributes including external features like concretion shape, size and spacing in the host rock as well as the internal structure of texture, mineralogy and diagenetic phases. Microscopic chemical and mineralogical characteristics including texture, mineral species and chemical cement gradients are documented. The synthesis of characteristics is used to interpret how concretions form and grow.

Mars Analog

In 2004, the Mars Exploration Rover (MER) Opportunity discovered hematite spherules (“blueberries”) in the Burns formation in Meridiani Planum, Mars (Grotzinger et al., 2005; McClennan et al., 2005). Navajo Sandstone concretions have been proposed as a terrestrial analog for these spherules (Chan et al., 2004; Ormö et al., 2004). The terrestrial analog characteristics are herein compared to a detailed characterization of the Mars examples (Calvin et al., 2008) as well as to other proposed terrestrial analogs from the literature to infer how abundant hematite spherules formed in the Burns formation.

Methods

Field work documents the location of different populations from different reaction fronts and measures size distributions. Thin sections of concretion samples are examined for textural analysis of cements. QEMSCAN, visible to near infrared (Vnir) reflectance spectroscopy and Mössbauer spectroscopy are used to determine chemical and mineralogical gradients and cement phases. These methods provide the resolution necessary to see mm to μm -scale *in situ* mineralogical gradients so X-ray diffraction (XRD) was not used (except the samples analyzed with Mössbauer spectroscopy were also analyzed with XRD).

Field Methods

Concretions were examined throughout the $\sim 120 \text{ km}^2$ Spencer Flat area and locations of different sizes, internal/external structures and geometries are documented here. Representative samples of typical and atypical concretions were collected from areas where loose populations of concretions are located (see Appendix A for sample locations and analyses performed).

Exterior colors of concretions range from dark- to light-colored and are described using the Munsell rock-color chart (1975; see Appendix A). The dark-colored concretions range from dusky brown (5YR 2/2) to dusky yellowish brown (10 YR 2/2) and the light-colored concretions range from moderate brown (5 YR 3/4) to grayish red (10 R 4/2). Interior colors can be red, yellow or brown. The red colors range from moderate red (5 R 4/6) to moderate reddish brown (10 R 4/6) through very dark red (5 R 2/6) to very dusky red (10 R 2/2). The yellow and brown colors range from dark yellowish orange (10 YR 6/6) to light brown (5 YR 5/6) to moderate yellowish brown (10 YR 5/4) to moderate

brown (5 YR 3/4).

Size diameters of concretions along the longest axis were measured using a digital caliper to document representative samples of different size populations and reaction fronts (Fig. 1.3) and for comparison with size data for Mars concretions. Measurements were made on 1,400 loose concretions that were weathered out and collected in topographic lows at eight sites. At two sites, *in situ* measurements of concretion diameters were made (200 measurements total) although these are a minimum value because the full diameter may not be exposed. However, loose concretions compared to *in situ* examples extracted from the host rock indicate very little effect of weathering on the concretion diameters. Measurements were taken to 0.01 mm accuracy. Frequency plots were compiled and are shown in the Results section.

Lab Measurements

Petrographic Microscopy

Thin sections from 90 concretion samples represent the variety of internal structures and different sizes from 1 cm in diameter up to 10 cm in diameter. These were examined petrographically to document cement textures. Thin sections of six host rock samples comprise a reference for comparison with the concretions.

QEMSCAN

QEMSCAN (Quantitative Elemental Mineralogy using a SCANNing electron microscope) is four high-speed energy dispersive detectors that produce a detailed mineralogical map of a sample (polished thin section or plug). QEMSCAN can



Fig. 1.3. Location map of representative populations measured for size distributions. Black dotted box in inset indicates large map area. Sample number descriptions are given in Appendix V.

distinguish variations in minerals and detect mineral cement phases present in amounts down to $1\mu\text{m}^2$ areas. These data are normally undetectable by other methods (such as XRD). Small variations in mineralogy, chemistry and texture allow inference of chemical and mineralogical gradients across the concretions. QEMSCAN can also image porosity and give area percent of any mineral phase or porosity in two dimensions.

Polished thin sections were made of five representative concretion samples. The carbon coated samples were taken to Xstrata Nickel in Sudbury, Ontario for QEMSCAN

analysis. A Species Identification Protocol (SIP) was developed for this data set. Mineralogical images of each sample in its entirety were made at a 10 μm pixel spacing, with detailed examinations within the rinds and interiors at 1 μm pixel spacing. Backscattered electron (BSE) images of the five samples were examined in conjunction with the QEMSCAN to compare textural properties with different mineral phases.

Visible to Near Infrared (Vnir) Reflectance Spectroscopy

Vnir reflectance spectroscopy is an effective method for determining mineral phases and compositions of cementation in the Navajo Sandstone (Bowen, 2007; Seiler, 2008). Vnir reflectance spectroscopy measures the unique spectral signature that is reflected when a light is shone on a sample and particular wavelengths of energy are captured in molecular bonds in the minerals. This type of spectroscopy measures reflectance in the 350-2500 nm range. The Navajo Sandstone consists of 91% quartz and 9% feldspar (calculated from QEMSCAN data); these minerals do not have distinct adsorption features in the 350-2500 nm range. HFO phases, kaolinite and illite, however, do have adsorption features in this range (Bowen et al., 2007). Therefore, Vnir reflectance spectroscopy is an excellent tool for determining HFO phases and clays present in this unit.

Characteristic adsorption features for minerals in this study are (Fig. 1.4): hematite (~871 nm), goethite (~894 nm), lepidocrocite (~933nm), ferrihydrite (~949 nm), kaolinite (~2200 nm) and illite (~2200 nm). Kaolinite is distinguished from illite by shoulders at ~2180 nm and 1490 nm. There are also OH^- adsorption features at ~1400 nm and ~1900 nm associated with ferrihydrite, lepidocrocite, kaolinite and illite; however, the clay adsorption features can interfere with the OH^- features of the HFOs when both clays and

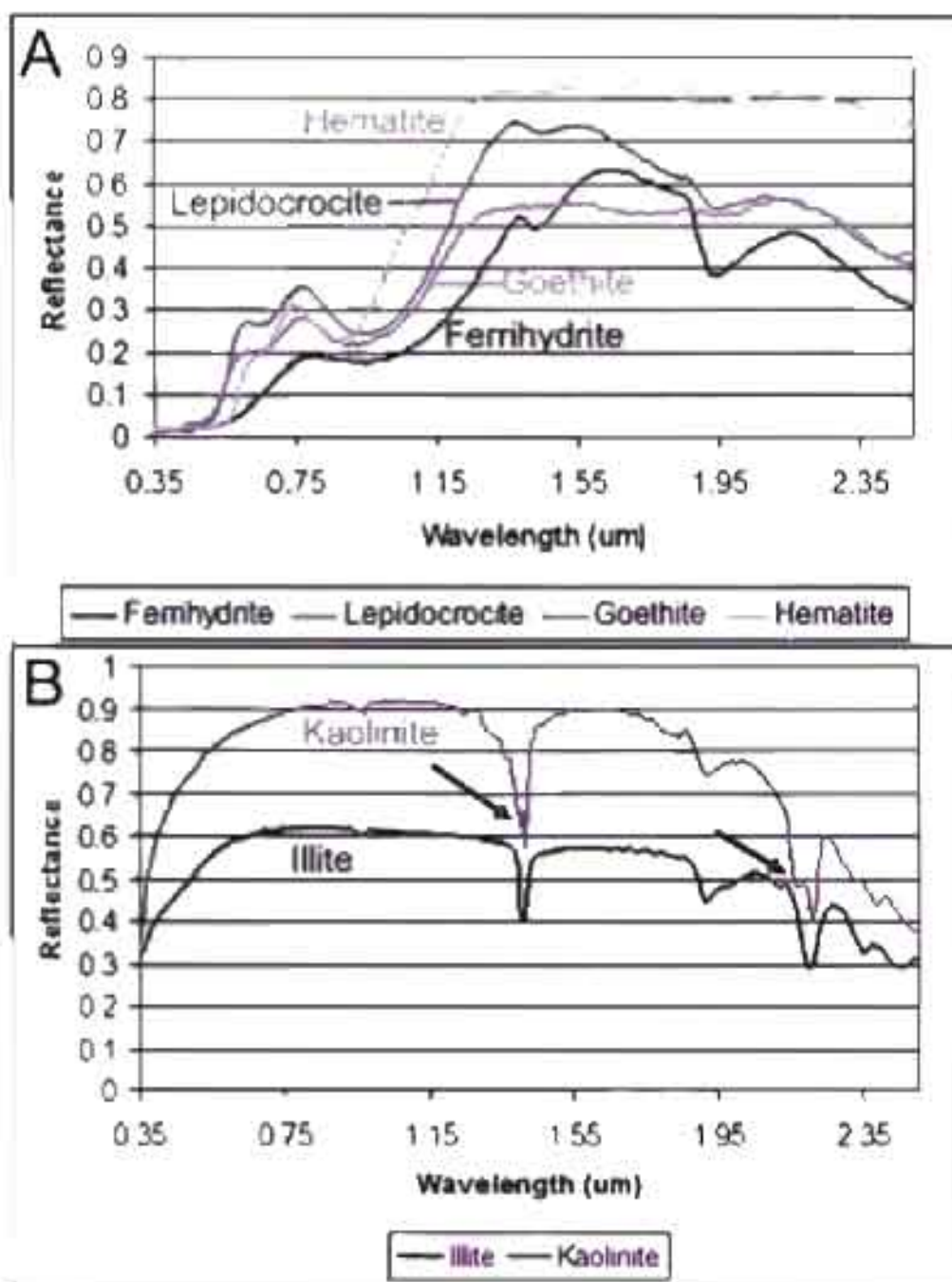


Fig. 1.4 VNIR reflectance spectral signatures of HFO (A) and clay mineral phases (B) from USGS spectral library 06a standards (Clark et al., 2007). Kaolinite and illite have similar absorption minima, but kaolinite has distinct shoulders at 1490 nm and 2200 nm (arrows).

HFOs are present (Clark et al., 1990; Clark, 1999).

Reflectance spectra in the range of 350 nm to 2500 nm were obtained on 22 samples (15 samples of rind concretions; 5 samples of layered concretions and 2 samples of solid concretions). Spectra could only be obtained for two solid concretions because not enough light is reflected from these dark colored concretions.

Concretion samples were prepared by cutting or breaking them in half. The fiber optic cable of the unit was positioned ~9 mm from the sample in order to obtain a 3 mm diameter field of view. Spectra were acquired in transects across the samples in overlapping intervals (see Appendix C for all data). The spectra were graphed and adsorption features were compared with standards from the USGS spectral library 06a (Clark et al., 2007) for analysis.

Mössbauer Spectroscopy

Mössbauer spectroscopy is used on five Navajo Sandstone concretion samples to examine the site occupancy and valence state of iron in the concretions, in order to help identify the iron oxides that are present (see Appendix D for all data). For these measurements, approximately 10-20 mg of the concretion's HFO cement was gently mixed with sugar, then heaped in a sample holder confined by kapton tape. Mössbauer spectra were acquired at 295K using a source of 60 mCi ^{57}Co in Rh on a WEB Research Co. model WT302 spectrometer (Mount Holyoke College).

Multiple sources of error contribute to the estimated uncertainties in the results. In Mössbauer spectroscopy, either a single peak, a doublet or a sextet represents iron in each individual site and valence state. The six peaks in a sextet have areas in the ratios of 3:2:1:1:2:3 unless the spins interact. In these samples, grain size interactions between the

spins of the iron atoms are interfering with the ordered iron oxide spectra so most of the spectra do not conform to the ideal 3:2:1 peak area ratio typical of magnetic sextets. In some cases, there is significant contribution (represented by a broad background peak) from a distribution of grain sizes and unresolved sextet structure. Although some sextets were fully-formed, others were incompletely ordered at 295K, making it impossible to assign them to specific phases (see discussion of results below for elaboration and figures). Ubiquitous overlap between peaks also contributed to difficulties in assignment of spectral features, as did the low percent absorption.

Textural and Geometric Characterization

The discussion of characterization is organized by concretion size: macro concretions (5 mm to 10+ cm in diameter; Fig. 1.5, 1.6), followed by micro concretions (~1-5 mm in diameter; Fig. 1.5, 1.6A), and then separate sections on conjoined forms and a final treatment of concretion size distributions. For the first group of macro concretions, these are divided into rind, layered and solid internal structure categories (Fig. 1.5A, B, C), with a general description of shape, color and exterior features, followed by interpretation of those features for each internal structure category. Summative analytical studies of petrography, QEMSCAN, Vnir spectroscopy and Mössbauer spectroscopy results and interpretations are given for the collective group of macro concretions. Micro concretions are generally too small for detailed analytical studies.

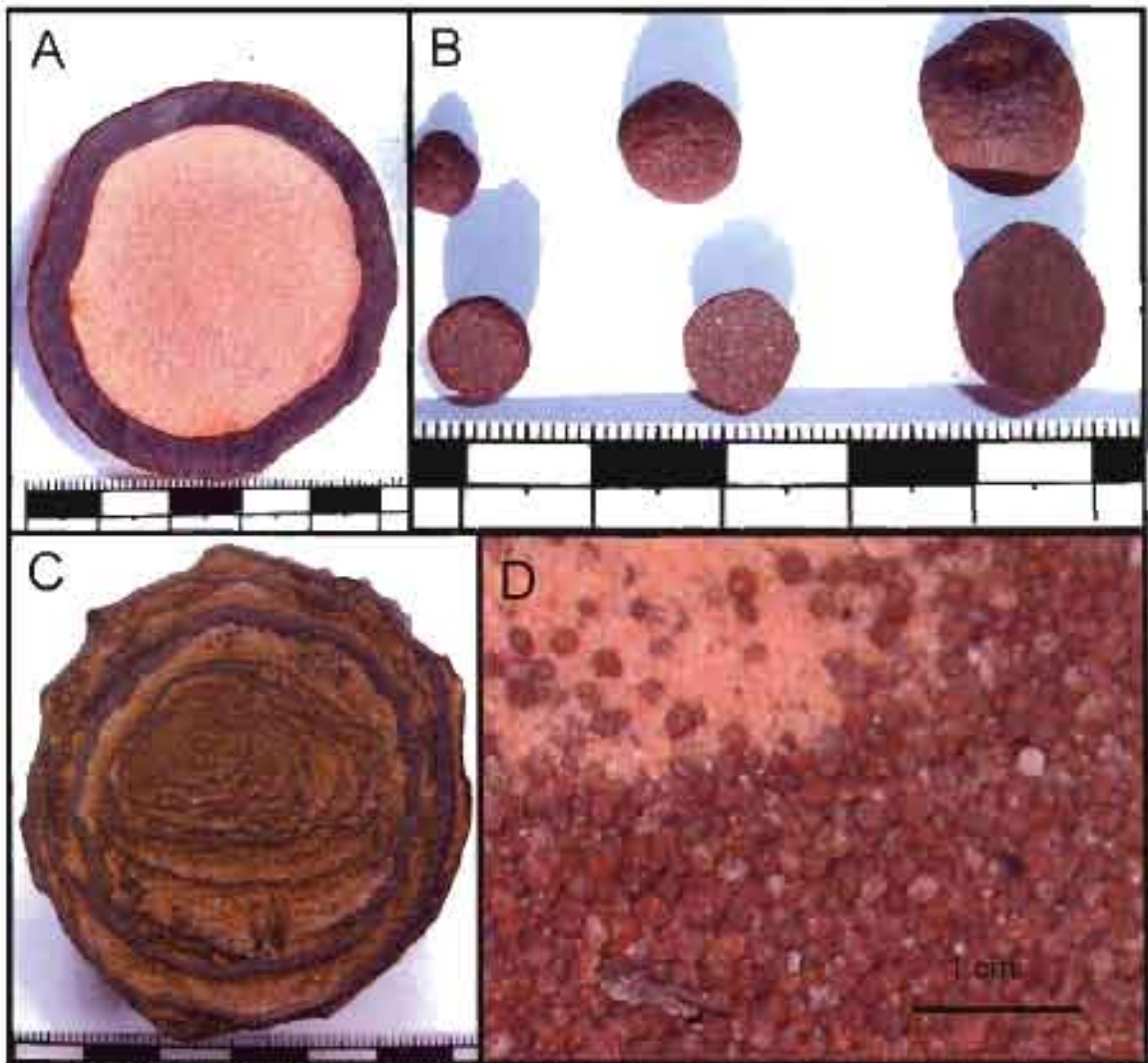


Fig. 1.5 Macro and micro concretions of the Navajo Sandstone and macro concretion internal structure end members. Large tick marks on scale bar are cm. A. Rind macro concretion end member with well-cemented rind surrounding interior relatively depleted of HFO cement. B. Solid macro concretion end members evenly cemented with HFO throughout the concretion. C. Layered macro concretion end member with HFO cemented layers throughout the interior. D. Loose micro concretions collected in topographic low.

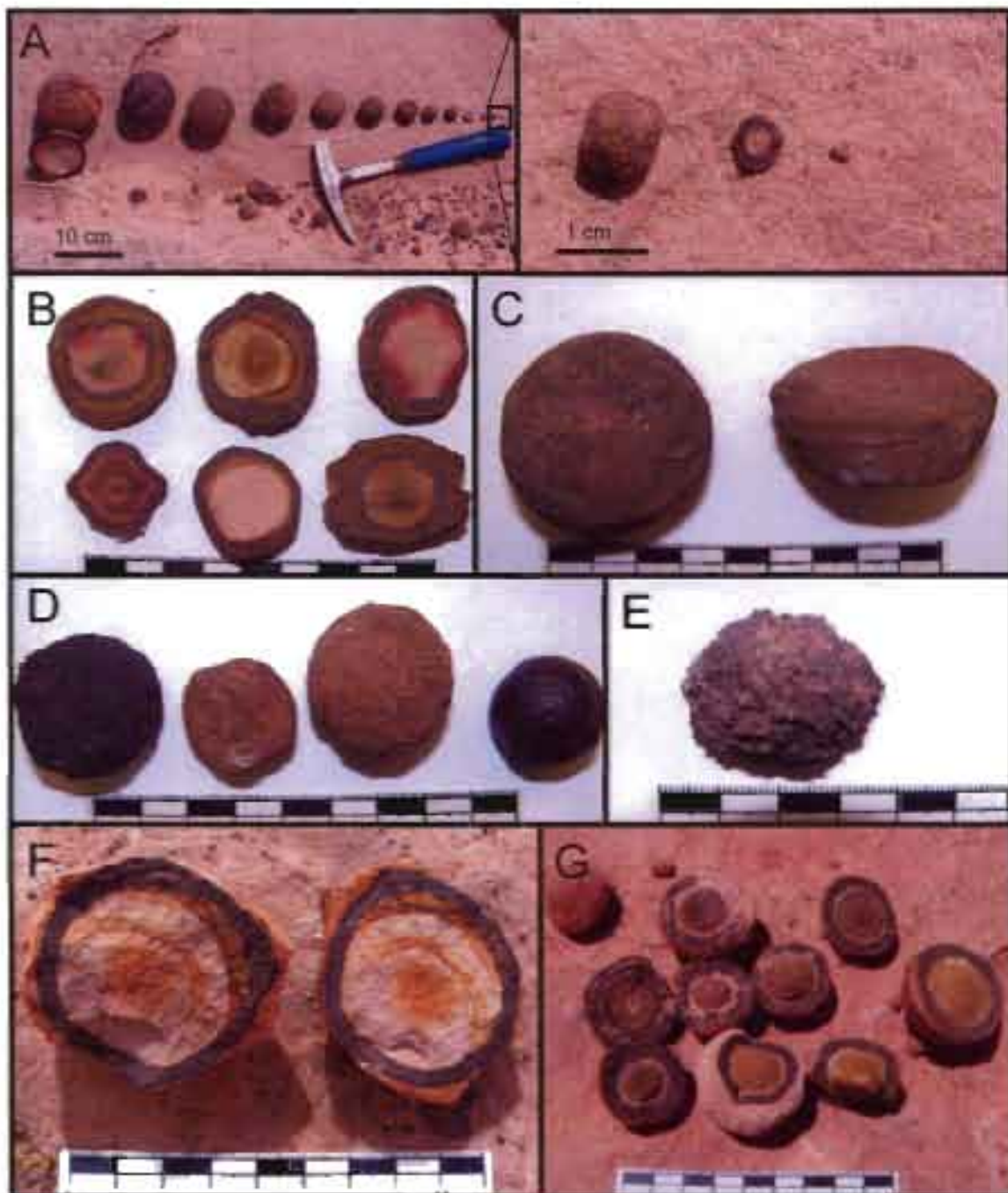


Fig. 1.6 Interior and exterior spheroidal HFO concretions structures. A. Range of sizes of concretions. Box outlines inset (right) of smallest sizes. B. Some of the varieties of interiors that blend end members between rind, layered and solid. C. Spheroidal and discoidal concretions. Spheroidal concretions are present in more homogenous sandstone. Where sandstone is differentiated due to grain size contrast, discoidal concretions are present. D. Range of exteriors: dark or light colored (see text for Munsell color descriptions), sandy and rough, and smooth and polished. E. Bumpy exterior that appears to consist of coalesced micro concretions. F. Asymmetrical Liesegang bands in interior of concretion. G. Interiors that are better cemented than rinds or layers.

Rind Macro Concretions

Description

Rind concretions - the most common type of macro concretion present in Spencer Flat - are typified by a thin (1 mm to 10 mm) spheroidal rind consisting of HFO cemented sandstone surrounding an interior that is relatively depleted of cement (Fig. 1.5A). Rinds typically comprise ~25% to 60% of concretion volume, estimated by subtracting the volume of the interior from the total volume of the concretion (and assuming perfect sphericity). Rind concretions are generally preferentially cemented relative to the surrounding host rock and weather out to collect in topographic lows (Fig. 1.1C).

Geometries of rind concretions (see Chapter 2 for geometrical details) range from truly spherical (aspect ratio=1) to nearly spherical (aspect ratio ≤ 1.06) to discoidal (aspect ratio > 1.06) depending on anisotropies in the host rock. In general, the spheroidal macro concretions (from diffusive mass transfer) occur in the upper portion of the Navajo Sandstone where much of the cross bedding has been disturbed (soft sediment deformation) and/or where the sandstone is massive. In the lower portions of the Navajo Sandstone where the cross bedding is more prevalent (and undisturbed), concretions can be either spheroidal (within thick grainflow beds) or discoidal where concretions grow in alternating wind ripple and grainflow laminae. Preferential discoidal growth tends to elongate along the more permeable grainflow laminae (e.g., flying saucer shapes reflect a central grainflow lamina).

Dark-colored concretions (see Field Methods for Munsell rock-color description) are typically well-cemented and when weathered out and loose, they may exhibit a shiny, smooth polish. Light-colored concretions can be well-cemented, but they have a sandy

exterior and do not exhibit a high polish. Some exteriors exhibit a bumpy, “avocado-skin” texture (Fig. 1.6E).

Interiors of the rind concretion end member are depleted of cement and are friable sandstone relative to the rind. However, interiors of rind concretions display varying degrees of cementation and commonly contain asymmetrical or concentric red, brown or yellow rings in self-organized, banded patterns called Liesegang bands (Fig. 1.6B, F).

Interpretation

Nearly spherical/spheroidal concretions imply even growth in isotropic media by diffusive mass transfer (Seilacher, 2001, McBride et al., 2003, Mozley and Davis, 2005). Macro concretions form via diffusive mass transfer through the host rock in reaction fronts. However, advection may have a role in mobilizing larger amounts of reactants to these diffusive reaction fronts. Where cross-bedded sandstone has alternating grainflow and wind ripple laminae, diffusion occurs preferentially along the more porous and permeable grainflow laminae where discoidal shapes form. This implies faster reactant transfer modifies the concretions from a perfectly spherical form to a more discoidal shape along the more permeable laminae. Where sandstone is more isotropic or homogenized (massive), concretions are more spherical in shape because diffusion rates are evenly distributed throughout the isotropic sandstone.

External color differences result from degree of cementation and/or differences in mineralogy or crystal size. Hematite crystals larger than 5 μm are grey and crystals smaller than 5 μm are reddish-brown (Lane et al., 1999; Glotch et al., 2004). Smooth, shiny exteriors occur only on weathered out concretions and could possibly be due to sandblasting or a desert varnish. Bumpy external texture results from micro concretions

coalescing to form larger, macro concretions in an Ostwald ripening type of process. This Ostwald ripening process results because smaller concretions nucleate more easily than larger concretions and nucleate preferentially where HFO is already precipitated (see Steefel and Van Cappellen, 1990, for a discussion of Ostwald ripening).

Layered Macro Concretions

Description

Layered concretions have the same type of exterior rind as the rind concretions (~1-5 mm thick) but also possess two or more (up to ~15 depending on the diameter of the concretion) preferentially cemented, thin, overlapping layers (~0.3-1 mm thick) that persist throughout the interior of the concretion (Fig. 1.5C, 1.7). These layers may extend throughout the entire interior of the concretion or the concretion may have a center depleted of cement similar to rind concretions (Fig. 1.7B). Layered concretions occur in all areas where rind concretions are present (See Appendix A for sample descriptions and locations). Layered concretions have the same exterior structure as rind concretions such as size, shape and exterior color and texture.

Interpretation

Layered macro concretions occur in reaction fronts with rind and solid macro concretions and are indistinguishable by external appearance from these other end members. These characteristics imply a similar genesis for all end members of macro concretions.

Although three end members of macro concretions are present (rind, layered and solid), concretions likely precipitate initially as rind concretions. The layered end

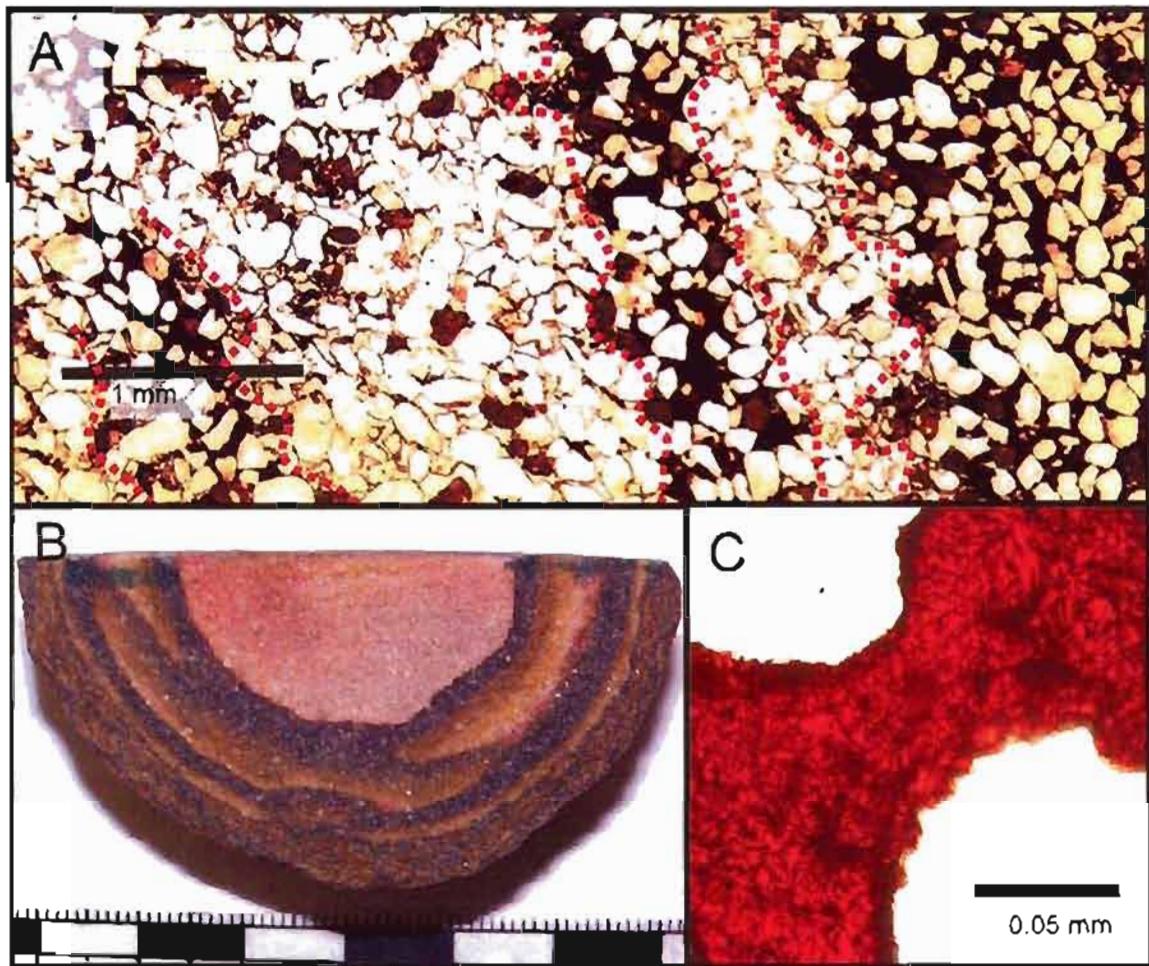


Fig. 1.7. Layered macro concretions. Large tick marks on scale bar = 1 cm A. Photomicrograph of layered concretion. Red dotted lines differentiate well-cemented layers from more friable areas. C. Layered macro concretion with a friable center depleted of HFO cement. D. Fine-grained HFO cement in an interior layer of layered macro concretion.

member consists of periodic precipitation bands (Liesegang bands) that can persist throughout the interior of the concretion. Liesegang bands form via diffusive reactant transfer (Ortoleva, 1994). Therefore, the internal structure of layered concretions may be modified as additional reactants (iron and/or oxygen) diffuse through outer rinds during late-stage precipitation events.

Another possibility is that reactants are drawn from interior sources and/or edges of the rinds and reprecipitate throughout the interiors; however, textural analysis suggests

diffusion of reactants through gel-like rinds is more likely. Isopachous cement textures suggest a pervasive growth model similar to carbonate concretions where original, retained porosity is infilled by subsequent precipitation events (see Petrographic Microscopy Results and Interpretation and Discussion for elaboration). Layered concretions may originally precipitate HFO cements that retain just enough porosity to allow more reactants to diffuse through semipermeable, gel-like rinds. This diffusive mass transfer modifies internal structures creating layered and solid interiors as well as internal structures intermediate between the end members.

Solid Macro Concretions

Description

Solid macro concretions (Fig. 1.5B) exhibit the same external or surface features as other macro concretions; however, internally, they are evenly cemented with HFO throughout the entire concretion (~23.5% HFO determined via QEMSCAN analysis). Solid concretions may have a rind that is slightly differentiated from the interior by color, but the interior is not depleted of HFO cement (Fig. 1.8A). Some solid interiors are preferentially harder than the rinds (Fig. 1.8B).

Interpretation

Solid macro concretions are present in reaction fronts with other end members (rind and layered) and these concretions are indistinguishable by external appearance from other types of macro concretions. This suggests that solid, rind and layered macro concretions all form via the same genetic processes. The presence of faint rinds in some solid macros suggests these interiors may also have been modified by late-stage

precipitation events (like layered concretions) that diffused reactants through semipermeable rinds.

Micro Concretions

Description

Micro concretions (Fig. 1.5D) are more common than other types of concretions and are ubiquitous throughout southern Utah and northern Arizona in the Navajo Sandstone. Micro concretions occur where macro concretions are present and also in areas where macro concretions are lacking. Micro concretions are typically present where regional secondary coloration has occurred. Micro concretions are generally cemented well enough to weather out of the host rock and collect in topographic lows; however, they do exhibit varying degrees of cementation. They can be associated with diffusive reaction fronts, occurring between Liesegang bands (Fig. 1.8E). Micro concretions also can coalesce to form thicker rinds of macro concretions, creating the bumpy external appearance resembling avocado skin (Fig. 1.8F,G) on some macro concretions.

Interpretation

The ubiquitous nature of spheroidal micro concretions, their association with Liesegang bands and their spheroidal geometry suggest micro concretions form via simple diffusion. Diffusive reaction fronts in the Navajo Sandstone are associated with diagnostic features such as Liesegang bands (Beitler et al., 2005; Seiler, 2008, Chapter 2) and micro concretions typically form in these reaction fronts. Spheroidal concretion formation is also indicative of diffusive mass transfer (Seilacher, 2001, McBride et al., 2003, Mozley and Davis, 2005).

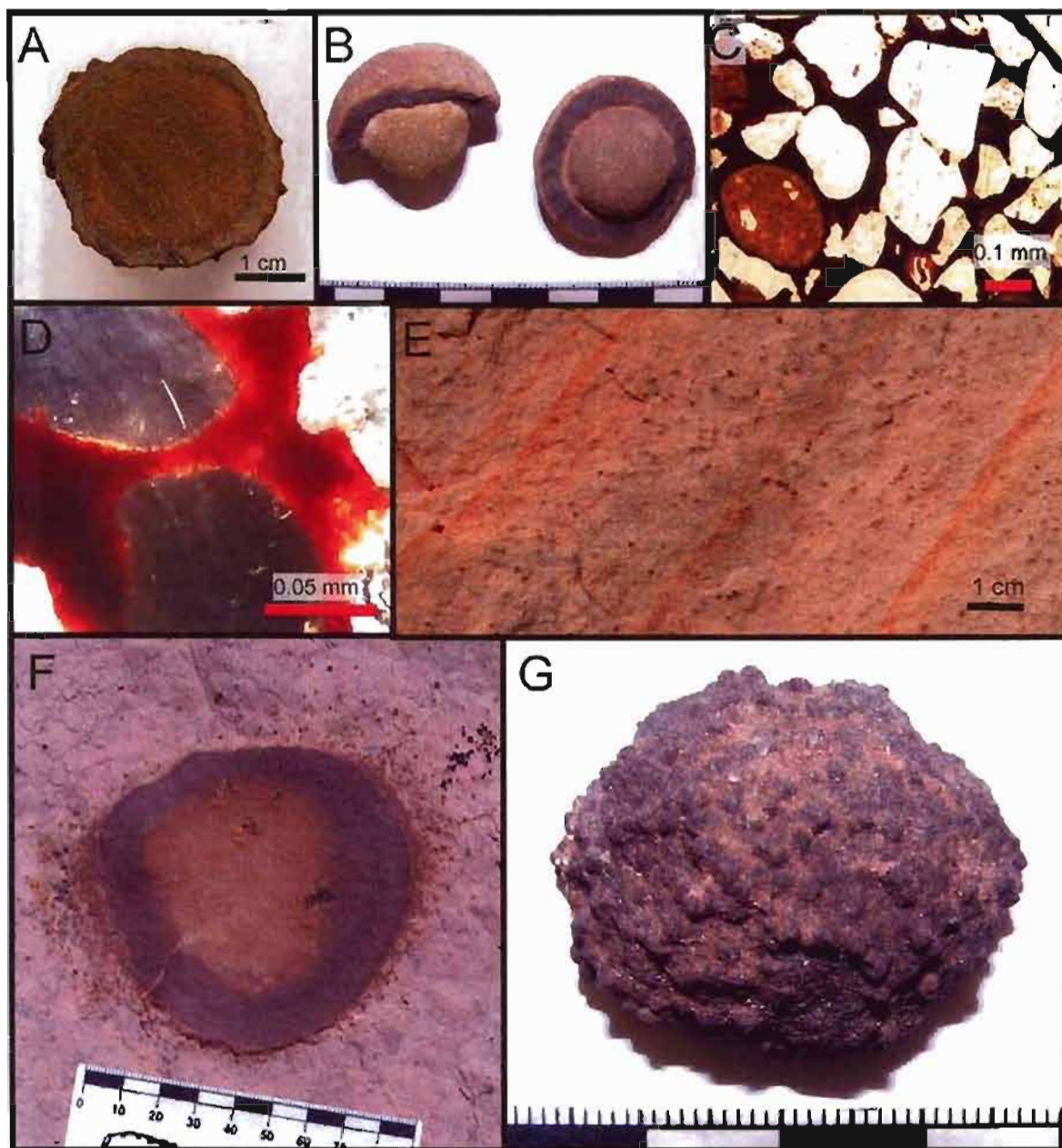


Fig. 1.8. Solid macro concretions and micro concretions. A. Solid macro concretion with interior differentiated from rind by color. B. Rind macro concretions with interiors harder than the rinds. Large tick marks on scale bar = 1 cm. C. Plane light photomicrograph of solid macro concretion. Cementation is solid throughout entire concretion. D. Polarized light photomicrograph of granular HFO cement in solid macro concretion. E. Micro concretions in between Liesegang bands in a diffusive reaction front. F. Micro concretions coalescing to form larger concretion. Scale bar in mm. G. Bumpy “avocado skin” exterior of concretion that seems to be formed from coalesced micro concretions. Smallest ticks on scale bar are mm.

The coalescing nature of micro concretions to form the bumpy-texture of the macro concretions suggests an Ostwald ripening type of process where smaller concretions nucleate more easily than larger sizes and HFO precipitates preferentially where crystals have already nucleated (see Steefel and Van Cappellen 1990 for a discussion of Ostwald ripening). This may contribute a component of radial growth to the bumpy-textured macro concretions (see Introduction and Discussion for explanation of pervasive and radial growth models).

Doublets and Triplets

Description

Doublets and triplets typically consist of equal-sized, conjoined concretions. Both macro and micro concretions can form doublets and triplets and conjoined forms are present both *in situ* and loose in topographic lows (Fig. 1.9). Doublets and triplets comprise ~5% or less of a typical loose collection where most of the concretions are single forms; however, one reaction front (~0.25 km²) in the study area contains ~95% macro concretion doublets (ranging from ~1 cm to 4 cm diameter for each side). *In situ* doublets and triplets in both types of reaction fronts (fronts that produce mostly single forms and fronts that produce mostly doublets) typically exhibit self-organized spacing like other spheroidal concretions.

Interior structure of conjoined forms ranges between the rind, layered and solid end members. Exterior structure is similar to single macro concretions; exteriors can be smooth or sandy (Fig. 1.9C, E). Exteriors can also be bumpy (“avocado skin”) indicating micro concretions coalesced to form the larger macro doublets (Fig. 1.9E). All conjoined forms typically share internal structure (Fig. 1.9D, F); they are not two discrete, fused

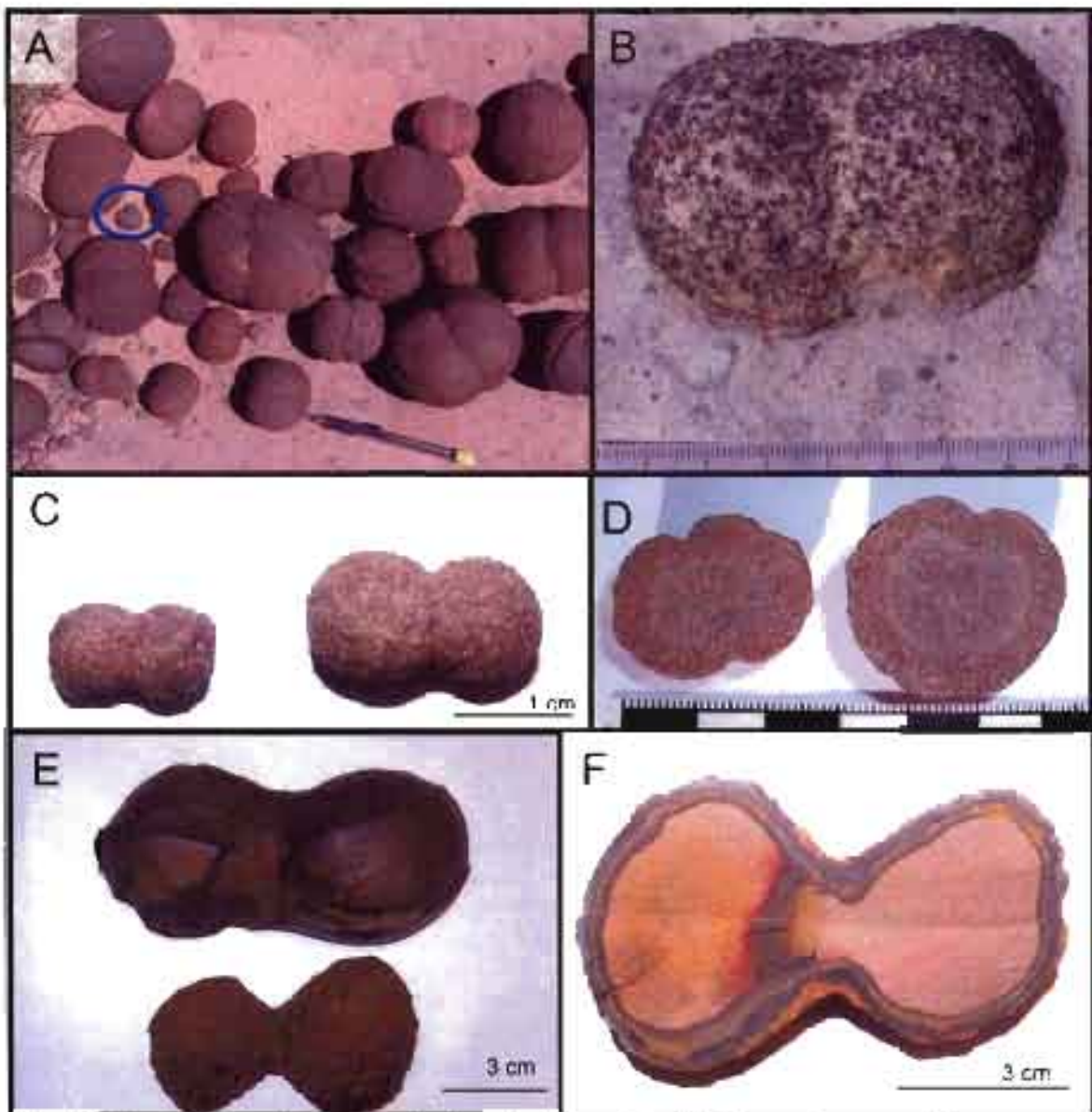


Fig. 1.9. Fused forms (macro and micro doublets). Small tick marks on scale bars – mm.
 A. Loose doublets from reaction front with mostly fused forms. Blue circle surrounds a triplet form. Note range of sizes of macro doublets (pencil for scale). B. *In situ* macro doublet with exterior formed from coalesced micro concretions. C. Micro doublets. D. Solid interior structure with faint rind defined by color difference. E. Macro doublets with smooth (top) and “avocado skin” (bottom) exterior structure. F. Layered macro concretion doublet with interior relatively depleted of cement. Doublets share internal structure and are not two joined concretions.

concretions.

Other multiple conjoined forms (i.e., clumped clusters of more than three spheroidal concretions) can occur but these are not as common as the other single, double or triple forms. These clusters form in localized reaction fronts (1-2 m²) and result from a nucleation pattern that produces clusters (possibly due to the presence of organics) instead of a geochemically self-organized spacing (see Chapter 2).

Interpretation

The equality of size for each conjoined section, the local abundance in one reaction front and the shared internal structure indicates that doublets and triplets likely form in one precipitation event where two (or three) conjoined concretions nucleate simultaneously. If a single concretion formed and a second was added in a subsequent precipitation event, the two fused concretions would likely be unequal in size and would share a dividing center rind between them.

Size Distribution

Description

Diameters of concretions were measured in the field from populations of loose, weathered out concretions to determine if more than one population is present and if the population(s) is normally distributed (see Appendix E for all measurements). Loose, weathered out concretions represent true diameters of concretions because there is no visible loss of diameter due to weathering when compared to *in situ* concretions extracted from the host rock. Frequency plots of the diameter measurements were compiled (Figs. 1.10a, 1.10b) and they are typically normally distributed or bimodal. The distribution of

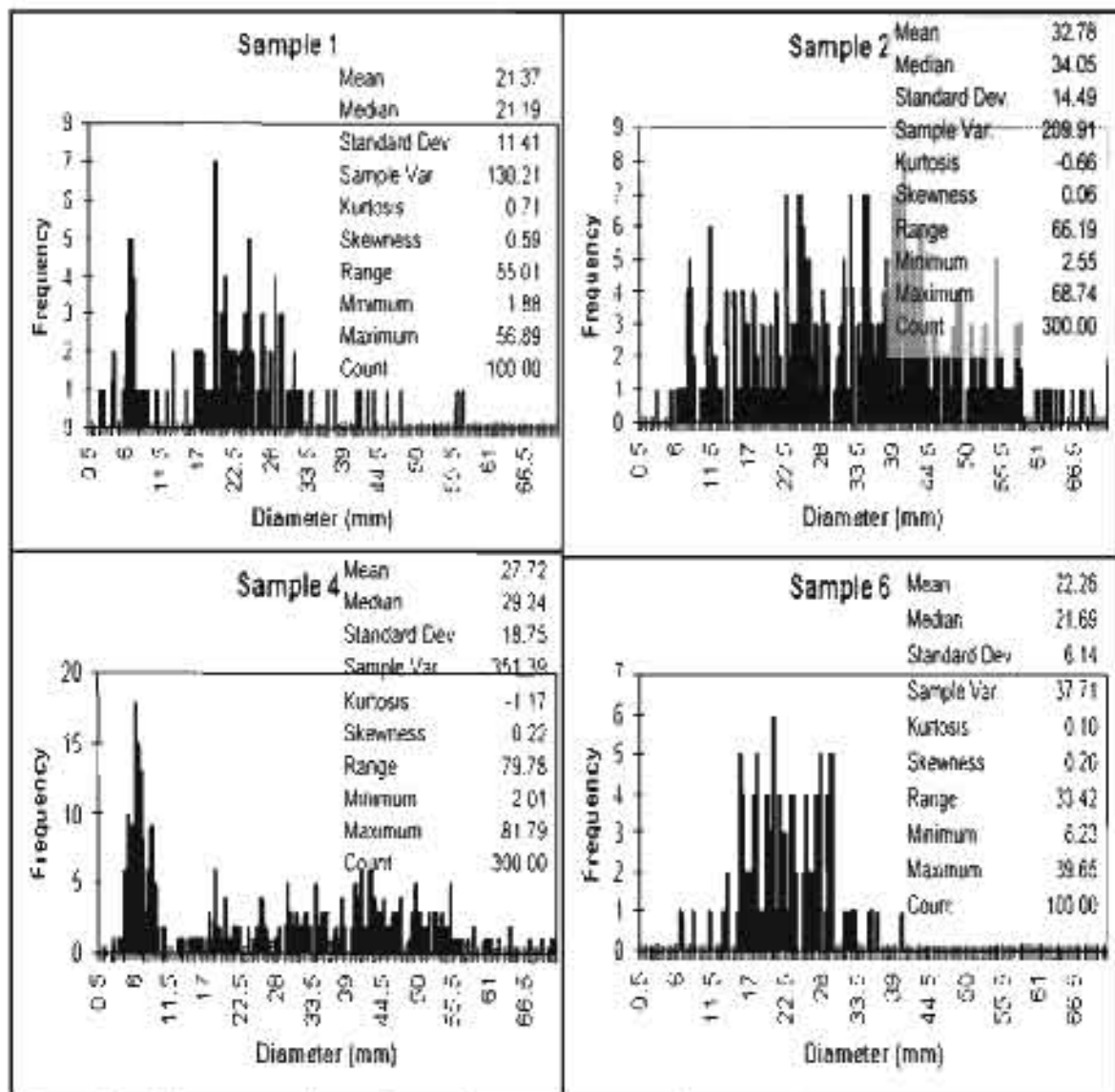


Fig. 1.10a: Frequency plot of concretions diameters for sample sites 1, 2, 4 and 6 (see Fig. 3 for locations of sample sites). Descriptive statistics for each site are shown in insets. (Sample site 3 was *in situ* population and sample site 5 had many conjoined forms so data are not shown for those sites.)

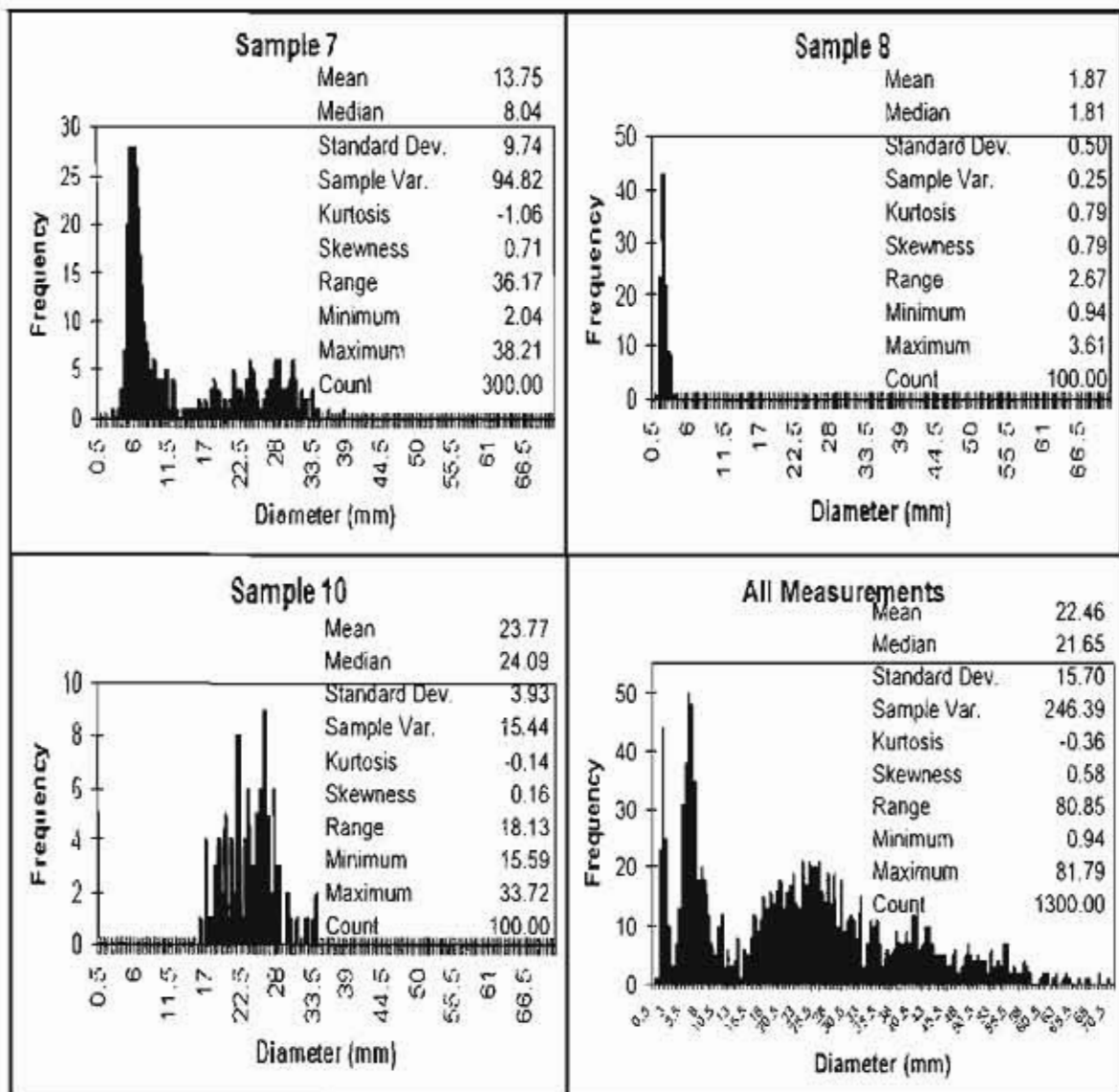


Fig. 1.10b. Frequency plots of concretion diameters for samples sites 7, 8, 10 and all measurements combined (see Fig. 3 for location map). Descriptive statistics for each site are shown in insets. (Sample site 9 was *in situ* population and is not shown.)

the combined measurements from all the sites is trimodal. Macro concretions (>5 mm diameter) are actually comprised of two dominant modes, although a range of sizes exists.

At two sites, concretion diameters were measured *in situ* (n=200; see Appendix E). The frequency plot of these concretions is normally distributed (mean=6.8363, median=5.86, mode=6.71). *In situ* measurements are not a true diameter; they only represent a minimum diameter exposed by weathering of the host rock.

Interpretation

There are three normally distributed populations in the size distribution of all measured, loose concretions. For this paper, we differentiate between macro concretions (> 5 mm diameter) and micro concretions (<5 mm diameter), but there is a natural division in the macro concretion population of two normally distributed size populations (5-12 mm and >12 mm). Typically, an accumulation of loose concretions in a topographically low area (1-2 m²) contains one or two size populations and these accumulations are a result of resistant concretions forming a “let down” lag as the host rock erodes. These lags represent 10s of meters of eroded section. More than one size population in a loose accumulation may represent stratigraphic size divisions or the populations may represent overlapping reaction fronts. The latter is more likely because two or more size populations can be present *in situ*. Nevertheless, different size populations represent discrete reaction fronts with varying reactant supply.

Size of reaction fronts is difficult to determine; however, a ~0.25 km² reaction front is documented (see Doublets and Triplets section for description of twin reaction front). A larger reaction front (~0.6 km²) is also recognized by a population of bumpy-textured

concretions. The abundance and localization of macro concretions throughout Spencer Flat suggests that a reaction front of these ~ 2-3 cm size concretions may be significantly larger (up to 120 km²).

Analytical Results

Petrographic Microscopy Results and Interpretation

In the outer layer of rind concretions, HFO cementation nearly occludes pore space (~27.0% HFO determined via QEMSCAN analysis), yet in the interiors, HFO cementation is sparse (~0.5% HFO) (Fig. 1.11A). The interior edges of the rinds are irregularly shaped and exhibit inward digitate growths toward the center of the concretion (Fig. 1.11B). Well-cemented rinds are low porosity (~1.8%) and friable interiors are high porosity (~29.1%).

In the rinds of macro concretions (rind and layered), three textures of HFO cement are distinguished through petrographic microscopy: 1. granular-textured cement coats and rims the grains, 2. tabular cement is adjacent to the granular and radiates into the pore space, and 3. late-stage pore filling consists of small, euhedral crystals (Fig. 1.11C). Rinds of layered concretions have the same three textural phases of HFO cement; however, the interior layers are comprised solely of a fine-grained phase (Fig. 1.7C). In solid concretions, the HFO cement is granular-textured (Fig. 1.8C, D).

Cement in the depleted interiors is primarily kaolinite (1.68%) present in blebs. Interior kaolinite blebs are not associated with the weathering of orthoclase grains (Fig. 1.11D). HFO is present in minor amounts (~0.5%) in pore throats and as grain coatings and the HFO is granular-textured (Fig. 1.11E). Many grains exhibit a thin illite coating visible with a petrographic microscope (Fig. 1.11F). Only two samples out of 90

contained what appeared to be euhedral pyrite crystal pseudomorphs in the HFO cement visible with a reflected light microscope.

At least three generations of isopachous cement indicate that late-stage precipitation of cements infilled the retained, original porosity. This suggests concretions grow via a pervasive growth model similar to some carbonate concretions where HFO nucleates at sites concomitantly throughout the concretion. These concretions precipitate HFO gel as a primary concretion cement that sets the radius and likely retains some porosity (see Raiswell and Fisher 2000 for a discussion on pervasive growth in carbonate concretions). Therefore, original porosity of the rinds would be much higher than present porosity (1.8% using QEMSCAN analysis) and reactants would be able to diffuse through these higher porosity gel-like HFO rinds to modify internal structures and precipitate additional isopachous cements that are present.

HFO likely precipitated originally as an amorphous gel that later dehydrated to the more stable phases of goethite and hematite (Steeffel and Van Cappellen, 1990). The lack of pyrite pseudomorphs or carbonate in the concretions suggests that the HFO precipitated directly rather than initially precipitating as an Fe^{2+} mineral (pyrite or siderite) that later oxidized to HFO.

QEMSCAN Results and Interpretation

QEMSCAN analysis provides mineralogical maps of samples. Images of five thin sections are compiled at 10 μm spacing and detailed areas are compiled at 1 μm spacing (Fig. 1.12). Cements in the rinds are identified and area percent measurements are

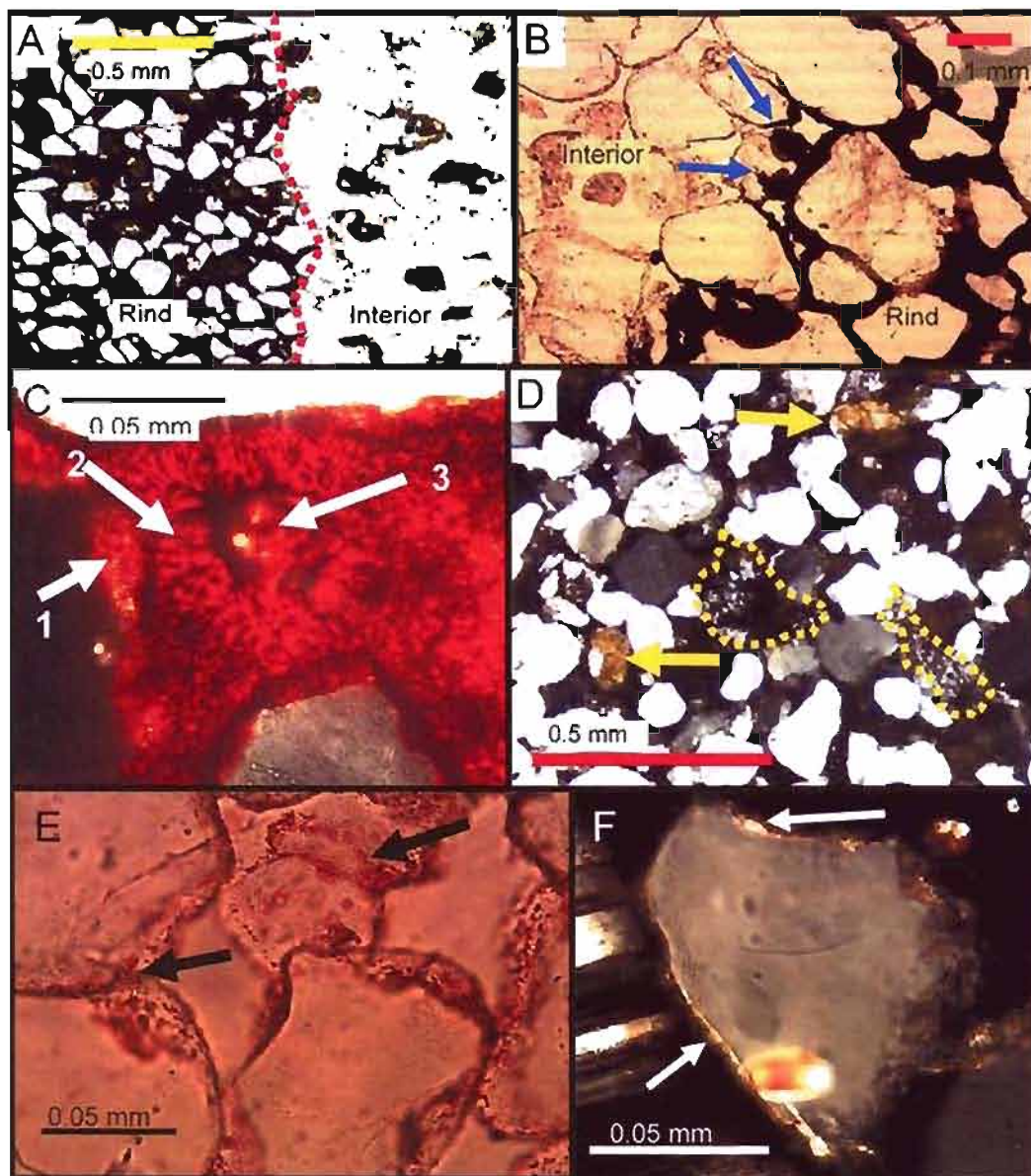


Fig. 1.11. Photomicrographs of rind macro concretions. A. Plane light photomicrograph of rind/interior boundary of a rind concretion. Red dotted line delineates boundary between well-cemented rind and interior relatively depleted of cement. B. Plane light photomicrograph of rind/interior boundary with digitate inward growths of HFO cement. C. Polarized light photomicrograph of three phases of HFO cement: 1. granular cement rimming edges of quartz grains, 2. tabular cement, and 3. small, euhedral crystals infilling remaining pore space. D. Polarized light photomicrograph of interior of rind macro concretion. Kaolinite cement is outlined with yellow dotted lines. Notice the kaolinite is not weathering replacement of feldspar grains. Yellow arrows point to feldspar grains (dyed yellow). E. Plane light photomicrograph of interior of rind macro concretion. Arrows point to granular HFO cement in pore throats and rimming quartz grains. F. Polarized light photomicrograph of quartz grain with high birefringence illite coating (arrows) in interior of rind macro concretion.

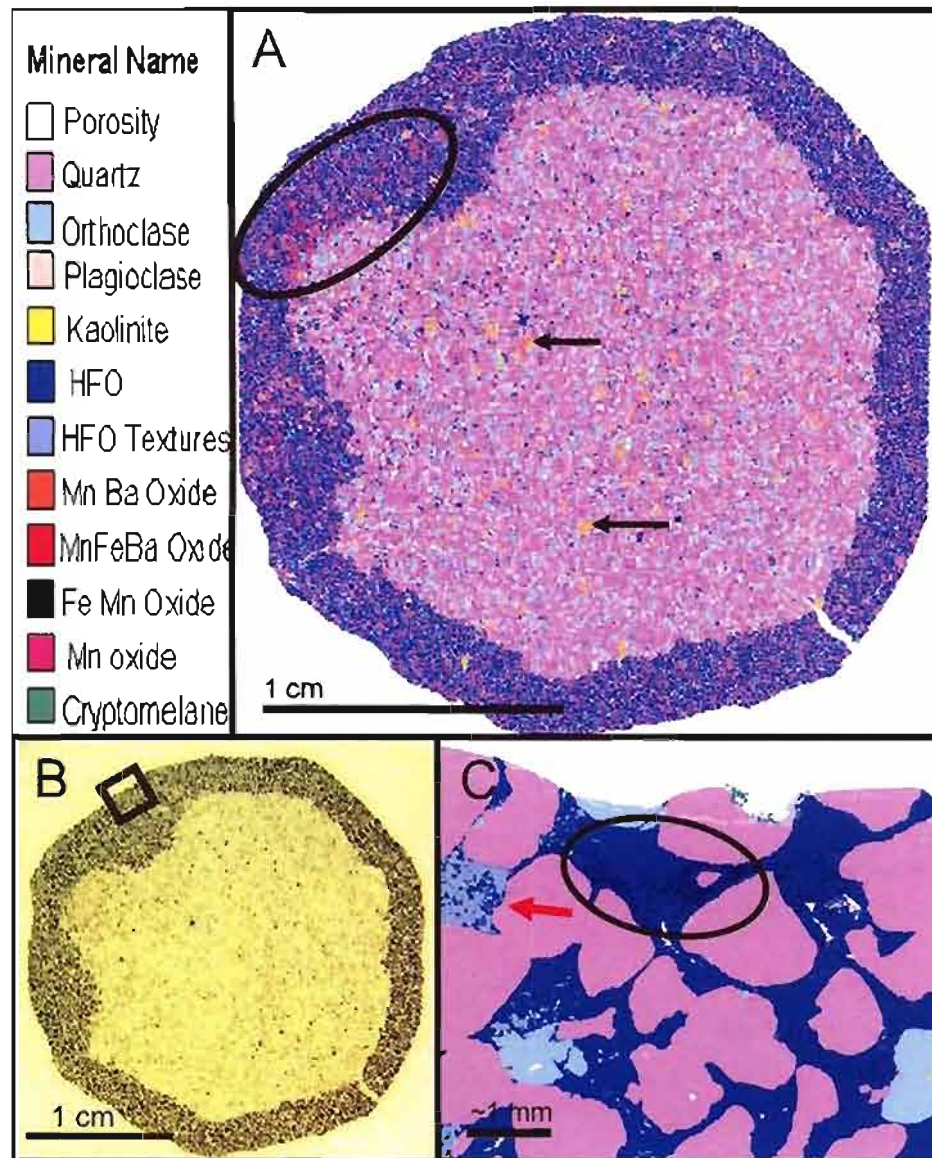


Fig. 1.12. QEMSCAN images of entire thin section at 10 μm spacing and detail at 1 μm spacing. A. QEMSCAN image of thin section "B" (10 μm spacing). Arrows point to blebs of kaolinite that are oriented independent of orthoclase grains. Oval encircles area on interior edge of rind where a concentration of MnO is present. B. Photo of thin section used for QEMSCAN images A and C. Black box outlines area of detail in "C". C. Detail of rind area (1 μm pixel spacing). Black oval encircles area with concentration of FeMnO in HFO cement. Arrow points to frothy HFO.

normalized to exclude framework grains and porosity (Fig. 1.13; see Appendix B for individual sample QEMSCAN mineralogy and porosity data).

Two textures of HFO cement are identified with QEMSCAN. The most abundant type is a smooth textured HFO visible in back scattered electron (BSE) images and labeled “HFO” in the figures (Fig. 1.14A). The other is a “frothy” textured cement in BSE images and is labeled “HFO frothy” in the figures (Fig. 1.14B). Percentages of cements given here indicate percentage of total cement normalized to exclude porosity and framework grains. Smooth-textured HFO is the most abundant phase in the rinds (94.5%), but in the interiors, the HFO cement is distributed evenly between smooth-textured (20.0%) and frothy-textured (26.8%). Kaolinite is present in both the rind and the interior, but it is the dominant cement in the interior (49.5%). Manganese oxide (MnO) is only present in detectable amounts in the rinds (0.2%). Pockets of MnO are located in interior edges of the rinds along more permeable laminae and are visible in BSE images (Fig. 1.14A, C, 1.15). Porosity in the solid sample analyzed with QEMSCAN is 4.2% and minor amounts of kaolinite are present (0.7%).

Rinds of rind macro concretions are well-cemented with very little porosity compared to the friable interiors. With QEMSCAN, two textural HFO phases are detected and are present in predictable places. The smooth texture from QEMSCAN is probably the tabular texture visible with petrographic microscopy and the “frothy” textured HFO from QEMSCAN is probably the granular texture in thin section.

MnO pockets also occur as a late-stage, pore filling typically along interior edges of rinds and along more permeable laminae (Fig. 1.14A, 1.15). The MnO could be due to a rise in pH in the mineralizing fluid because MnO is precipitated at a slightly higher pH

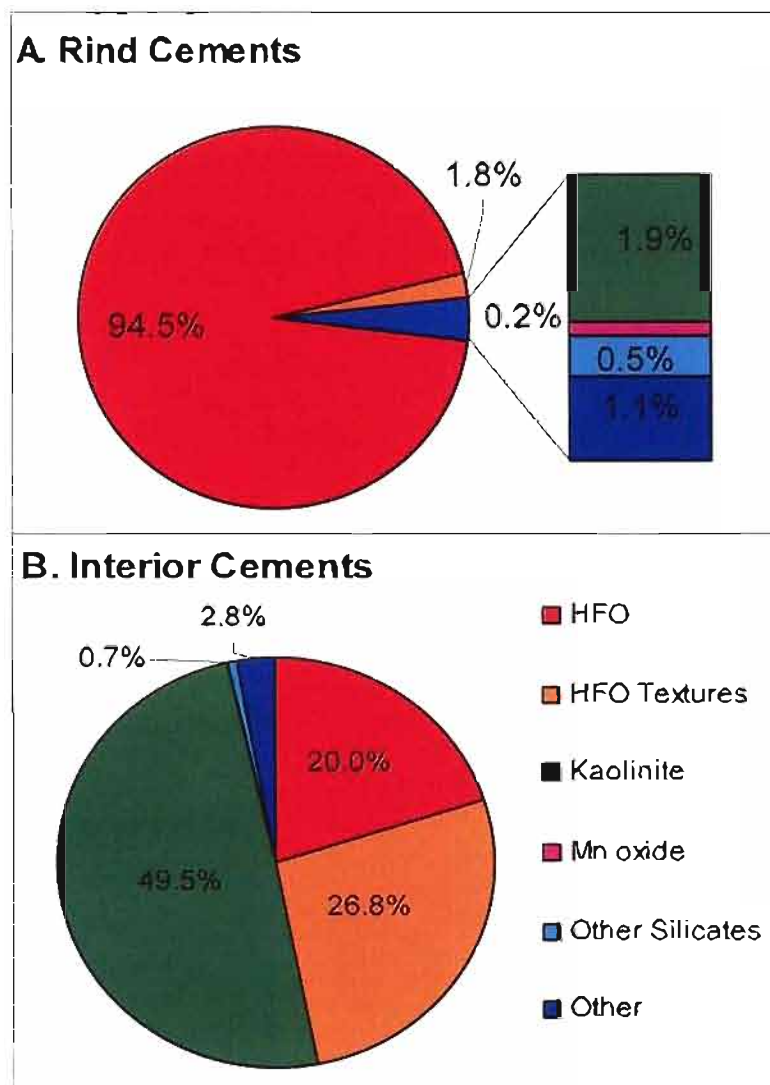


Fig. 1.13. Rind (A) and interior (B) cements normalized to exclude framework grains and porosity. The most abundant smooth-textured HFO is labeled "HFO" in the key. "Frothy" textured cement is labeled "HFO Textures." HFO in the rinds is mostly smooth textured HFO; in the interior, HFO is both smooth and frothy textured. Kaolinite is the dominant cement in the interiors. MnO is present in detectable amounts (0.2%) only in the rind.

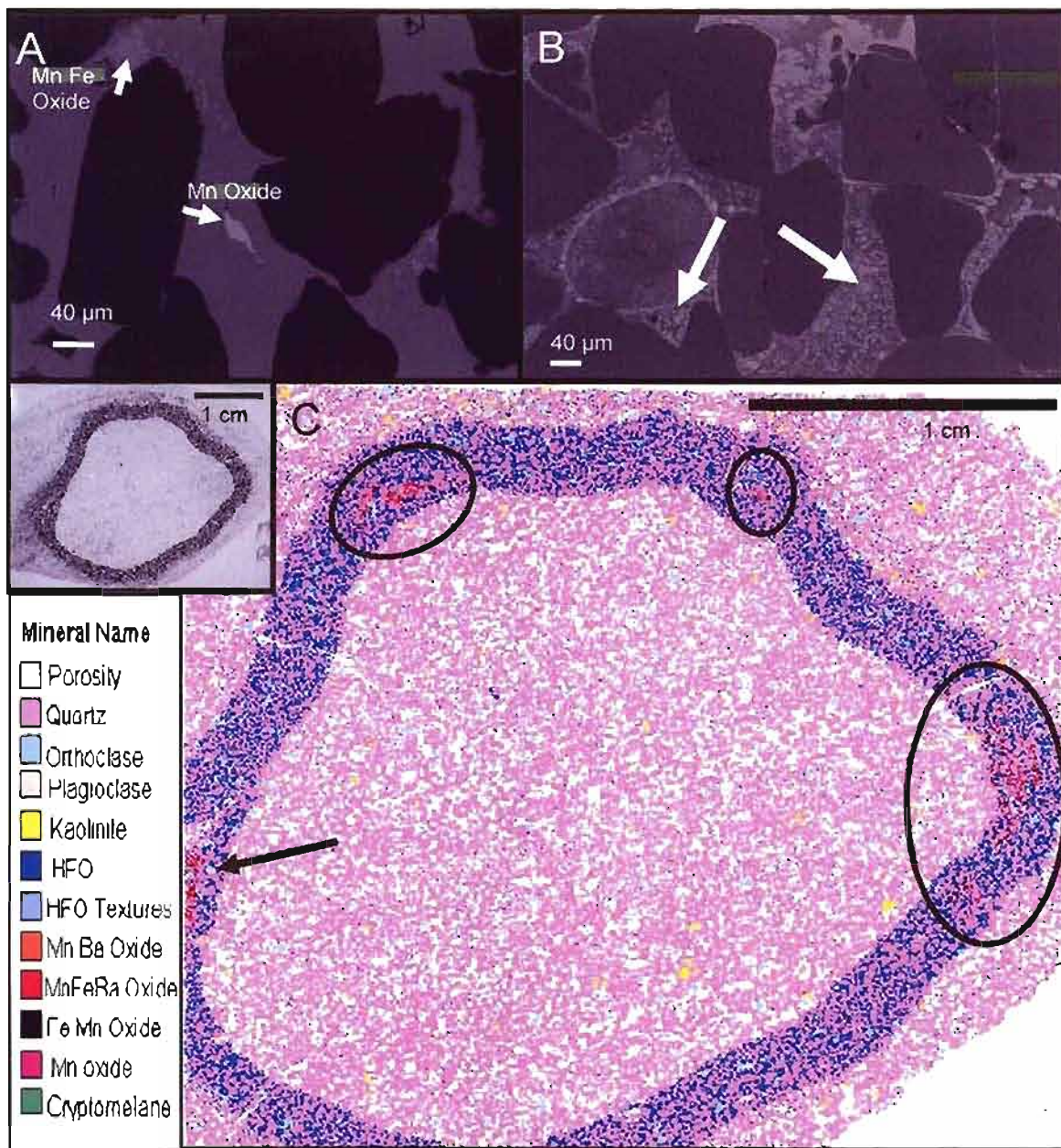


Fig. 1.14. BSE and QEMSCAN images. A. BSE image of rind. Arrows point to late-stage MnO pore filling shown in light gray. Dark gray is the more abundant, smooth textural phase of HFO labeled "HFO" in key. Black areas are quartz grains. B. BSE image of "frothy" textured cement (arrows) in rind. C. QEMSCAN image of concretion. Inset is thin section of concretion used to acquire QEMSCAN image. Arrow and circles point to pockets of MnO. These pockets occur along more permeable eolian grainflow laminae of the host rock.

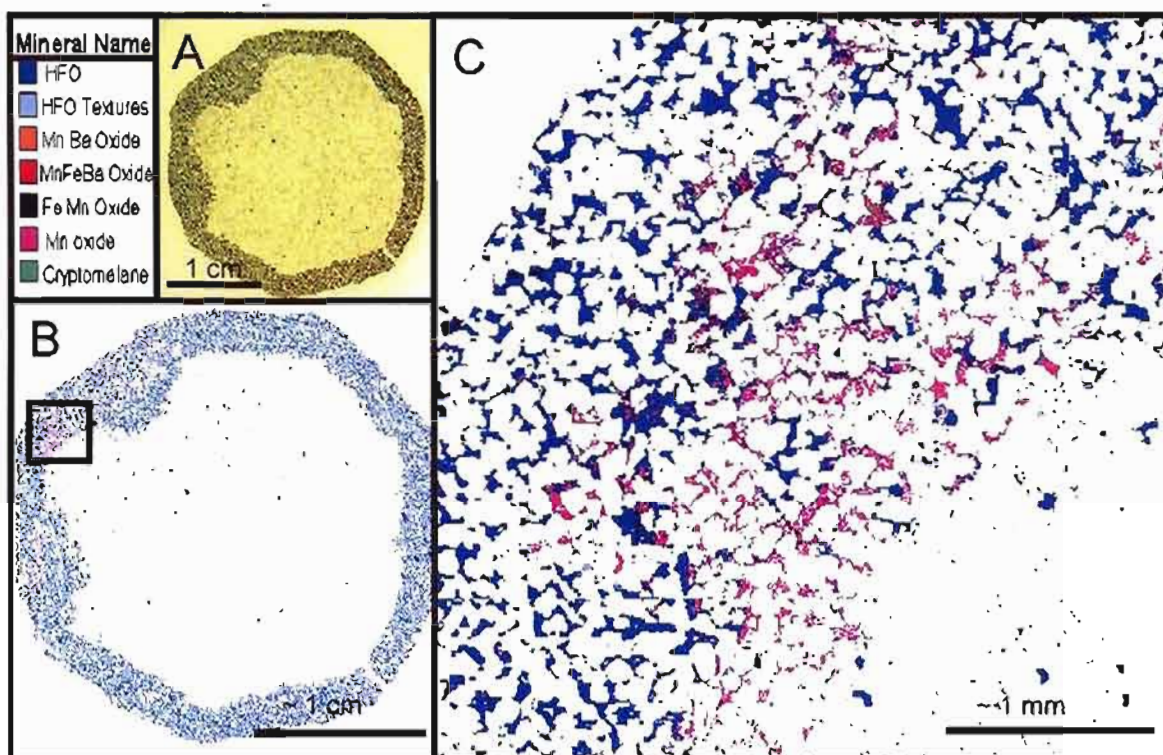


Fig. 1.15. QEMSCAN images showing only HFO and MnO cements. A. Thin section used for QEMSCAN analysis. B. QEMSCAN image at 10 μm pixel spacing. (Black box indicates area shown in C.) C. Close up of MnO and HFO cements. Note that MnO has precipitated along interior edge of rind.

than HFO.

Vnir Reflectance Spectroscopy Results and Interpretation

Vnir reflectance spectroscopy was used to determine iron mineral phases and clays in the cement in a transect across the concretions (Fig. 1.16, see Appendix C for complete data). Only HFO phases are detected in the concretion cement (for rind, layered and solid concretions) and at least three phases of HFO (amorphous HFO, goethite, hematite) are present in the rind macro concretions. Spectra of the rind areas on opposite

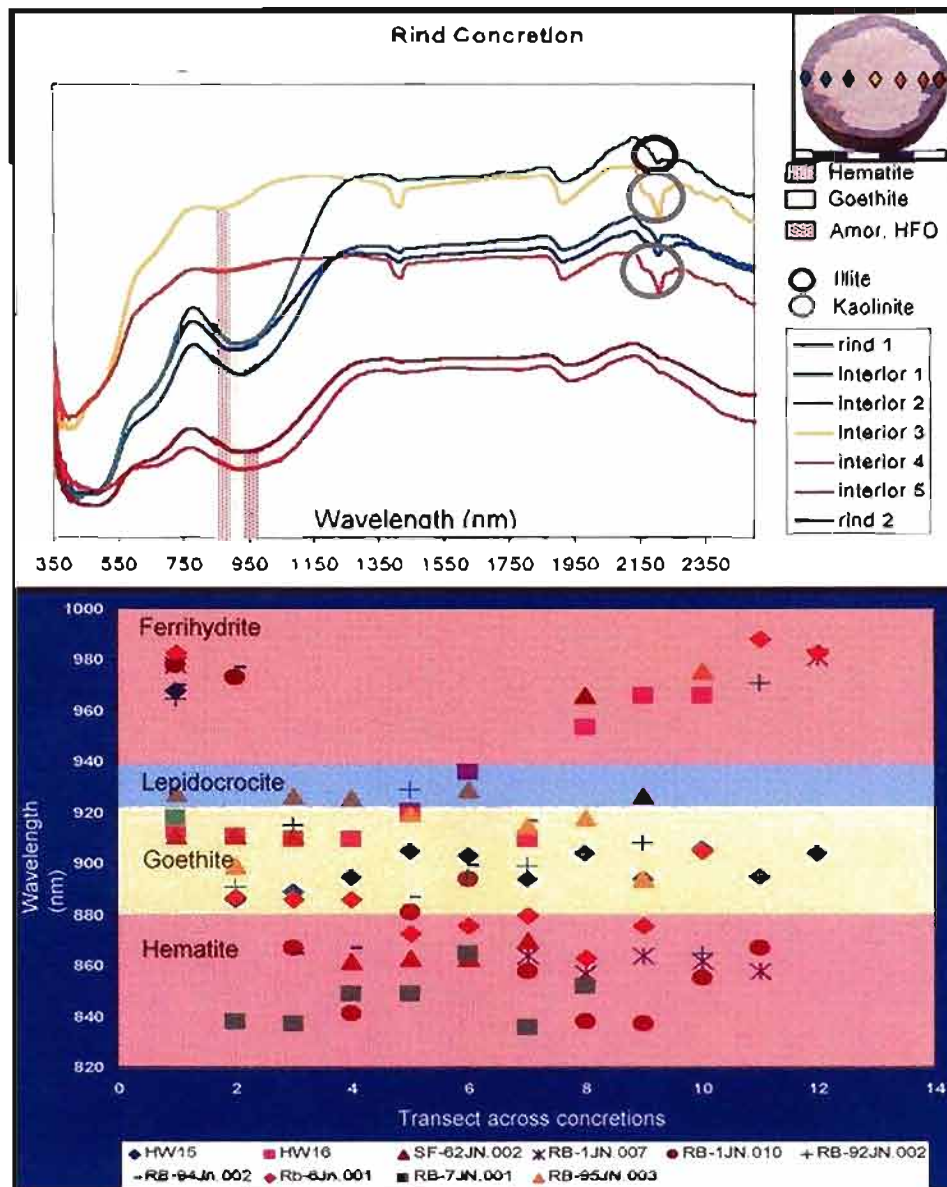


Fig. 1.16. Vnir spectroscopy results for rind concretions. A. Typical spectra for rind concretion. Transect across the center of the concretion is shown in photo. Rind 1 has adsorption feature in the range of goethite; Rind 2 is amorphous HFO (possibly lepidocrocite); interior 3 and 4 are hematite. Kaolinite peaks are circled with gray; possible illite peak is circled with black. B. HFO adsorption peaks (y-axis) in a transect across rind concretion samples (x-axis represents individual readings across a concretion). First and last points for each sample are adsorption minima for rinds and other points are interior minima. The colors correspond to the range of minima for each mineral. Minerals with minima in the lepidocrocite and ferrihydrite ranges are classified as amorphous HFO because of the ambiguity discussed in the text. Six of the first rind readings are amorphous HFO and four are goethite. All of the interior readings are hematite, goethite or a combination of those two minerals.

sides of the concretions show amorphous HFO is the dominant cement in at least one rind. The opposite rinds are either amorphous HFO or goethite except for two samples that were hematite. The HFO phases in the interiors are hematite, goethite or a mixture of hematite and goethite. Kaolinite is present in all the interiors and one of the rind spectra; minor illite is possibly detected in one of the interiors.

For layered concretions, Vnir spectroscopy shows that the HFO cements are predominately goethite with one sample in the amorphous HFO range (Fig. 1.17). One sample of a layered concretion with a depleted interior shows hematite cement in the interior (Fig. 1.17).

Vnir spectra are difficult to obtain for solid concretions because the dark color does not reflect light well, so results were only obtained from two samples (one solid – Fig. 1.18, the other a rind concretion with a well-cemented center – Fig. 1.8B). Spectral data for solid concretions show they are amorphous HFO and goethite (Fig. 1.18). One sample is in the ferrihydrite range for adsorption minima, but the shoulder feature of lepidocrocite is present. The other sample is goethite across the entire transect. Neither sample contains any detectable hematite.

The goethite and hematite phases are straightforward to interpret; however, the amorphous HFO phase is problematic. The amorphous HFO phase present in the concretions typically has an adsorption feature >940 nm. This would indicate that it is possibly ferrihydrite. Ferrihydrite is a poorly defined, X-ray amorphous, nanophase $\text{Fe}(\text{OH})_3$. Ferrihydrite has similar Mössbauer parameters to the nanophase Fe^{3+} oxide detected in the concretions ($\text{IS} = 0.35$ and $\text{QS} = 0.83\text{-}0.90$ or 0.53 mm/s; see following

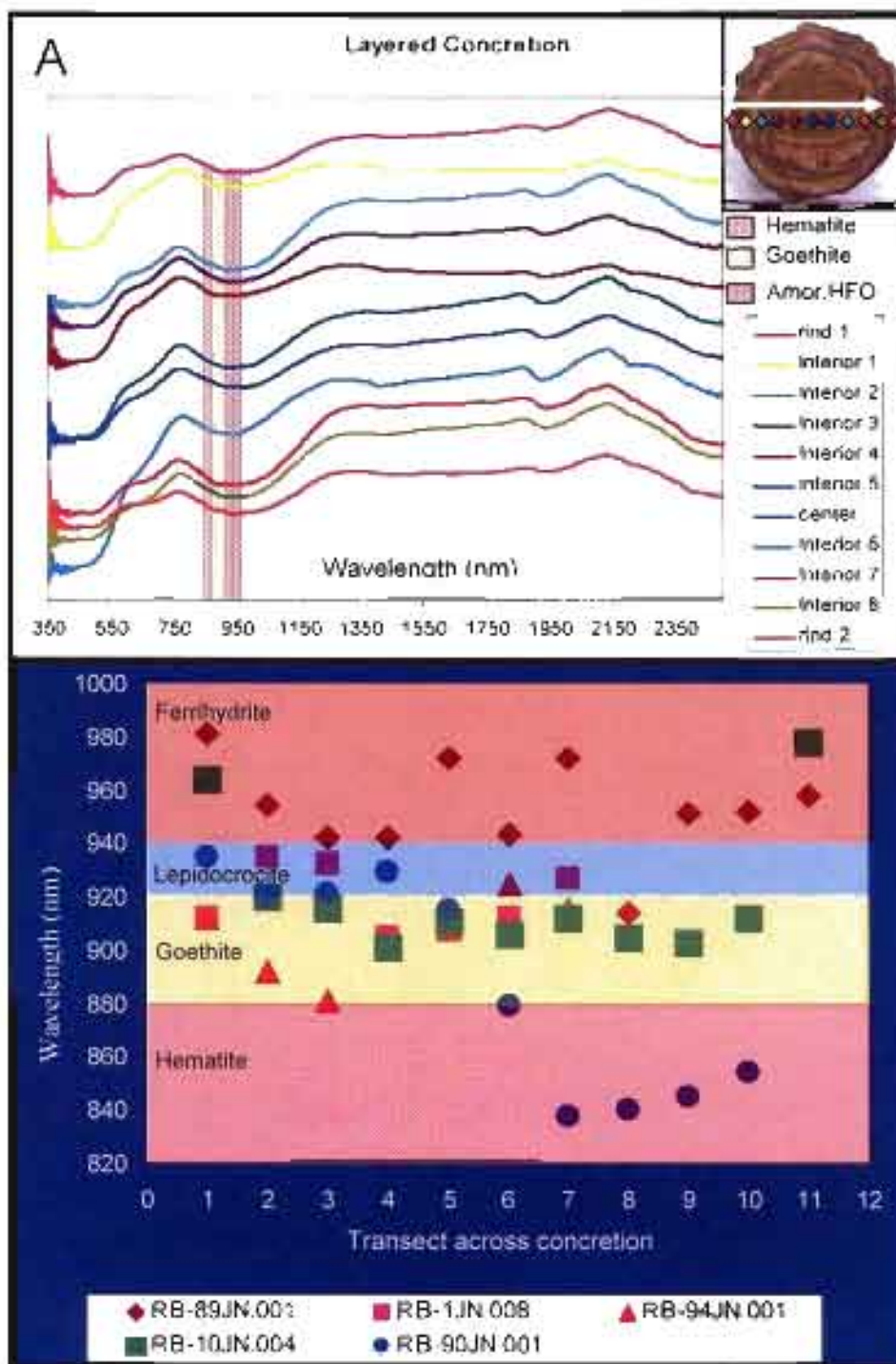


Fig.1.17. Vnir reflectance spectroscopy results for layered macro concretions. A. Spectroscopy results for Sample RB-89JN.001. HFO phases throughout the transect are amorphous HFO. Interior 6 may have minor illite (~2200 nm), but most of the readings show no clays probably due to interference with the HFO. B. Graph of HFO adsorption peaks of transects of five concretions which are predominately in the goethite range. See Fig. 1.16 for explanation of graph. Sample RB-90JN.001 has a depleted center with some hematite cement.

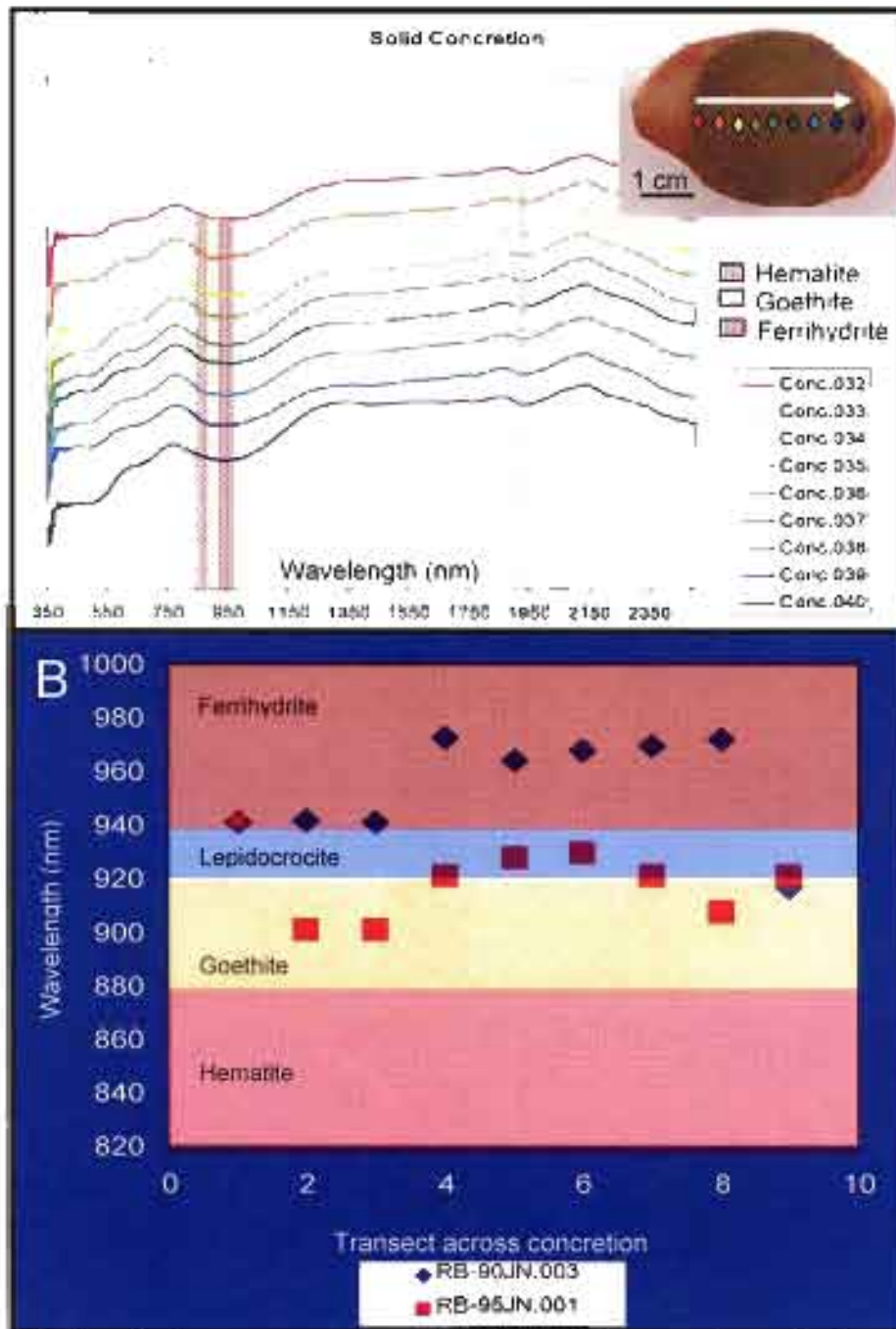


Fig 1.18. Vnir reflectance spectroscopy data for solid concretions. A. Spectra from a transect across sample RB-90JN 003. Sample includes some host rock, but spectra are only shown for concretion. B. Graph of HFO adsorption peaks. Sample RB-95JN 001 is shown in Fig. 13B.

section for Mössbauer spectroscopy results). However, ferrihydrite is a very unstable HFO phase and at intermediate pH, it quickly recrystallizes to more stable phases.

Another possibility is that this phase at >940 nm is lepidocrocite. Lepidocrocite is a metastable γ -FeOOH. Lepidocrocite has a distinct shoulder at ~ 670 nm and an adsorption minimum of ~ 930 nm. The shoulder feature is present in the amorphous HFO phase in the concretions, but many of the adsorption minima are >940 nm.

HFO can precipitate as an amorphous gel that dehydrates to goethite and then hematite with heat or age (Klein and Bricker, 1977). The Navajo Sandstone represents a low temperature diagenetic system ($<100^\circ$ C; Parry et al., 2004); therefore, the amorphous HFO is younger phase (because the minerals dehydrate via age rather than heat). Similarly, the goethite is interpreted to be intermediate in age and the hematite is likely the oldest phase.

A late precipitation event is documented in the study area (~ 5 Ma; see Chapter 2), so a very young, unstable HFO phase could be overprinted on the concretions. This young HFO (identified herein as amorphous HFO) could be amorphous, nanophase ferrihydrite or ferrihydrite that later partially recrystallized while still retaining the ferrihydrite range (>940 nm) adsorption peak (Bishop et al., 2006). The presence of the three HFO phases implies that the HFO was precipitated as a gel-like, amorphous ferrihydrite and has dehydrated to more stable phases with time instead of precipitating directly as hematite or goethite. Further work is necessary to more accurately determine the composition of the amorphous HFO phase.

The spectra obtained from the rind areas on opposite sides of the concretions typically show amorphous HFO on one side and the older, more stable goethite phase on the

opposite side. The presence of a younger HFO phase on one side of the concretions could represent addition of HFO during late-stage advective fluid flow (see Chapter 2). The younger HFO phase throughout the interiors of the layered and solid concretions (relative to the interiors of rind concretions) suggests that concretion interiors may have been modified during late-stage precipitation events. Gel-like, higher initial porosity rinds may have allowed reactants to diffuse through and modify internal structures creating solid and layered interiors.

Mössbauer Spectroscopy Results and Interpretation

All five samples for Mössbauer spectroscopy were representative concretions from different reaction fronts from various sites throughout southern Utah spatially over as much as ~100 km apart (Table 1.1, see Appendix D for results for all concretions from Colorado Plateau that were analyzed).

Sample UT97-20A Jn was reported by XRD to have only hematite. Mössbauer spectra of both the interior and exterior of that sample show three distributions of peaks in sextets with parameters that are consistent with hematite. Both spectra also contain a small Fe^{3+} doublet with parameters that are roughly similar to those of a nanophase (NP) Fe^{3+} oxide (e.g., hematite, as reported in Morris et al., 1989, which are ~0.33 mm/s for isomer shift and ~0.5-0.8 mm/s for quadrupole splitting).

For sample UT00-10A, again both an interior and an exterior sample were measured (Fig. 1.19). In this case, the samples are quite different. In the interior sample, the spectrum is dominated by a doublet resulting from a nanophase Fe^{3+} oxide. A poorly-resolved sextet with parameters roughly similar to those of goethite is also observed. In the exterior of UT00-10A, the doublet was not observed. Instead, the spectrum shows

Table 1.1. Mössbauer spectroscopy results for Navajo Sandstone samples. δ represents isomer shift; Δ represents quadrupole splitting. See Appendix IV for all results and Appendix 3 for sample locations.

		UT97- 8A	AZ-03 Pg In	UT00-10A int	UT00-10A ext	UT00-10B ext	UT97 20A int	UT97-20A ext
Mn Fe ₃₊ oxide	δ	0.39	0.22	0.32			0.17	0.23
	Δ	0.72	0.71	0.97			0.98	0.89
	Γ	0.64	0.4	0.58			0.94	0.75
	area	34	00	02			9	13
Mn Fe ₃₊ oxide	δ		0.06					
	Δ		0.4					
	Γ		0.37					
	area		50					
Goethite	δ							
	Δ							
	Field							
	Γ							
Goethite	δ							
	Δ				0.38	0.4		
	field				-0.25	-0.28		
	Γ				324.7	341.7		
Hematite	δ							
	Δ							
	field							
	Γ							
Hematite	δ					0.35	0.38	0.38
	Δ					-0.28	-0.22	-0.21
	field					507	495.7	495.1
	Γ					0.39	0.25	0.32
Hematite	δ							
	Δ							
	field							
	Γ							
Hematite or Goethite	δ					0.44	0.37	0.37
	Δ					-0.28	-0.3	-0.29
	field					535	515.7	514.1
	Γ					0.5	0.25	0.25
Hematite or Goethite	δ							
	Δ							
	field							
	Γ							
Hematite or Goethite	δ			0.39	0.39	0.44		
	Δ			-0.16	-0.17	-0.15		
	field			290.1	276.4	273		
	Γ			0.37	0.42	0.95		
Unresolved	δ	0.485				0.5	0.5	
	Δ	2.78				1.18	1.18	
	Γ	3.952				0.4	0.7	
	area	48				7	10	
Unresolved	δ					-0.3		
	Δ					2.99		
	Γ					4.6		
	area					25		
Σ		8.78	1.55	0.98	8.35	4.91	18.42	6.98

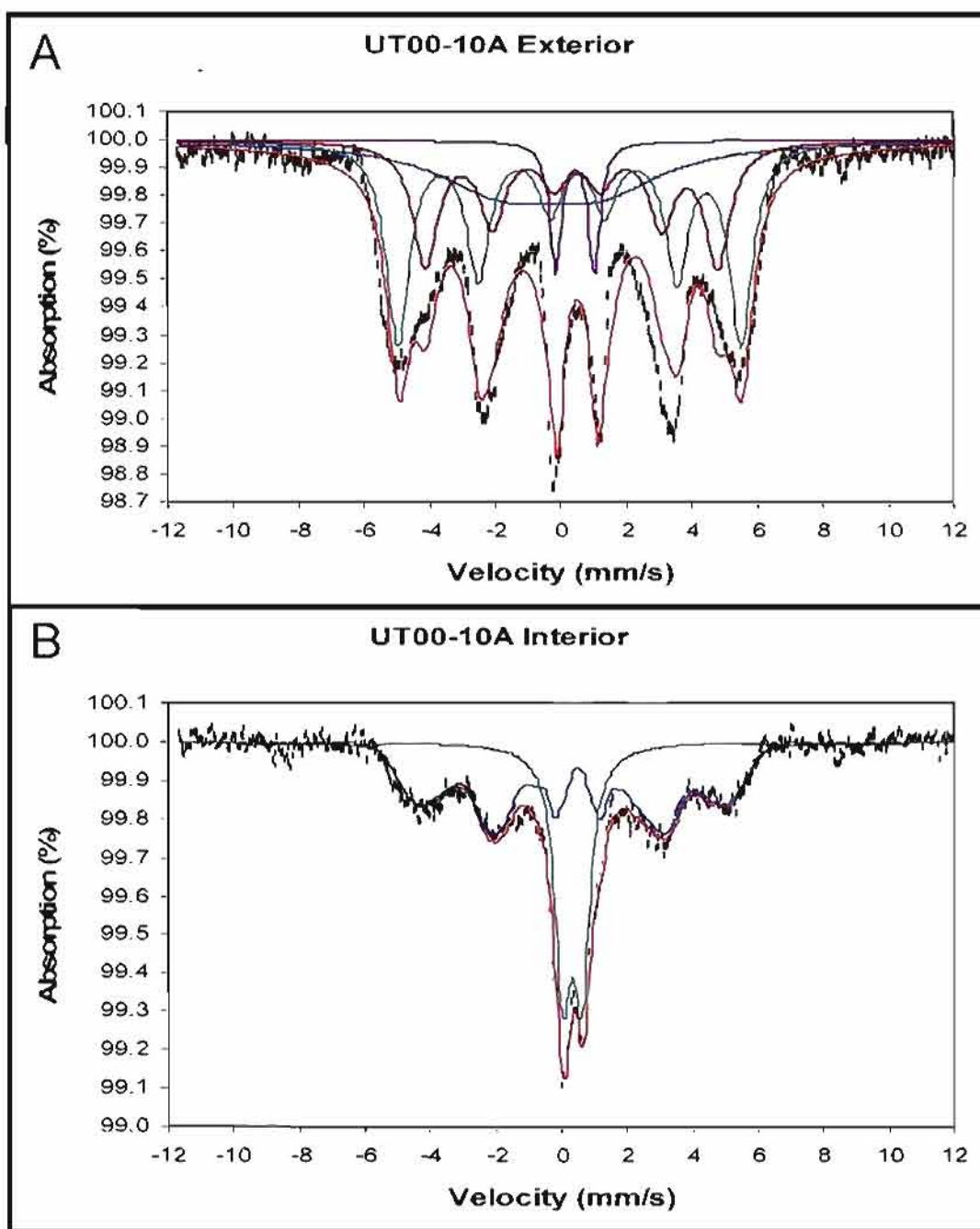


Fig. 1.19. Mössbauer spectroscopy results for Sample UT00-10A. A. Mössbauer results for the exterior of the rind macro concretion with two well-resolved sextets that probably represent goethite and two poorly resolved doublets that probably represent nanophase Fe^{3+} oxide. B. Results for the interior of the rind macro concretion sample shows a doublet from a nanophase Fe^{3+} oxide. A poorly resolved sextet with parameters roughly similar to those of goethite is also observed.

two well-resolved sextets (probably both goethite) and two poorly-resolved Fe^{3+} doublets probably representing distributions of unresolved, fine-grained Fe^{3+} oxide.

For sample UT00-10B, we ran only the exterior. Mössbauer spectra show the presence of both goethite and hematite as sextets, in addition to a nanophase Fe^{3+} oxide doublet. Sample AZ03-Pg Jn is all nanophase Fe^{3+} oxide. Even though it appears that there is suggestion of sextet structure in the baseline of this spectrum, closer analysis reveals the “features” to be only scatter. Sample UT97-44 is a mixture of a prominent nanophase Fe^{3+} oxide doublet and a very broad, unresolvable mixture of contributions from unknown oxides.

Even though the Mössbauer is not well resolved in many of these samples, generally the results show at least three phases of HFO: a nanophase (or amorphous) HFO, goethite and hematite. These phases are consistent with the three phases (amorphous HFO, goethite and hematite) detected with Vnir reflectance spectroscopy. Only hematite was detected using X-ray diffraction.

Discussion

The range of physical characteristics, internal structures and cement phases (textural, mineralogical and chemical) all suggest a complex diagenetic history with multiple precipitation events. Multiple generations of isopachous HFO (and minor MnO) cements indicate that concretions grow via a pervasive growth model similar to some carbonate concretions. Some additional radial growth is possible due to an Ostwald ripening process where micro concretions coalesce to form larger macro concretions. The major implications of this research are the complexities of the concretion formation model (proposed herein), and the establishment of diagnostic criteria for distinguishing

diagenetic concretions.

Interpretation of Cement Phases

A synthesis of the results suggests multiple precipitation events have overprinted original HFO concretions with additional cements (HFO and MnO) throughout the diagenetic history of the Navajo Sandstone in Spencer Flat. Textural analysis via QEMSCAN and petrographic microscopy distinguishes at least three generations of isopachous cement in the rinds of macro concretions (Fig. 1.6C). QEMSCAN analysis also shows small amounts of a late-stage MnO pore filling (0.2% of cement; Fig. 1.14. 1.15). At least three mineral phases of HFO cement (amorphous HFO, goethite and hematite) are identified with Vnir spectroscopy and these phases occur in predictable places throughout the concretions. Multiple phases of HFO are also detected with Mössbauer spectroscopy. Although there does not seem to be a consistent pattern of particular HFO phases in specific locations, Mössbauer spectroscopy does show different phases in different locations in the concretion samples. This suggests that even in disparate sample locations (~100 km apart), multiple fluids and precipitation events have influenced the mineralogy and structure of the concretions.

Pervasive Growth Model

Multiple generations of isopachous cement (HFO and MnO) in the Navajo Sandstone concretions indicate formation via a pervasive growth model similar to carbonate concretions where HFO crystals nucleate concomitantly throughout the concretions (Fig. 1.2) (see Feistner, 1989; Mozley, 1989; Fisher et al., 1998; Raiswell and Fisher, 2000 for a discussion of pervasive growth in carbonate concretions). The presence of three HFO

cement phases and late-stage MnO pore filling provide further evidence for this pervasive growth model.

Our model proposes that concretions originally precipitate as an amorphous HFO gel that sets the diameter of the concretion and retains some porosity, which allows for late-stage cement precipitation and pore filling. Macroscopic and microscopic digitate inward crystal growth suggests concretions grow inward from the set radius. Late-stage MnO pore filling is present predominately on the interior edges of the rind, which also supports the inward growth model.

HFO can result from the oxidation of reduced iron mineral phases such as pyrite or siderite; however, three lines of evidence support the direct precipitation of primary HFO cement interpretation: 1. the lack of pyrite pseudomorphs (only two samples out of 90 thin sections had apparent pyrite pseudomorphs), 2. lack of any siderite in the studied concretion cements and, 3. lack of Fe^{2+} valance state in the concretions. The possibility that all of the siderite has been oxidized is unlikely because carbonate interdune deposits (calcite and siderite) are still present throughout the Navajo Sandstone (Parrish and Falcon, 2007) as well as in the Spencer Flat study area. There is also no detected sulfur remaining in the concretions or the host rock, which would be unlikely if the concretions were originally pyrite (See Chapter 2; Beitler et al., 2005).

In rind macro concretions, younger phases of HFO (amorphous HFO, goethite) are typically located in the rinds and older phases (hematite) are located in the interiors. The locations of these younger HFO phases in the exteriors of rind concretions suggest that late-stage precipitation events added younger HFO pore fill to the rinds as reactants diffused into semipermeable, gel-like rinds. In contrast, layered and solid macro

concretions are typically amorphous HFO or goethite throughout. These younger HFO phases throughout the interiors suggest late-stage precipitation events are likely responsible for internal structural variations as reactants diffused through the rinds. The presence of MnO as a latest stage pore fill suggests a slight rise in pH of the precipitating fluid.

Mars Spherules and Analog Comparisons

Important characteristics of the spherules (Calvin et al., 2008) in the Burns formation in Meridiani Planum are presented here to show why the spherules are concretions and not formed by other processes that can generate spherical geometries. The discussion is ordered by: 1. a summary of the Burns formation host rock (Squyres et al., 2004; Grotzinger et al., 2005, Calvin et al., 2008), 2. a summary of Mars spherules characteristics, 3. other models for spherule formation from the literature that propose a mechanism for a spheroidal shape, but do not adequately explain varied geometries and *in situ* spacing and finally, 4. the more compelling Navajo Sandstone comparison and characterization, with diagnostic criteria for diagenetic concretion formation.

Burns Formation (Host Rock), Meridiani Planum, Mars

The Burns formation in Meridiani Planum, Mars, is a fine-grained, homogenous, eolian, sedimentary unit that is at least 10 m thick (Grotzinger et al., 2005). The formation extends laterally for >100,000 km² as tracked by the MER Opportunity (Calvin et al., 2008). The sands consist of jarosite, and calcium and magnesium sulfates. A basaltic precursor is responsible for the high ferromagnesian content of the sands (Squyres et al., 2004; Grotzinger et al., 2005). Three units are described by Grotzinger et

al. (2005): 1. a lower unit consisting of large-scale cross-bedded strata interpreted as an eolian dune field, 2. a middle unit consisting of planar lamination and low angle cross-bedding interpreted as a sand sheet facies, and 3. an upper unit with sedimentary structures similar to the middle unit but distinguished by a diagenetic boundary. All three units contain hematite spherules.

Mars Spherule Characteristics

Hematite spherules in the Burns formation are nearly spherical (mean aspect ratio=1.06) (McLennan et al., 2005). The spherules exhibit a nonrandom spacing throughout the host rock, indicating a geochemically self-organized pattern (McLennan et al., 2005). They are distributed in three dimensions throughout the host rock (instead of only along bedding planes). Spherules extend vertically through the section for 10s of meters as well as laterally for several kilometers (Calvin et al., 2008, Squyres et al., 2009). The spherules decrease in size with elevation within Victoria Crater, suggesting a decrease in reactants (probably water) at the top of the stratigraphic section (Squyres et al., 2009).

Although hematite spherules exhibit a spheroidal geometry, surficial, latitudinal ridges are occasionally present. When these ridged spherules are *in situ*, the ridges align with bedding planes (Calvin et al., 2008). Spherules are preferentially cemented relative to the host rock so they weather out and collect in topographic lows. Some spherules weather out with host rock preferentially cemented around the spherules and adhered to the spherule (Calvin et al., 2008). Occasionally, conjoined forms (doublets or triplets) occur and in one locality near an impact crater, there is an abundance of these doublets. Spherule diameter distribution is bimodal and the two normally distributed size ranges

are <1 mm and 1-2 mm to ~5 mm. Both size ranges are present in the same horizon in outcrop (Calvin et al., 2008).

Spherules are composed of hematite (37-60 wt. %) and the abundance of hematite likely varies between spherules (Glotch and Bandfield, 2006). The mini-TES (thermal emission spectrometer) data suggest that the hematite exhibits a platy crystal habit with radial crystal growth and that it formed from a precursor goethite phase at low temperatures (Glotch and Bandfield, 2006, Calvin et al., 2008). The spherules are enriched in Ni relative to the host rock (Knauth et al., 2005) and contain about 3% Ni (Morris et al., 2006).

Proposed Terrestrial Analogs to Mars

Four main terrestrial analogs have been proposed for the Burns formation spherules largely based on the spheroidal geometry: impact lapilli (Knauth et al., 2005), Mauna Kea spherules (Morris et al., 2005, Golden et al., 2008), Western Australian acid saline lake concretions (Benison, 2006; Benison and Bowen, 2006; Benison et al., 2007; Bowen et al., 2008), and Navajo Sandstone HFO concretions (Chan et al., 2004, 2005). The following discussion orders the other analogs cited in the literature from least similar to most similar to Mars, ending with the Navajo Sandstone examples.

Impact Lapilli

Impact lapilli have some similarities to Martian spherules such as enrichment in Ni relative to the host rock (Mars spherules contain about 3% Ni), size (1-5 mm diameter) and morphology (spherical). Impact lapilli also occasionally have concentric layering. However, terrestrial lapilli analogs are dissimilar in mineralogy (glass or magnetite).

Lapilli are typically not distributed vertically throughout the section nor do they exhibit self-organized spacing. Surficial ridges or furrows - indicative of diagenetic cementation in a sandstone – are absent in lapilli analogs (Knauth et al., 2005). It is also unlikely that impact lapilli would produce the narrow size range distributions of the Martian spherules because terrestrial accretionary lapilli have an order of magnitude difference between the median and the maximum diameters (Schumacher and Schmincke, 1991).

Mauna Kea

The spherules at Mauna Kea are similar to Martian spherules in shape (spherical or discoidal) and mineralogy (hematite) (Morris et al., 2005). They also exhibit similar radial crystal growth patterns (Golden et al., 2008) possibly due to formation temperature >100°C (Catling and Moore, 2003). The Mauna Kea spherules, however, only have one size range (10 to 100 µm diameter) that is much smaller than the Mars spherules. A population in that size range may be present on Mars because another hematite signature is detected, but it is below the resolution of current instrumentation. Mauna Kea spherules occur due to high temperature alteration of volcanic tephra via acid sulfate fluid. The geochemical constituents of this analog are reasonable, because of the volcanic origin and the abundance of basaltic (Fe, Mn) components for the sediments at Meridiani Planum. However, the Burns formation is a sedimentary rock altered via diagenetic fluid flow (McLennan et al., 2005) probably at a low temperature (Glotch and Bandfield, 2006).

Western Australian Acid Saline Lakes

The acid saline lakes in Western Australia are a good modern analog for the Burns

formation because of the geochemical and mineralogical similarities to Meridiani Planum. Mineralogical similarities include the presence of Ca and Mg sulfates, jarosite, hematite, chloride and a siliciclastic component. Sedimentary similarities include planar laminations, cross-bedding, hematite concretions, displacive crystals, ripple marks and mudcracks. The concretions in the acid saline lake sediments form from diagenetic fluid flow in fine- to medium-grained reactive sediments (Benison, 2006; Benison and Bowen, 2006; Benison et al., 2007; Bowen et al., 2008). These sediments are similar to the Burns formation sediments (shallow lacustrine evaporites/eolian sands); however, the Western Australian concretions form during early diagenesis prior to lithification.

Navajo Sandstone HFO Concretions

Of the aforementioned models, Navajo Sandstone concretions (hereafter referred to as the “Utah” example for brevity) preserve the most genetic similarities compared to the rock records in Meridiani Planum (Table 1.2). There are similarities with the host rock, and spherule characteristics such as geometry, external and internal structure, mineralogy, size distribution and distribution throughout the host rock.

Host Rock

The Navajo Sandstone and the Burns formation are both fine-grained, homogenous eolian sandstones that extend over an area of 100s of square kilometers (Fig. 1.20). The Burns formation is composed of more soluble sulfate sands than the clean quartz arenite composition of the Navajo Sandstone. Both units, however, are porous and

Table 1 2. Similarities between the Burns formation spherules and proposed terrestrial analogs. Entries based on characterization of Martian blueberries and comparison to terrestrial analogs by Calvin et al. (2008), but including data from this study.

Analog and Models	Mars	Utah (ancient)	Western Australian acid saline lake concretions (modern)	Mauna Kea spherules	Lacustrine/marine ferromanganese nodules	Impact lapilli
Host Rock Characteristics						
Fine-grained, homogenous, eolian sedimentary host rock	X	X				
Host rock spans >100,000 km ² area	X	X			X	X
Host rock composition	sulfate, basaltic	quartz arenite	evaporites	basalt	shales	greenstone belt
Concretion Characteristics						
Spheroidal geometry	X	X	X		X	X
Surficial, latitudinal ridges or furrows	X	X	?			
Occasionally doublets or triplets	X	X	?			
Doublet population locally abundant	X	X	?			
Preferentially cemented host rock occasionally adhered to exteriors	X	X	?			
Interior structure	solid	ring, layered, solid	solid	solid ring?	concentric zonation	solid
Cement mineralogy	hematite (goethite precursor)	hematite goethite amor. HFO	hematite, jarosite	hematite	ferromanganese	glass precursor
Enriched in Ni relative to host rock	X	X				x
Radial crystal growth	X	rare	x			
Polymodal distribution	binodal	trimodal				
< 1mm dia	X			X		
1-2mm to 5mm dia	X	X			X lacustrine	X
> 5mm dia		X	X		X	
Two size ranges in single horizon	X	X	?			
Self-organized spacing	X	X	?			
Vertically distributed through 10s of meters of section	X	X	?			
Three dimensional distribution throughout host rock	X	X	?			

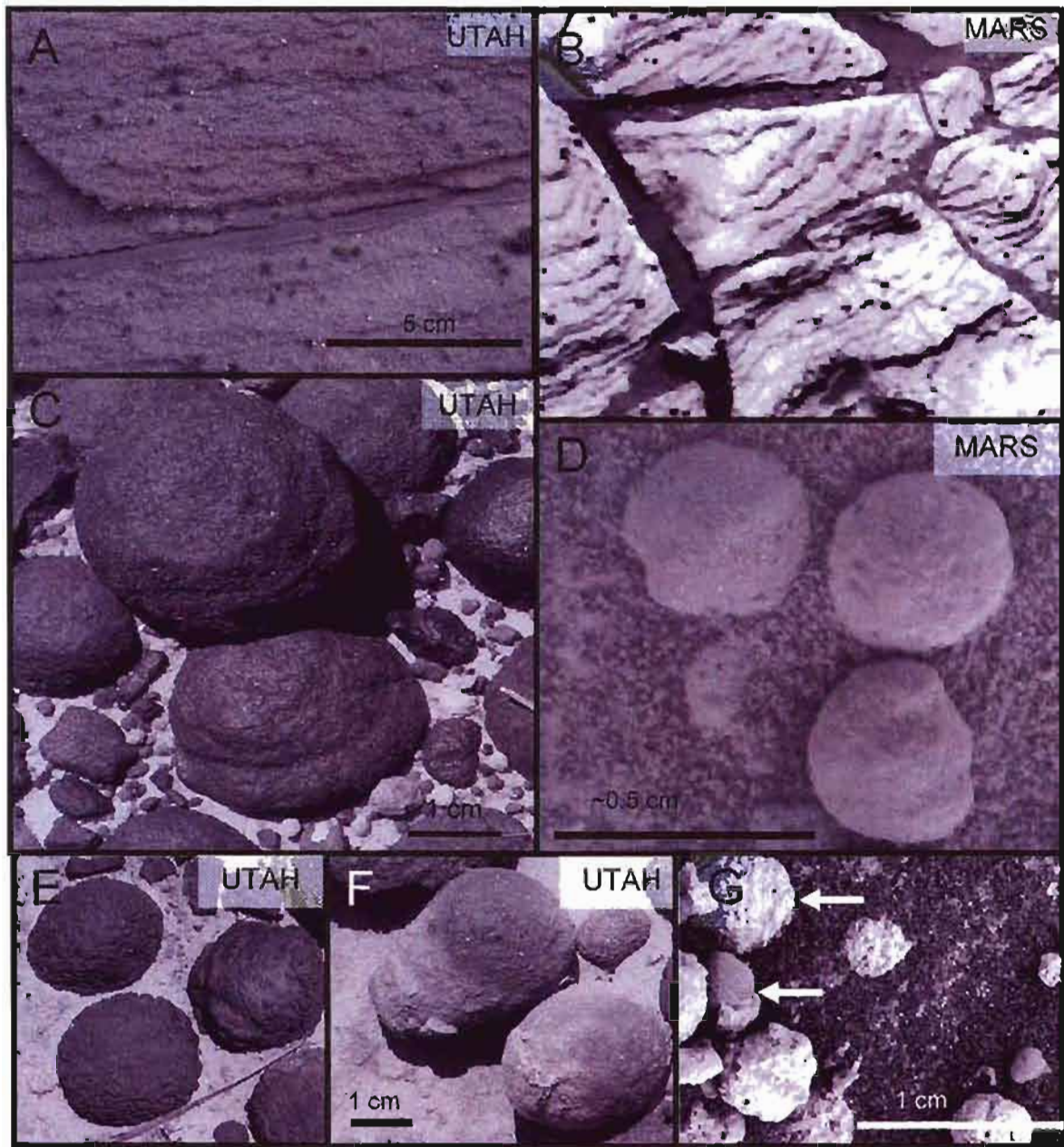


Fig. 1.20. Host rock and exterior structural similarities between Utah and Mars. A. Navajo Sandstone with *in situ* concretions. B. Burns formation with *in situ* spherules. Spherules are $< 5\mu\text{m}$ in diameter. C. and D. Arrows point to furrows and ridges. E and G. Bumpy-textured spherules (Top arrow in Fig. G.). F. and G. Weathered out spherules with adhered host rock. (Bottom arrow in Fig. G.) Mars images: NASA/JPL/Comell.

permeable media in which there is evidence of groundwater diagenetic histories.

External Structure

The concretions range from spheroidal (aspect ratio ranges from 1.00 to 1.06) to discoidal (aspect ratio >1.06). Surficial, latitudinal ridges or furrows around the perimeter of the spherules are present in both examples (Fig. 1.20C, D). These ridges align with laminae when concretions are *in situ* and are a result of cementation in a sedimentary rock.

Both the Utah and Mars examples occasionally exhibit a bumpy texture that resembles an avocado skin (Fig. 1.20E, G). In Utah, this is due to multiple nucleation sites precipitating clusters of micro concretions that coalesce to form the larger concretions in an Ostwald ripening type of process. It has been suggested that a similar nucleation phenomenon could be responsible for bumpy-textured concretion formation on Mars where smaller spherules dissolve and reprecipitate on larger spherules (Calvin et al., 2008).

Occasional doublets or triplets and “duckbill” shapes occur in both Utah concretions and Mars spherules (Fig. 1.21). In Meridiani Planum, an abundance of doublets occurs near a large impact crater (Calvin et al., 2008) very similar to an abundant population of doublets in the Spencer Flat area, suggesting localized nucleation processes responsible for the doublet morphology.

Well-cemented concretions and spherules occasionally weather out with some preferentially cemented host rock adhered to the exterior. In Utah, this preferential

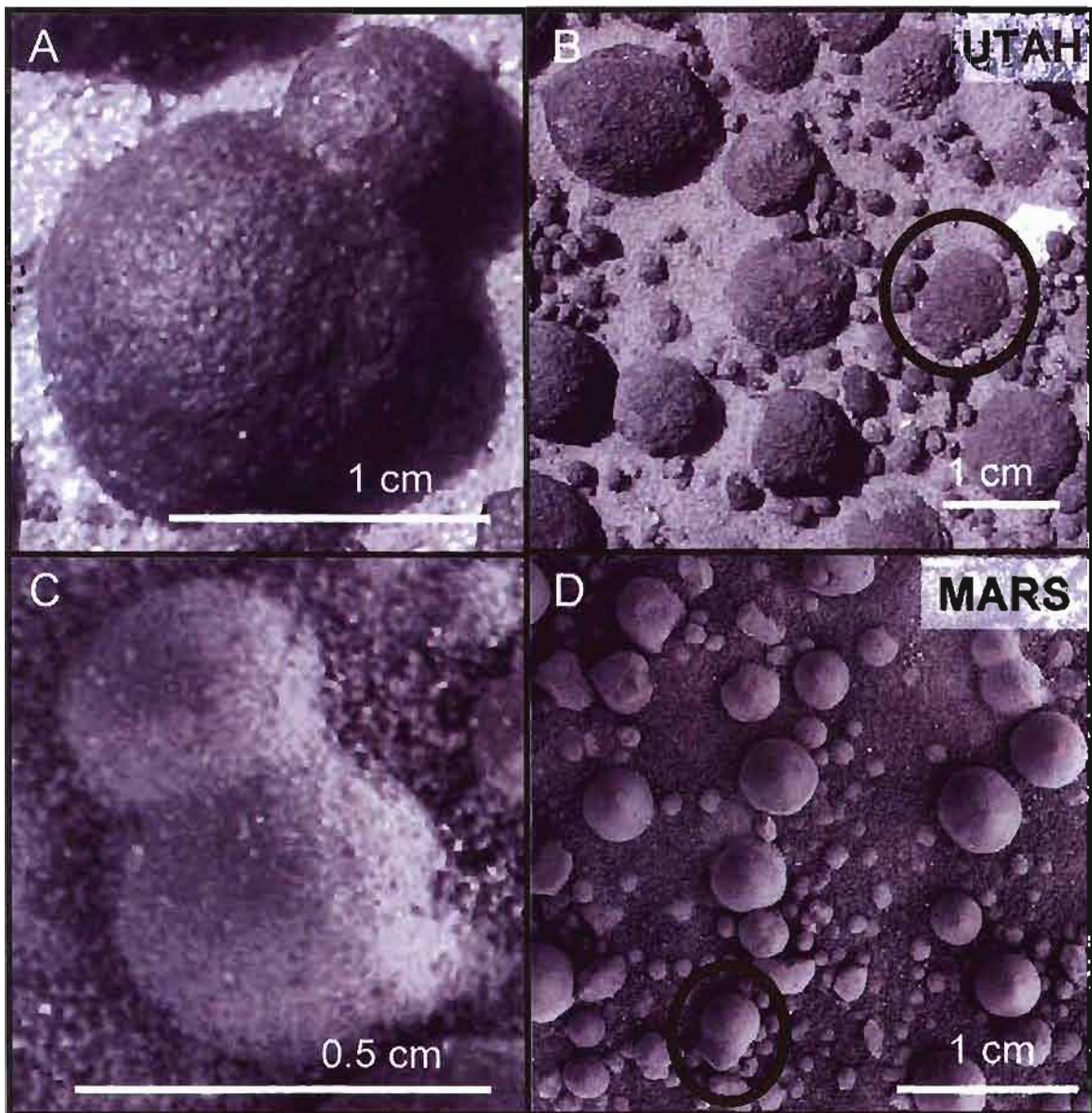


Fig. 1.21. Weathered out doublets and "duckbill" shapes in Utah (A, B) and Mars (C, D). A. Doublet in Utah. B. Two size populations of weathered out concretions and a "duckbill" shape (circle) in Utah. C. Doublet in Meridiani Planum. D. Two size populations of weathered out spherules with "duckbill" shape (circle) in Meridiani Planum. Mars images: NASA/JPL/Cornell.

cementation surrounding *in situ* concretions results from late-stage precipitation events that preferentially cement host rock grains in a “comet tail” shape in the direction of fluid flow (see Chapter 2) (Fig. 1.20F,G). The presence of similarly cemented asymmetric forms on Mars suggests that although the diagenetic history is simpler, more than one precipitation event occurred or there was a combination of diffusive and advective mass transfer of reactants during the precipitation of hematite spherules.

Internal Structure

Internal structure of the Utah concretions is more varied than their Mars counterparts, but some macro and micro concretions in Utah have solid internal structure similar to Mars spherules (Fig. 1.22). Possible rind internal structures are also present on Mars (Calvin et al., 2008), although these structures are not nearly as common as they are in Utah (Fig. 1.22A, B). In Utah, multiple phases of HFO cement and young HFO phases throughout layered and solid interiors suggest that the variations in internal structure are due to multiple precipitation events diffusing reactants into the interiors of concretions. Therefore, these variations imply the Navajo Sandstone has a much more complex diagenetic history than the Burns formation.

Mineralogy and Crystallography

The iron oxide cement mineralogy is interpreted to be more complex in Utah than on Mars. Three phases of HFO cement (amorphous HFO, goethite, hematite) are present in the Utah concretions. In the Meridiani Planum spherules, only hematite with a goethite

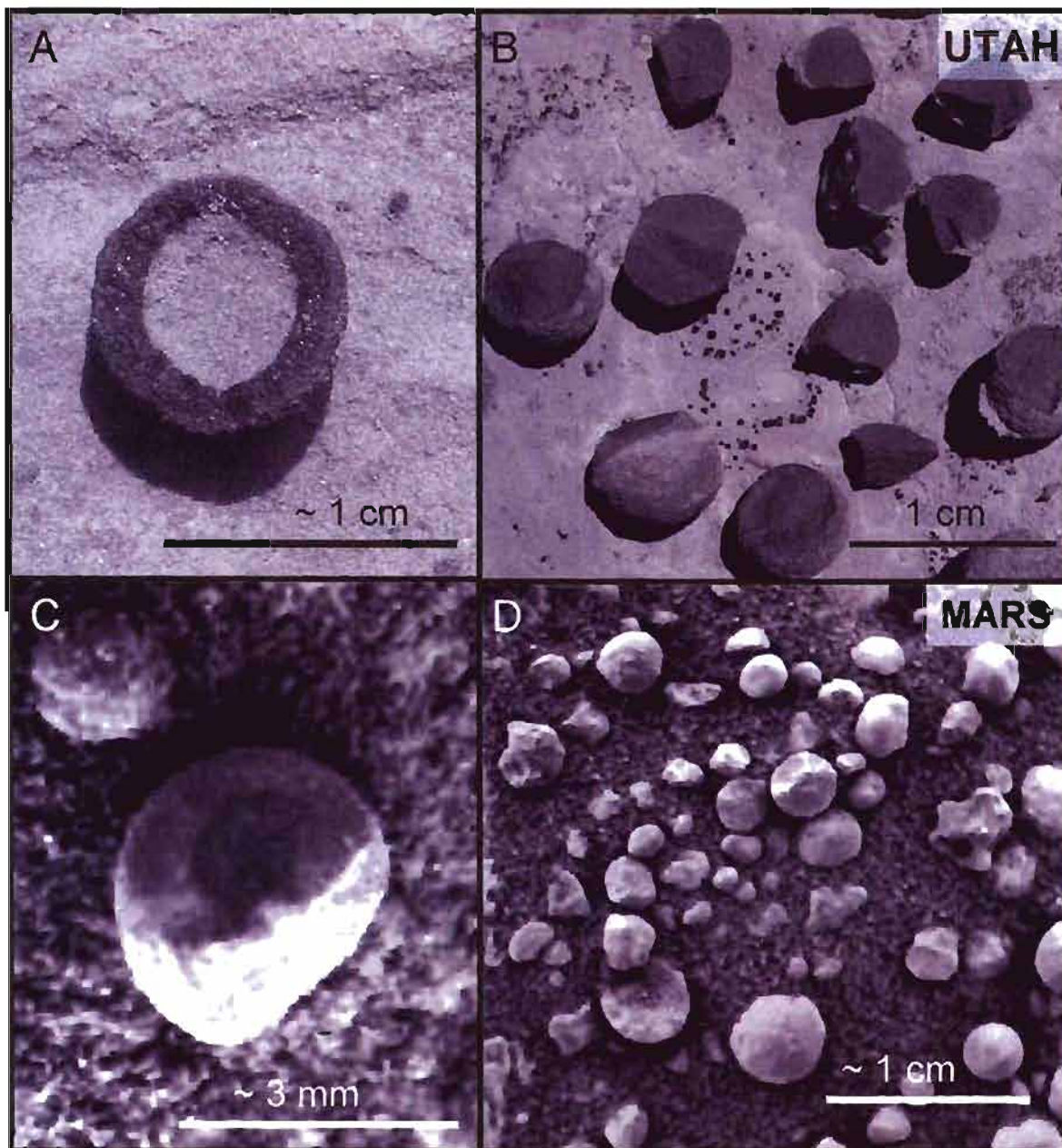


Fig. 1.22. Internal structural similarities between Utah concretions (A, B) and Mars spherules (C, D). A and C. Rind or concentric zonation in Utah and on Mars. B and D. Solid internal structure in Utah and on Mars. Mars images: NASA/JPL/Cornell.

precursor phase has been detected to date (Glotch and Bandfield, 2006) as there are limitations with the available remote sensing MER instrumentation on Mars. Physical samples of the Utah examples allow more complete characterization of the mineralogy by multiple methodologies.

In Utah, the concretions likely precipitated as amorphous HFO gel and dehydrated with age to more stable goethite and hematite (Klein and Bricker, 1977). The shape of the Mini-TES spectra indicates that the Martian spherules likely precipitated as an oxyhydroxide precursor mineral phase (like a precursor gel phase) that later dehydrated to hematite (Glotch et al., 2006).

Both the Utah concretions and the Mars spherules are enriched in Ni relative to the host rock (Mars data from Morris et al., 2006). The Mössbauer spectroscopy suggests that the Navajo Sandstone concretions are hematite or goethite with a nanophase Fe^{3+} oxide. A similar nanophase Fe^{3+} oxide signature is present in the Burns formation (Klingelhöfer et al. 2004; Morris et al. 2006).

One crystallographic difference between the Mars and the Utah examples is that the Mars spherules have radial crystal structure and high crystallinity (Calvin et al., 2008). The sulfate sandstone of the Burns formation is comprised of reactive, soluble grains that dissolved during or prior to the precipitation of the spherules to allow more space for euhedral crystal growth. The Navajo Sandstone is a quartz arenite formed from relatively insoluble grains so the HFO precipitate would not have the same room to form crystals preferentially oriented along the c-axis as on Mars. The Mars spherules may also exhibit a higher degree of crystallinity due to greater iron abundance in the Burns formation sediments that have an iron-rich basaltic precursor. This more euhedral crystal structure

on Mars would also account for color differences between Mars and Utah spherules because hematite crystals are grey when they are larger than 5 μm and reddish brown when they are smaller than 5 μm .

Size Distribution Comparison

The Utah concretions and the Mars spherules show more than one size population *in situ* within the outcrop and are distributed *in situ* in three dimensions with a geochemically self-organized spacing. In both examples, spherules are present in a km-scale areal extent and through 10s of meters of vertical section. The Mars population is bimodal and in Utah, the population is trimodal (Fig. 1.23), although another hematite signature is identified in the Burns formation that is below the resolution of current instrumentation. This other hematite may represent a third, smaller size population (Calvin et al., 2008).

The two size populations in Meridiani Planum have similar divisions of micro and macro populations, although the Mars spherules are much smaller than most terrestrial examples. Mars micro spherules are <1 mm diameter and macro spherules are typically 1-6 mm diameter. Calvin et al. (2008) also suggest that the geochemical reaction that formed the spherules on Mars is water-limited. Water-limited geochemical conditions on Mars could result in small, size-limited spherules, in contrast to the long history of abundant water conditions in the Navajo Sandstone reservoir. The size difference between Utah and Mars suggests that although groundwater was present on Mars at some point, it may have been more scarce and ephemeral relative to the Earth.

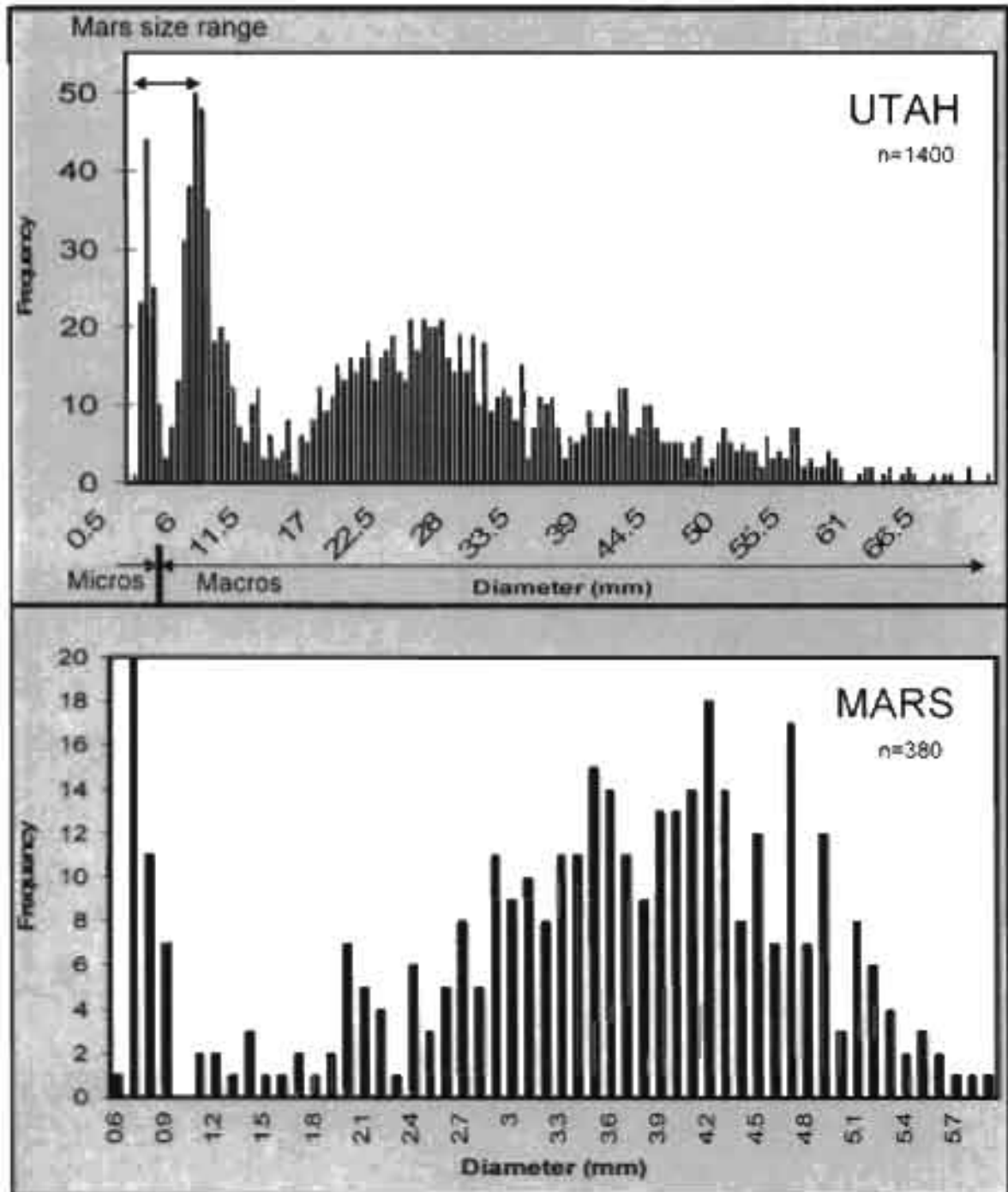


Fig. 1.23. Comparison of Utah and Mars concretion diameter data. Mars data is from Calvin et al. (2008). Note Mars size range compared to Utah (top left on Utah graph).

Strengths and Weaknesses of Utah Analog

The mineralogy of the Utah concretions is more easily determined because it is not limited to remote sensing analysis. Nevertheless, even with multiple analytical methods there is difficulty in pinpointing the exact HFO phases throughout the concretions. It is likely that as additional analytical methods are included in future Mars exploration missions, other mineral phases and more accurate clues to the diagenetic history of the spherules will be detected in Meridiani Planum.

Characterization of terrestrial concretions provides diagnostic criteria for determining formation via diagenetic processes. The other nonconcretion analog models proposed can generate spheroidal geometry but lack other key characteristics. The Navajo Sandstone concretions share similarities to all the characteristics of the Burns formation spherules and thus, it is clear that diagenetic groundwater fluid flow and diffusive mass transfer are responsible for the formation of the Mars spherules.

Conclusions

Navajo Sandstone spheroidal HFO concretions (Table 1.3) are classified by size: 1. macro concretions are >5 mm in diameter, and 2. micro concretions are <5 mm in diameter. Macro concretions are divided into three end members based on internal structure. 1. Rind concretions have a well-cemented HFO rind surrounding an interior relatively depleted of HFO cement. 2. Layered concretions have a rind similar to rind concretions but have ≥ 2 well-cemented, overlapping layers throughout the interior. 3. Solid concretions are evenly well-cemented with HFO throughout the interior of the concretion. Micro concretions have two end members: rind and solid.

Table 1.3. Navajo Sandstone HFO concretion characterization summary.









		DESCRIPTION	INTERPRETATION
MACRO		> 5 mm in diameter; 3 internal structure end members; mostly nearly spherical; occasional conjoined forms	Form by combination of diffusive/advective mass transfer in reaction fronts
INTERIOR STRUCTURE			
	Rind	Thin (1-10mm) spheroidal well-cemented HFO rind surrounding an interior relatively depleted of HFO cement.	End member; macro concretion
	Layered	Rind with two or more well-cemented, concentric layers that persist throughout the interior of the concretion	End member; macro concretion
	Solid	Evenly cemented with HFO throughout entire concretion; >5 mm diameter	Concretion type end member; macro concretion
MICRO		<5 mm in diameter; 2 internal structure end members; mostly nearly spherical; occasional conjoined forms	Form by diffusive mass transfer in reaction fronts
INTERIOR STRUCTURE			
	Rind	Similar structurally to Macro concretion rind and solid end members	
	Solid		
Intermediate between end members		Interior structure can vary between end members (Fig. 4)	Late-stage mineralization events alter internal structure
SIZE			
Range		0.8 mm to 8+ cm diameter	Macros >5 mm in diameter; micros <5 mm diameter. Two populations of macros: 5-12 mm and >12 mm
Mean		22.46 mm diameter	
Distribution		trimodal: 0.8-5 mm, 5-12 mm, 12-80+ mm	
GEOMETRY			
Aspect ratio		Range: 1.00-1.97; mean=1.10; median=1.06	Nearly spherical concretions occur in homogenized host rock; discoidal concretions occur in more permeable laminae
		Perfectly spherical (aspect ratio=1.00)	
		Nearly spherical (aspect ratio ≤1.06)	
		Discoidal (aspect ratio >1.06)	
EXTERIOR STRUCTURE			
Color		Black or brown	Dependant on mineralogy and crystal size
Texture		Smooth and shiny	Weathering, possible desert varnish
		Rough and sandy	Not as densely cemented
		Bumpy "avocado skin" texture	Micros coalesce to form larger macros

Table 1.3 continued.

	DESCRIPTION	INTERPRETATION
CEMENT (MICROSCOPY)		
Rind concretions		
rind	Three textural phases: 1. granular grain coatings 2. tabular 3. fine-grained euhedral pore filling	Pervasive growth.
interior	Kaolinite blebs, some illite grains coatings, granular HFO	Interiors depleted of cement relative to rinds
Layered concretions		
rind	Rind similar to rind concretions	Pervasive growth
interior	Fine-grained, granular HFO in layers, kaolinite in blebs	
Solid concretions	Granular HFO throughout concretion	Possible combination of radial and pervasive growth
MINERALOGY (QEMSCAN)		
Rind concretions		
rind	Smooth textured HFO (94.5%), frothy textured HFO (1.8%), kaolinite (1.9%), MnO (0.2%)	MnO occurs along more permeable laminae as a late-stage pore fill.
interior	Smooth textured HFO (20.0%), frothy textured HFO (26.8%), kaolinite (49.5%)	Frothy textured HFO probably the granular texture seen with petrographic microscope
MINERALOGY (Vnir SPECTROSCOPY)		
Rind concretions		
rind	Amorphous HFO or goethite	Multiple precipitation events add younger phases by diffusion through rinds
interior	Goethite near outer edge; hematite in center	
Layered concretions	Amorphous HFO or goethite throughout; hematite in depleted center of one sample	Late-stage precipitation events alter interior structure by diffusion of reactants through rinds (rinds initially are more porous)
Solid concretions	Amorphous HFO or goethite throughout	

Navajo Sandstone HFO concretions form by a pervasive growth model similar to some carbonate concretions where the radius is set as HFO crystals nucleate concomitantly throughout the concretion. Concretions initially precipitate as an amorphous HFO gel precursor that sets the diameter of the concretions and likely retains some porosity. Cement textures imply that concretions grow inward from the set radius. Subsequent precipitation events infill retained porosity by diffusing reactants through the semipermeable, gel-like rinds. The amorphous HFO dehydrates to more stable phases (goethite, then hematite). The location of younger, more unstable HFO phases in the interiors of layered and solid concretions suggests that internal structural variations are probably due to diffusion of reactants into the interiors of the concretions during late-stage precipitation events. Spherical and nearly spherical geometries indicate that concretions grow via diffusive mass transfer of reactants.

The Navajo Sandstone concretions in southern Utah provide an excellent analog for the Burns formation spherules on Mars. Key diagnostic similarities show that the Mars spherules are concretions formed via diagenetic diffusive mass transfer of reactants. The Utah example suggests the possibility of precursor mineral phases to hematite in the Burns formation in Meridiani Planum where concretions on Mars may have undergone an evolution of cements similar to the Navajo Sandstone concretions.

Navajo Sandstone HFO concretions record a complex diagenetic history of a porous reservoir unit. Although the host rock generally records only the latest precipitation or mobilization event, the concretions may preserve a longer and more detailed history of water-rock interactions. It is likely that concretions initially form quickly (1000 yr-scale) and subsequent precipitation events add cements and modify internal structures

throughout the burial history. Thus, concretions can contain a detailed record of reservoir fluid compositions and the evolution of diagenetic fluids. The ability to infer multiple precipitation events and how concretions grow has far-reaching implications for understanding reservoir diagenesis.

References

- Barge, L.M., Petruska, J., 2007. Iron precipitation patterns in gels; implications for the formation of hematite concretions at Meridiani Planum, Mars. *Lunar and Planetary Science XXXVIII*, Abstract 1676.
- Beitler, B., Chan, M.A., Parry, W.T., 2003. Bleaching of Jurassic Navajo Sandstone on Colorado Plateau Laramide highs; evidence of exhumed hydrocarbon supergiants? *Geology*, 31, 1041-1044.
- Beitler, B., Parry, W.T., Chan, M. A., 2005. Fingerprints of fluid flow: chemical diagenetic history of the Jurassic Navajo Sandstone, southern Utah, U.S.A. *JSR*, 75, 547-561.
- Benison, K.C., 2006. A Martian analog in Kansas: Comparing Martian strata with Permian acid saline lake deposits. *Geology*, 34, 5, 385-388.
- Benison, K.C., Bowen, B.B., 2006. Acid saline lake systems give clues about past environments and the search for life on Mars. *Icarus*, 183, 225-229.
- Benison, K.C., Bowen, B.B., Oboh-Ikuenobe, F.E., Jagniecki, E.A., LaClair, D.A., Story, S.L., Mormile, M.R., Hong, B., 2007. Sedimentology of acid saline lakes in southern Western Australia: newly described processes and products of an extreme environment. *JSR*, 77, 366-388.
- Bishop, J.L., Dyar, M.D., Parente, M., Drief, A., Mancinelli, R.L., Lane, M.D., Murad, E., 2006. Understanding surface processes on Mars through study of iron oxides/oxyhydroxides: clues to surface alteration and aqueous processes. *Lunar and Planetary Science XXXVII*, Abstract 1438.
- Bjørlykke, K., 1973. Origin of limestone nodules in the Lower Paleozoic of the Oslo region. *Norsk Geologisk Tidsskrift*, 53, 419-431.
- Boles, J.R., Landis, C., Dales, P., 1985. The Moeraky boulders: anatomy of some septarian concretions. *JSP*, 55, 398-406.

- Bowen, B.B., Martini, B.A., Chan, M.A., Parry, W.T., 2007. Reflectance spectroscopic mapping of diagenetic heterogeneities and fluid-flow pathways in the Jurassic Navajo Sandstone. *AAPG Bulletin*, 91, 173–190.
- Bowen, B.B., Benison, K.C., Oboh-Ikuenobe, F.E., Story, S., Mormile, M.R., 2008. Active hematite concretion formation in modern acid saline lake sediments, Lake Brown, Western Australia. *ESPL*, 268, 52-63.
- Calvin, W.M., Shoffner, J.D., Johnson, J.R., Knoll, A.H., Pockock, J.M., Squyres, S.W., Weitz, C.M., Arvidson, R.E., Bell J.F., III, Christensen, P.R., de Souza, P.A., Jr., Farrand, W.H., Glotch, T.D., Herkenhoff, K.E., Jolliff, B.L., Knudson, A.T., McLennan, S.M., Rogers, A.D., Thompson, S.D., 2008. Hematite spherules at Meridiani: results from MI, Mini-TES and Pancam. *JGR*, 113, E12S37.
- Catling, D.C., Moore, J.M., 2003. The nature of coarse-grained crystalline hematite and its implications for the early environment of Mars. *Icarus*, 165, 277-325.
- Chan, M.A., Parry, W.T., Bowman, J.R., 2000. Diagenetic hematite and manganese oxides and fault-related fluid flow in Jurassic sandstone, southeastern Utah. *AAPG Bulletin*, 84, 1281-1310.
- Chan, M.A., Beitler, B., Parry, W.T., Ormö, J., Komatsu, G., 2004. A possible terrestrial analogue for hematite concretions on Mars. *Nature*, 429, 731-734.
- Chan, M.A., Bowen, B.B., Parry, W.T., Ormö, J., Komatsu, G., 2005. Red rock and red planet diagenesis: comparison of Earth and Mars concretions. *GSA Today*, 15, 4-10.
- Clark, R.N., Trude, V.V., King, M.K., Swayze, G.A., Vergo, N., 1990. High spectral resolution reflectance spectroscopy of minerals. *JGR*, 95, 653–680.
- Clark, R.N., 1999. Spectroscopy of rocks and minerals, and principles of spectroscopy. In: A. N. Rencz, (Ed.), *Manual of Remote Sensing*, v. 3: Remote Sensing for the Earth Sciences, New York, John Wiley and Sons, chapter 1, pp. 3–58.
- Clark, R.N., Swayze, G.A., Wise, R., Livo, E., Hoefen, T., Kokaly, R., Sutley, S.J., 2007. USGS digital spectral library splib06a: U.S. Geological Survey, Digital Data Series 231, <http://speclab.cr.usgs.gov/spectral.lib06>.
- Clifton, H E., 1957. The carbonate concretions of the Ohio shale. *The Ohio Journal of Science*, 57, 114-124.
- Coleman, M.L., Raiswell, R., 1981. Carbon, oxygen and sulphur isotope variations in concretions from the upper Lias of N.E. England. *Geochimica et Cosmochimica Acta*, 45, 329-340.

- Coleman, M.L., Raiswell, R., 1995. Source of carbonate and origin of zonation in pyritiferous carbonate concretions; evaluation of a dynamic model. *AJS*, 295, 282-308.
- Criss, R.E., Cooke, G.A., Day, S.D., 1988. An organic origin for the carbonate concretions of the Ohio shale. *USGS Bulletin*, 1836. 1-21.
- Dickson, J.A.D., Barber, C., 1976. Petrography, chemistry and origin of early diagenetic concretions in the Lower Carboniferous of the Isle of Man. *Sedimentology*, 23, 189-211.
- Feistner, E.W.A., 1989. Petrographic examination and re-interpretation of concretionary carbonate horizons from Kimmeridge Bay, Dorset. *Journal of the Geological Society*, London, 146, 345-350.
- Fisher, Q.J., Raiswell, R., Marshall, J.D., 1998. Siderite concretions from non-marine shales (Westphalian A) of the Pennines, England: controls on their growth and composition. *JSR*, 68, 1034-1045.
- Glotch, T.D., Morris, R.V.; Christensen, P.R., Sharp, T.C., 2004. Effect of precursor mineralogy on the thermal infrared emission spectra of hematite; application to Martian hematite mineralization. *JGR*, 109.
- Glotch, T.D., Bandfield, J.L., 2006. Determination and interpretation of surface and atmospheric Miniature Thermal Emission Spectrometer spectral end-members at the Meridiani Planum landing site. *JGR*, 111, E12S06.
- Golden, D.C., Ming, D.W., Morris, R.V., Graff, T.G., 2008. Hydrothermal synthesis of hematite spherules and jarosite: implications for diagenesis and hematite spherule formation in sulfate outcrops at Meridiani Planum, Mars. *Am. Mineralogist*, 93, 1201-1214.
- Grotzinger, J.P., Arvidson, R.E., Bell, J.F., III, Calvin, W.M., Clark, B.C., Fike, D.A., Golombek, M.P., Greeley, R., Haldemann, A., Herkenhoff, K.E., Jolliff, B.L., Knoll, A.H., Malin, M.C., McLennan, S.M., Parker, T., Soderblom, L., Sohl-Dickstein, J.N., Squyres, S.W., Tosca, N.J., Watters, W.A., 2005. Stratigraphy and sedimentology of a dry to wet eolian depositional system, Burns Formation, Meridiani Planum, Mars. *EPSL*, 240, 11-72.
- Hedges, E.S., Myers, J.E., 1926. *The Problem of Physico-chemical Periodicity*. London, Arnold.
- Hesselbo, S.P., Palmer, T.J., 1992. Reworked early diagenetic concretions and the bioerosional origin of a regional discontinuity within British Jurassic marine mudstones. *Sedimentology*, 39, 1045-1065.

- Hudson, J.D., 1978. Concretions isotopes and the diagenetic history of the Oxford Clay (Jurassic) of central England. *Sedimentology*, 25, 339-370.
- Huggett, J.M., 1994. Diagenesis of mudrocks and concretions from the London Clay formation in the London Basin. *Clay Minerals*, 29, 693-707.
- Jordan, M.M., Curtis, C.D., Aplin, A.C., Coleman, M.L., 1992. Access of pore waters to carbonate precipitation sites during concretions growth. In: Kharaka, Y., Maest, A.S., (Eds.), *Proceedings of the 7th International Symposium on Water-Rock Interactions*, Balkema, Rotterdam, pp. 1239-1242.
- Klein C., Jr., Bricker, O.P., 1977. Some aspects of the sedimentary and diagenetic environment of Proterozoic banded iron-formation. *Economic Geology*, 72, 1457-1470.
- Klingelhöfer, G., Morris, R.V., Bernhardt, B., Schröder, C., Rodionov, D.S., de Souza Jr., P.A., Yen, A., Gellert, R., Evlanov, E.N., Zubkov, B., Foh, J., Bonnes, U., Kankeleit, E., Gutlich, P., Ming, D.W., Renz, F., Wdowiak, T., Squyres, S.W., Arvidson, R.E., 2004. Jarosite and hematite at Meridiani Planum from Opportunity's Mössbauer spectrometer. *Science*, 306, 1740-1745.
- Knauth, L.P., Burt, D.M., Wohletz, K.H., 2005. Impact origin of sediments at the Opportunity landing site on Mars. *Nature*, 438, 1123-1128.
- Lane, M.D., Morris, R.V., Christensen, P.R., 1999. The spectral behavior of hematite at visible/near infrared and midinfrared wavelengths. In: *Fifth International Conference on Mars*, LPI Contrib. 972, abstract 6085, Lunar and Planet. Sci., Houston, Tex.
- Liesegang, R.E., 1896. Ueber einige Eigenschaften von Gal-lerten [On some properties of gelatin]. *Naturwissenschaftliche Wochenschrift*, 11, 353-362.
- Lyons, T.W., Raiswell, R., Robinson, A., Scott, C., Chu, X., Li, C., Love, G., Sessions, A., Gill, B., 2007. Carbonate concretions as a window to the evolving chemistry of the early ocean and atmosphere. *Geochimica et Cosmochimica Acta*, 71, A606.
- McBride, E.F., Picard, M.D., Milliken, K.L., 2003. Calcite-cemented concretions in Cretaceous sandstone, Wyoming and Utah, U.S.A. *JSR*, 73, 462-484.
- McLennan, S.M., Bell, J.F., Calvin, W.M., Christensen, P.R., Clark, B.C., de Souza, P.A., Farmer, J., Farrand, W.H., Fike, D.A., Gellert, R., Ghosh, A., Glotch, T.D., Grotzinger, J.P., Hahn, B., Herkenhoff, K.E., Hurowitz, J.A., Johnson, J.R., Johnson, B., Jolliff, G., Klingelhöfer, A.H., Knoll, Z., Learner, M.C., Malin, H.Y., McSween, S.S., Pockock, J., Ruff, S.W., Soderblom, L.A., Squyres, S.W., Tosca, N.J., Watters, W.A., Wyatt, M.B., Yen, A., 2005. Provenance and diagenesis of the evaporite-bearing Burns formation, Meridiani Planum, Mars. *EPSL*, 240, 95-121.

- Morris, R.V., Agresti, D.G., Lauer, H.V. Jr., Newcomb, J.A., Shelfer, T.D., Murali, A.V., 1989. Evidence for pigmentary hematite on Mars based on optical, magnetic, and Mossbauer studies of superparamagnetic (nanocrystalline) hematite. *JGR*, 94, 2760-2778.
- Morris, R.V., Ming, D.W., Graff, T.G., Arvidson, R.E., Bell, J.F., Squyres, S.W., Mertzman, S.A., Gruener, J.E., Golden, D.C., Le, L., Robinson, G.A., 2005. Hematite spherules in basaltic tephra altered under aqueous, acid-sulfate conditions on Mauna Kea volcano, Hawaii: possible clues for the occurrence of hematite-rich spherules in the Burns formation at Meridiani Planum, Mars. *EPSL*, 240, 168-178.
- Morris, R.V., Klingelhofer, G., Schroeder, C., Rodionov, D.S., Yen, A., Ming, D.W., de Souza, P.A., Jr., Wdowiak, T., Fleischer, I., Gellert, R., Bernhardt, B., Bonnes, U., Cohen, B.A., Evlanov, E.N., Foh, J., Guetlich, P., Kankleit, E., McCoy, T.J., Mittlefehldt, D.W., Renz, F., Schmidt, M.E., Zubkov, B., Squyres, S.W., Arvidson, R.E., 2006. Mössbauer mineralogy of rock, soil, and dust at Meridiani Planum, Mars: Opportunity's journey across sulfate-rich outcrop, basaltic sand and dust, and hematite lag deposits. *JGR*, 111, E12S15.
- Mozley, P.S., 1989. Complex zonation in concretionary siderite: implications for geochemical studies. *JSP*, 59, 815-818.
- Mozley, P.S., 1996. The internal structure of carbonate concretions in mudrocks: a critical evaluation of the conventional concentric model of concretions growth. *Sed. Geol.*, 103, 85-91.
- Mozley, P.S., and Davis, J.M., 2005. Internal structure and mode of growth of elongate calcite concretions; evidence for small-scale, microbially induced, chemical heterogeneity in groundwater. *GSA Bulletin*, 117, 1400-1412.
- Munsell Rock-Color Chart, 1975. Prepared by The Rock-Color Chart Committee, Distributed by The Geological Society of America, Boulder Colorado.
- Ormö, J., Komatsu, G., Chan, M.A., Beitler, B., Parry, W.T., 2004. Geological features indicative of processes related to the hematite formation in Meridiani Planum and Aram Chaos, Mars: a comparison with diagenetic hematite deposits in southern Utah, U.S.A. *Icarus*, 171, 295-316.
- Ortoleva, P.T., 1994. *Geochemical Self-Organization*. Oxford Univ. Press.
- Ostwald, W., 1925. *Kolloid Z.* 36, 330.
- Pantin, H.M., 1958. Rate of formation of a diagenetic calcareous concretion. *JSP*, 28, 366-371.

- Parrish, J.T., Falcon, H.J., 2007. Coniferous trees associated with interdune deposits in the Jurassic Navajo Sandstone Formation, Utah, U.S.A. *Palaeontology*, 50, 829–843.
- Parry, W.T., Chan, M.A., Beitler, B., 2004. Chemical bleaching indicates episodes of fluid flow in deformation bands in sandstone. *AAPG Bulletin*, 88, 175-191.
- Prosser, D.J., Daws, J.A. Fallick, A.E., Williams, B.P.J., 1994. The occurrence and δS^{34} of authigenic pyrite in Middle Jurassic Brent Group sediments. *JPG*, 17, 407-428.
- Raiswell, R., 1976. The microbiological formation of carbonate concretions in the upper Lias of NE England. *Chemical Geology*, 18, 227-244.
- Raiswell, R., Fisher, Q.J., 2000. Mudrock-hosted carbonate concretions: a review of growth mechanisms and their influence on chemical and isotopic composition. *Journal of the Geological Society London*, 157, 239-251.
- Schumacher, R., Schmincke, H., 1991. Internal structure and occurrence of accretionary lapilli — a case study at Laacher See Volcano. *Bulletin of Volcanology*, 53, 612-634.
- Sefton-Nash, E., Catling, D.C., 2008. Hematitic concretions at Meridiani Planum, Mars: their growth timescale and possible relationship with iron sulfates. *EPSL*, 269, 366–376.
- Seiler, W.M., 2008. Jurassic Navajo Sandstone of Coyote Buttes, Utah/Arizona: Coloration and diagenetic history, preservation of a dinosaur trample surface, and a terrestrial analog to Mars. M.S. Thesis, University of Utah, Salt Lake City, Utah, U.S.A.
- Seilacher, A., 2001. Concretion morphologies reflecting diagenetic and epigenetic pathways. *Sed. Geo.*, 143, 41-57.
- Steeffel, C. I., Van Cappellen, P., 1990. A new kinetic approach to modeling water-rock interaction: the role of nucleation, precursors, and Ostwald ripening. *Geochimica et Cosmochimica Acta*, 54, 2657-2677.
- Stern, K.H., 1954. The Liesegang Phenomenon. *Chem. Rev.*, 54, 79-99.
- Sultan, R., Ortoleva, P., DePasquale, F., Tartaglia, P., 1990. Bifurcation of the Ostwald-Liesegang supersaturation-nucleation-depletion cycle. *Earth-Science Reviews*, 29, 163-173.
- Squyres, S.W., Grotzinger, J.P., Arvidson, R.E., Bell, J.F., III, Calvin, W.M., Christensen, P.R., Clark, B.C., Crisp, J.A., Farrand, W.H., Herkenhoff, K.E., Johnson, J.R., Klingelhoefer, G., Knoll, A.H., McLennan, S.M., McSween, H.Y., Morris, R.V., Rice, J.W., Rieder, R., Soderblom, L.A., 2004. In situ evidence for an ancient aqueous environment at Meridiani Planum, Mars. *Science*, 306, 1709-1714.

Squyres, S.W., Knöfl, A.H., Arvidson, R.E., Ashley, J.W., Bell, J.F., III, Calvin, W.M., Christensen, P.R., Clark, B.C., Cohen, B.A., de Souza, P.A., Jr., Edgar, L., Farrand, W.H., Fleischer, I., Gellert, R., Golombek, M.P., Grant, J., Grotzinger, J., Hayes, A., Herkenhoff, K.E., Johnson, J.R., Jolliff, B., Klingelhöfer, G., Knudson, A., Li, R., McCoy, T.J., McLennan, S.M., Ming, D.W., Mittlefehldt, D.W., Morris, R.V., Rice, J.W., Jr., Schröder, C., Sullivan, R.J., Yen, A., Yingst, R.A., 2009. Exploration of Victoria Crater by the Mars Rover Opportunity. *Science*, 324, 1058-1061.

CHAPTER 2

JOINT-CONTROLLED FLUID FLOW PATTERNS IN JURASSIC NAVAJO SANDSTONE: ANALOG IMPLICATIONS FOR MARS HEMATITE

Sally L. Potter and Marjorie A. Chan, University of Utah, Department of Geology and Geophysics, 115 S. 1460 E. Rm. 383, FASB, Salt Lake City, UT 84112

Abstract

Prominent clusters of NE-striking joints lined with hydrous ferric oxide (HFO) display emanating asymmetrical fluid flow and precipitation patterns in the Jurassic Navajo Sandstone of Grand Staircase Escalante National Monument (GSENM), Utah. Three types of Navajo Sandstone HFO precipitation geometries are: 1. common macro concretions (>5mm diameter), 2. ubiquitous micro concretions (<5mm diameter), and 3. localized HFO-lined northeast-striking joints with associated asymmetrical loopy mineralization and banded precipitation patterns (Liesegang bands). The spheroidal geometries indicate diffusive mass transfer whereas asymmetrical mineralization implies advective directional fluid flow through the sandstone. Liesegang bands parallel to asymmetrical mineralization denote a diffusive mass transfer component perpendicular to flow direction.

Cross-cutting relationships between different concretionary geometries indicate a relative timing sequence. Macro concretions formed during the post-Laramide (<55Ma), prior to and independent of the joints. The joints formed during the Miocene and

provided conduits for oxidizing fluids that precipitated HFO lining on the joint faces. Advective mass transfer overprinted the area with preferentially cemented loop banding and asymmetrical mineralized flow lines approximately 5Ma, coincident with development of a hydraulic low to the southeast of the region.

Utah micro concretions show strong similarities to Mars “blueberries” such as ubiquitous accumulations, self-organized *in situ* distributions, and spheroidal geometries. This terrestrial analog example implies that the Mars spherules probably formed by simple diffusion under nearly isotropic fluid flow conditions. The small, relatively uniform hematite concretions on Mars may be the result of simpler diagenetic processes compared to the complex Navajo Sandstone diagenetic history that produced multiple generations of precipitation geometries.

Introduction

The eolian Jurassic Navajo Sandstone is a porous and permeable quartz arenite widely exposed throughout southern Utah and northern Arizona (Blakey et al., 1988; Blakey, 1994; Chan et al., 2005). This unit is renowned for its spectacular coloration created by a diagenetic history of paleo-fluid imprinting iron precipitation. Local to regional coloration patterns and a large variety of spheroidal concretions record cement precipitation during burial diagenesis.

Established geochemical and paleo-hydrological models explain the mobilization and precipitation of iron in the Navajo Sandstone with a model for iron cycling detailed by Chan et al. (2000, 2004, 2005, 2006, 2007), Beitler et al. (2003, 2005) and Parry et al. (2004). This model is tripartite. 1. Iron source - Iron precipitates as hematite grain coatings due to the syndepositional to early diagenetic breakdown of ferromagnesian

minerals upon deposition and early burial of the erg. 2. Iron mobilization - The iron mobilizes as Fe^{2+} when a reducing fluid infiltrates into the reservoir. 3. Iron precipitation - Hydrated ferric oxide (HFO) precipitates when this iron-bearing reducing fluid meets and mixes with an oxidizing fluid, forming concretions and other precipitation geometries in the sandstone unit. Beitler et al. (2003, 2005) and Parry et al. (2004) show that Laramide-aged (~55Ma) blind thrusts acted as conduits for buoyant, reducing fluids (possibly hydrocarbon) to infiltrate the sandstone reservoir.

Diagenetic facies are mapped for various regions of the Navajo Sandstone where it is exposed in southern Utah and northern Arizona (Beitler et al., 2005, Beitler Bowen et al. 2007, Seiler, 2008). Beitler et al. (2005) describe diagenetic facies in the Navajo Sandstone that included a primary red facies which exhibits a uniform red color in outcrop and a localized secondary red facies which exhibits a patchy or mottled appearance in outcrop. The difference between the two facies is apparent in thin section: the primary red facies contains uniform grain coatings of hematite and the secondary red facies exhibits small (~10 μm), concentrated blebs of HFO (such as amorphous HFO, goethite, and hematite phases) in pore throats.

Purpose of Study

The Spencer Flat field area located in Grand Staircase Escalante National Monument (GSENM) (Fig.2.1) exhibits spectacular precipitation geometries including HFO-lined resistant northeast-striking joint faces with associated loopy asymmetrical mineralization

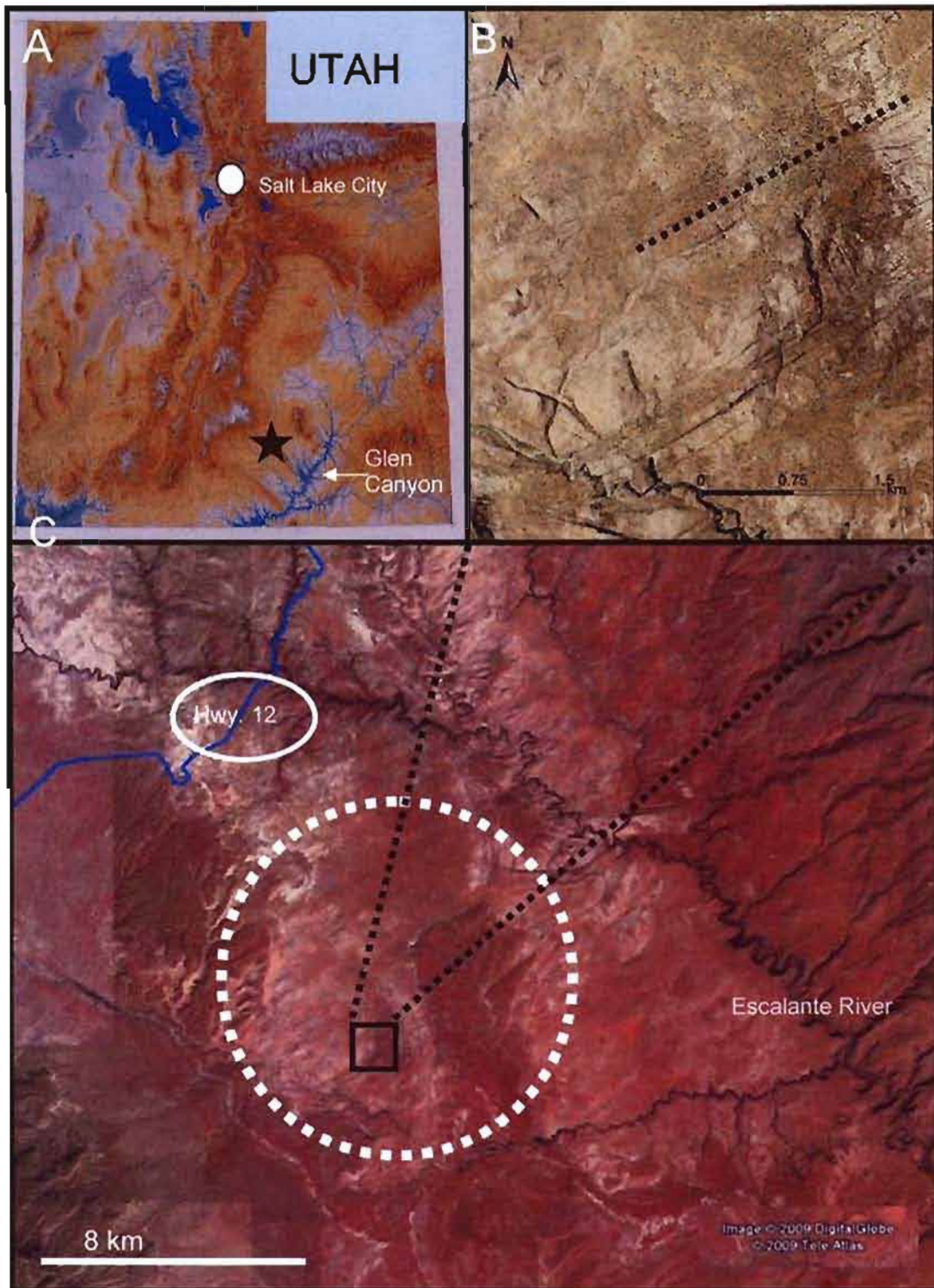


Fig. 2.1. Spencer Flat area in GSENM A. Utah, USA. Star shows Grand Staircase Escalante National Monument study area to the northeast of Glen Canyon. B. Aerial photo of study area. Dotted line delineates strike of northeast striking joints. C. Google Earth image of Spencer Flat Study area south of Hwy. 12 ($\sim 37^{\circ} 41' N$ and $111^{\circ} 22' W$). Black box is area shown in B.

and banded precipitation patterns. This area is particularly noted for spheroidal HFO concretions with a range of sizes and interior morphologies (Figs. 2.4, 2.5). Evidence of iron cycling in the Navajo Sandstone (Parry et al., 2004, Beitler et al., 2005, Chan et al., 2007, Seiler, 2008) and its correlative unit, the Aztec Sandstone (Eichubel et al., 2004), raises questions about the process of mass transfer and how it affects HFO concretionary forms.

The purpose of this study is to document concretionary geometries and their distributions in the Spencer Flat study area, and interpret the iron cycling processes of advective and diffusive mass transfer. The relative timing of precipitation events is established by observations of field relationships between precipitation geometries. These data distinguish how mass transfer processes affect concretionary geometries and whether concretions are formed in one event or several discrete events.

Terrestrial Analog to Mars

Previous authors have proposed the Navajo Sandstone spheroidal concretions as a terrestrial analog for Mars spheroidal concretions (Chan et al., 2004, 2005; Ormö et al., 2004). The Burns formation host rock in Meridiani Planum, Mars (Grotzinger et al., 2005) displays three important similarities to the Navajo Sandstone. 1. It is a porous and permeable eolian unit with some cross-stratification and planar stratification. 2. It has an extended diagenetic history with the uppermost unit formed subaqueously due to a risen water table. 3. Paleo groundwater played a large role in the geochemical diagenesis of the

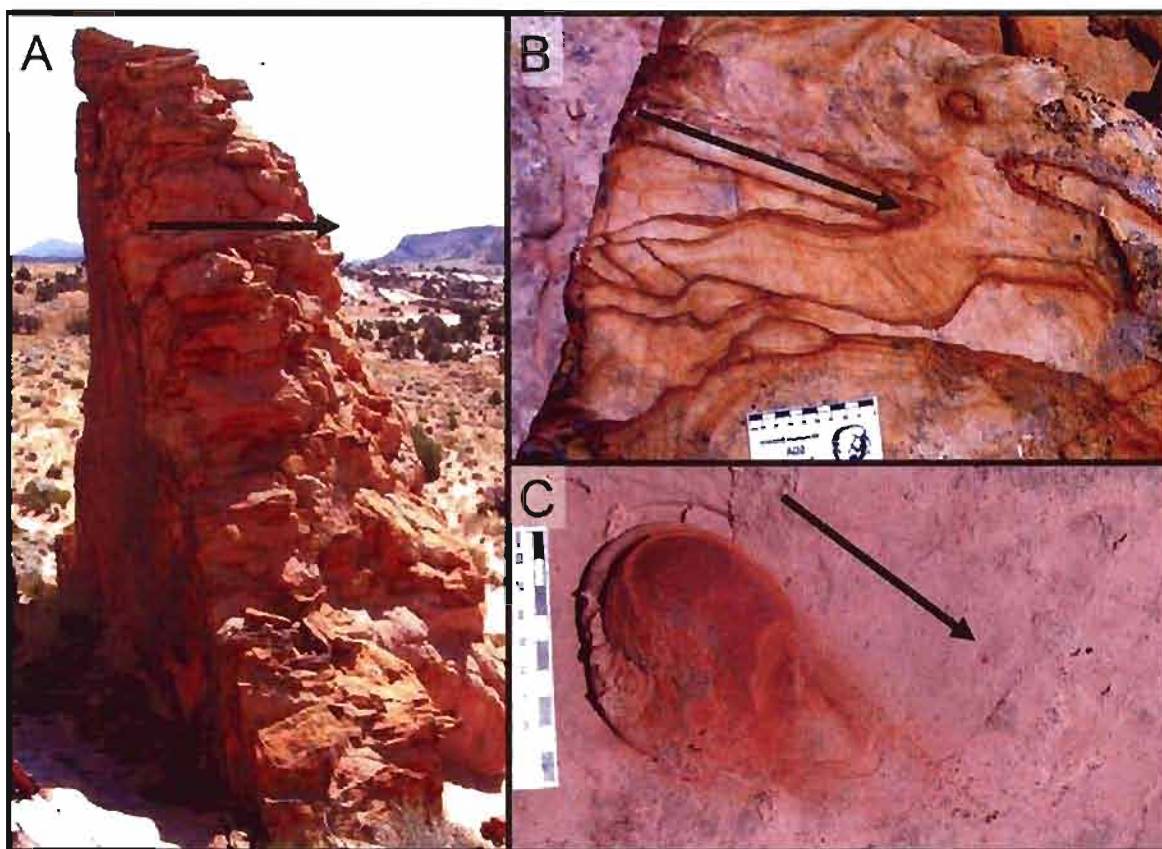


Fig. 2.2. Northeast-striking HFO-lined joints and associated asymmetrical mineralization. Arrows point southeast in the direction of advective flow of reactants. A. Resistant face of a northeast joint with HFO cementation and asymmetrical mineralization to the southeast. B. Map view of a northeast joint with loopy, asymmetrical mineralization to the southeast. Liesegang bands parallel the well-cemented loops. C. Elongate halo around an *in situ* concretion. Large tick marks on scale bars in views B and C are equal to 1 cm.

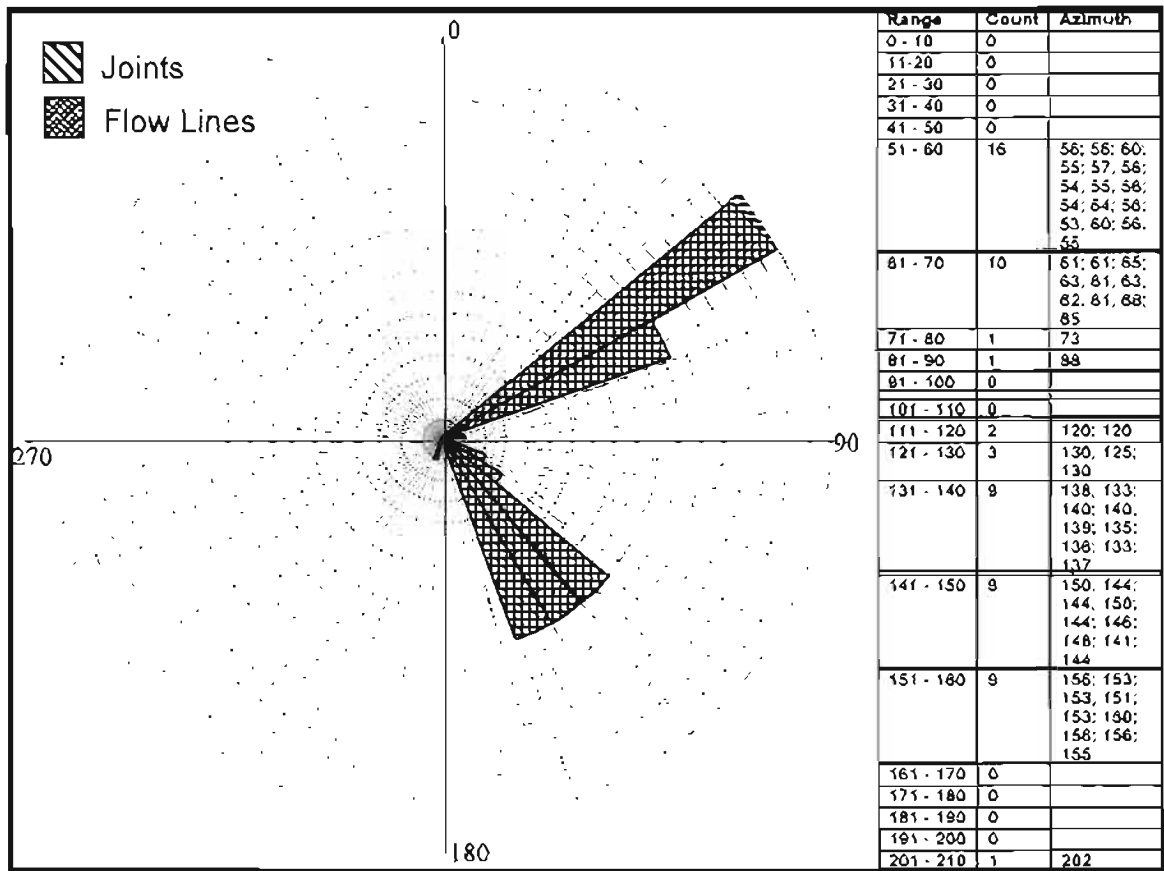


Fig. 2.3. Rose diagram of joints (striped, $n=29$) and related asymmetrical flow lines (cross-hatched, $n=32$).

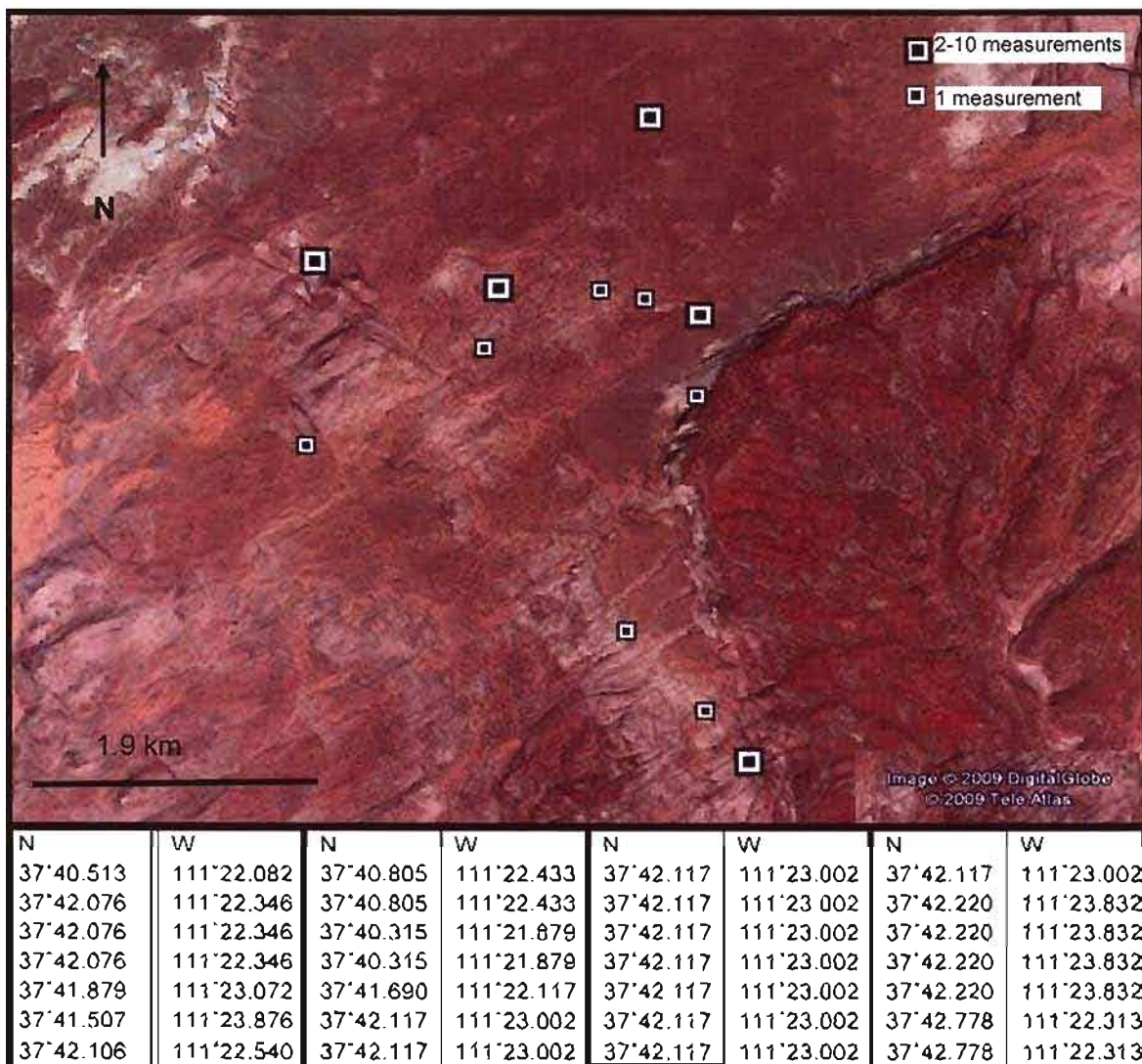


Fig. 2.4. Location of joint and asymmetrical mineralization measurements in Spencer Flat area. Chart gives waypoint locations of measurements.

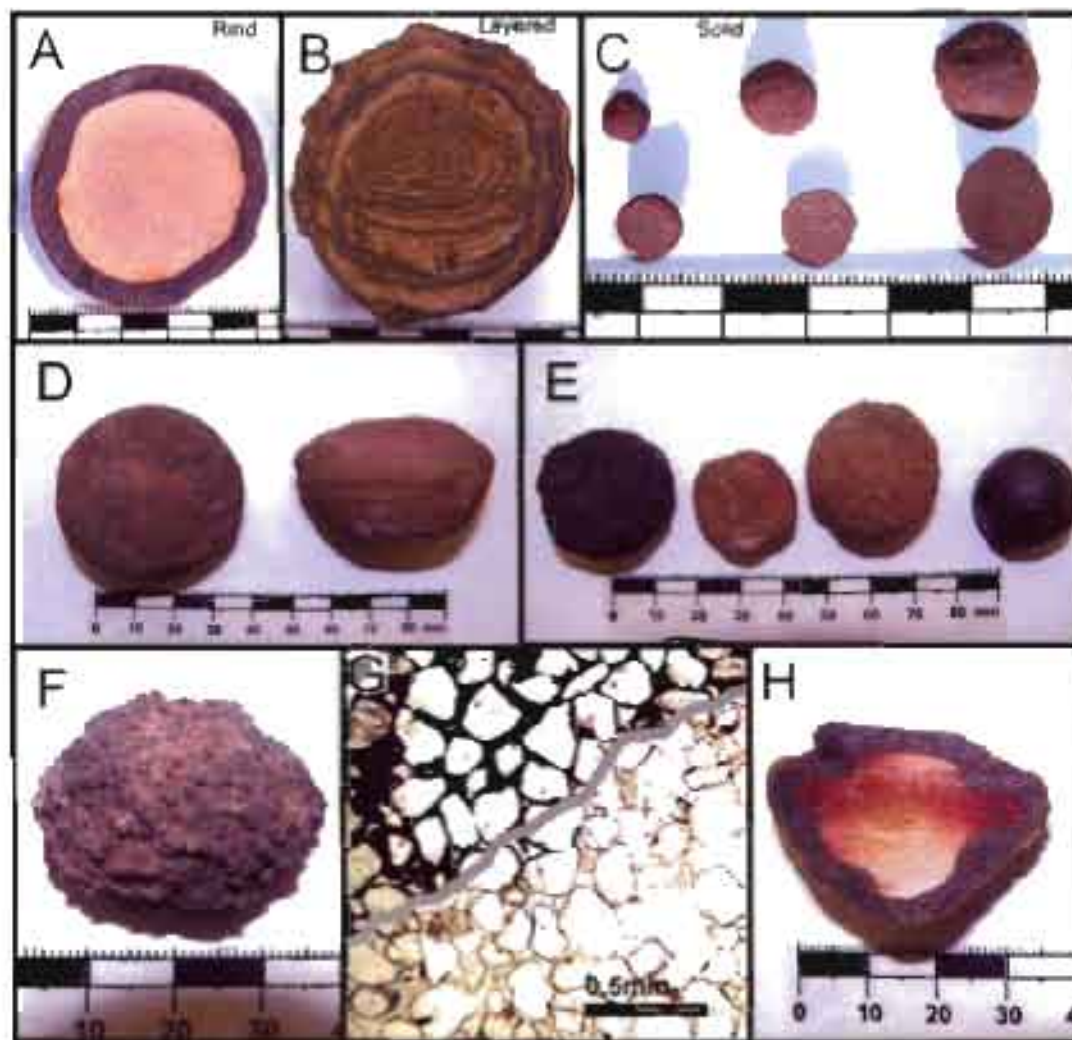


Fig. 2.5 Macro concretion characteristics. Large tick marks on scale bars are cm. A Rind concretion end member with friable interior depleted of HFO cement. B Layered concretion end member. C Cut interiors of solid concretion end member. D Spheroidal and discoidal exterior structure. E Exterior structures (from left to right): Black, rough exterior, sandy brown exteriors (middle two samples); dark, smooth exterior. F "Avocado skin" exterior formed from coalesced micro concretions. G Photomicrograph of rind concretion. Line delineates well cemented rind (above line) from friable interior (below line). $\times 3X$ magnification. Plane light. H Rind concretion with diffusive interior coloration inward along coarser grained, more permeable laminae.

unit including the precipitation of hematite concretions termed “blueberries” (McLennan, 2005, Squyres et al., 2006). These “blueberries” are geometrically similar to the Navajo Sandstone concretions and they are likewise more resistant to weathering than the host rock and weather out to collect in topographic lows (Chan et al., 2004; Ormö et al., 2004)

It is further proposed that the hematite “blueberries” formed in a low temperature, nearly stagnant water table (McLennan et al., 2005). A reasonable geochemical analog is the low temperature acid-sulfate reactions that form similar hematite concretions in acid-saline lake sediments in Western Australia (Bennison et al., 2006; Bowen et al., 2008). Other proposed models to explain a spheroidal geometry for Mars spherules call upon hydrothermal heating of an acid-sulfate brine (McCullom and Hynek, 2005; Morris et al., 2005; Golden et al., 2008) or impact lapilli (Knauth et al. 2005). However, these hydrothermal and impact lapilli models do not generate the observed *in situ* distribution present in both the Burns formation spherules and the Navajo Sandstone concretions. Mars spherules have many features in common with diagnostic characteristics of the Navajo Sandstone concretions (see Chapter 1) to conclude that the spherules are diagenetic concretions.

Methods

Field studies were conducted in several ~100 m² areas of Spencer Flat in GSENM where *in situ* and multiple generation geometries are preserved. The Munsell Rock-Color Chart (1975) was used to describe colors of host rock and concretions. Exteriors of concretions exhibit a range of colors from dark brown (dusky brown [5YR 2/2]) to dusky yellowish brown [10 YR 2/2]) to light brown (moderate brown [5 YR 3/4]) to grayish red [10 R 4/2]). Interior colors range from yellowish grey (5 Y 8/1) when they are depleted of

HFO cement to light brown when they are solidly cemented. Interiors also exhibit a wide variety of red (5-10 R 2-5/ 2-6), yellow (5-10 YR 5-8/2-6) and brown patterns (5-10 YR 2-4/ 2-6). The HFO lining of northeast joints is dusky brown and the asymmetrical loopy mineralization is a dark reddish brown (10 R 3/4). Associated with the loopy mineralization are dark yellowish orange streaks (10 YR 6/6) which overprint the host rock. Secondary red facies is primarily light to moderate red (5 R 6-5/6-4) and the bleached facies is predominately yellowish grey.

Measurements for statistical analyses of nearest neighbor spacing and volumetric density were made in the field and from photographs using JMicroVision software. The nearest neighbor spacing of *in situ*, spheroidal micro (<5 mm diameter) and macro (>5 mm diameter) concretions was measured on two-dimensional surfaces (see Appendix F for all measurements). Nearest neighbor distances of *in situ* macro concretions were measured in 4 m² areas (three in the field and one from a photograph). Micro concretions were measured in 10 areas (usually 9 cm²) from photographs. Measurements were made to 0.1 mm accuracy. Photographs were taken from a straight on position with the camera face parallel to the outcrop surface to minimize distortion. Using the random point generator in the software, the same number of random points as concretions for the specific area was generated on the photograph. These points (see Nearest Neighbor Spacing Description and Interpretation for number of points measured) were then also measured for nearest neighbor distance. A chi-squared goodness-of-fit test was performed to test whether the concretion spacing is the same data set as the random spacing. Volumetric density of rind concretions was estimated using the volumetric density formula from McLennan et al. (2005), $V = \pi m l^2 / 6A$ where m is the number of

spherules on a planar rock surface with area A and ℓ equals mean spherule diameter. Volumetric density varies by location so nearest neighbor spacing was analyzed separately for each site for greater accuracy rather than grouping all measurements together.

Whole rock analysis was performed by ALS Chemex using induced plasma coupled-atomic emission (ICP-AE) spectroscopy (see Appendix G for complete results). A total of 13 *in situ* macro concretion samples and 32 host rock samples were sent for analysis. Host rock samples were collected in transects at 10 cm intervals on either side of the *in situ* concretions. Additional macro rind concretions with depleted interiors (n=6) were separated by hand, and the rinds and the interiors were analyzed separately. Two <0.02 kg samples of micro concretions were also analyzed.

Field Observations

This section begins with a description of the three types of HFO concretion geometries present Spencer Flat in the following order: common spheroidal macro concretions (>5 mm diameter), ubiquitous spheroidal micro concretions (<5 mm diameter) and localized HFO-lined northeast-striking joints and associated loopy asymmetrical mineralization. For clarity and to differentiate the loopy, asymmetrical HFO mineralization from other precipitation geometries, it is referred to as asymmetrical mineralization although it is a concretionary, diagenetic precipitation of cement rather than a vein-filling mineral. Field relationships between these concretionary geometries are documented followed by interpretations of a relative timing sequence of precipitation events.

Precipitation Geometries (Description)

Macro Concretions

Common spheroidal macro concretions are present *in situ* and loose in topographic lows. *In situ* macro concretions are spaced evenly throughout the host rock in a self-organized pattern (see below for statistical analysis of concretion spacing and volumetric density discussion). Macro concretions range in size from 5 mm to 10+ cm in diameter, and exhibit a variety of interiors. Interior structure is typified by three end member categories: 1. rind concretions with a friable interior depleted of HFO cement, 2. layered concretions with well-cemented, overlapping layers that extend throughout the concretion, and 3. solid concretions with evenly cemented interiors (Fig. 2.5 A,B,C). Interior structure can encompass a range of variety between these end members (Fig. 2.6).

Concretion geometries range from spherical to discoidal (Fig. 2.5D, 2.7). Aspect ratios of concretions (n=123) were measured in two dimensions with a digital caliper to determine if diffusive or advective mass transfer processes are responsible for concretion formation and for comparison with Mars data. Concretion geometries range from perfectly spherical (aspect ratio = 1.00) to nearly spherical (aspect ratio ≤ 1.06) to discoidal (aspect ratio = 1.07 to 1.97). The average aspect ratio is 1.10 and the median is 1.06 (Fig. 2.7).

Rind concretions typically exhibit thin (<1 mm) to thick (up to 1 cm) spheroidal rims of HFO cement that nearly or completely occludes the pore space (Fig. 2.5G).

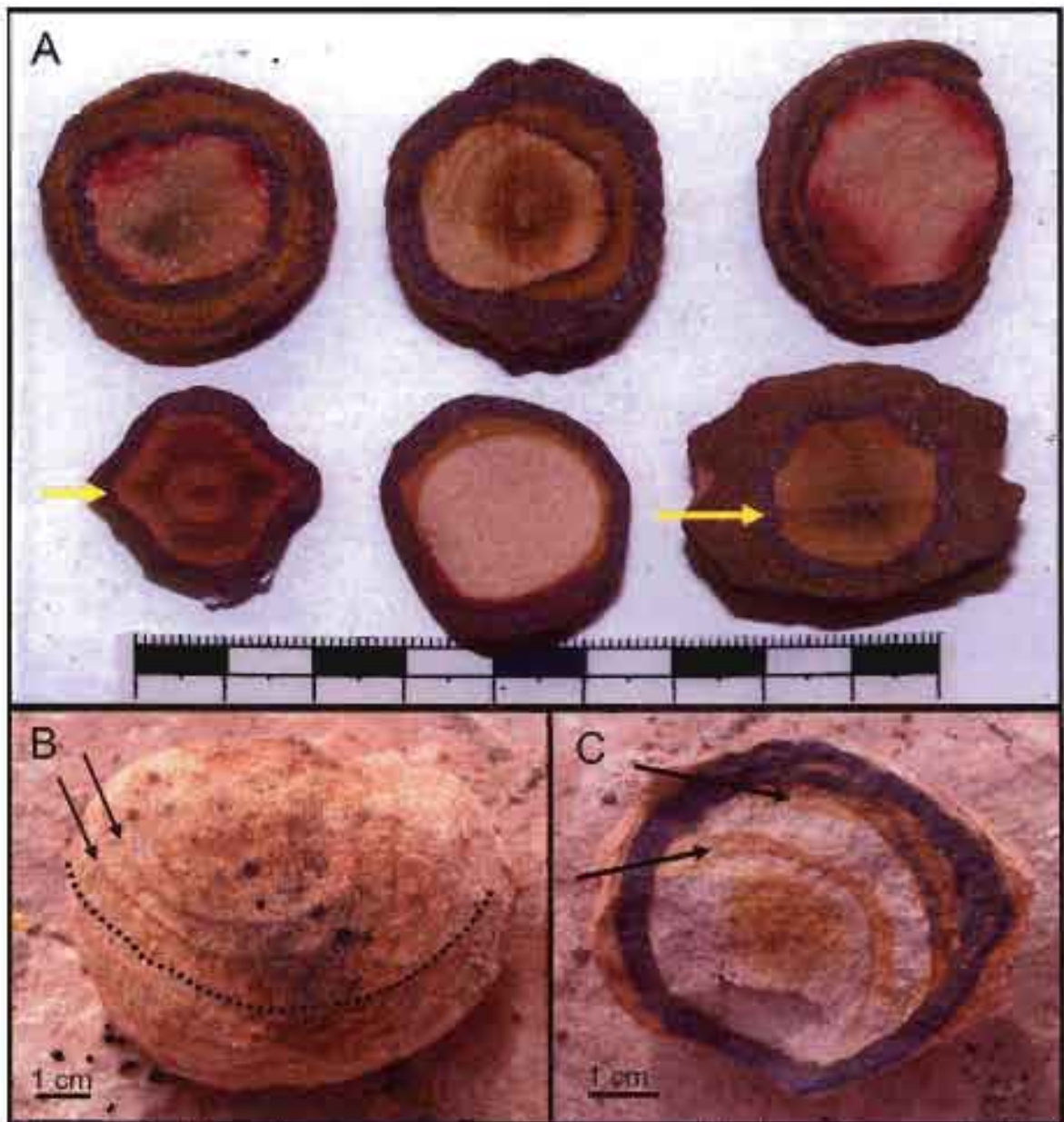


Fig 26. Varieties of macro concretion interiors. A. Varieties of asymmetrical and symmetrical interiors of layered and rind concretions. Arrows point to more permeable laminae. Large tick marks equal 1 cm. B. Liesegang bands overprinted on exterior of concretion. Dotted line outlines a band and arrows point to subparallel bands. C. Liesegang bands mirrored on interior of rind concretion. Arrows point to subparallel bands.

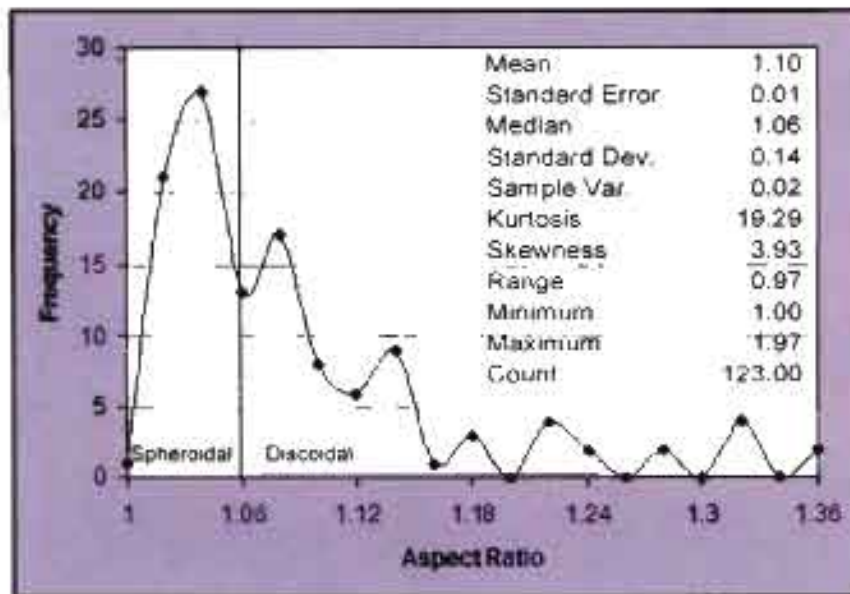


Fig. 2.7. Aspect ratio of concretion diameters in x and y direction (n=123). Aspect ratios <1.06 are considered nearly spherical.

Exteriors are smooth (even and well-cemented) to rough (weakly cemented), or humpy like an avocado skin (likely coalesced micro concretions) (Fig. 2.5F). The interiors of rind concretions are commonly depleted in cement and are friable, containing only traces (~1.4 wt % from whole rock analysis) of HFO cement. Some concretion interiors show HFO coloration oriented preferentially along more porous and permeable laminae near the rinds (Fig. 2.5H). Throughout the study area, interiors exhibit a wide variety of coloration patterns such as concentric circles of red, yellow and brown, asymmetrical bands, and shading along the interior sides of the rinds (Fig. 2.6A). Differing degrees of cementation render some interiors so friable they can be scraped out with a spoon whereas other interiors are better cemented than the rinds and preferentially harder (Fig. 2.8A).

Layered concretions have rinds similar to rind concretions but have ≥ 2 overlapping layers formed from HFO cementation throughout the interiors (Fig. 2.8B, C, D). The

inner layers are typically thin (1-2 mm), but the outer rind may be thicker (1 mm – 6 mm). In the layered end member, pore space is completely occluded with HFO cement within the cemented layers (Fig. 2.8B). These layers, resembling layers of an onion, can persist throughout the concretion or the concretion can have an interior depleted of cement similar to rind concretions (Fig. 2.8C). Some larger concretions exhibit small bulbous inward digitate cementations that slightly resemble inward crystal growth of geodes (Fig. 2.8D).

Solid concretions have a range of exteriors similar to rind and layered concretions but exhibit cementation evenly throughout the concretion (Fig. 2.5C). In some solid concretions, a faint rind (distinguishable by color) is visible, but unlike rind concretions, the interior is not depleted of HFO cement (Fig. 2.9). Although solid concretions are cemented evenly throughout the concretion, some porosity (~4% determined via QEMSCAN; Chapter 1) is retained (Fig. 2.9).

Micro Concretions

Ubiquitous micro concretions are defined as small spheroidal concretions <5 mm in diameter (Fig. 2.9B, C, D). Internal structures range between two end members: rind and solid. Micro concretions are present *in situ* and are generally cemented well enough to weather out of the host rock and collect in topographic lows (Fig. 2.9D). They can form in between Liesegang bands from diffusive mass transfer of reactants (Fig. 2.9F). Micro concretions can also coalesce to form larger concretions (Fig. 2.9G), resulting in a bumpy-textured exterior similar to an avocado skin (Fig. 2.5F). Micro concretions are

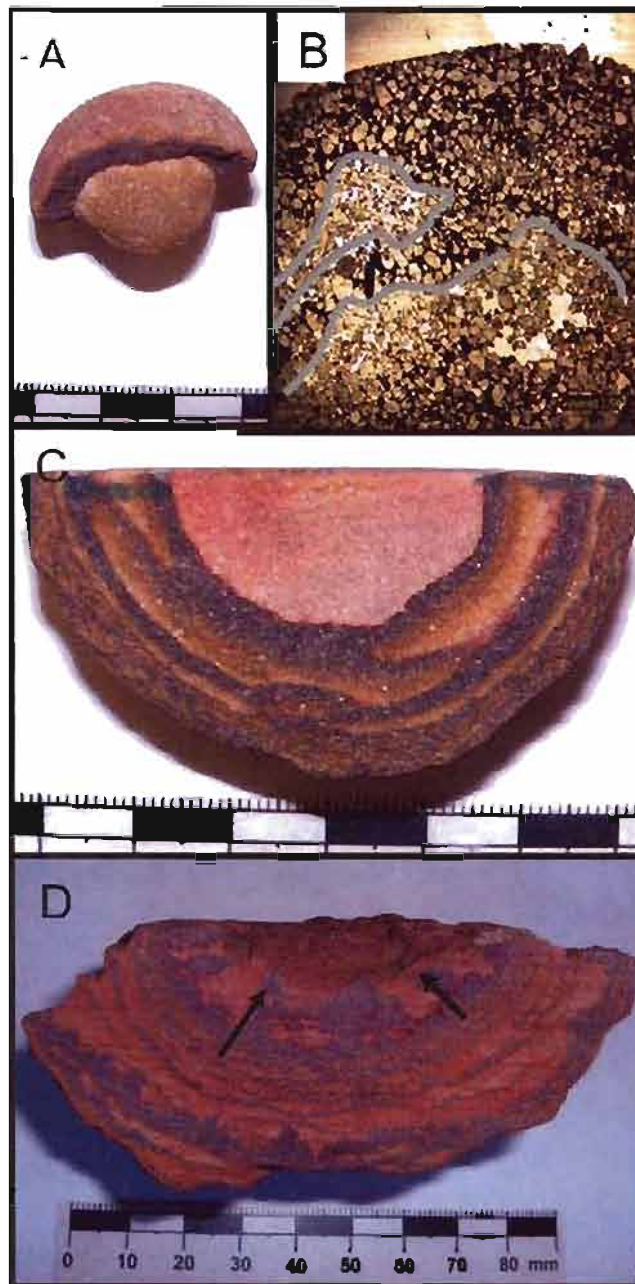


Fig. 2.8. Interior structures of concretions. Large tick marks on scale bars are cm. A. Rind concretion with preferentially cemented interior. B. Photomicrograph of layered concretion. Line delineates well-cemented layers from poorly cemented areas. 2.5X magnification, plane light. C. Layered concretion with friable interior. D. Layered concretion with inward digitate cementation. Arrows indicate direction of inward growth.

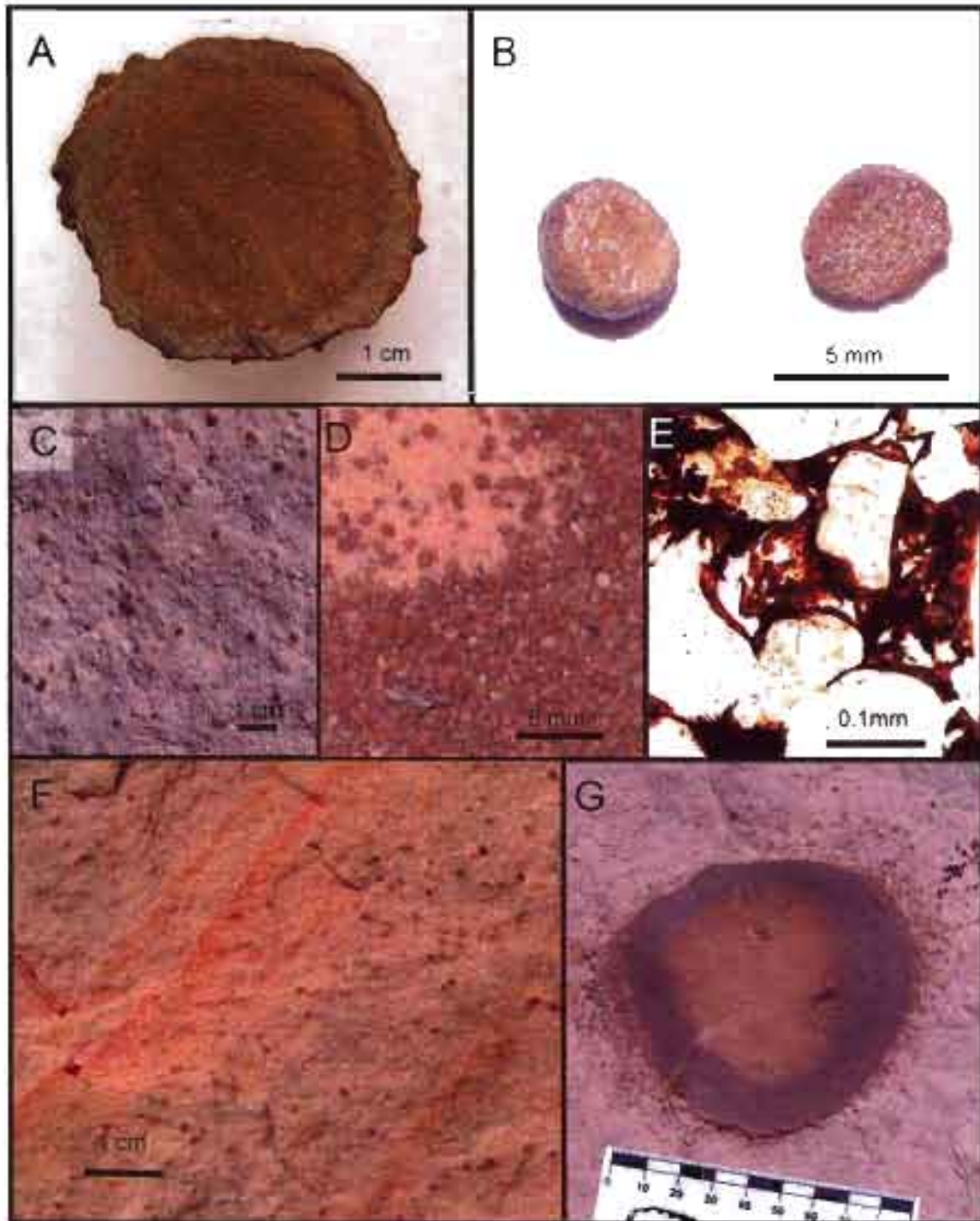


Fig. 2.9. Solid and micro concretions. A. Solid concretion (with "avocado skin" exterior) has a rind that is faintly distinguishable from the interior. B. Micro concretions in cross section. Note lack of interior structure. C. *In situ* micro concretions. D. Micro concretions weathered out and collected in topographic low. E. Micrograph of interior of solid concretions. Pore space has some retained porosity. F. Micro concretions *in situ* between Liesegang bands formed in diffusive reaction front. G. *In situ* micro concretions clustered around and forming a larger rind concretion.

ubiquitous throughout southern Utah and northern Arizona in the Navajo Sandstone in areas where the sandstone has undergone diagenetic mobilization and precipitation of HFO. Their volumetric density in the host rock is typically an order of magnitude greater than macro concretions where both size ranges are present *in situ* (see Analytical Investigation section for discussion of volumetric density).

HFO-lined Joints and Asymmetrical Mineralization

Platy HFO precipitation forms up to 1 cm thick concretionary linings on the faces of many parallel northeast-striking joint surfaces (Figs. 2.1, 2.2, 2.3, 2.4) prominent in the study area. These joints typically range in length from meters to 10s of meters although a few very prominent joints are ~1 km long.

Asymmetrical mineralization extends from the joints in a southeast direction, commonly in loopy, HFO-cemented patterns (Fig. 2.2, 2.3). Close to the joints, this asymmetrical mineralization occurs in 3-4 mm wide cemented lines and loops that are dark reddish brown and well-cemented relative to the surrounding rock. This asymmetrical mineralization can extend ~0.5 m to 2 m from the joints. At ~2 m distance from the joints, the asymmetrical mineralization becomes less pronounced and not as dark colored. Between ~2-5 m distance from the joints, the lines and loops fade to dark yellowish orange streaks that overprint the host rock. These streaks can extend 10s of meters distance from the joints.

Extending parallel to the asymmetrical mineralization lines and loops are periodic, self-organized Liesegang bands (Fig. 2.2B). Liesegang bands are a banded precipitation pattern that result of diffusive mass transfer of reactants along a chemical gradient (Liesegang, 1896; Hedges and Meyers, 1926; Stern, 1954; Ortoleva, 1984;

Ortoleva et al., 1987; Sultan et al., 1990) and indicate a diffusive component of reactant transfer in a perpendicular direction to the fluid flow.

Where macro concretions are *in situ* on the southeast side of the joints, the dark yellowish orange streaks surround the concretions in elongate halos or tails that extend to the southeast (Fig. 2.2C). Some concretions are overprinted with Liesegang bands on the exteriors and these bands are mirrored in the interiors (Fig. 2.6B, C).

Field Relationships and Relative Timing of Events

Description

The described concretion geometries (spheroidal macro and micro concretions and HFO-lined joints) exhibit three specific relationships that record a relative timing of precipitation and mobilization events (Fig. 2.10, 2.11, 2.12, Table 2.1). 1. Macro concretions and micro concretions occur on both the north and south sides of the northeast-striking, HFO-lined joints. They occur in equal distributions and spacing. The loopy asymmetrical mineralization only occurs on the southeast side on the joints. 2. In other areas, macro concretions and micro concretions occur where northeast joints are lacking. 3. Northeast joints are present in still other areas - with associated loopy asymmetrical mineralization - where *in situ* macro concretions are lacking. Micro concretions are present in all of these settings (see Fig. 2.10 for schematic representation of these relationships).

The relationship between different diagenetic facies and the associated concretion geometries helps to establish the timing of precipitation events. There is an area (~0.3 km²) where a localized secondary red coloration occurs adjacent to a bleached facies

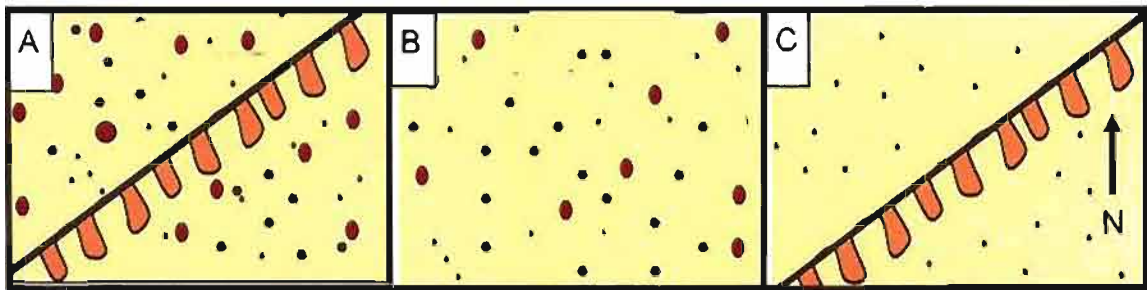


Fig. 2.10. Three relationships between macro concretions (large dots), micro concretions (small dots) and northeast joints (diagonal lines) with associated loopy, asymmetrical mineralization. Loopy mineralization is always to the southeast of joints. A. Macro concretions and micro concretions are present on both sides of joints. B. Rind/layered/solid concretions and micro concretions are present where there are no northeast joints. C. Northeast joints have loopy mineralization on southeast side, but no rind/layered/solid concretions are present. Micro concretions are present.

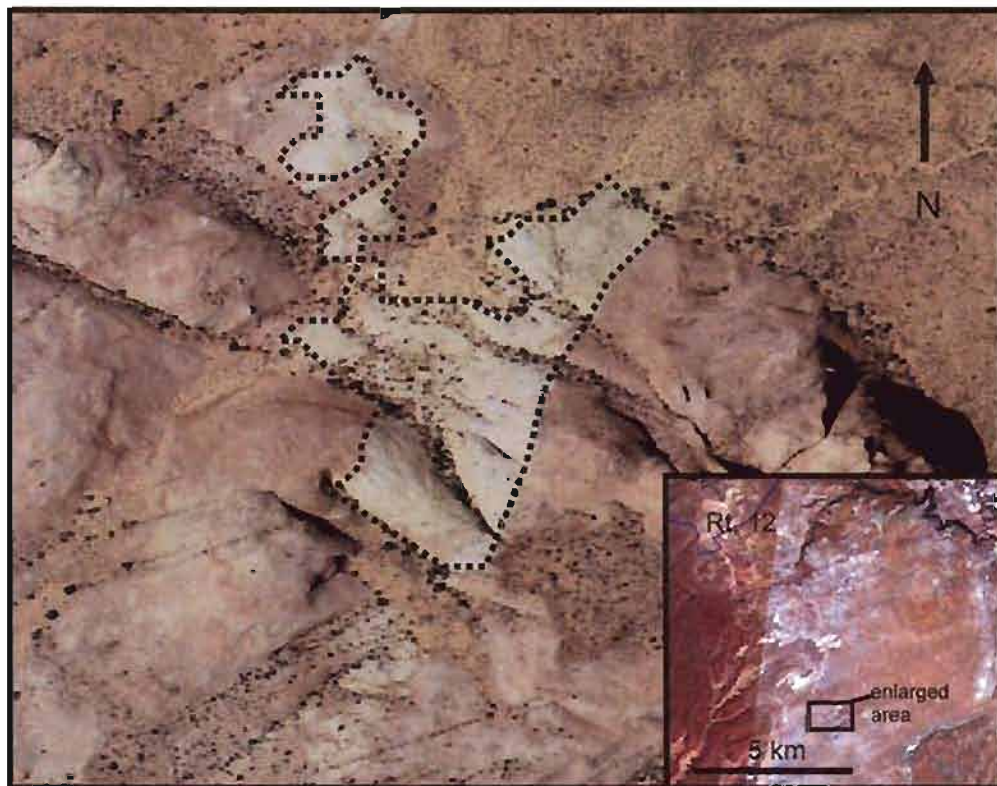


Fig. 2.11. Aerial photo of adjacent secondary red and bleached facies. Dotted line outlines bleached facies. Site located at N 37° 42.220' W 111° 23.832' and is ~0.3 km².

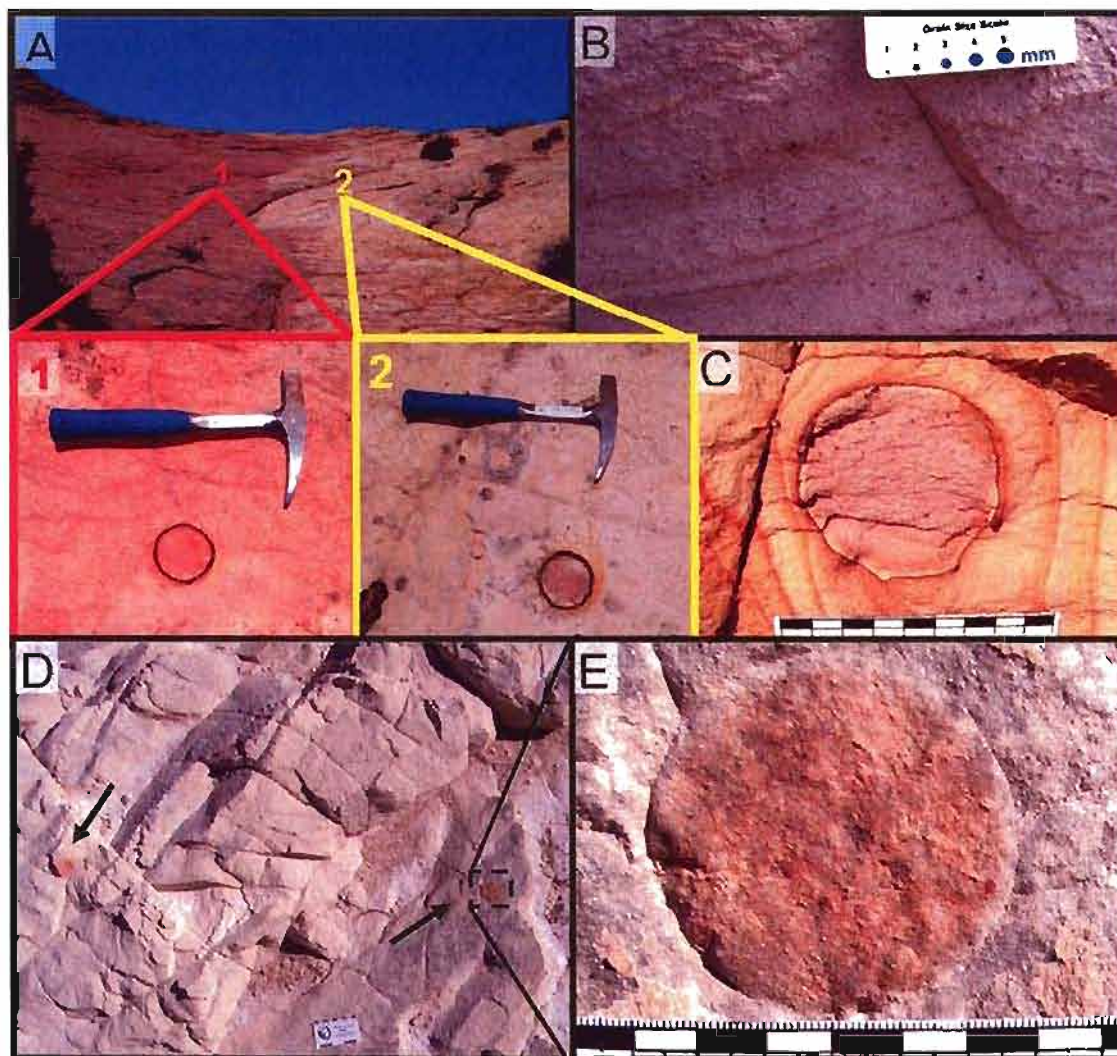


Fig. 2.12. A. Landscape view of adjacent secondary red (1) and bleached (2) facies. (See Fig. 2.11 for location.) View 1 is an *in situ* rind concretion with secondary red interior in secondary red facies. View 2 is an *in situ* rind concretion of similar size with secondary red interior in bleached facies. B. "Freckle" micro concretions in secondary red facies. C. Very thin (~ 1 mm) rind concretion in bleached facies with Liesegang bands from joint mineralization surrounding concretion. Note the secondary red facies with "freckle" micro concretions preserved in the interior of concretion. D. Bleached facies without joint mineralization overprinting. Arrows point to secondary red, rind-less concretions. E. Close up of preserved interior of secondary red with "freckle" micro concretions. Note the circular crack where former rind cementation may have been dissolved.

Table 2.1. Field observations of precipitation geometries present in the Spencer Flat area in GSENM.




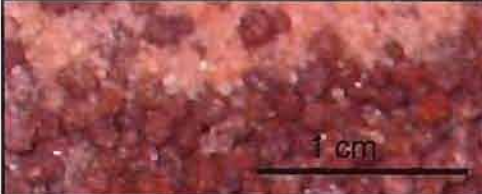
FIELD OBSERVATIONS		
Precipitation Geometries	DESCRIPTION	INTERPRETATION
HFO-lined NE joints		
	NE joints (51° to 70°) lined with HFO concretionary masses	Reservoir contains reducing solution saturated with Fe ²⁺ - oxidizing fluid infiltrates through joints - HFO precipitates
Loopy, asymmetrical mineralization		
	Extend SE of joints (111° to 160°); Liesegang bands parallel loopy mineralization lines	Advective, directional flow orthogonal to the joints form flow lines; diffusion orthogonal to direction of flow form Liesegang bands
Macro concretions		
	Spheroidal; >5 mm diameter; resistant to weathering; present <i>in situ</i> and loose in topographic lows (shown)	Three internal structure end member categories: rind, layered, solid
Micro concretions		
	Spheroidal; <5 mm diameter; resistant to weathering; present <i>in situ</i> and loose in topographic lows (shown)	Two internal structure end member categories: rind, solid

Table 2.1. continued

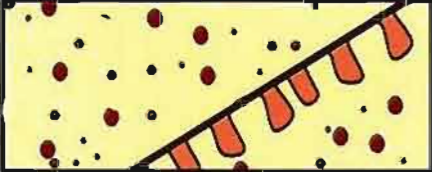
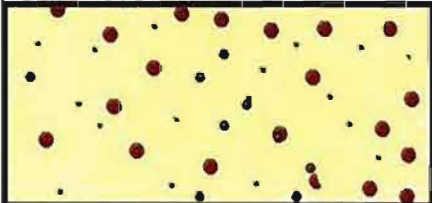
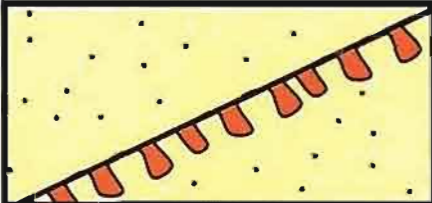

FIELD OBSERVATIONS		
Concretions/NE joint relations	DESCRIPTION	INTERPRETATION
<i>In situ</i> macro and micro concretions/NE joints:		
Observation #1		
	Macros and micros <i>in situ</i> on N and S sides of NE joints; flow lines extend to SE	Concretions form independently from NE joints
Observation #2		
	Macros and micros <i>in situ</i> ; no NE-striking joints	
Observation #3		
	Micros <i>in situ</i> N and S of joints; no macros	
Observation #4		
	Micros occasionally present in between the Liesegang bands associated with SE flow lines	Micros form via simple diffusion

Table 2.1. continued









FIELD OBSERVATIONS		
Relative timing relations	DESCRIPTION	INTERPRETATION
<i>In situ</i> macro concretions/NE joints		
	Elongate halos surround <i>in situ</i> macros on SE side of joints and extend to the SE	Macro concretions form prior to advective precipitation event associated with the NE-striking joints
Secondary red facies/ adjacent bleached facies		
	Secondary red facies adjacent to bleached facies	Chemical boundary between the two facies where a reducing fluid became saturated with Fe^{2+}
Micro concretions/ secondary red facies		
	Secondary red facies contains micro concretion "freckles"	Micro concretion "freckles" form penecontemporaneously with secondary red facies.
Macro concretions/ secondary red facies		
	Macros <i>in situ</i> in secondary red facies. Interiors of concretions preserve secondary red facies with micro concretion "freckles".	Concretion formation post-dates the precipitation of secondary red facies
Macro concretions/ bleached facies		
	<i>In situ</i> macros in bleached facies have secondary red facies with micro concretion "freckles" in their interiors	Bleaching event post-dates concretion formation and secondary red facies precipitation events

Table 2.1. continued

FIELD OBSERVATIONS		
Relative timing relations	DESCRIPTION	INTERPRETATION
Macro concretions/ bleached facies		
	Where no overprinting with flow lines is present, thin rinds or circular cracks in the rock surround circles of secondary red facies.	A reducing fluid infiltrates the reservoir after formation of macros and dissolves the rinds, leaving the interiors intact
Macro concretions/ bleached facies/ asymmetrical flow lines		
	Bleached facies overprinted with flow lines; macros present with thin rinds and secondary red facies in the interiors, flow lines/Liesegang bands distorted around concretions	Overprinting by late-stage fluid flow preserves or reprecipitates thin rinds.
Macro concretions/SE fluid flow/Liesegang bands		
	Macros with preferentially adhered host rock cemented with Liesegang bands; bands mirrored in interior.	Late-stage precipitation events alter internal structure and preferentially adhere host rock to exteriors.
<p>Relative timing from oldest to youngest event from the observed field relations:</p> <ol style="list-style-type: none"> 1. secondary red facies with micro concretions precipitate, 2. macro concretion formation, 3. bleaching event, 4. joint formation, 5. asymmetrical flow lines/Liesegang bands precipitate. 		

(Fig. 2.11, 2.12). This secondary red facies is distinguished by the mottled color of the outcrop and *in situ* micro concretions. These localized micro concretions are unusual because they weather flat along with the host rock instead of being more resistant to weathering. As a result, they appear like “freckles” in the facies (Fig. 2.12B).

In both the bleached and secondary red facies, rind concretions of similar size and spacing are present (Fig. 2.12A1, 2). Where macro concretions are present in the bleached facies, the interiors preserve the distinctive secondary red facies and associated micro concretion “freckles” (Fig. 2.11C,D,E).

This localized area is also fractured by northeast joints. Loopy, asymmetrical mineralization extends from the joints in a southeast direction. Dark yellowish orange streaks overprint both the bleached facies and the secondary red facies and form elongate halos and tails extending to the southeast around the *in situ* macro concretions present in both facies.

In situ macro concretions are also present in some bleached areas that are not overprinted with the dark yellowish orange streaks. These macro concretions sometimes display very thin or faint rinds (Fig. 2.12C) or rinds may be nonexistent, with only a circular crack in the rock around a secondary red, “freckled” interior (Fig. 2.12D,E). These cracks surrounding secondary red interiors suggest a rind was present at one time, but has since dissolved away.

Throughout this localized area, small reaction fronts (1-4 m² areas) of typical micro concretions - well-cemented enough to weather out of the host rock - are present in both the bleached facies and the secondary red facies (that contains associated micro concretion “freckles”). In some cases typical micro concretions are present in between

Liesegang bands that parallel the southeast asymmetrical mineralization lines (Fig. 2.9F). The typical micro concretions are preferentially cemented and quite distinct from the “freckle” micro concretions, so they likely formed in a different reaction fronts.

Interpretation

Field observations and a review of published literature, establish the relative timing of seven iron mobilization and precipitation events for Spencer Flat (Fig. 2.13). For each event, the relevant relationships are explained. Micro concretions overlap and are associated with precipitation events (3), (4) and (7) so micro concretion formation is discussed in a separate section following the documented precipitation and mobilization events.

1. Jurassic hematite grain coatings (~190 Ma)

Thin hematite grain coatings form penecontemporaneously with deposition of the erg from the weathering of ferromagnesian minerals during the Jurassic (Chan et al. 2000, 2004, 2005, 2006, 2007; Beitler et al. 2003, 2005; Parry et al. 2004).

2. Laramide to post-Laramide bleaching event (~80-55 Ma)

During the Laramide to post-Laramide, blind thrust faults create conduits for a buoyant bleaching fluid (likely hydrocarbon) to infiltrate the reservoir, reducing the Fe^{3+} in the hematite grain coatings to Fe^{2+} and mobilizing the iron into solution. This resulted in widespread bleaching across nearly all Laramide structures in the Navajo Sandstone (Beitler et al., 2003, 2005; Parry et al., 2004; Seiler, 2008).

3. Post-Laramide oxidizing event (< 55 Ma)

After the Laramide deformation and its associated bleaching event, an oxidizing fluid (probably meteoric water) infiltrates the reservoir and the iron precipitates as HFO, in

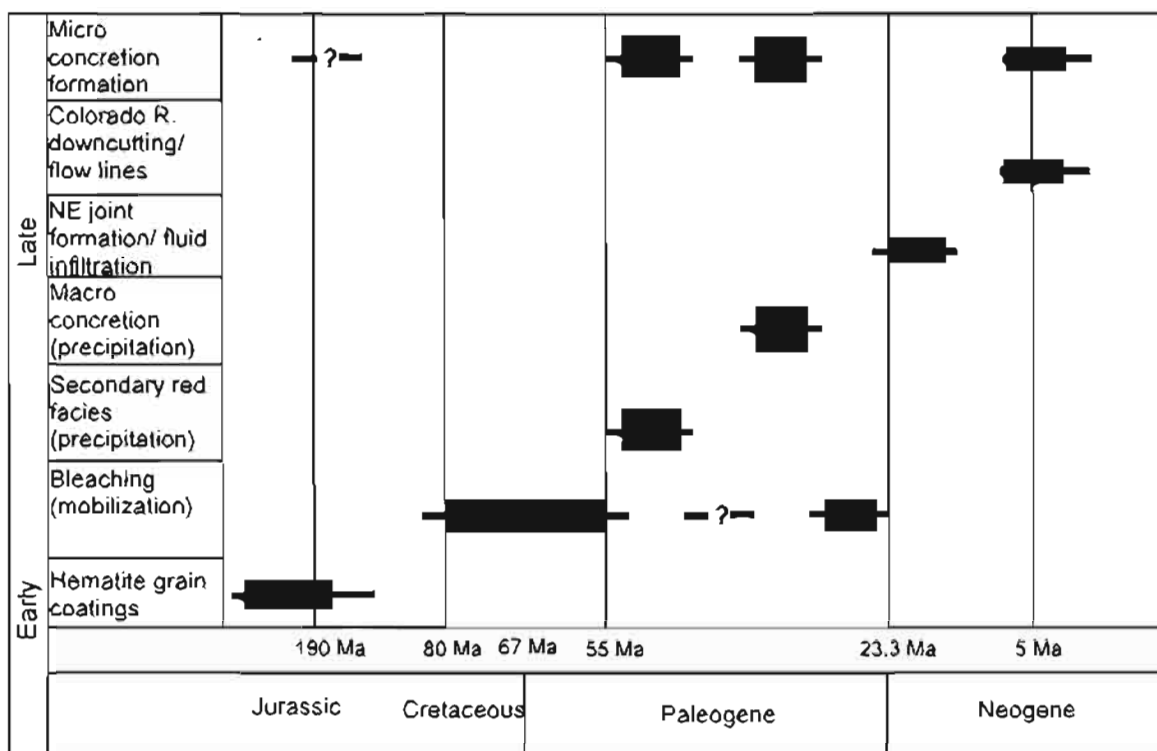


Fig. 2.13. Paragenetic sequence diagram showing mineralization/ mobilization events throughout the diagenetic history of the Navajo Sandstone.

minor amounts (<20% of cement) in the secondary red facies as described by Beitler et al. (2003, 2005) and Parry et al. (2004). The localized secondary red facies described in this study contains micro concretion “freckles”. Because these micro concretion “freckles” are so distinct from the typical micro concretions and are only associated with the localized secondary red facies, the micro concretion “freckles” likely developed penecontemporaneously with the secondary red facies in Spencer Flat.

4. Post-Laramide macro concretion formation (<55 Ma)

Field observations provide evidence for multiple bleaching and precipitation events. Interiors of rind macro concretions preserve secondary red facies with micro concretion “freckles” (in the area shown in Fig. 2.11). These concretions with the distinct interiors are present in both the secondary red facies and the bleached facies; therefore macro

concretion formation postdates the precipitation of the secondary red facies and predates a second localized bleaching event.

5. Post-Laramide second bleaching event (<55 Ma)

The sharp boundary between the localized bleached facies and the secondary red facies in Spencer Flat represents a chemical boundary where a reducing fluid became saturated with iron (Fig. 2.11, 2.12A). This second bleaching event likely dissolved the smaller crystals in the secondary red facies, but was unable to completely dissolve the larger crystals in the rinds of the concretions, so concretions with thin rinds and secondary red facies interiors were preserved. Smaller HFO crystals in the secondary red facies would be more easily mobilized because of their greater surface area relative to the larger crystals in the rinds (see Steefel and Van Cappellin (1990) for a discussion of Ostwald ripening). However, even where the rind seems to be dissolved or faint, circles of secondary red facies are preserved in the bleached facies suggesting that the bleaching fluid was at or near iron saturation (Fig. 2.12D,E).

6. Miocene (< 23.3Ma) formation of NE joints and infiltration of fluid

The northeast-striking joints likely formed during the Miocene (<23.3Ma) based on field mapping (Fig. 2.3) and comparison with other structures in the region. North of the study area, there are joints along the same strike that crosscut Miocene-aged basalts (Davis, 1999). Although deformation in this region has occurred since the Laramide, Basin and Range deformation (50-0Ma) likely produced the stress responsible for the northeast joints in Spencer Flat. No other structures in the region are of similar strike and extensional stress. These joints created conduits for infiltration of a fluid, likely an

oxidizing meteoric water (Beitler, 2005), that precipitated the concretionary HFO lining of the joints.

7. Colorado River downcutting (< 5 Ma) and loopy asymmetrical mineralization

The loopy, asymmetrical mineralization extends to the southeast from the northeast joints (Fig. 2.3) and is interpreted as directional flow lines by the fluid that infiltrated through the joints. Similar directional fluid flow lines are present in the correlative Aztec Sandstone in Valley of Fire, Nevada (Eichhubl et al., 2004). Eichhubl et al. (2004) interpret the similar HFO precipitation features present in Valley of Fire as meteoric water that infiltrated along Miocene-aged joints and then flowed to the southeast when the downcutting of the Colorado River created a hydraulic low to the southeast. Similar southeast flow lines are also present in Zion National Park to the west of Spencer Flat and east of Valley of Fire (Nielsen, 2007).

Rapid incision of the Colorado River through Glen Canyon southeast of Spencer Flat (Fig. 2.1) began 5Ma due to uplift of the Colorado Plateau (Eichhubl et al., 2004; Lucchitta, 1987). The loopy asymmetrical mineralization is the youngest of the precipitation events and it overprints precipitation geometries that occurred <50 Ma, so uplift from the Laramide orogeny is not responsible for the directional fluid flow. The downcutting of the Colorado River through Glen Canyon is the most likely cause of the hydraulic low responsible for southeast directional fluid flow.

Micro concretion formation

Typical micro concretions are numerous, closely spaced, and thoroughly ubiquitous in the Navajo Sandstone throughout southern Utah and northern Arizona. In most places, macro concretions are not present but highly colorful mineralization of the host rock is

common (i.e., Coyote Buttes in northern Arizona and Yellow Rock in southern central Utah [Seiler, 2008]). In the Spencer Flat study area, micro concretions formed during the previously described precipitation events: (3) secondary red facies (micro concretion “freckles”; Fig. 2.12), (4) macro concretion formation where coalescence of micro concretions creates a bumpy-textured exterior on the larger concretions (Fig. 2.5F, 2.9G), and (7) loopy, asymmetrical mineralization where micro concretions form in between Liesegang bands in diffusive reaction fronts that emanate perpendicular to southeast advective flow (Fig. 2.9).

Analytical Investigation

Analytical results from field and laboratory data are presented here in three sections:

1. statistical analysis of nearest neighbor spacing for 14 field sites,
2. volumetric density of concretions relative to the host rock, and
3. whole rock analysis (WRA).

Nearest Neighbor Spacing Description and Interpretation

A chi-squared goodness-of-fit test compared observed measurements to a hypothetical random set of measurements. The statistical test produced P values for most of the comparisons of $<<0.001$. All P values were <0.01 (the data sets are considered different for P values <0.01 ; Table 2.2). Therefore, the null hypothesis is rejected and the observed distance measurements are not the same data set that a random spacing produces.

The Navajo Sandstone concretions are uniformly spaced throughout the host rock, in contrast to a random spacing that would not be so evenly distributed (Fig. 2.14). This organization suggests that nucleation only requires one site with thermodynamics

Table 2.2. Statistical analysis of measured nearest neighbor spacing compared to random nearest neighbor spacing. A chi-squared goodness-of-fit test, average concretion diameter and calculated volumetric density were used to analyze spacing and estimate volumetric density. DF = degrees of freedom, which represents the number of concretions measured per area.

Sample #	Chi Squared Goodness of Fit			Average Diameter (mm)	Volumetric Density (%)
	DF	Chi-Square	P-Value		
Macro concretions					
62107 1361	10	2917.6	<<0.001	7.7	0.6
WP002 081407MA	13	2885.4	<<0.001	20.9	0.1
WP020 52807	13	282.3	<<0.001	15.9	0.1
WP012 52507	9	1092.9	<<0.001	32.4	0.2
Average	11			19.2	0.2
Micro concretions					
WP016 62107	24	80.1	<<0.001	1.0	2.7
6192007 1345	50	394.0	<<0.001	1.2	1.2
WP024 62207	24	60.1	<<0.001	0.8	1.1
71807	24	46.5	0.004	1.0	1.5
WP002 081407	19	36.9	0.008	2.4	6.6
8150037	23	81.0	<<0.001	1.5	0.6
WP004 81707	11	146.8	<<0.001	1.8	1.9
52507 181	13	208.4	<<0.001	0.8	0.3
805 95	31	79.7	<<0.001	0.5	0.6
6192007 1349	15	982.4	<<0.001	5.4	0.9
Average	23			1.8	1.7

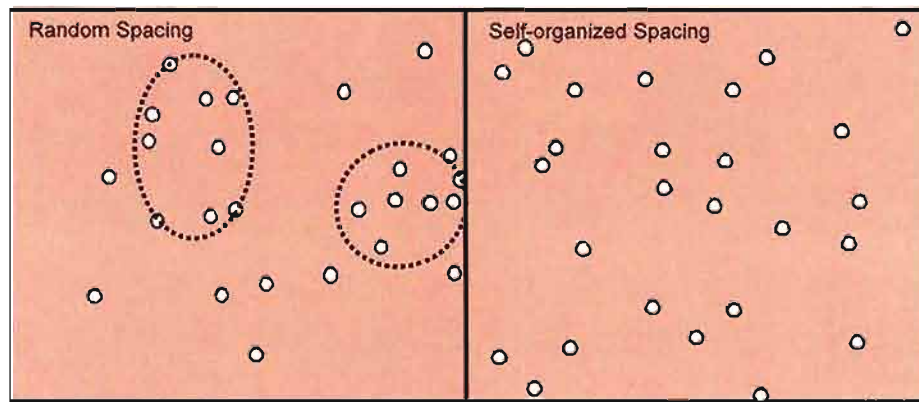


Fig. 2.14. Schematic representation on right was made from a photograph of Navajo Sandstone micro concretions (bottom edge is 6cm in the photograph and dots represent actual location of concretions). The schematic representation on the left was generated using the Jmicrovision software random point generator in the same area, with the same number of concretions as the photograph. Note the clusters of randomly spaced concretions (dotted circles) surrounded by open spaces. Self-organized concretions on right are more evenly spaced throughout the rock. Macro concretions show similar distribution of self-organization although they are more difficult to measure and image.

favorable to overcome the precipitation threshold and begin the reaction to produce many concretions throughout the host rock. Concretion spacing and growth is limited by the radius of reactants being used to form the nearest neighbor concretion due to Oswald ripening where fewer, but larger concretions precipitate (Ortoleva, 1984).

Volumetric Density Description and Interpretation

Volumetric density for macro concretions ranges from 0.1% to 0.6% with an average volumetric density of 0.2%. Micro concretions range in volumetric density from 0.3% to 6.6% with an average volumetric density of 1.7% (Table 2.2). Average diameter of *in situ* macro concretions is 19.2 mm and average diameter of *in situ* micro concretions is 1.64 mm. This is not a true diameter, only a minimum, because the true diameter may not be completely exposed in a weathered rock face. However, diameters of concretions extracted from the host rock are similar to diameters of weathered concretions, indicating weathering has a minimal effect on concretion diameters.

Micro concretions have an average volumetric density (1.7%) that is an order of magnitude greater than macro concretions (0.2%). This indicates that micro concretions are more densely populated in the host rock than macro concretions. Both macro and micro concretions can be present together in the same stratigraphic horizon, although typically, the number of micro concretions is much greater than the number of macro concretions in an outcrop. With geochemical self-organization, volumetric density is inversely correlated with size because concretion spacing and growth is limited by the radius of reactants surrounding the nearest neighbor and larger concretions form farther apart than smaller ones (Ortoleva, 1984).

Whole Rock Analysis Description and Interpretation

Trace elements in the *in situ* macro rind concretions were normalized to the host rock samples (Fig. 2.15A). The concentrations of the trace elements in the rinds of concretions were normalized to the depleted interiors (Fig. 2.15B). The trace elements in the depleted interiors were normalized to the host rock (Fig. 2.15C). The metals Co, Ni, V and Zn are all enriched by at least an order of magnitude in the concretions relative to the host rock (concentration in concretions: Co=63.0 ppm, Ni=89.0 ppm, V=132.2 ppm, Zn=319.8 ppm) and in the rinds relative to the interiors (concentration in rinds: Co=134.9 ppm, Ni=175.8, V=105.5 ppm, Zn = 669.8 ppm). The metals are enriched in the interiors relative to the host rock but to a lesser extent than the total concretions (concentration in interiors: Co=4.0 ppm, Ni=9.2 ppm, V=8.5 ppm, Zn=37.7 ppm). Uranium and As are enriched in the concretions relative to the host rock (concentration in concretions: U=1.4 ppm, As=66.4 ppm). These elements are also enriched in the rind relative to the interior by approximately the same amount (concentration in rinds: U=1.62 ppm, As=66.3 ppm). They are enriched in the interiors relative to the host rock (concentration in interiors: U=0.3 ppm; As=4.1 ppm) but by much less.

All of the trace elements discussed (Co, Ni, V, Zn, U, As) are more abundant in the rind than the interior. This enrichment in the HFO-cemented rinds supports the contention of Beitler et al. (2005) that these elements are present as adsorbed species of the HFO. Two of the most important trace elements that are present with the HFO are Ni and As. These elements allow inference of fluid composition when HFO is in solution in a reservoir and give insight into how concretions form. These trace elements can function as diagnostic criteria for diagenetic formation of HFO concretions.

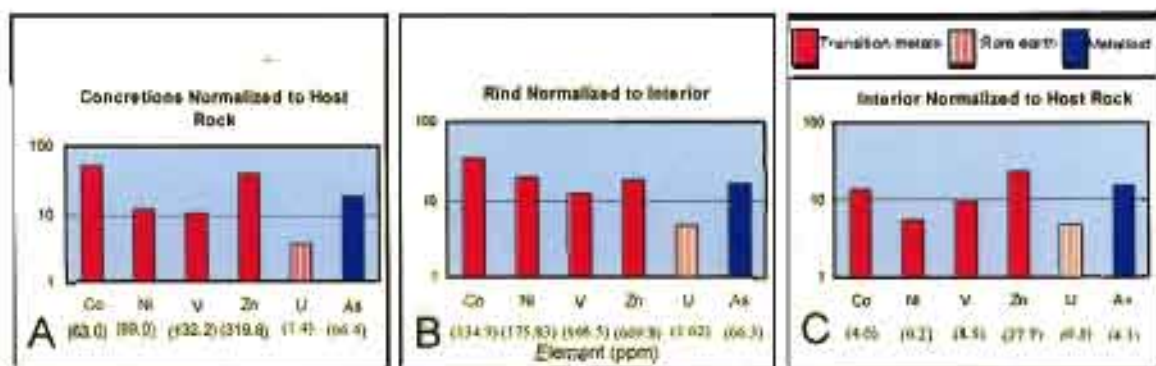


Fig. 2.15. Selected trace element concentration determined via whole rock analysis of rind concretions. Actual concentrations in ppm are listed in parentheses. A. Whole rind concretion ($n=13$) trace element concentrations normalized to trace element concentrations in host rock samples ($n=32$). B. Trace element concentrations in rinds normalized to concentrations in depleted interiors ($n=6$). C. Trace element concentrations in interiors of concretions ($n=6$) normalized to trace element concentrations in host rock samples ($n=32$).

Adsorbed As is greatly enriched in the concretions relative to the host rock by an order of magnitude. This has implications for people who use the Navajo Sandstone as a drinking water reservoir as many communities do in southern Utah. The current standard for safe levels of As is 10ppb (www.epa.gov, 2009). The levels of As in the concretions are 66.4ppm. If there is As bound with HFO precipitation in these aquifers, a slight change in water chemistry could be potentially disastrous (i.e., Brammer and Ravenscroft, 2009, on Bangladesh) and should be monitored carefully.

Sulfur (S) is present in very minor amounts in six samples (0.01-0.04ppm) and either lacking or in undetectable amounts in the others (see Appendix G). This implies that HFO is a primary concretion cement. If concretions were precipitated as a reduced iron mineral such as pyrite that later oxidized to HFO, larger concentrations of S would likely be present.

Discussion

At least seven precipitation and mobilization events are interpreted for the diagenetic history of the Jurassic Navajo Sandstone in the Spencer Flat area of GSENM (Fig. 2.12). The documented precipitation events result in varied precipitation geometries (macro concretions, micro concretions, and HFO-lined northeast joints with loopy, asymmetrical mineralization) that are dependent upon a complex combination of diffusive and advective mass transfer of reactants. These mass transfer processes are discussed followed by a comparison of Utah spheroidal concretions to Mars “blueberries”.

Diffusive Mass Transfer

Diffusive mass transfer is molecular transfer across a concentration gradient between two species. Spheroidal concretions indicate diffusive reactant mass transfer (Clifton, 1957; Berner 1968, 1980; Raiswell, 1971; Johnson, 1989; McBride et al., 1994; Mozley and Goodwin, 1995; McBride et al., 2003; Mozley and Davis, 2005). When diffusion is the principle mode of reactant transfer and the host rock is fairly homogenous, spherical concretions precipitate because spheres require the least amount of free energy to form (Ortoleva, 1994; Chan et al., 2004).

Navajo Sandstone spheroidal concretions (both macro and micro concretions) form via diffusive mass transfer. Where concretions form along more permeable laminae, they are typically discoidal. This modification from a spherical form occurs because higher permeability allows reactants to diffuse more quickly.

Macro concretions likely form via pervasive growth (similar to pervasive growth in carbonate concretions [Raiswell and Fisher, 2000]; see Chapter 1 for application to HFO concretions) where a poorly cemented HFO gel precipitates in a set radius and

cement structures grow inward. Concretions are initially precipitated with some retained porosity and pore space is filled by late-stage precipitation events (see Chapter 1). Even though rinds of macro concretions are low porosity at present (1.8%; see Chapter 1), they were originally much more porous. The higher porosity rinds allowed reactants to diffuse through and modify interior structure during late-stage precipitation events. Interior structural variations of concretions are due to the complex diagenetic history of multiple precipitation events in the Navajo Sandstone.

Advective Mass Transfer

Advective mass transfer occurs via fluid movement through permeable sediments (Drever, 1997). Advective flow typically precipitates elongate concretionary bodies parallel with direction of flow. The loopy asymmetrical southeast flow lines associated with the northeast joints are evidence of advective paleo flow through the Navajo Sandstone in Spencer Flat. This loopy asymmetrical mineralization always occurs on the southeast side of the northeast joints and is preferentially cemented (Figs. 2.2, 2.3). Liesegang bands parallel to the flow lines are self-organized, macroscopic bands of precipitated cement that indicate diffusive mass transfer of reactants through the rock in a direction perpendicular to the advective flow.

Macro concretions formed independently of the loopy asymmetrical, advective flow; flow lines around the macro concretions indicate these concretions were in place prior to the late-stage advective precipitation event. There are no macro concretions associated with the late-stage event because spheroidal concretions precipitate in nearly stagnant fluid via diffusive mass transfer. Therefore, advection may have overpowered diffusion

in the late-stage event and the conditions conducive to spheroidal macro concretion formation did not occur.

Mars Comparison

The Navajo Sandstone concretions exhibit remarkable similarities to the Mars “blueberries” such as self-organized spacing, volumetric density, geometry and mineralogy. McLennan et al. (2005) report that the probability of random spacing for the hematite spherules found in Meridiani Planum is $P < 0.001$. Thus the spacing of the Burns formation concretions is not random, but self-organized. The range of volumetric density is 1.2% to 4.0% and the average volumetric density is 3.2% with a mean spherule diameter of 4.2 mm. By comparison, volumetric density in Utah ranges from 0.1% to 6.6% for all concretion sizes with an average volumetric density (for all sizes) of 1.2% with a mean diameter of 6.7 mm (for all *in situ* sizes measured throughout the study area from multiple reaction fronts). Because both examples exhibit self-organized spacing, nucleation likely requires only one site to initiate the reaction front that forms concretions (McBride et al., 2003) as opposed to each concretion nucleating individually.

The Mars “blueberries” are enriched in Ni relative to the host rock and contain ~3% Ni (Knauth et al., 2005; Morris et al., 2006). Utah concretions are also enriched in Ni relative to the host rock by over an order of magnitude. The Burns formation consists of basaltic sand which would be a ready source of Ni. Nickel (Ni) enrichment in the spherules on Mars relative to the host rock is consistent with concretion formation and does not need an external source of Ni such as meteor impact to explain the enrichment. The diagenetic process of concretion formation mobilizes and precipitates Ni with the iron. Therefore, Ni enrichment in the Mars spherules is also supportive evidence for

groundwater diagenesis in the Burns formation where Ni could be an adsorbed species on the hematite.

Spherules on Mars and in Utah are comparable in geometry. On Mars, “blueberries” are nearly spherical (average aspect ratio = 1.06) (McLennan et al., 2005). In Utah, concretions are also nearly spherical, ranging from perfectly spherical to discoidal (aspect ratio ranges from 1.00 to ~2.00; mean aspect ratio = 1.10; median aspect ratio = 1.06).

The simple, ubiquitous, solid hematite spherules with little size variation and lack of advective precipitation forms (elongate geometries) suggest the diagenetic history of the Burns formation is dominated by one diffusive, iron-rich reaction front and represents a much simpler hydrologic regime compared to the complex history of multiple precipitation/mobilization events in the Navajo Sandstone (showing both advection and diffusion). Overall, the hydrologic regimes in the Utah example are a good comparative analog for diagenetic processes in Meridiani Planum for generating the spatial distributions, size distributions and concretion geometries. The hematite concretions in the Burns formation suggest a diagenetic history with significant iron mobilization and reprecipitation.

Conclusions

The Navajo Sandstone in Spencer Flat exhibits three types of HFO concretion geometries: 1. spheroidal macro concretions (>5 mm diameter), 2. spheroidal micro concretions (< 5 mm diameter), and 3. HFO-lined northeast-striking joints with associated asymmetrical mineralization. Cross-cutting relationships between the different precipitation geometries record the relative timing of seven iron cycling events from earliest to latest: 1. Hematite grain coatings precipitated upon deposition of the erg. 2.

This iron from grain coatings was mobilized during a Laramide to post-Laramide bleaching event when reducing fluid infiltrated the reservoir. 3. A precipitation event formed a secondary red diagenetic facies. 4. Macro concretions precipitated. 5. A second bleaching event occurred. 6. Northeast joints formed during the Miocene allowing infiltration of meteoric water and precipitating HFO lining of the joints. 7. The downcutting of the Colorado River ~5 Ma created directional advective fluid flow to the southeast overprinting the region with late-stage precipitation.

The different precipitation geometries document a complex history of diffusive and advective mass transfer of reactants through the porous Navajo Sandstone, a well-known subsurface reservoir. Spheroidal macro and micro concretions indicate processes dominated by diffusive mass transfer and more discoidal geometries of macro concretions suggest a faster diffusion rate of reactants along more permeable laminae. Analysis of nearest neighbor spacing shows that concretions exhibit a geochemically self-organized spacing. Volumetric density estimations show that micro concretions are more densely populated than macro concretions and this also supports the self-organized spacing conclusion. Concretion size is limited by the radius of reactants being used to form nearest neighbor concretions so that larger concretions would be spaced farther apart (and use a larger volume of reactants) than smaller ones.

Whole rock analysis indicates that some trace elements (such as Ni and As) are mobilized and precipitated as adsorbed species with the iron as part of the concretion formation process. Ni and As (and other trace elements) are enriched in the concretions relative to the host rock and in the rinds relative to the interiors and a Ni or As fingerprint is diagnostic of diagenetic concretion formation.

Utah micro concretions are a good terrestrial analog for Mars concretions due to similarities such as geometry, size, interior structure, preferential cementation, self-organized spacing and mineralogy. These similarities suggest Mars concretions likely formed by diffusive mass transfer; however, the range of internal structures, particularly advective components, in the Navajo Sandstone concretions implies a much more complex diagenetic history than the Burns formation. The geochemical reactions responsible for iron mobilization and precipitation were likely water-limited in the Burns formation in contrast to the history of abundant fluid flow through the Navajo Sandstone reservoir. Overall the hydrologic regimes in the Navajo Sandstone are a valuable rock record analog for iron cycling and the diagenetic processes that form concretions in the Burns formation of Mars.

References

- Beitler, B., Chan, M.A., Parry, W.T., 2003. Bleaching of Jurassic Navajo Sandstone on Colorado Plateau Laramide highs; evidence of exhumed hydrocarbon supergiants? *Geology*, 31, 1041-1044.
- Beitler, B., Parry, W.T., Chan, M.A., 2005. Fingerprints of fluid flow: chemical diagenetic history of the Jurassic Navajo Sandstone, southern Utah, U.S.A. *JSR*, 75, 547-561.
- Benison, K.C., Bowen, B.B., 2006. Acid saline lake systems give clues about past environments and the search for life on Mars. *Icarus*, 183, 225-229.
- Berner, R.A., 1968. Rate of concretion growth. *Geochimica et Cosmochimica Acta*, 32, 477-483.
- Berner, R.A., 1980. *Early Diagenesis: A Theoretical Approach*. Princeton, New Jersey, Princeton University Press.
- Blakey, R.C., Peterson, F., Kocurek, G., 1988. Synthesis of late Paleozoic and Mesozoic eolian deposits of the western interior of the United States. *Sed. Geol.*, 56, 3-125.

- Blakey, R.C., 1994. Paleogeographic and tectonic controls on some lower and middle Jurassic erg deposits, Colorado Plateau. In: Caputo, M.V., Peterson, J.A., Franczyk, K.J. (Eds.), *Mesozoic Systems of the Rocky Mountain Region, U.S.A.* SEPM, Rocky Mountain Section, 273–298.
- Bowen, B.B., Martini, B.A., Chan, M.A., Parry, W.T., 2007. Reflectance spectroscopic mapping of diagenetic heterogeneities and fluid-flow pathways in the Jurassic Navajo Sandstone. *AAPG Bulletin*, 91, 173–190.
- Bowen, B.B., Benison, K.C., Oboh-Ikuenobe, F.E., Story, S., Mormile, M.R., 2008. Active hematite concretion formation in modern acid saline lake sediments, Lake Brown, Western Australia. *ESPL*, 268, 52-63.
- Brammer, H., Ravenscroft, P., 2009. Arsenic in groundwater: a threat to sustainable agriculture in South and South-east Asia. *Environment International*, 35, 647-654.
- Chan, M.A., Parry, W.T., Bowman, J.R., 2000. Diagenetic hematite and manganese oxides and fault-related fluid flow in Jurassic sandstone, southeastern Utah. *AAPG Bulletin*, 84, 1281-1310.
- Chan, M.A., Beitler, B., Parry, W.T., Ormö, J., Komatsu, G., 2004. A possible terrestrial analogue for hematite concretions on Mars. *Nature*, 429, 731-734.
- Chan, M.A., Bowen, B.B., Parry, W.T., Ormö, J., Komatsu, G., 2005. Red rock and red planet diagenesis: comparison of Earth and Mars concretions. *GSA Today*, 15, 4-10.
- Chan, M.A., Johnson, C.M., Beard, B.L., Bowman, J.R., Parry W.T., 2006. Iron isotopes constrain the pathways and formation mechanisms of terrestrial oxide concretions: a tool for tracing iron cycling on Mars? *Geosphere*, 2, 324-332.
- Chan, M.A., Ormö, J., Park, A.J., Stich, M., Souza-Egipsy, V., Komatsu, G., 2007. Models of iron oxide concretion formation: field, numerical, and laboratory comparisons. *Geofluids*, 7, 1–14.
- Clifton, H E., 1957. The carbonate concretions of the Ohio shale. *The Ohio Journal of Science*, 57, 114-124.
- Davis, G.H., 1999. Structural geology of the Colorado Plateau regional of southern Utah, with special emphasis on deformation bands. *Special Paper - GSA*, 342, 157.
- Drever, J.I., 1997. *The Geochemistry of Natural Waters: Surface and Groundwater Environments*. third ed., Prentice Hall, New Jersey.
- Eichhubl, P., Taylor, W.L., Pollard, D.D., Aydin, A., 2004. Paleo-fluid flow and deformation in the Aztec Sandstone at the Valley of Fire, Nevada—Evidence for

the coupling of hydrogeologic, diagenetic, and tectonic processes. *GSA Bulletin*, 116, 1120–1136.

Environmental Protection Agency, Fact Sheet: Drinking Water Standard for Arsenic, http://www.epa.gov/safewater/arsenic/regulations_factsheet.html, May 15, 2009.

Golden, D.C., Ming, D.W., Morris, R.V., Graff, T.G., 2008. Hydrothermal synthesis of hematite spherules and jarosite: implications for diagenesis and hematite spherule formation in sulfate outcrops at Meridiani Planum, Mars. *Am. Mineralogist*, 93, 1201-1214.

Grotzinger, J.P., Arvidson, R.E., Bell, J.F., III, Calvin, W.M., Clark, B.C., Fike, D.A., Golombek, M.P., Greeley, R., Haldemann, A., Herkenhoff, K.E., Jolliff, B.L., Knoll, A.H., Malin, M.C., McLennan, S.M., Parker, T., Soderblom, L., Sohl-Dickstein, J.N., Squyres, S.W., Tosca, N.J., Watters, W.A., 2005. Stratigraphy and sedimentology of a dry to wet eolian depositional system, Burns Formation, Meridiani Planum, Mars. *ESPL*, 240, 11-72.

Hedges, E.S., Myers, J.E., 1926. *The Problem of Physico-chemical Periodicity*. London, Arnold, 95 pp.

Johnson, M.R., 1989. Paleogeographic significance of oriented calcareous concretions in the Triassic Katberg Formation, South Africa. *Jour. of Sed. Pet.*, 59, 1008-1010.

Knauth, L.P., Burt, D.M., Wohletz, K.H., 2005. Impact origin of sediments at the Opportunity landing site on Mars. *Nature*, 438, 1123-1128.

Liesegang, R.E., 1896. *Naturwiss. Wochenschr*, 11, 353.

Lucchitta, I., 1987, The mouth of the Grand Canyon and edge of the Colorado Plateau in the Upper Lake Mead area, Arizona. In: Beus, S.S. (Ed.), *Centennial Field Guide Volume 2: Rocky Mountain Section of the Geological Society of America*, pp. 365–370.

McBride, E.F., Picard, M.D., Folk, R.L., 1994, Oriented concretions, Ionian Coast, Italy: evidence of groundwater flow direction. *JSR*, 64, 535-540.

McBride, E.F., Picard, M.D., Milliken, K.L., 2003. Calcite-cemented concretions in Cretaceous sandstone, Wyoming and Utah, U.S.A. *JSR*, 73, 462-484.

McCullom, T.M., Hynke, B.M., 2005. A volcanic environment for bedrock diagenesis at Meridiani Planum on Mars. *Nature*, 438, 1129-1131.

McLennan, S.M., Bell, J.F., III, Calvin, W.M., Christensen, P.R., Clark, B.C., de Souza, P.A., Farmer, J.D., Farrand, W.H., Fike, D.A., Geller, R., Ghosh, A., Glotch, T.D., Grotzinger, J.P., Hahn, B., Herkenhoff, K.E., Hurowitz, J.A., Johnson, J.R.,

- Johnson, S.S., Jolliff, B.J., Klingelhöfer, G., Knoll, A.H., Lerner, Z., Malin, M.C., McSween, H.Y., Jr., Pocick, J., Ruff, S.W., Soderblom, L.A., Squyres, S.W., Tosca, N.J., Watter, W.A., Wyatt, M.B., Yen, A., 2005. Provenance and diagenesis of the evaporite-bearing Burns Formation, Meridiani Planum, Mars. *EPSL*, 240, 95-121.
- Morris, R.V., Ming, D.W., Graff, T.G., Arvidson, R.E., Bell, J.F., III, Squyres, S.W., Mertzman, S.A., Gruener, J.E., Golden, D.C., Le, L., Robinson, G.A., 2005. Hematite spherules in basaltic tephra altered under aqueous, acid-sulfate conditions on Mauna Kea volcano, Hawaii; possible clues for the occurrence of hematite-rich spherules in the Burns Formation at Meridiani Planum, Mars. *EPSL*, 240, 168-178.
- Morris, R.V., Klingelhöfer, G., Schroeder, C., Rodionov, D.S., Yen, A., Ming, D.W., de Souza, P.A., Jr., Wdowiak, T., Fleischer, I., Gellert, R., Bernhardt, B., Bonnes, U., Cohen, B.A., Evlanov, E.N., Foh, J., Guetlich, P., Kankeleit, E., McCoy, T. J., Mittlefehldt, D.W., Renz, F., Schmidt, M.E., Zubkov, B., Squyres, S.W., Arvidson, R.E., 2006. Moessbauer mineralogy of rock, soil, and dust at Meridiani Planum, Mars; Opportunity's journey across sulfate-rich outcrop, basaltic sand and dust, and hematite lag deposits. *JGR*, 111, E12S15.
- Mozley, P.S., Goodwin, L., 1995. Patterns of cementation along a Cenozoic normal fault: a record of paleoflow orientations. *Geology*, 23, 539-542.
- Mozley, P.S., Davis, J.M., 2005. Internal structure and mode of growth of elongate calcite concretions: evidence for small-scale microbially induced, chemical heterogeneity in groundwater. *GSA Bulletin*, 117, 1400-1412.
- Munsell Rock-Color Chart, 1975. Prepared by The Rock-Color Chart Committee, Distributed by The Geological Society of America, Boulder, Colorado.
- Nielsen, G.B. Chan, M.A., 2007. Major diagenetic features associated with iron oxide enrichment and depletion, Jurassic Navajo Sandstone, southwestern Utah. *Abstracts with Programs - Geological Society of America*, 39, 14.
- Ormö, J., Komatsu, G., Chan, M.A., Beitler, B., Parry, W.T., 2004. Geological features indicative of processes related to the hematite formation in Meridiani Planum and Aram Chaos, Mars: a comparison with diagenetic hematite deposits in southern Utah, U.S.A. *Icarus*, 171, 295-316.
- Ortoleva, P., 1984. The self organization of Liesegang bands and other precipitate patterns. G. Nicolis, F. Baras (Eds.), *Chemical Instabilities*, pp. 289-297.
- Ortoleva, P., Merino, E., Moore, C., Chadam, J., 1987. Geochemical self-organization I: Reaction-transport feedbacks and modeling approach. *American Journal of Science*, 287, 979-1007.

- Ortoleva, P.T., 1994. *Geochemical Self-Organization*. Oxford Univ. Press.
- Parry, W.T., Chan, M.A., Beitler, B., 2004. Chemical bleaching indicates episodes of fluid flow in deformation bands in sandstone. *AAPG Bulletin*, 88, 175-191.
- Raiswell, R., 1971. Cementation in some Cambrian concretions, South Wales. Johns Hopkins University, *Studies in Geology*, 19, 196-197.
- Raiswell, R., Fisher, Q.J., 2000. Mudrock-hosted carbonate concretions: a review of growth mechanisms and their influence on chemical and isotopic composition. *Journal of the Geological Society London*, 157, 239-251.
- Seiler, W.M., 2008. Jurassic Navajo Sandstone of Coyote Buttes, Utah/Arizona: coloration and diagenetic history, preservation of a dinosaur trample surface, and a terrestrial analog to Mars. M.S. Thesis, University of Utah, Salt Lake City, Utah, U.S.A.
- Steeffel, C.I., Van Cappellen, P., 1990. A new kinetic approach to modeling water-rock interaction: the role of nucleation, precursors, and Ostwald ripening. *Geochimica et Cosmochimica Acta*, 54, 2657-2677.
- Stern, K.H., 1954. The Liesegang phenomenon. *Chem. Rev.*, 54, 79-99.
- Squyres, S.W., Knoll, A.H., Arvidson, R.E., Clark, B.C., Grotzinger, J.P., Joliff, B.L., McLennan, S.M., Tosca, N., Bell, J.F., III, Calvin, W.M., Farrand, W.H., Glotch, T.D., Golombek, M.P., Herkenhoff, K.E., Johnson, J.R., Klingelhöfer, G., McSeen, H.Y., Yen, A.S., 2006. Two years at Meridiani Planum: results from the Opportunity Rover. *Science*, 313, 1403-1407.
- Sultan, R., Ortoleva, P., DePasquale, F., Tartaglia, P., 1990. Bifurcation of the Ostwald-Liesegang supersaturation-nucleation-depletion cycle. *Earth-Science Reviews*, 29, 163-173.

APPENDIX A

SAMPLES: LOCATION AND ANALYSES

The following table identifies samples collected and the locations (GPS lat/long) where they were collected. This appendix also provides a brief description of the sample and lists the analyses that were performed. Mössbauer samples and locations are listed in a separate table at the end. Samples are numbered in the following manner: UT06-SF-1JN = State, year, location, sample number, formation. These are the location abbreviations: SF=Spencer Flat; RB=Red Breaks; HW=Harris Wash; MR=Moqui Rock; CM= Center and Main (near perpendicular joints in the north of study area). All samples are Jurassic Navajo Sandstone except two of the Mössbauer samples (formations noted in table).

Table A.1. Sample locations and analyses

SAMPLE	latitude	longitude	NOTES/ROCK DESCRIPTION	thin section	WRA	Vnir spec	QEMSCAN
UT06-SF-1JN	N37 40.737	W111 22.539	typical and atypical concretions; some twins				
0.001				x			
0.002							x
0.003				x			
0.004				x			
0.005				x			
0.006			~4.5 cm diameter; thick rind, depleted interior		x		
UT06-RB-3JN							
0.001			thin rind; ~2 cm diam., earthy red int.	x			x
0.002				x			x
0.003				x			x
0.004				x			x
0.005				x			
0.006			thick rind with diffusive red coloration toward rind	x			
0.020			thick rind with discreet center, ~3cm diam.		x	x	
0.021			medium rind, ~2.5cm diam., some red diffuse coloration around edge, black specs throughout int.		x		

Table A.1. continued

SAMPLE	latitude	longitude	NOTES/ROCK DESCRIPTION	thin section	WRA	Vnir spec	QEMSCAN
UTO6-RB-4JN							
0.003			green/brown/yellow center with diffuse coloration along laminae; thin red coloration along rind; thick rind; bulbous outward digitation along "spaceship" edge with dark red coloration in the int.~4 cm diam.		x		
0.004			dark green/brown/yellow center; red coloration along "spaceship" protrusions; medium rind. ~4cm diam.		x		
0.005			thin rind; diffuse coloration in interior		x		
0.006				x			
0.007				x			
0.008				x			
0.009				x			
0.010							
UT07-SF-11JN	N37° 40.505'	W 111° 22.059'	<i>in situ</i> transect of concretion and host rock		x		
0.001			concretion		x		
0.002			host rock		x		
0.003			host rock		x		
0.004			host rock		x		
0.005			host rock		x		
0.006			host rock		x		
UT07-SF-13JN	N37° 42.106'	W 111° 22.540'	<i>in situ</i> concretion and transect of host rock; .004 had small concretion near it		x		
0.001			concretion		x		
0.003			host rock		x		
0.004			host rock - near concretion		x		
0.005			host rock		x		
0.006			host rock		x		
0.007			host rock		x		
UT07-HW-1JN	N37° 41.879'	W 111° 23.072'	<i>in situ</i> concretion and transect of host rock; .006 is ~10-20cm from .005		x		
0.001			concretion		x		
0.002					x		
0.003					x		
0.004					x		
0.005					x		
0.006					x		
UT07-HW-2JN	N37° 41.164'	W 111° 24.917'	<i>in situ</i> twin concretion and transect of host rock				
0.001			concretion		x		
0.002			host rock		x		
0.003			host rock		x		
0.004			host rock		x		
0.005			host rock		x		
0.006			concretion		x		
0.007			host rock		x		
0.008			other half of concretion .001	x			

Table A.1. continued

SAMPLE	latitude	longitude	NOTES/ROCK DESCRIPTION	thin section	WRA	Vnir spec	QEMSCAN
UT07-SF-17JN	N37° 42.117'	W 111° 23.002'	<i>in situ</i> concretion/ transect of host rock; .007 was on a red stripe		x		
0.001			concretion		x		
0.002			host rock		x		
0.003			host rock		x		
0.004			host rock		x		
0.005			host rock		x		
0.006			host rock		x		
0.007			red stripe		x		
UT07-SF-18JN	N37° 42.220'	W 111° 23.832'	<i>in situ</i> concretion/ transect of host rock		x		
0.001			concretion		x		
0.002			host rock - near concretion		x		
0.003			host rock		x		
0.004			host rock		x		
0.005			host rock		x		
0.006			host rock		x		
0.007			host rock		x		
UT07-SF-20JN	N37° 42.117'	W 111° 23.002'	multiples and singles weathered out concretions				
0.001			thick rind, depleted interior		x		
0.002			thick rind, depleted interior		x		
0.003			thin rind, depleted interior		x		
UT07-RB-1JN	N37° 42.788'	W 111° 22.313'	weathered out concretion				
0.001			thick rind, depleted interior		x		
0.002			medium rind, depleted interior w/ some diffusive coloration		x		
0.003			medium rind, depleted interior w/ some diffusive coloration		x		
0.007						x	
0.008						x	
0.009						x	
0.010						x	
UT07-RB-2JN	N37° 42.788'	W 111° 22.313'	host rock		x		
UT07-RB-3JN	N37° 42.651'	W 111° 20.167'	large concretions (out of 3 populations)				
0.001				x			
0.002			thick rind with inward growth and interior concentric diffusive coloration	x			
0.003			solid center	x			
0.004				x			
UT07-RB-4JN	N37° 42.651'	W 111° 20.167'	small concretion (out of 3 populations)				
0.001				x			
0.002				x			
UT07-RB-6JN	N37° 42.668'	W 111° 20.989'	weathered out concretions				
0.001			rind concretion	x		x	
0.002				x			
0.003				x			
UT07-RB-7JN	N37° 42.908'	W 111° 20.582'	layered/rind concretions				
0.001			rind concretion	x		x	
0.002				x			
0.003				x			

Table A.1. continued

SAMPLE	latitude	longitude	NOTES/ROCK DESCRIPTION	thin section	WRA	Vnir spec	QEMSCAN
UT07-RB-8JN	N37° 43.021'	W 111° 20.567'	concretion from red stripe				
0.001			host rock	x			
0.002			concretion	x			
UT07-RB-9JN	N37° 43.021'	W 111° 20.567'	concretion from white stripe				
0.001			host rock	x			
0.002			concretion	x			
UT07-RB-10JN	N37° 42.723	W 111° 20.978'	concretion diffuse coloration in interiors				
0.001				x			
0.002				x			
0.003				x			
0.004				x		x	
UT07-SF-62JN	N37° 40.864'	W 111° 22.582'	weathered out concretions; some w/ red overprinting				
0.001			thick rind, depleted interior	x			
0.002			thick rind, red and brown stripes (diffusive coloration) in interior	x		x	
UT07-HW-20JN	N37° 42.480'	W 111° 23.798'	<i>In situ</i> concretion w/ red interior from outcrop ~50 m from sample UT07-HW-21Jn				
0.001				x			
UT07-HW-21JN	N37° 42.480'	W 111° 23.798'	red host rock	x			
UT07-RB-83JN	N37° 42.472'	W 111° 20.653'	flat concretions and joint material				
0.001			joint plating	x			
0.002			concretion	x			
0.003			concretion	x			
UT07-RB-84JN	N37° 42.323'	W 111° 19.925'	avocado skin population				
0.001				x			
0.002				x			
UT07-RB-85JN	N37° 42.323'	W 111° 19.925'	smooth, small concretions				
0.001				x			
0.002				x			
UT07-RB-86JN	N37° 42.323'	W 111° 19.925'	micros		x		
UT07-RB-87JN	N37° 42.583'	W 111° 20.914'	concretions - some solid				
0.001				x			
0.002				x			
UT07-RB-88JN	N37° 42.795'	W 111° 20.425'	thick rinds w/ halos in middle; some solid, some pea sized				
0.001				x			
0.002			3 cm diameter solid	x			
0.003				x			
0.004			.5 cm	x			
UT07-RB-89JN	N37° 42.886'	W 111° 20.236'	concretions w/ solid centers				
0.001			layered concretion	x		x	
0.002				x			
0.003				x			

Table A.1. continued

SAMPLE	latitude	longitude	NOTES/ROCK DESCRIPTION	thin section	WRA	Vnir spec	QEMSCAN
UT07-RB-90JN	N37° 42.886'	W 111° 20.236'	concretions w/ red and white stripes and others				
0.001			layered concretion w/ red and yellow diffusion in center	x		x	
0.002			thick rind with harder center	x			
0.003			solid concretion w/ red and white stripes in host rock	x		x	
UT07-SF-85JN	N37° 42.051'	W 111° 24.168'	large concretion				
0.001			concretion w/ red circles from SE flow	x			
0.002			concretion w/ red circles from SE flow	x			
UT07-RB-92JN	N37° 44.510'	W 111° 21.342'	rind and layered concretions				
0.001			1.5 cm layered	x			
0.002			doublet	x		x	
0.003			avocado skin - small (1-2 cm)	x			
0.004			avocado skin - small (1-2 cm)	x			
UT07-RB-93JN	N37° 44.560'	W 111° 21.295'	layered concretions and ~1 cm population				
0.001			3 cm layered	x			
0.002				x			
UT07-RB-94JN	N37° 44.564'	W 111° 21.264'	concretions with variety of interiors				
0.001			layered w/ digitate inward growth	x		x	
0.002			diffusive yellow coloration w/ some inward digitate growth	x		x	
0.003			rind concretion	x		x	
UT07-RB-95JN	N37° 44.467'	W 111° 20.998'	bumpy concretions w/ hard brown interiors				
0.001			solid	x		x	
0.002				x			
0.003			3 mm rind w/ dark brown interior	x		x	
UT07-RB-96JN	N37° 44.537'	W 111° 21.022'	avocado skin w/ solid interiors				
0.001				x			
0.002				x			
0.003				x			
UT07-HW-14JN	N37° 42.086'	W 111° 23.558'	black concretions				
0.001				x			
0.002				x			
UT07-HW-15JN	N37° 42.016'	W 111° 23.576'	concretions w/ Liesegang bands overprinted				
0.001				x		x	
UT07-HW-16JN	N37° 41.904'	W 111° 23.539'	concretions w/ range of sizes				
0.001				x		x	
0.002				x			
0.003				x			

Table A.1 continued

SAMPLE	latitude	longitude	NOTES/ROCK DESCRIPTION	thin section	WRA	Vnir spec	QEMSCAN
UT07-HW-17JN	N37° 41.730'	W 111° 23.880'	rind w/ depleted interiors from edge of reaction front	x			
0.001				x		x	
0.002				x		x	
0.003				x			
0.004				x			
UT07-HW-21JN	N37° 41.886'	W 111° 22.419'	concretions w/ sparkly rinds, depleted interiors, large concretions w/ solid and asymmetrical layered interiors				
0.001			asymmetrical diffusive interior coloration, thick rind	x		x	
0.002			asymmetrical diffusive interior coloration, thick rind	x			
UT07-RB-97JN	N37° 42.713'	W 111° 21.961'	micros				
0.001					x		
UT07-MR-1JN	N37° 42.249'	W 111° 23.906'	burrows on bounding surface w/ iron fixation,				
0.001			burrows in white coating	x			
0.002			red burrows	x			
UT07-CM-1JN	N37° 42.940'	W 111° 20.128'	concretions w/ black and brown exterior colors				
0.001			black exterior	x			
0.002			black exterior	x			
0.003			brown exterior	x			

Table A.2. Mössbauer samples

Sample	Formation	Age	Latitude	Longitude	Location	Description	Composition (XRD)
UT 97-20A Jn	Navajo SS	Jurassic	38°41.987	109°54.489	Back Rainbow Rx, Moab, UT	cross section from a small thin vertical pipe, that shows various iron-oxide layers	hematite
UT00-10A Jn	Navajo SS	Jurassic	37°41.545	111°22.788	Spencer Flat, GSENM, UT	golf ball concretion with internal layering. Also doing Fe isotopes on this	goethite
UT00-10B jn	Navajo SS	Jurassic	37°41.545	111°22.788	Spencer Flat, GSENM, UT	marble size with smooth outer surface	goethite
UT04-SdH-13A Jn	Navajo SS	Jurassic	37°07.785	113°23.162	Sand Hollow, UT	small ~ 1cm size	hematite & goethite
UT04-SdH-13B	Navajo SS	Jurassic	37°07.785	113°23.162	Sand Hollow, UT	should be same as sample above, but these are more blueberry size	
AZ03-Pg Jn	Navajo SS	Jurassic	36°52.862'	111°30.652'	South of Page, AZ	small, poorly to moderately developed concretion balls in situ w host	
UT97037 Jes	Entrada SS Slickrock Member	Jurassic	38°41.25	109°54.59	Rainbow Rx, Moab, UT	concretion forms in tar saturated sandstone	hematite ?, pyrite precursor?
UT04-Mo-5 Kd	Dakota SS	Cretaceous	38°14.663'	109°16.233'	Lisbon Valley, Moab, UT	hematite ball inside of green malachite concretion from mineralized fault zone, seems to have pyrite & goethite that later replaced by hematite?	hematite & goethite + pyrite
UT97-44	Navajo SS	Jurassic	38°40' 15"	109°55' 51"	Moab, UT Dellenbaugh Tunnel	Fracture fill, similar to razorback on Mars	goethite?

APPENDIX B

QEMSCAN AREA PERCENT MINERALOGY AND POROSITY

Mineralogy and porosity are listed as area percent. Porosity was calculated as part of the whole data set and then the minerals were normalized to exclude porosity. Apatite is present as inclusions in the quartz grains. HFO designates smooth textured HFO and HFO Textures designates HFO with a “frothy” texture.

Table B.1. QEMSCAN area percent and porosity.

	UT06-SF-1JN.002		UT06-RB-3JN.002		Host rock	
	Interior	Rind	Interior	Rind		
Porosity	30.39	1.10	25.13	0.41	23.78	
Framework Grains						
Quartz	82.39	60.78	92.66	67.91	90.12	
Orthoclase	12.11	7.87	6.02	2.63	6.05	
Plagioclase	0.01	0.00	0.01	0.00	0.04	
Kaolinite	3.04	0.93	0.87	0.12	2.19	
Apatite	0.07	0.05	0.11	0.02	0.08	
Cement						
HFO	1.53	28.93	0.09	28.49	0.60	
HFO Textures	0.59	1.05	0.07	0.16	0.81	
Mn Ba Oxide	0.00	0.00	0.00	0.12	0.00	
Mn Fe Ba Oxide	0.00	0.00	0.00	0.01	0.00	
Fe Mn Oxide	0.00	0.07	0.00	0.11	0.00	
Mn oxide	0.00	0.03	0.04	0.18	0.01	
Cryptomelane	0.00	0.00	0.00	0.00	0.00	
Other Silicates	0.04	0.19	0.02	0.11	0.02	
Other	0.22	0.11	0.10	0.12	0.08	
	UT06-RB-3JN.001 (solid)		UT06-RB-3JN.003		UT06-RB-3JN.004	
	Interior	Rind	Interior	Rind	Interior	Rind
Porosity	7.99	0.41	31.93	0.45	29.08	5.38
Framework Grains						
Quartz	62.34	67.91	85.48	60.12	86.01	70.39
Orthoclase	10.42	2.63	12.04	8.11	10.74	6.95
Plagioclase	0.01	0.00	0.02	0.00	0.03	0.05
Kaolinite	1.40	0.12	2.14	0.96	2.52	1.18
Apatite	0.42	0.02	0.06	0.04	0.05	0.10
Cement						
HFO	18.93	28.49	0.07	29.87	0.24	20.07
HFO Textures	1.02	0.16	0.12	0.43	0.27	0.46
Mn Ba Oxide	0.00	0.12	0.00	0.00	0.00	0.00
Mn Fe Ba Oxide	0.00	0.01	0.00	0.00	0.00	0.00
Fe Mn Oxide	0.03	0.11	0.00	0.00	0.00	0.00
Mn oxide	0.03	0.18	0.00	0.00	0.01	0.00
Cryptomelane	0.00	0.00	0.00	0.00	0.00	0.00
Other Silicates	0.15	0.11	0.01	0.15	0.02	0.13
Other	5.26	0.12	0.06	0.32	0.12	0.68

APPENDIX C

VNIR REFLECTANCE SPECTROSCOPY

This appendix contains graphs of individual spectra obtained in transects across macro (rind, layered and solid) concretions. Fig. 1.11 from the text (copied below) shows HFO adsorption minima to aid with interpretation of the graphs. A brief description of the concretion and the interpretation of the Vnir spectroscopy results accompany each graph. Field locations of samples can be found in Appendix I.

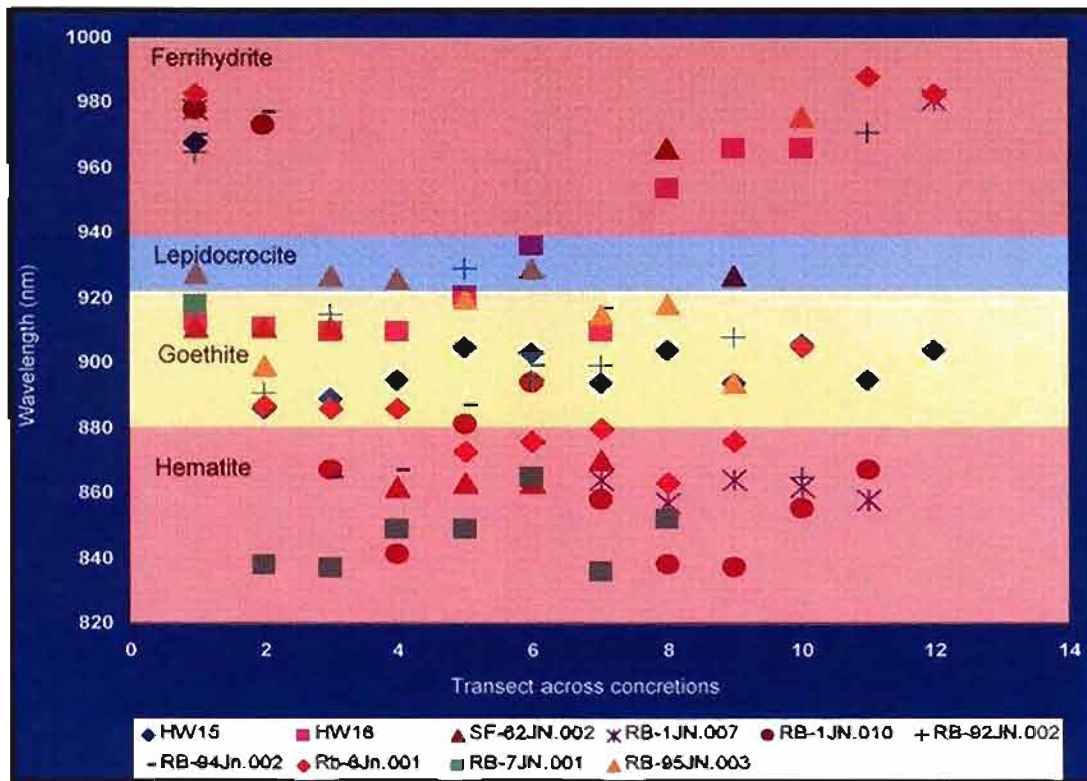


Fig. 1.11. Adsorption minima in transects across rind concretions.

RIND CONCRETIONS

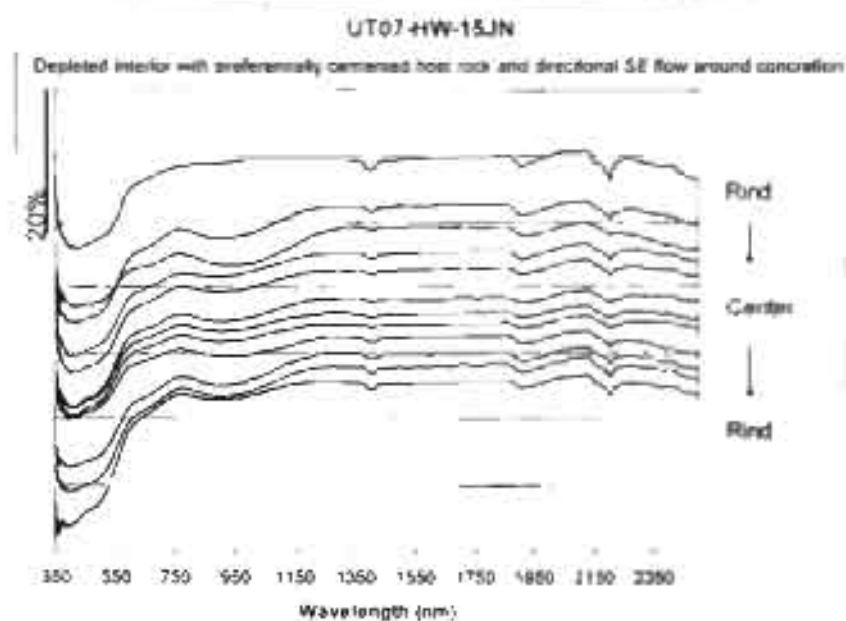


Fig. C.1 Rinds are amorphous HFO with kaolinite; interiors are amorphous HFO/goethite with kaolinite

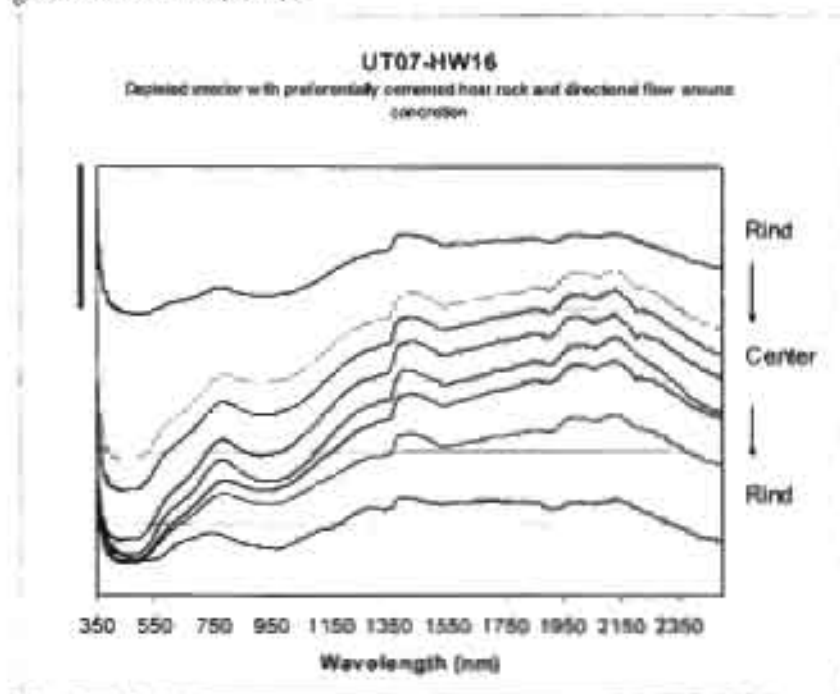


Fig. C.2. Rinds are amorphous HFO, interiors are goethite with kaolinite or illite

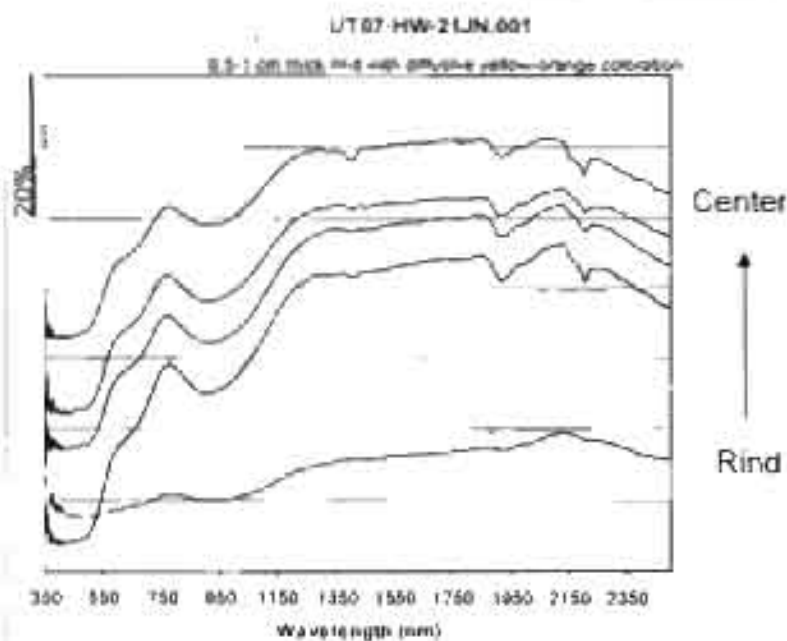


Fig. C 3 Rinds are amorphous HFO, interiors are goethite/ hematite with kaolinite or illite.

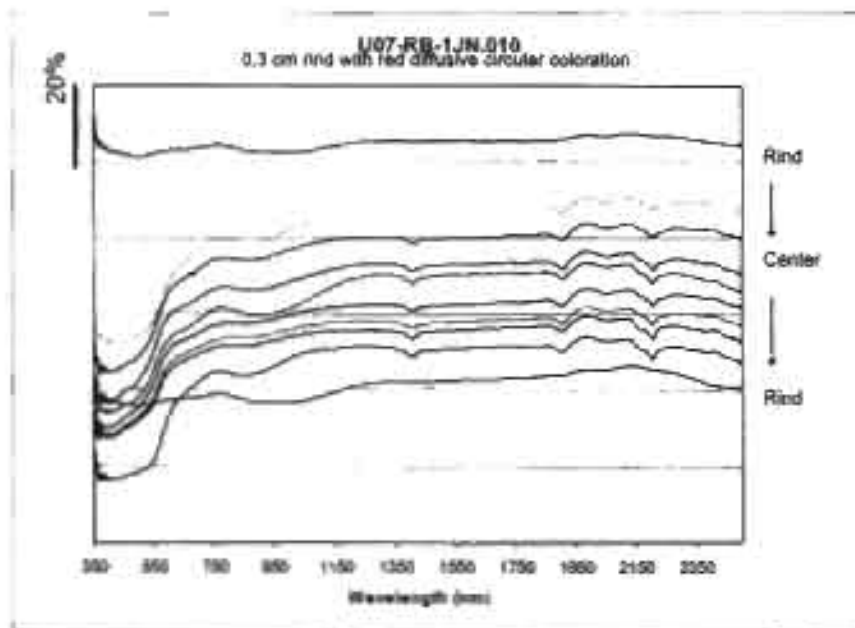


Fig. C 4 Rind is amorphous HFO, red coloration is hematite, center is goethite. Kaolinite is present in some interior readings

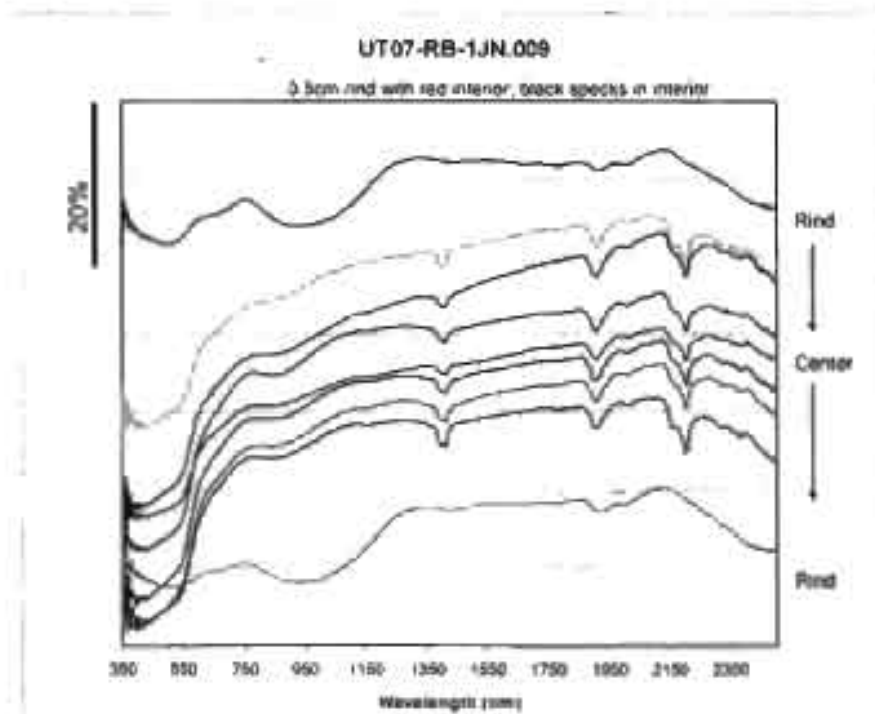


Fig. C.5 Rind is goethite; interior is hematite with kaolinite

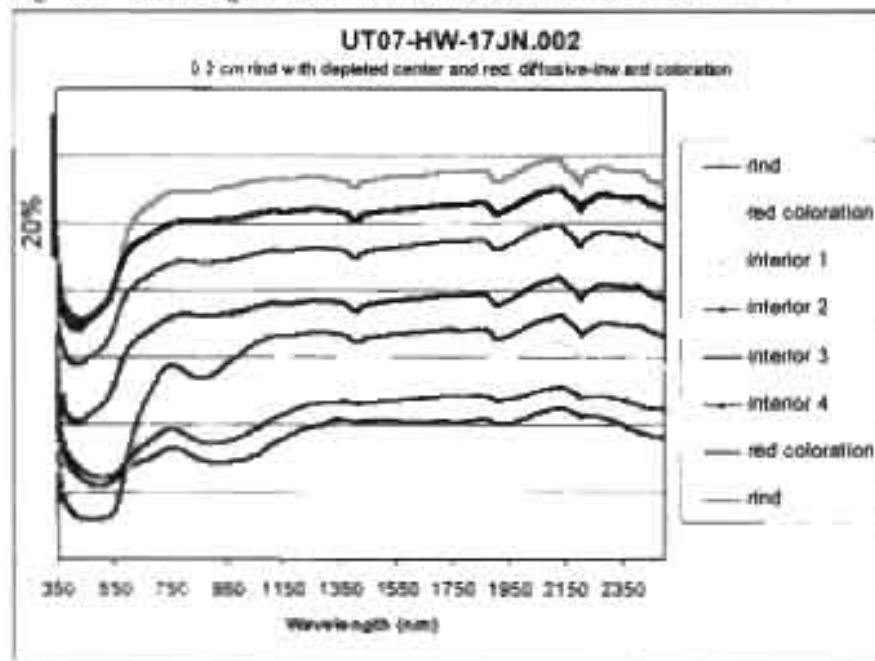


Fig. C.6. Rinds and interiors are goethite; red coloration is hematite. Kaolinite is present in interiors

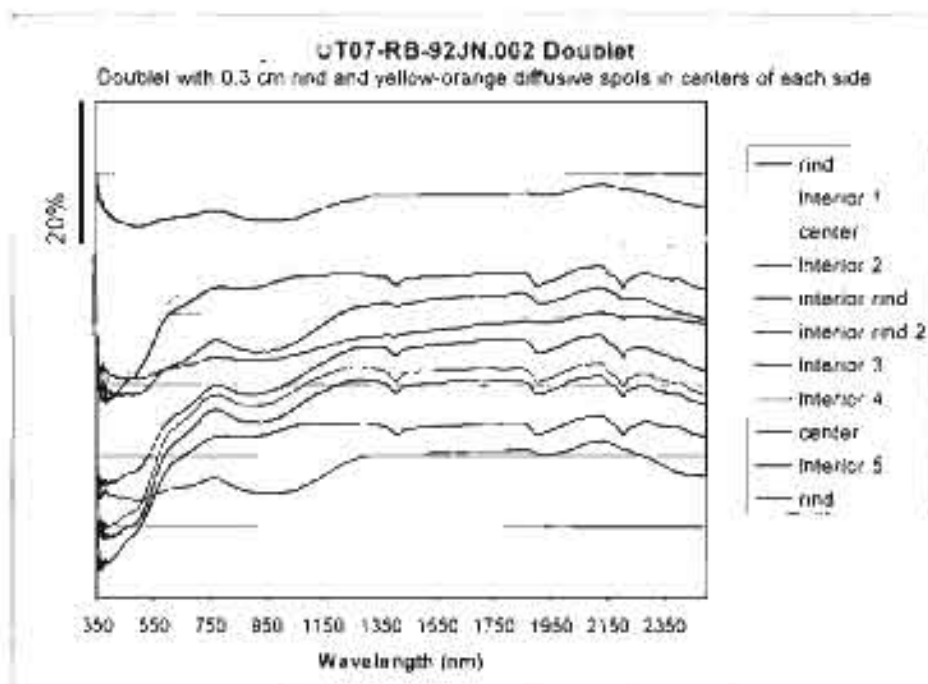


Fig. C 7 Rinds are amorphous HFO; interiors are goethite with kaolinite.

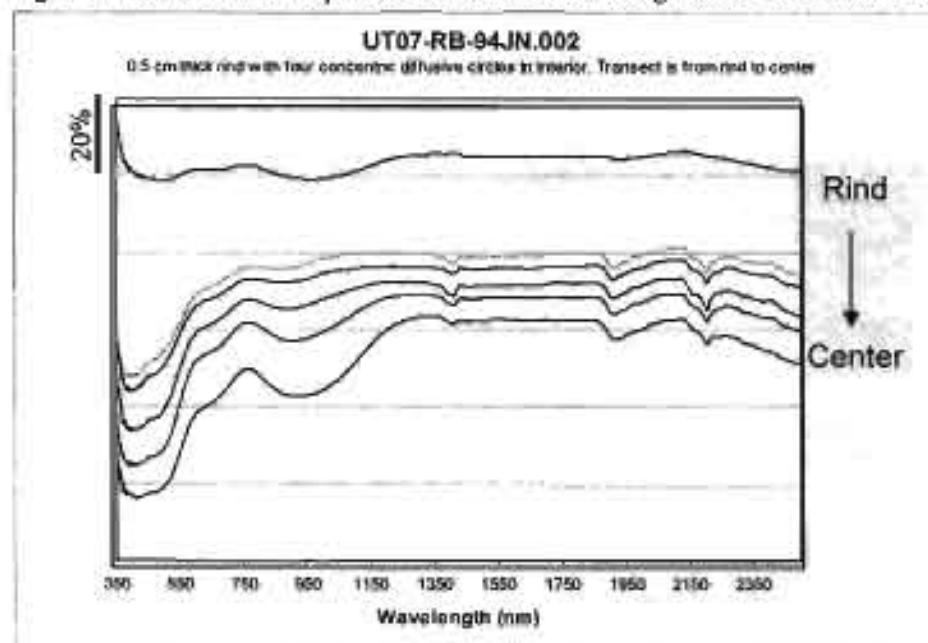


Fig. C 8 Rinds are amorphous HFO, interior near rinds are hematite with kaolinite, centers are goethite with kaolinite

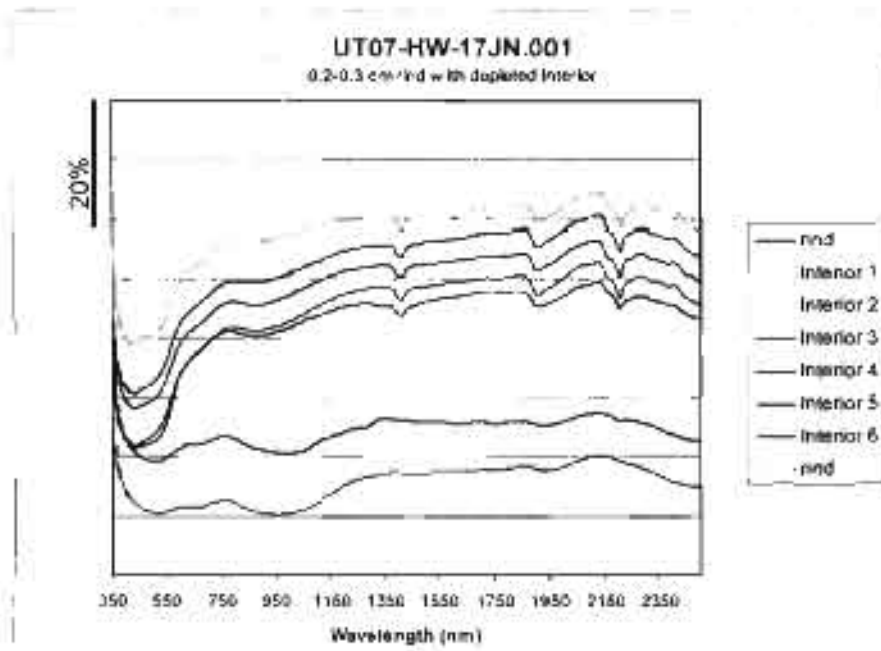


Fig. C.9. Rinds are amorphous HFO; interiors near edge are goethite; centers are goethite/hematite. Kaolinite is present in interiors

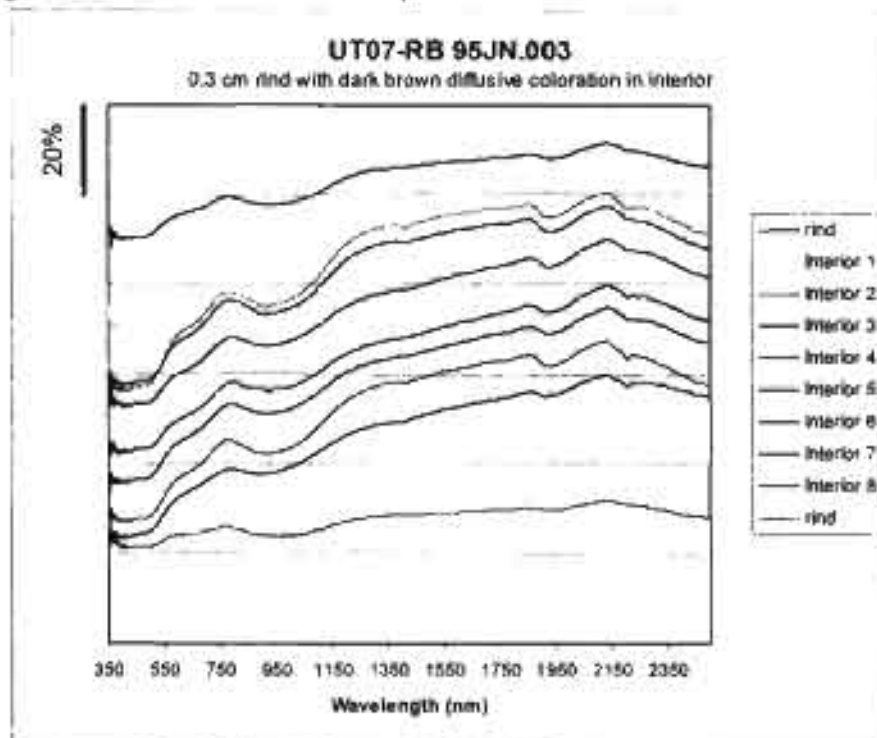


Fig. C.10 Rind is amorphous HFO; interior is goethite with kaolinite or illite.

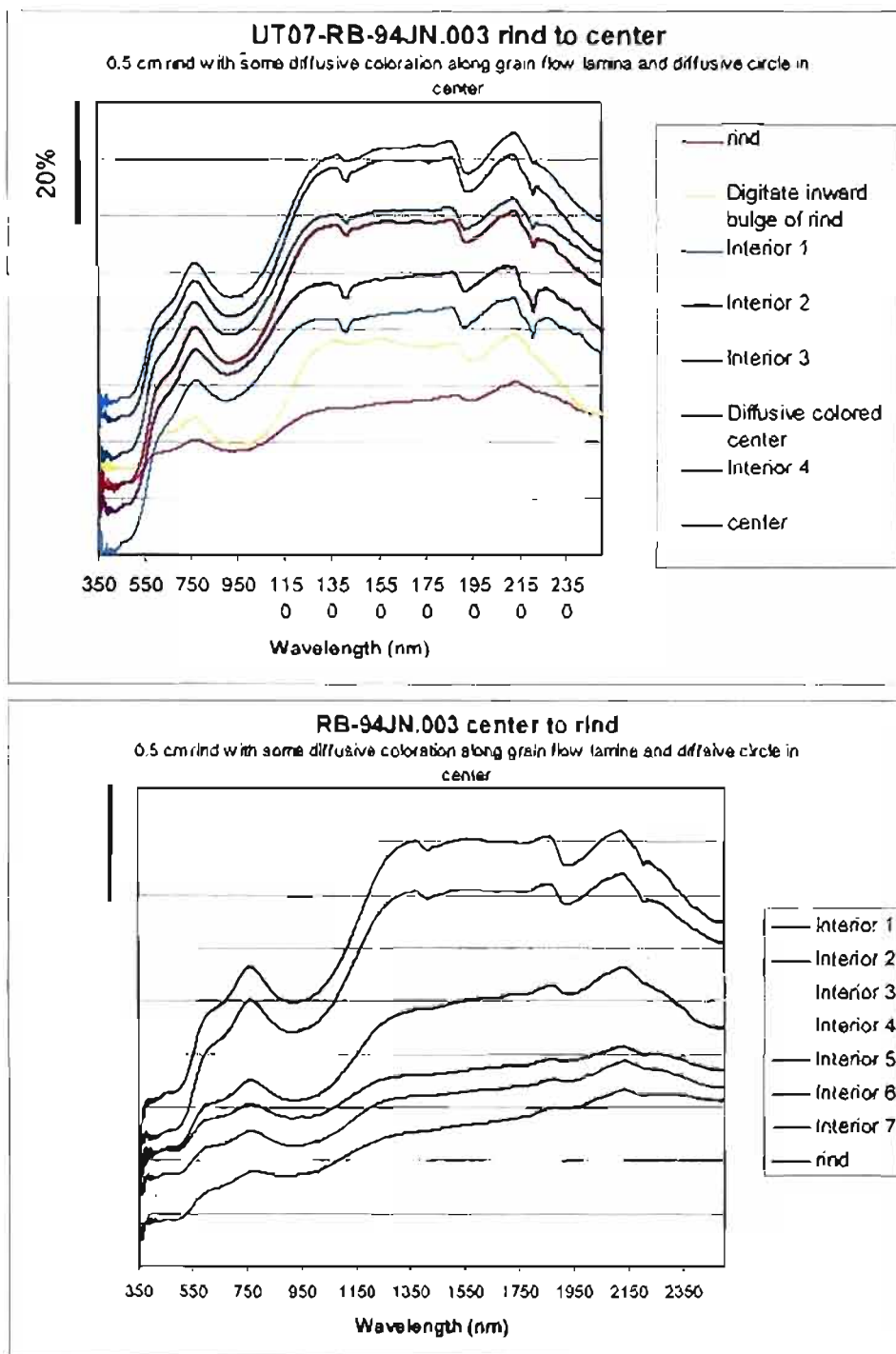


Fig. C.11. Rinds are amorphous HFO; interiors are goethite with minor kaolinite or illite.

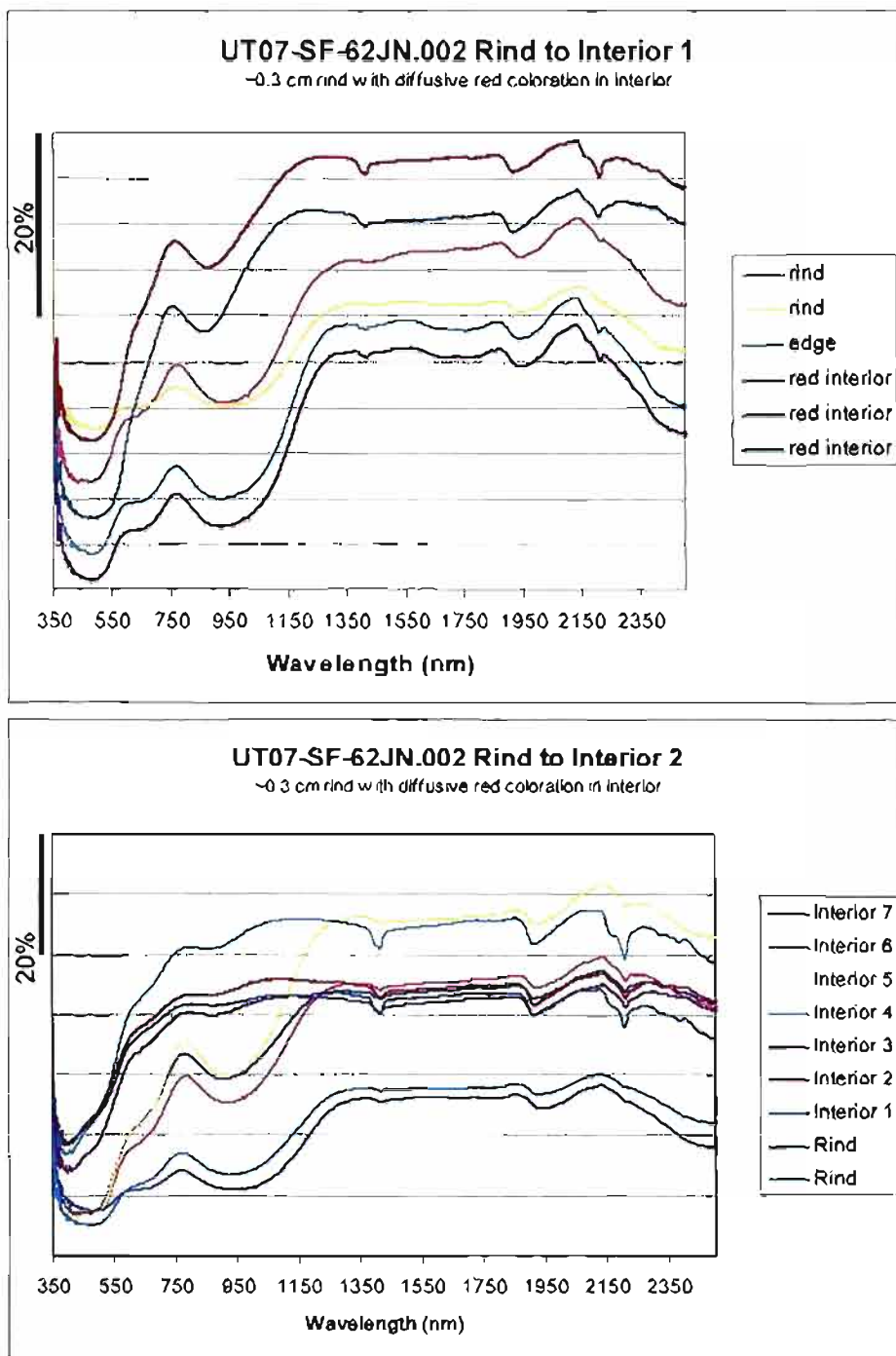


Fig. C.12. Rinds are amorphous HFO; edges near rinds are goethite; centers are hematite. Illite is present in rinds; kaolinite is present in interiors.

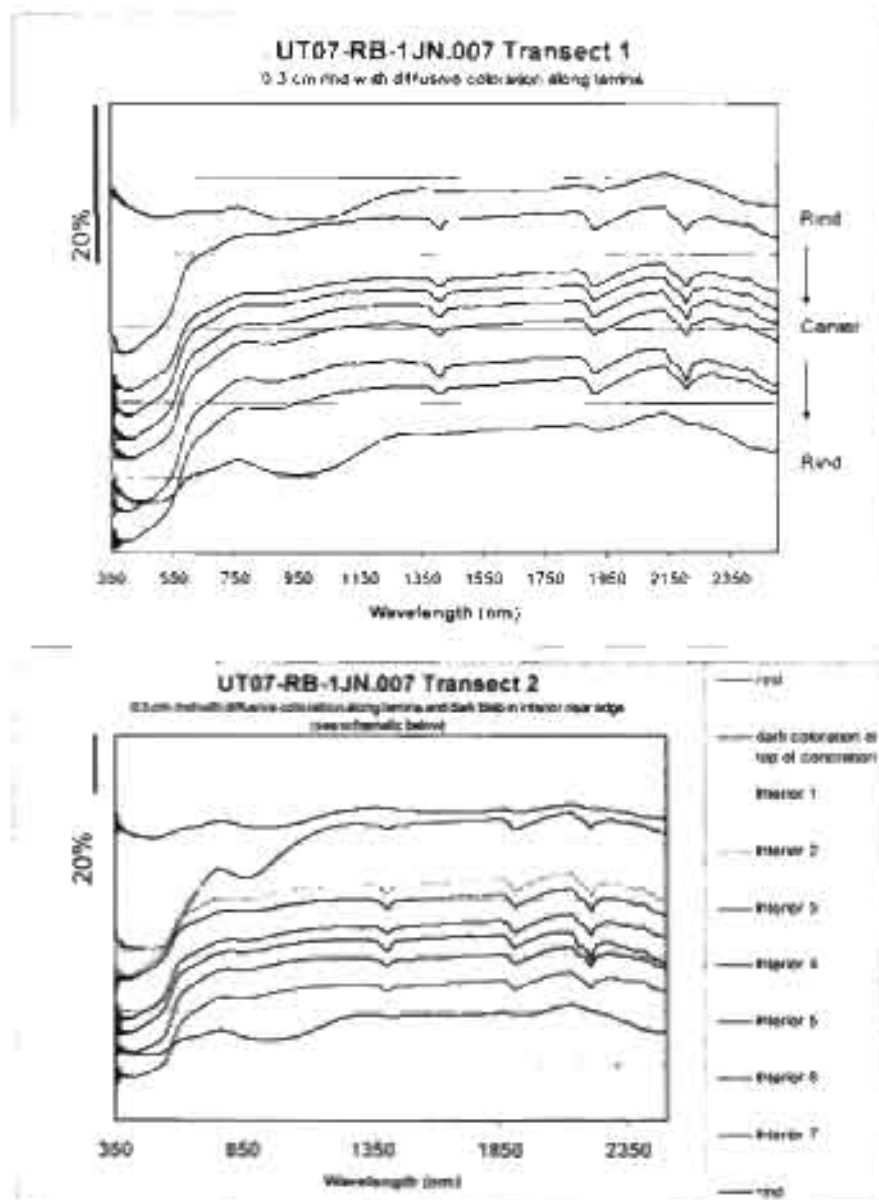
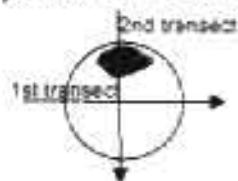


Fig. C.13 Rinds are amorphous HFO, interiors are hematite. Bleh is goethite. Kaolinite is present in interiors; illite is present in interior edges



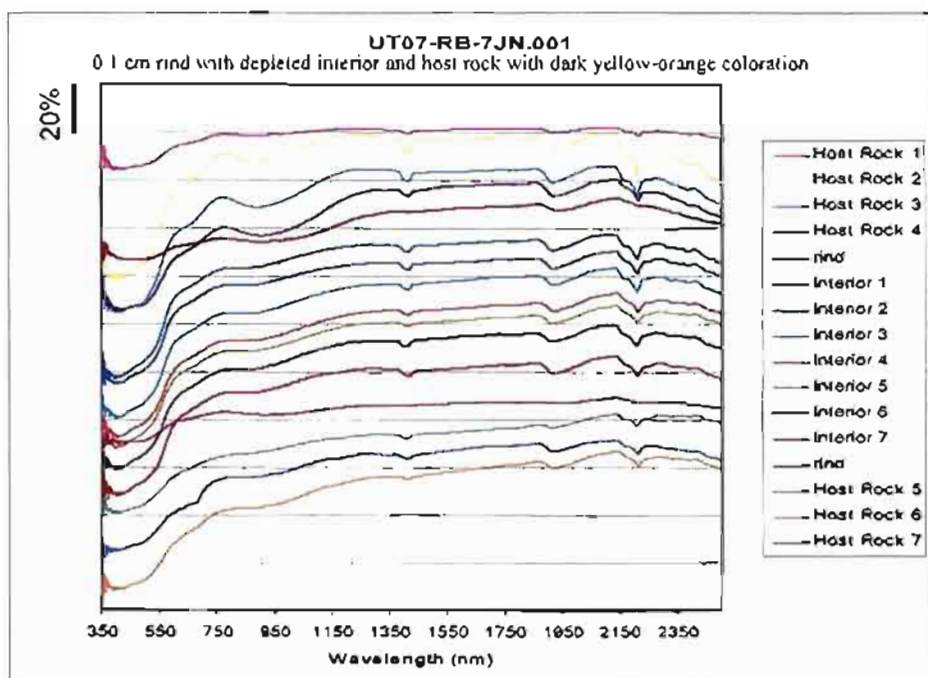


Fig. C.14. Rinds are amorphous HFO; interiors are goethite/ hematite. Kaolinite/ illite is present throughout.

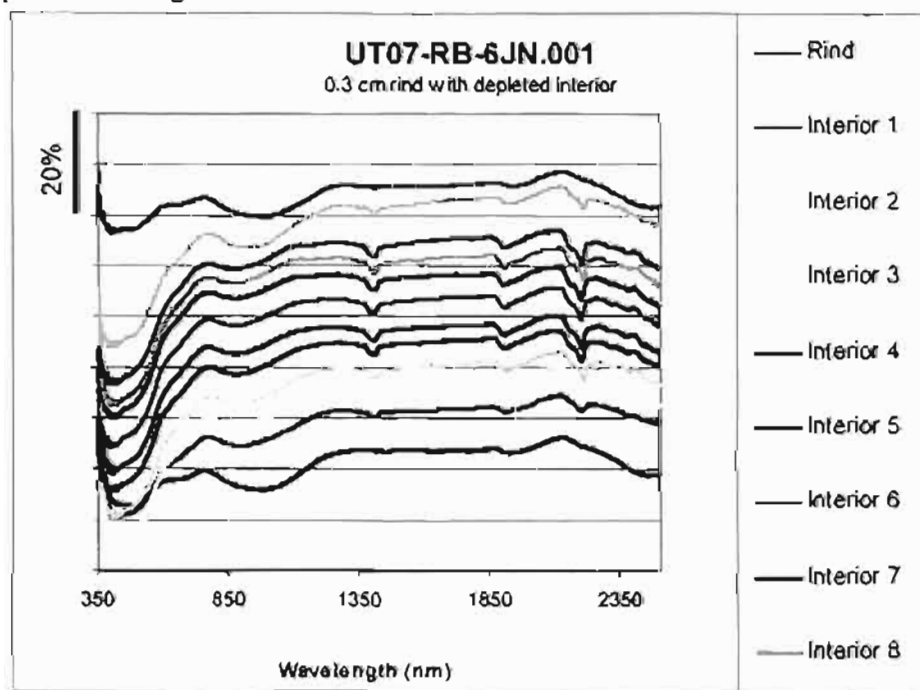


Fig. C.15. Rinds are amorphous HFO; interiors near edge are goethite; centers are goethite/hematite. Kaolinite is present in interiors.

LAYERED CONCRETIONS

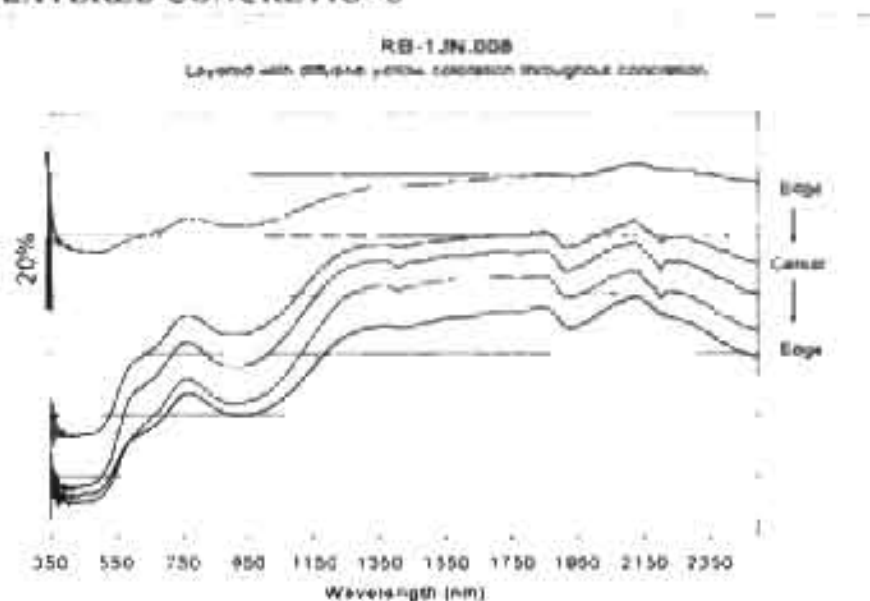


Fig.C 16. One side is amorphous HFO (pink, yellow, lt. blue) and minima shifts through transect to goethite. Illite/kaolinite is present in three interior readings.

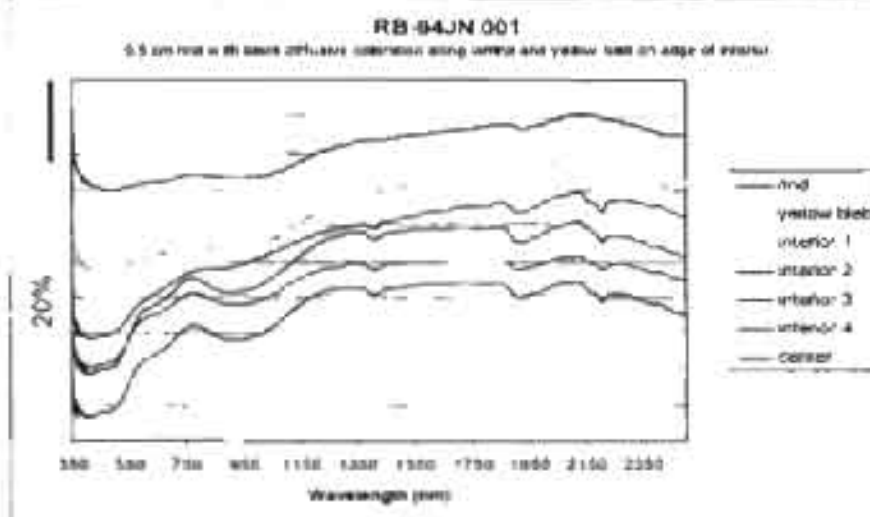


Fig C.17. Rim and yellow bleb are amorphous HFO; interiors are goethite. Kaolinite is present in interior.

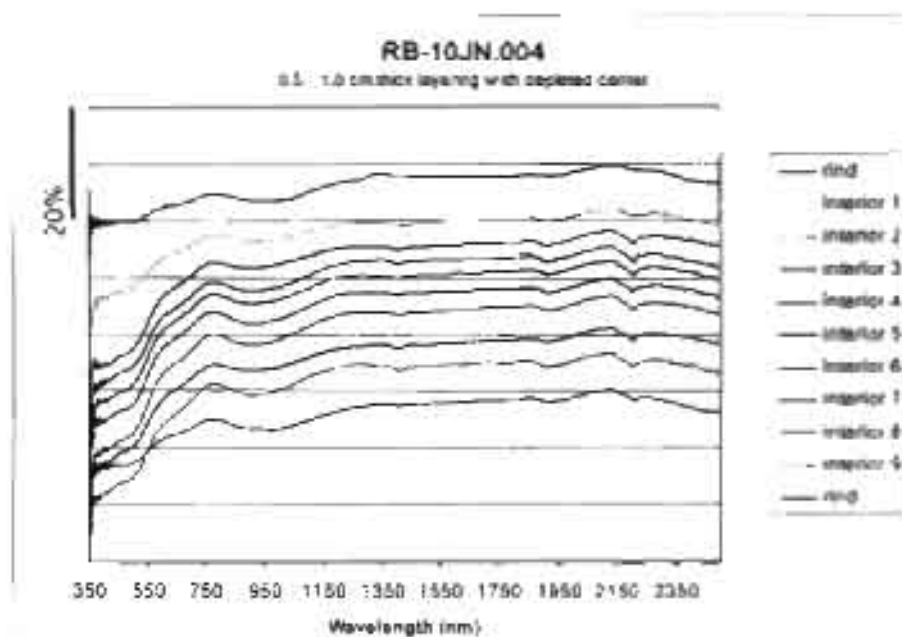


Fig. C.18 Rinds are amorphous HFO, interiors are goethite. Kaolinite/illite is present in all but one rind reading.

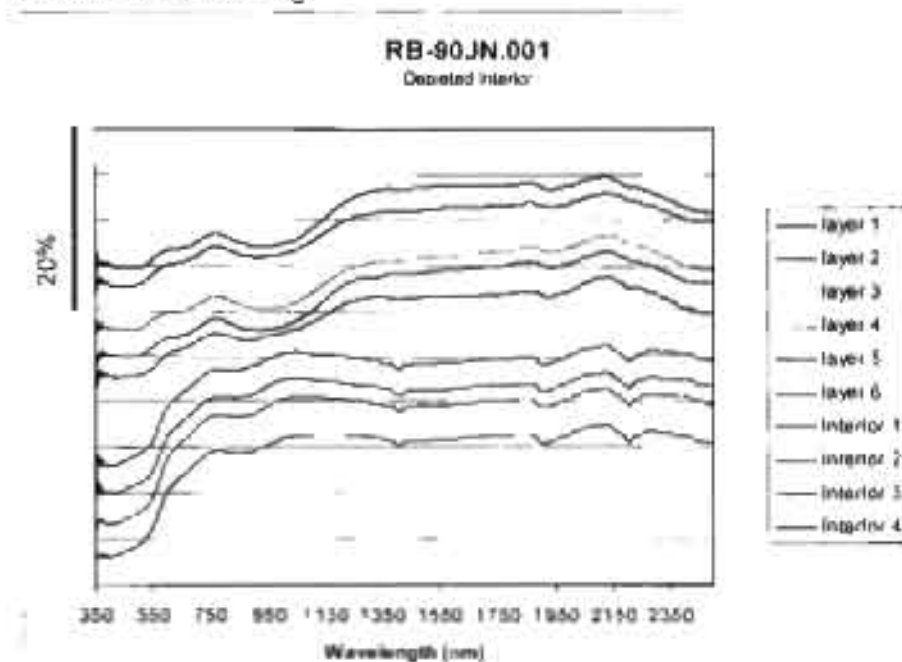


Fig. C.19. Layers are amorphous HFO; depleted interiors are goethite. Kaolinite or illite is present in depleted interior

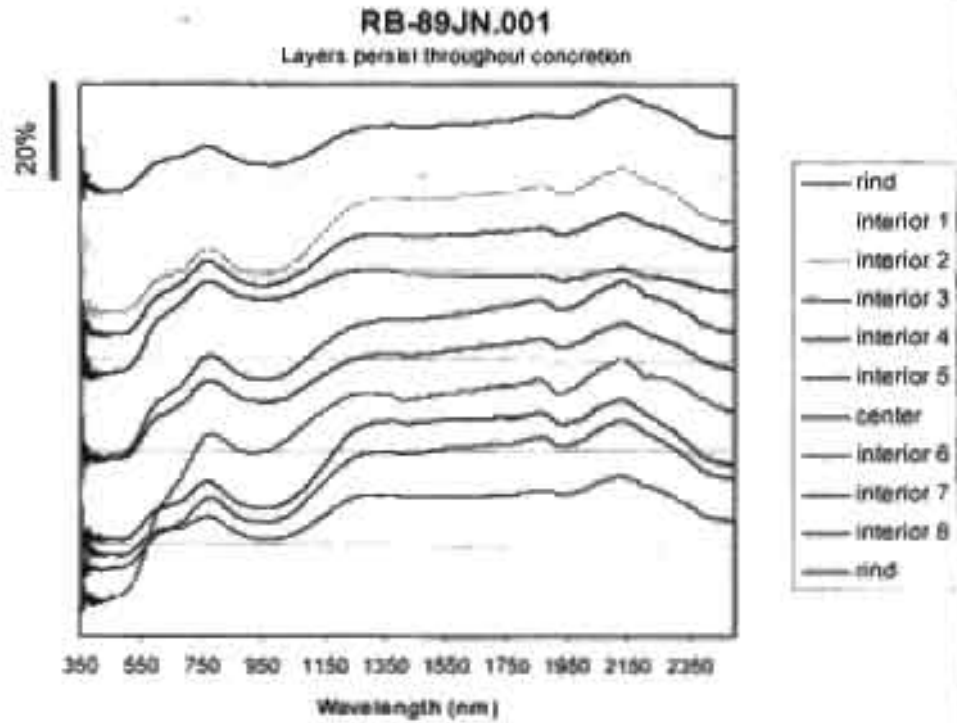


Fig. C.20. Concrete is amorphous HFO/ goethite

SOLID CONCRETIONS

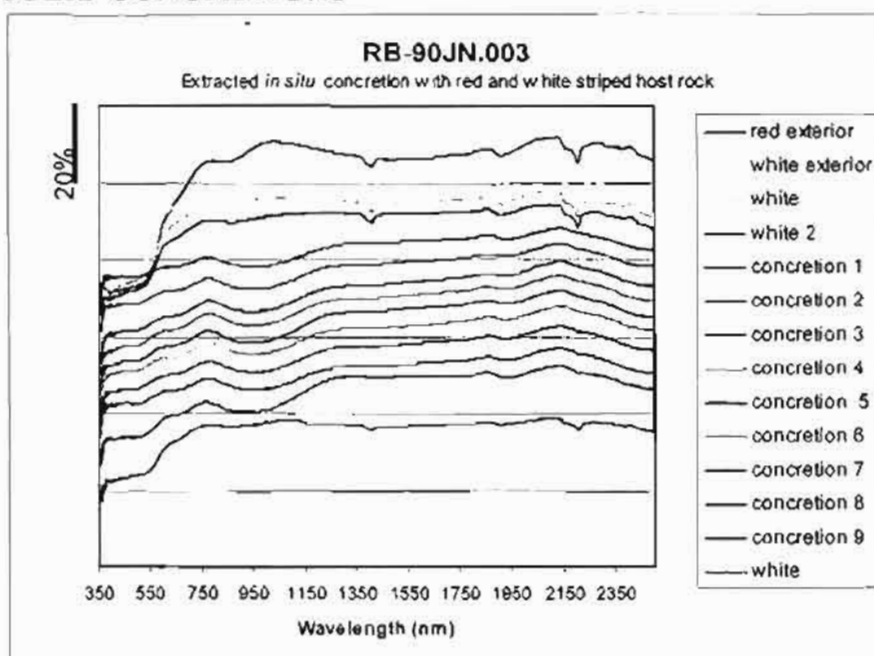


Fig. C.21. Concretion is amorphous HFO. Hematite and kaolinite is present in both red and white host rock although hematite is more prominent in red stripes.

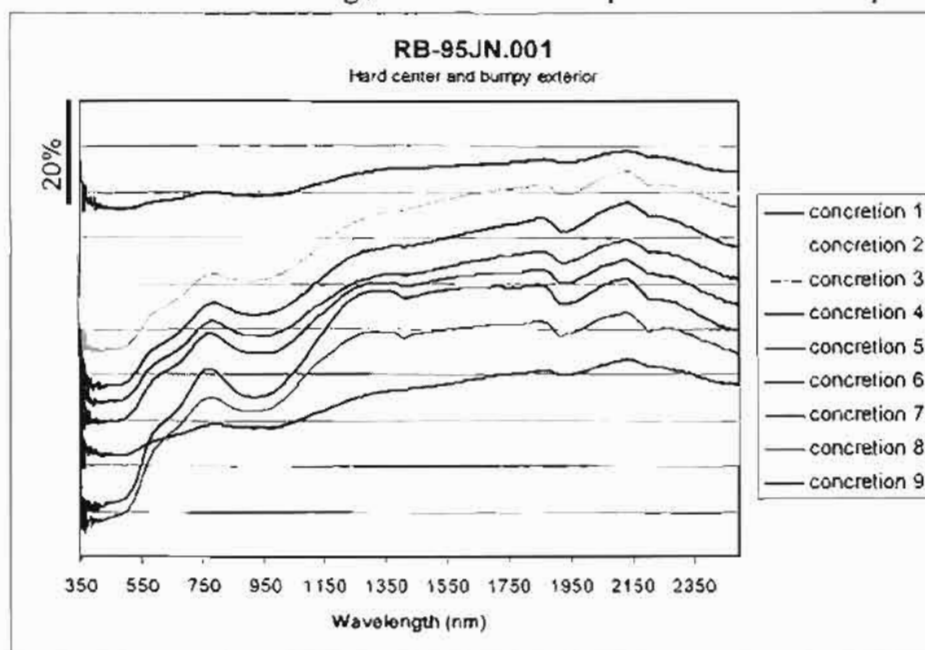


Fig. C.22. Concretion 1 and 9 are amorphous HFO; other readings are goethite with minor kaolinite.

APPENDIX D

MÖSSBAUER SPECTROSCOPY

Mössbauer spectroscopy analysis was done on nine concretion samples from different sedimentary units on the Colorado Plateau by M. Darby Dyar and Elizabeth Sklute from Mt. Holyoke College. Results for each sample are listed below in the text. A table follows with results. Graphical representations of results follow the table. See Appendix A (p. 129) for sample locations, descriptions and XRD results.

1. Sample UT97-20A Jn was reported by XRD to have only hematite. Mössbauer spectra of both the interior and exterior of that sample show three distributions of peaks in sextets with parameters that are consistent with hematite. Both spectra also contain a small Fe^{3+} doublet with parameters that are roughly similar to those of a nanophase (NP) Fe^{3+} oxide (e.g., hematite, as reported in Morris et al., 1989, which are ~ 0.33 mm/s for isomer shift and ~ 0.5 - 0.8 mm/s for quadrupole splitting) or possibly pyrite.
2. For sample UT00-10A, again both an interior and an exterior sample were measured. In this case, the samples are quite different. In the interior sample, the spectrum is dominated by a doublet resulting from a nanophase Fe^{3+} oxide (possibly mixed with pyrite; the parameters are identical). A poorly-resolved sextet with parameters roughly similar to those of goethite is also observed. In the exterior of UT00-10A, the doublet was not observed. Instead, the spectrum shows two well-resolved sextets (probably both

goethite) and two poorly-resolved Fe^{3+} doublets probably representing distributions of unresolved, fine-grained Fe^{3+} oxide.

3. For sample UT00-10B, we ran only the exterior. Mössbauer spectra show the presence of both goethite and hematite as sextets, in addition to a nanophase Fe^{3+} oxide doublet (or pyrite).

4. The spectrum of sample UT04-sdH-13A is dominated by well-resolved goethite and hematite sextets. Sample UT04-sdH-13B has well-resolved hematite sextet structure and smaller, less well-resolved goethite sextets. Sample AZ03-Pg Jn is all nanophase Fe^{3+} oxide or possibly a mixture of oxide and pyrite. Even though it appears that there is suggestion of sextet structure in the baseline of this spectrum, closer analysis reveals the “features” to be only scatter.

5. Sample UT97037 Jes contains a doublet representing nanophase Fe^{3+} oxide doublet, or possibly a mixture of oxide and pyrite and sextets (resolved to varying extents) representing goethite and hematite.

6. Sample UT04-Mo-5 Kd contains a prominent doublet representing nanophase Fe^{3+} oxide doublet, or possibly a mixture of oxide and pyrite and a sextet resulting from hematite. Unlike the XRD, Mössbauer analysis finds no indication for the presence of goethite.

7. Sample UT97-44 is a mixture of a prominent nanophase Fe^{3+} oxide doublet, or possibly a mixture of oxide and pyrite, and a very broad, unresolvable mixture of contributions from unknown oxides.

Table D.1. Mössbauer spectroscopy data.

		UT97-44	UT97037 J66	AZ-03 Pg Jn	UT04-sdH-13A	UT04-sdH-13B	UT00-10A Int	UT00-10A ext	UT00-10B ext	UT04-Mo-5 Kd	UT97-20A Int	UT97-20A ext
NP Fe ³⁺ oxide or pyrite	δ	0.36	0.26	0.23			0.32			0.31	0.17	0.23
	Δ	0.72	0.61	0.71			0.57			0.64	0.66	0.69
	Γ	0.64	0.65	0.40			0.59			0.53	0.84	0.75
	area	54	7	50			62			32	6	13
NP Fe ³⁺ oxide or pyrite	δ			0.06								
	Δ			0.40								
	Γ			0.37								
	area			50								
goethite	δ		0.48		0.41							
	Δ		-0.30		-0.25							
	field		370.4		372.6							
	Γ		0.38		0.57							
	area		6		34							
goethite	δ		0.44		0.44	0.43		0.38	0.40			
	Δ		-0.17		-0.17	-0.38		-0.25	-0.28			
	field		347.6		341.9	325.7		324.7	341.7			
	Γ		0.49		0.36	0.90		0.83	0.84			
	area		11		11	38		41	32			
Hematite	δ		0.38		0.40	0.38			0.38	0.37	0.38	0.35
	Δ		-0.28		-0.36	-0.28			-0.28	-0.24	-0.22	-0.21
	field		507.1		511.1	507.0			507.0	506.4	496.7	495.1
	Γ		0.70		0.53	0.25			0.39	0.46	0.25	0.32
	area		37		20	3			7	38	10	11
Hematite	δ		0.44		0.37	0.44			0.44	0.53	0.37	0.37
	Δ		-0.28		-0.13	-0.28			-0.28	-0.41	-0.30	-0.29
	field		535.1		536.6	535.0			535.0	535.6	515.7	514.1
	Γ		0.30		0.33	0.50			0.50	0.42	0.26	0.25
	area		5		8	4			4	17	35	30
Hem or Goethite	δ				0.8	0.09			0.38	0.39	0.40	0.42
	Δ				-0.11	-0.30			-0.18	-0.21	-0.17	-0.23
	field				191.3	213.30			309.00	481.40	543.90	541.40
	Γ				0.36	0.76			0.35	0.42	0.52	0.57
	area				7	18			10	13	50	47
Hem or Goethite	δ		0.52		0.52	0.37	0.39	0.39	0.44			
	Δ		-0.10		-0.07	-0.09	-0.18	-0.17	-0.15			
	field		283.7		288.3	278.2	290.3	276.4	273.0			
	Γ		0.78		0.52	0.77	0.37	0.42	0.95			
	area		31		21	26	38	27	39			
Unresolved	δ	0.485	0.5			0.5		0.5	0.5			
	Δ	2.78	1.46			1.20		1.16	1.19			
	Γ	3.952	0.3			0.5		0.4	0.7			
	area	46	3			10		7	10			
	x^*	6.78	4.63	1.85	7.06	2.25	0.66	8.36	4.91	1.71	16.42	6.98

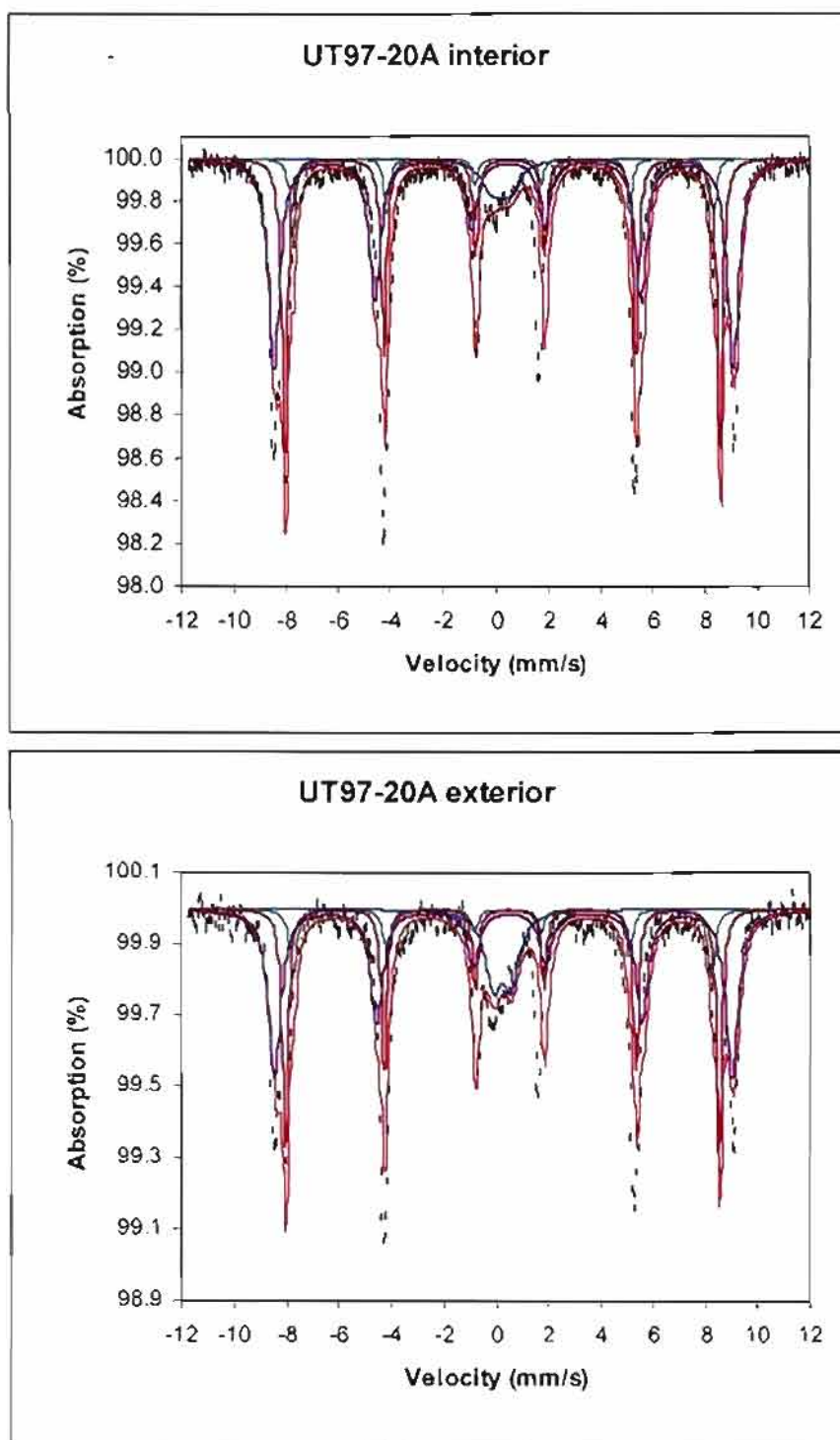


Fig. D.1. Sample UT97-20A interior and exterior.

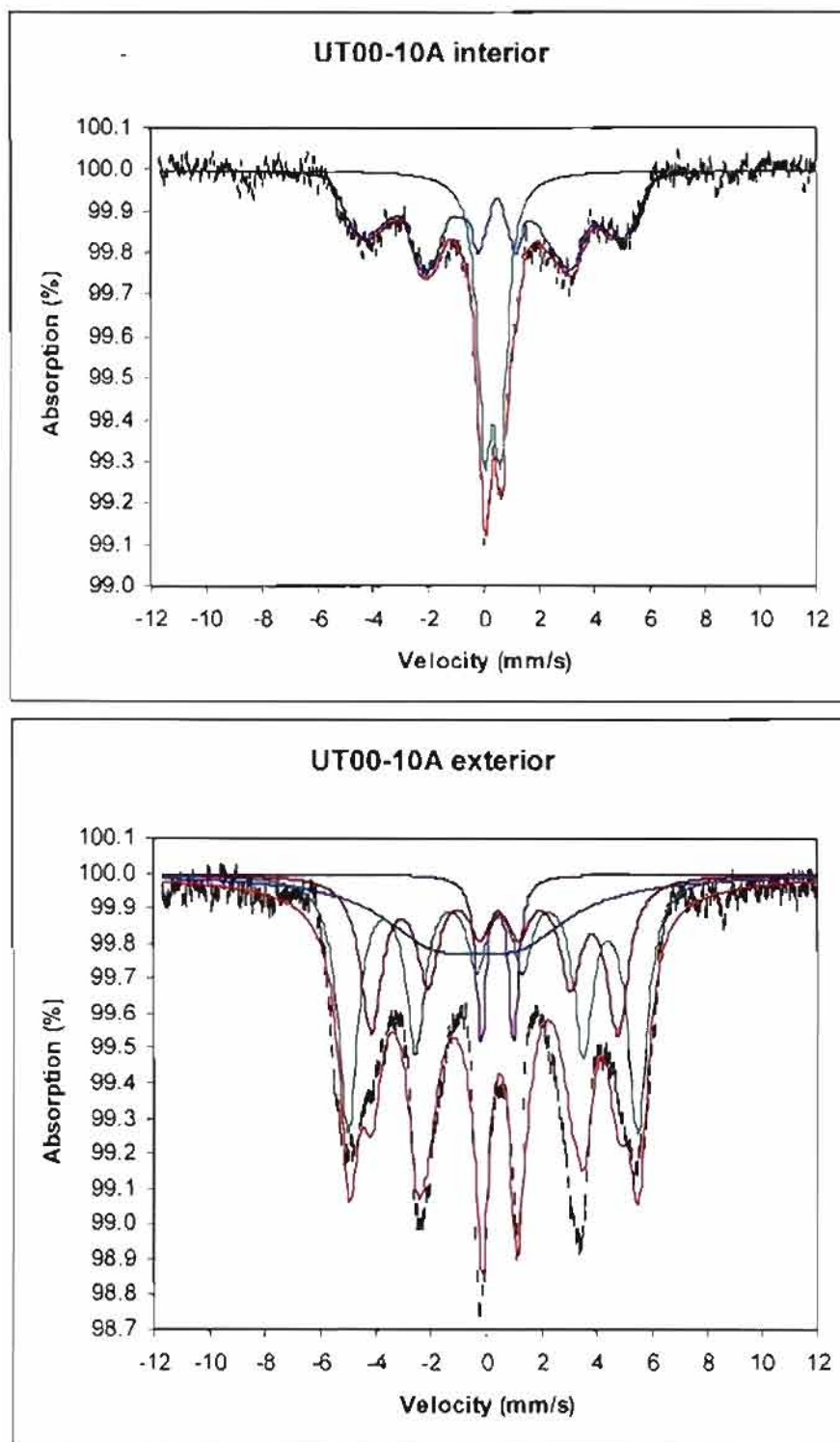


Fig. D.2. Sample UT00-10A

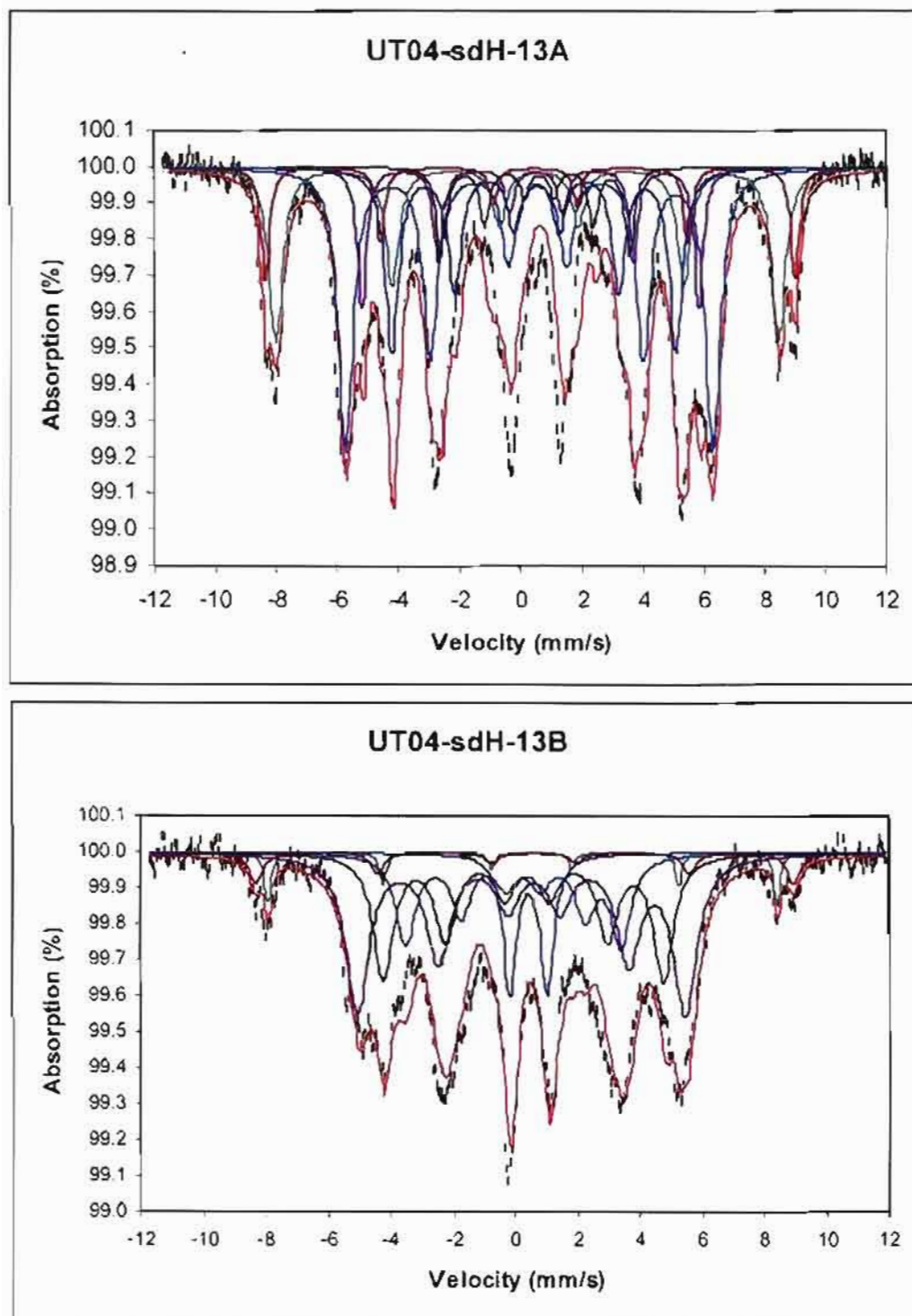


Fig. D.3. Samples UT04-skH-13A, B.

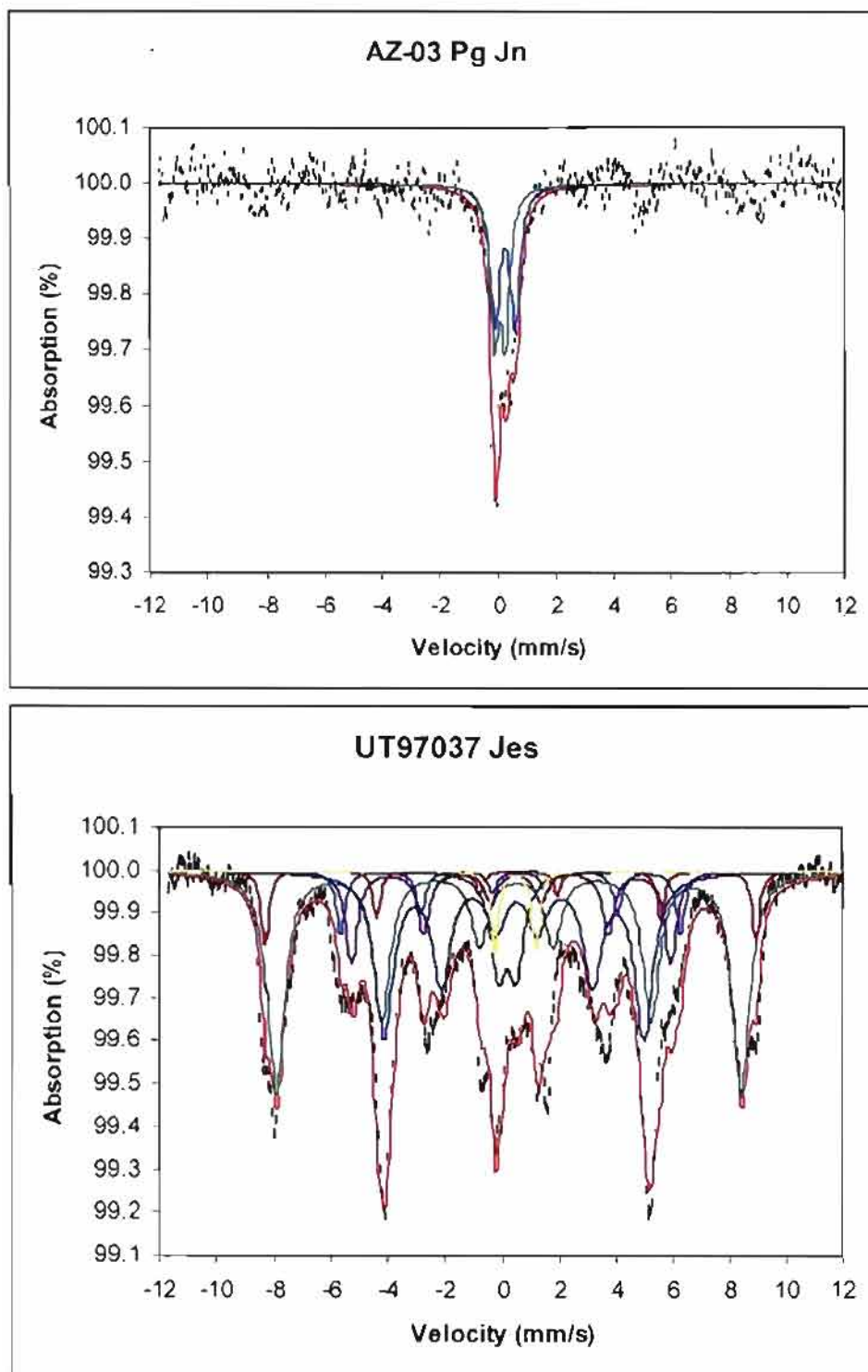


Fig. D.4. Samples AZ-03 Pg Jn and UT97037 Jes

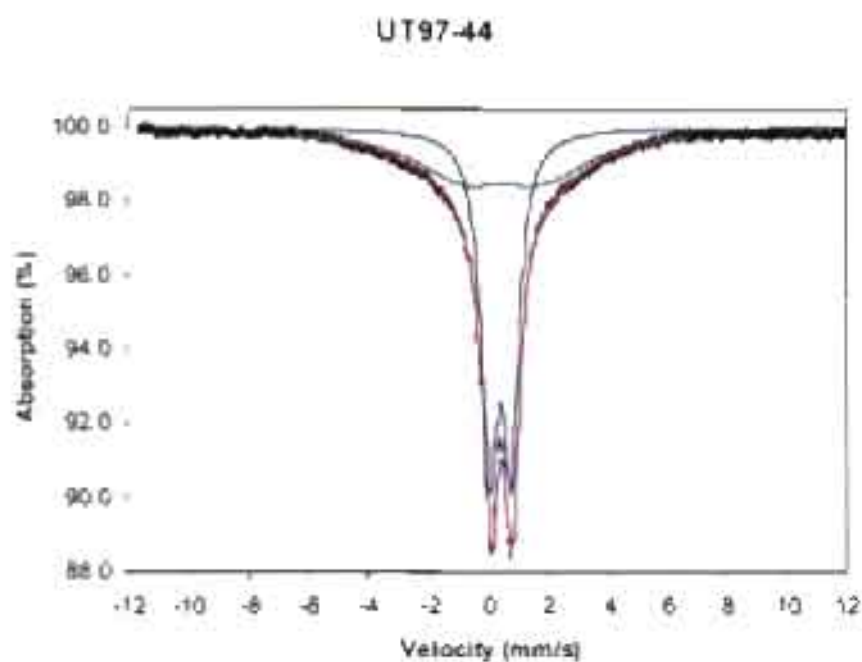
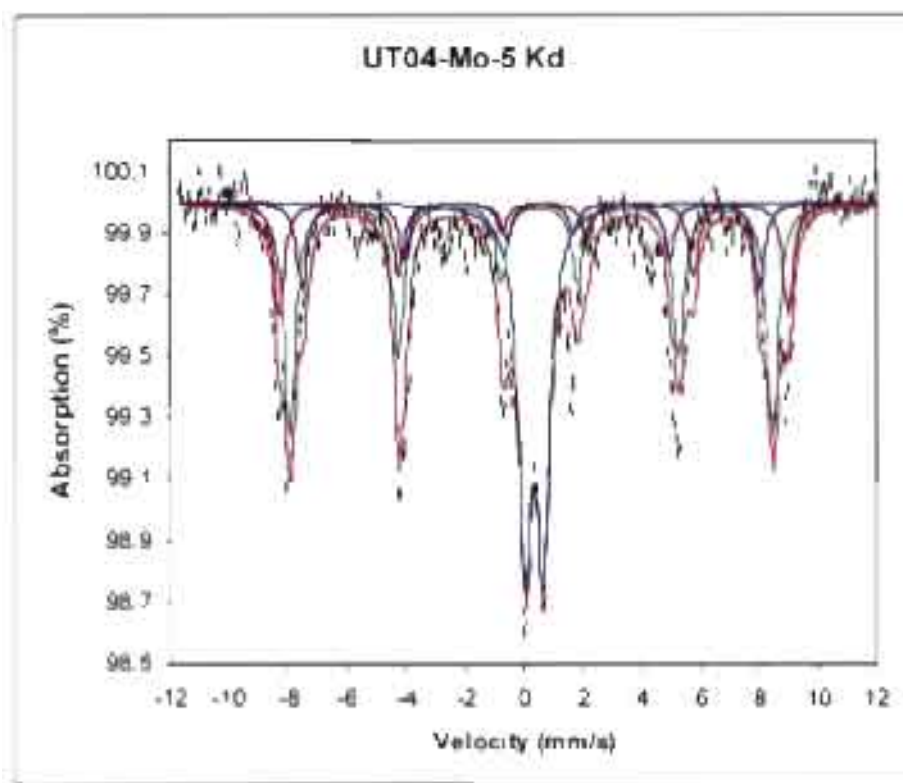


Fig. D.5. Samples UT04-Mo-5Kd and UT97-44.

APPENDIX E

CONCRETION DIAMETER MEASUREMENTS

Concretion diameters were measured in GSENM from concretions that had weathered out of the host rock and collected in topographic lows. Concretions are well-cemented and have comparable diameters to extracted *in situ* concretions. Sample 3 and Sample 9 are measurements of *in situ* concretions and are therefore not representative of true diameters, but rather only the exposed diameter.

Table E.1. Sample 1.

Sample 1							
Lat/Long							
N 37 42.138'		W 111 22.591'					
#	Diam.(mm)	#	Diam.(mm)	#	Diam.(mm)	#	Diam.(mm)
1	20.57	31	28.25	61	3.74	91	6.18
2	25.60	32	28.35	62	6.31	92	31.20
3	14.89	33	10.38	63	40.77	93	7.78
4	17.43	34	6.51	64	19.20	94	21.64
5	23.83	35	20.94	65	19.31	95	8.48
6	16.97	36	33.54	66	5.97	96	32.16
7	29.48	37	12.55	67	1.88	97	23.69
8	21.93	38	7.42	68	16.02	98	31.60
9	23.41	39	28.39	69	17.37	99	6.69
10	19.32	40	23.04	70	24.92	100	12.78
11	26.14	41	19.06	71	6.02		
12	26.05	42	6.99	72	6.10		
13	8.57	43	19.75	73	28.22		
14	19.20	44	47.02	74	23.97		
15	41.05	45	37.47	75	20.12		
16	30.33	46	56.89	76	22.47		
17	22.02	47	26.04	77	16.54		
18	24.89	48	45.18	78	24.46		
19	11.91	49	22.84	79	5.97		
20	27.46	50	20.62	80	5.61		
21	27.37	51	17.56	81	6.74		
22	29.40	52	18.43	82	24.45		
23	42.09	53	20.16	83	21.44		
24	24.34	54	24.17	84	55.84		
25	24.15	55	31.33	85	3.97		
26	29.39	56	20.34	86	20.56		
27	43.13	57	19.19	87	21.5		
28	18.98	58	6.41	88	26.68		
29	16.17	59	36.38	89	5.25		
30	30.82	60	19.16	90	2.31		

Table E.2. Sample 2.

Sample 2											
Lat/Long											
N 37 42.172'											
W 111 22.786											
#	Diam. (mm)	#	Diam. (mm)	#	Diam. (mm)	#	Diam. (mm)	#	Diam. (mm)	#	Diam. (mm)
1	10.58	51	10.00	101	50.92	151	14.48	201	15.97	251	57.70
2	36.10	52	42.62	102	63.05	152	34.52	202	32.49	252	23.39
3	14.43	53	48.20	103	15.94	153	48.33	203	50.18	253	48.90
4	34.32	54	17.01	104	39.40	154	24.08	204	35.10	254	54.87
5	46.71	55	34.82	105	40.41	155	26.94	205	28.43	255	54.45
6	46.12	56	36.96	106	40.39	156	33.45	206	38.67	256	40.52
7	68.74	57	25.38	107	65.68	157	62.26	207	47.85	257	11.02
8	33.44	58	38.49	108	24.72	158	55.77	208	14.53	258	12.35
9	14.04	59	16.17	109	38.22	159	25.97	209	24.80	259	13.29
10	10.55	60	25.41	110	40.99	160	50.52	210	43.75	260	35.06
11	52.09	61	20.47	111	52.25	161	20.91	211	33.94	261	37.24
12	30.35	62	26.89	112	2.55	162	47.97	212	10.83	262	27.56
13	7.24	63	41.54	113	41.91	163	41.69	213	13.45	263	8.30
14	35.27	64	44.71	114	15.26	164	32.40	214	15.69	264	53.24
15	22.08	65	41.25	115	34.05	165	57.52	215	38.58	265	34.04
16	60.25	66	24.43	116	42.20	166	28.62	216	34.33	266	4.62
17	38.90	67	18.58	117	28.31	167	57.21	217	17.11	267	38.83
18	17.56	68	37.70	118	57.47	168	37.37	218	23.83	268	46.67
19	7.89	69	48.36	119	54.47	169	30.75	219	32.39	269	47.83
20	32.37	70	24.81	120	37.17	170	25.75	220	42.88	270	23.15
21	39.25	71	26.13	121	51.59	171	51.84	221	60.56	271	22.15
22	10.57	72	16.07	122	43.00	172	61.97	222	39.48	272	31.20
23	30.77	73	28.67	123	7.86	173	49.53	223	48.49	273	54.11
24	27.49	74	22.66	124	45.20	174	39.75	224	41.09	274	42.89
25	20.97	75	7.35	125	24.6	175	43.95	225	7.98	275	47.03
26	52.53	76	43.34	126	40.02	176	34.54	226	10.59	276	17.20
27	11.10	77	36.35	127	21.08	177	25.97	227	30.67	277	37.94
28	17.44	78	40.95	128	25.32	178	42.46	228	48.81	278	30.35
29	13.39	79	20.59	129	36.15	179	24.14	229	34.72	279	18.13
30	7.86	80	31.40	130	21.73	180	40.13	230	40.20	280	56.33
31	33.65	81	37.43	131	25.34	181	43.14	231	44.66	281	10.27
32	48.61	82	64.09	132	35.71	182	28.56	232	40.96	282	24.84
33	38.32	83	67.44	133	44.32	183	42.83	233	51.46	283	7.61
34	34.54	84	50.06	134	38.74	184	24.42	234	11.54	284	53.85
35	26.98	85	31.13	135	40.67	185	29.78	235	8.36	285	56.74
36	19.66	86	26.24	136	22.50	186	38.89	236	37.90	286	42.78
37	37.87	87	34.25	137	24.13	187	34.52	237	33.38	287	42.29
38	22.13	88	57.34	138	23.72	188	22.26	238	54.03	288	39.08
39	36.56	89	37.64	139	24.89	189	19.32	239	10.65	289	38.46
40	21.21	90	27.68	140	40.42	190	32.23	240	6.47	290	41.47
41	24.39	91	18.81	141	31.13	191	25.60	241	7.28	291	34.67
42	16.06	92	13.16	142	19.58	192	27.93	242	6.90	292	36.98
43	28.09	93	24.42	143	32.12	193	22.19	243	9.32	293	40.11
44	20.78	94	15.65	144	41.80	194	52.07	244	7.48	294	45.11
45	22.65	95	39.33	145	32.16	195	40.15	245	17.82	295	39.23
46	10.36	96	19.67	146	34.08	196	31.43	246	14.13	296	39.43
47	48.73	97	18.76	147	31.75	197	35.58	247	28.00	297	25.52
48	46.04	98	5.98	148	25.11	198	41.88	248	10.43	298	55.47
49	44.77	99	22.25	149	23.18	199	34.06	249	16.95	299	58.00
50	43.11	100	54.24	150	23.97	200	54.91	250	38.52	300	50.30

Table E.3. Sample 3.

Sample 3 (<i>in situ</i>)					
Lat/Long					
N 37 42.172'					
W 111 22.786'					
#	Size (mm)	#	Size (mm)	#	Size (mm)
1	8.73	35	6.39	69	4.74
2	8.58	36	6.71	70	5.43
3	7.63	37	6.81	71	4.98
4	3.32	38	5.72	72	7.54
5	2.71	39	6.56	73	7.03
6	5.23	40	6.18	74	5.57
7	7.89	41	2.08	75	5.88
8	6.71	42	7.14	76	3.69
9	5.74	43	4.55	77	7.03
10	7.95	44	6.23	78	5.34
11	6.3	45	4.9	79	5.75
12	6.32	46	3.23	80	4.96
13	11.76	47	5.55	81	7.25
14	5.9	48	4.23	82	5.12
15	5.01	49	5.89	83	5.48
16	4.32	50	4.83	84	6.44
17	5.6	51	7.32	85	3.14
18	2.99	52	28.8	86	4.66
19	5.12	53	7.76	87	3.42
20	8.85	54	5.48	88	4.41
21	6.41	55	7.92	89	6.46
22	5.3	56	6.13	90	5.95
23	3.64	57	7.19	91	5.82
24	7.68	58	5.66	92	5.9
25	2.56	59	6.02	93	6.15
26	7.75	60	7.41	94	4.02
27	5.04	61	7.85	95	4.83
28	5.36	62	5.48	96	3.32
29	5.12	63	4.05	97	2.83
30	4.87	64	4.72	98	2.35
31	6.78	65	30.47	99	4.06
32	6.57	66	5.74	100	9.45
33	6.71	67	5.02		
34	5.93	68	6.97		

Table E.4. Sample 4.

Sample 4 Lat/Long N 37 42.650' W 111 23.762'													
#	Size (mm)	#	Size (mm)	#	Size (mm)	#	Size (mm)	#	Size (mm)	#	Size (mm)	#	Size (mm)
1	18.23	51	44.58	101	44.31	151	40.78	201	7.08	251	5.94		
2	29.12	52	37.7	102	52.64	152	43.94	202	5.5	252	6.94		
3	21.85	53	18.98	103	50.65	153	60.32	203	5.79	253	6.13		
4	42.70	54	30.91	104	45.19	154	40.54	204	5.05	254	8.13		
5	48.83	55	29.82	105	52.16	155	18.21	205	4.18	255	6.51		
6	42.51	56	28.05	106	42.20	156	17.25	206	4.35	256	6.11		
7	41.53	57	28.08	107	43.38	157	14.91	207	3.89	257	4.88		
8	20.30	58	26.4	108	81.79	158	17.39	208	5.69	258	6.44		
9	41.68	59	33.67	109	48.41	159	17.01	209	10.14	259	4.85		
10	42.47	60	30.87	110	43.85	160	33.71	210	3.15	260	6.99		
11	32.37	61	29.33	111	21.11	161	48.95	211	4.89	261	6.77		
12	19.72	62	35.31	112	53.82	162	33.57	212	4.50	262	6.11		
13	53.10	63	9.32	113	52.56	163	44.28	213	7.56	263	6.32		
14	49.89	64	35.5	114	37.48	164	39.4	214	5.69	264	6.63		
15	46.85	65	62.04	115	15.28	165	49.3	215	6.88	265	6.00		
16	32.06	66	51.42	116	29.15	166	37.53	216	5.62	266	6.70		
17	54.75	67	53.11	117	50.81	167	24.64	217	4.72	267	6.77		
18	59.76	68	36.23	118	32.58	168	21.39	218	5.93	268	6.18		
19	29.99	69	51.29	119	19.66	169	40.91	219	5.54	269	5.10		
20	31.51	70	48.88	120	25.40	170	19.80	220	5.18	270	7.58		
21	29.32	71	53.27	121	25.24	171	46.64	221	4.63	271	5.52		
22	55.04	72	66.53	122	17.77	172	34.84	222	5.73	272	6.56		
23	38.04	73	49.64	123	23.26	173	63.82	223	5.84	273	5.53		
24	40.96	74	25.61	124	39.7	174	42.42	224	5.56	274	6.34		
25	53.92	75	15.83	125	39.01	175	35.28	225	5.20	275	4.75		
26	58.17	76	13.41	126	16.06	176	43.85	226	2.01	276	6.53		
27	31.20	77	21.87	127	49.44	177	40.30	227	6.34	277	4.89		
28	34.08	78	18.06	128	37.67	178	30.40	228	8.73	278	6.26		
29	60.99	79	24.47	129	44.28	179	31.66	229	6.04	279	6.73		
30	54.99	80	40.26	130	36.70	180	43.26	230	7.42	280	6.05		
31	40.24	81	39.80	131	63.98	181	46.16	231	8.86	281	7.78		
32	54.66	82	56.49	132	34.32	182	50.25	232	8.41	282	14.47		
33	45.70	83	19.28	133	36.71	183	55.79	233	6.95	283	6.91		
34	32.12	84	39.92	134	18.93	184	57.19	234	8.13	284	7.66		
35	25.59	85	18.49	135	46.16	185	41.44	235	5.64	285	8.13		
36	25.03	86	12.72	136	32.72	186	29.54	236	7.93	286	8.14		
37	23.31	87	10.35	137	37.63	187	70.34	237	6.29	287	4.19		
38	49.11	88	12.24	138	34.90	188	29.42	238	8.07	288	4.28		
39	24.56	89	19.74	139	33.59	189	38.18	239	8.23	289	5.08		
40	25.01	90	49.03	140	42.19	190	49.41	240	4.62	290	8.14		
41	30.89	91	52.11	141	54.36	191	45.63	241	6.03	291	8.54		
42	34.79	92	27.62	142	54.95	192	52.11	242	7.57	292	7.32		
43	44.82	93	54.47	143	39.55	193	44.03	243	4.90	293	5.39		
44	39.98	94	20.91	144	42.19	194	42.20	244	5.86	294	5.92		
45	68.55	95	18.38	145	50.39	195	49.97	245	5.13	295	4.33		
46	45.15	96	31.49	146	42.59	196	46.94	246	8.74	296	5.37		
47	43.11	97	18.44	147	40.82	197	45.78	247	5.58	297	6.04		
48	30.30	98	51.28	148	41.18	198	54.62	248	6.03	298	9.04		
49	46.37	99	46.71	149	40.88	199	33.64	249	5.88	299	4.61		
50	58.49	100	27.44	150	42.87	200	40.22	250	8.87	300	8.21		

Table E.5. Sample 6.

Sample 6					
Lat/Long					
N37 42.772' W 111 22.375'					
#	Diam.(mm)	#	Diam.(mm)	#	Diam.(mm)
1	20.37	35	16.41	69	22.52
2	26.02	36	26.95	70	29.15
3	19.7	37	24.76	71	15.84
4	28.84	38	26.86	72	25.09
5	22.94	39	16.23	73	21.43
6	17.2	40	8.22	74	17.44
7	27.09	41	20.11	75	10.8
8	6.23	42	20.07	76	16.83
9	18	43	21.44	77	15.84
10	23.35	44	32.02	78	29.1
11	17.38	45	17.81	79	25.19
12	17.62	46	20.91	80	34.79
13	18.56	47	26.26	81	26.76
14	27.44	48	17.42	82	20.18
15	19.98	49	19.08	83	29.28
16	13.03	50	16.65	84	29.4
17	14.92	51	26.81	85	27.39
18	15.08	52	23.46	86	25.57
19	28.9	53	17.59	87	36.23
20	15.31	54	23.16	88	22.83
21	21.79	55	18.04	89	25.13
22	21.59	56	22.36	90	27.41
23	15.09	57	39.65	91	31.5
24	28.69	58	23.14	92	13.29
25	15.45	59	32.63	93	17.89
26	12.88	60	21.37	94	22.89
27	15.83	61	20.34	95	23.96
28	15.49	62	20.3	96	21.88
29	19.29	63	28.28	97	31.95
30	23.98	64	20	98	35.45
31	25.46	65	24.84	99	19.09
32	27.29	66	28.91	100	15.96
33	29.31	67	19.15		
34	21.39	68	25.58		

Table E.6. Sample 7.

Sample 7 Lat/Long N 37042.697 W 111 20.797		(measurements 201-300 are mostly micros)									
#	Diam.(mm)	#	Diam.(mm)	#	Diam.(mm)	#	Diam.(mm)	#	Diam.(mm)	#	Diam.(mm)
1	31.61	51	29.21	101	5.40	151	7.39	201	4.28	251	6.44
2	28.30	52	23.34	102	5.38	152	9.93	202	6.04	252	5.67
3	28.41	53	33.29	103	6.58	153	10.41	203	6.45	253	6.05
4	30.12	54	26.67	104	5.52	154	4.53	204	3.42	254	3.72
5	38.21	55	28.28	105	6.13	155	4.85	205	5.50	255	6.93
6	29.82	56	18.17	106	6.21	156	8.51	206	8.79	256	17.87
7	24.53	57	30.19	107	7.28	157	7.81	207	13.38	257	4.91
8	21.07	58	27.13	108	6.56	158	17.23	208	5.88	258	6.99
9	30.31	59	29.58	109	19.04	159	6.18	209	5.68	259	6.18
10	29.09	60	33.15	110	18.24	160	4.95	210	6.68	260	4.90
11	30.18	61	33.30	111	6.78	161	7.23	211	6.42	261	4.39
12	27.52	62	23.21	112	4.36	162	5.60	212	6.44	262	9.58
13	25.54	63	26.72	113	6.32	163	10.05	213	5.92	263	5.58
14	31.65	64	21.50	114	10.96	164	9.25	214	3.69	264	5.31
15	32.16	65	27.82	115	4.97	165	6.44	215	4.88	265	5.15
16	26.27	66	20.94	116	10.72	166	7.58	216	5.30	266	4.05
17	19.97	67	18.95	117	6.98	167	5.02	217	6.08	267	8.69
18	29.15	68	23.60	118	5.99	168	8.45	218	4.60	268	9.01
19	23.55	69	24.62	119	15.72	169	5.34	219	5.79	269	6.10
20	30.37	70	32.36	120	5.21	170	6.21	220	6.27	270	10.09
21	35.79	71	27.87	121	2.04	171	10.98	221	5.39	271	11.65
22	28.90	72	25.75	122	7.10	172	4.58	222	7.86	272	7.14
23	27.85	73	29.69	123	5.36	173	4.22	223	4.77	273	7.42
24	27.02	74	17.56	124	9.49	174	8.05	224	5.03	274	7.15
25	31.65	75	24.12	125	5.87	175	5.18	225	5.14	275	5.04
26	18.95	76	23.99	126	5.22	176	6.69	226	5.52	276	6.00
27	28.59	77	26.80	127	5.67	177	5.97	227	5.24	277	4.86
28	26.26	78	28.42	128	10.90	178	6.32	228	22.17	278	15.13
29	20.81	79	27.42	129	5.36	179	5.87	229	16.15	279	8.36
30	18.27	80	26.93	130	6.81	180	11.02	230	7.95	280	6.71
31	14.89	81	23.73	131	4.95	181	16.81	231	5.35	281	5.86
32	21.44	82	33.55	132	4.96	182	10.58	232	4.37	282	5.72
33	30.43	83	27.62	133	5.92	183	4.72	233	5.10	283	6.39
34	30.53	84	31.23	134	8.84	184	5.79	234	7.53	284	5.53
35	28.64	85	20.24	135	17.71	185	6.52	235	5.56	285	5.23
36	26.48	86	21.74	136	6.54	186	18.83	236	8.85	286	5.35
37	29.92	87	22.00	137	4.94	187	9.90	237	4.89	287	12.16
38	30.94	88	21.47	138	15.91	188	7.57	238	5.24	288	5.31
39	24.43	89	21.66	139	16.99	189	6.84	239	6.58	289	4.53
40	25.40	90	19.62	140	11.99	190	9.34	240	5.43	290	6.83
41	23.74	91	24.79	141	7.32	191	10.21	241	4.48	291	6.14
42	22.99	92	22.44	142	8.13	192	8.02	242	5.77	292	4.83
43	23.89	93	34.30	143	5.84	193	6.05	243	5.51	293	14.48
44	24.24	94	27.71	144	6.36	194	6.49	244	6.02	294	7.65
45	21.33	95	30.92	145	3.66	195	8.58	245	7.60	295	5.34
46	23.07	96	27.28	146	5.66	196	13.87	246	4.76	296	4.83
47	24.41	97	22.43	147	18.38	197	11.77	247	5.88	297	5.55
48	28.22	98	22.60	148	11.51	198	6.35	248	6.98	298	5.29
49	23.37	99	24.29	149	6.50	199	5.77	249	5.01	299	6.03
50	30.84	100	28.07	150	7.35	200	7.24	250	6.57	300	9.57

Table E.7. Sample 8.

Sample 8					
Lat/Long					
N 37 42.697 W 111 20.797					
#	Diam.(mm)	#	Diam.(mm)	#	Diam.(mm)
1	2.31	35	2.10	69	1.28
2	2.11	36	1.56	70	1.24
3	1.69	37	1.81	71	2.19
4	1.50	38	1.88	72	1.50
5	3.61	39	1.08	73	1.29
6	2.01	40	3.23	74	1.60
7	2.81	41	2.53	75	1.47
8	1.75	42	1.75	76	1.20
9	2.43	43	1.95	77	1.92
10	1.36	44	1.81	78	2.36
11	2.02	45	1.74	79	1.65
12	1.51	46	2.81	80	2.03
13	2.92	47	1.87	81	1.63
14	2.31	48	1.94	82	2.19
15	1.68	49	1.84	83	1.73
16	1.28	50	1.63	84	2.68
17	2.20	51	1.82	85	2.46
18	1.75	52	2.09	86	1.62
19	1.91	53	1.12	87	1.53
20	1.69	54	1.97	88	1.53
21	1.63	55	2.18	89	1.96
22	1.72	56	2.13	90	1.69
23	2.55	57	2.37	91	1.72
24	1.48	58	2.85	92	2.34
25	2.92	59	2.30	93	1.44
26	1.18	60	1.41	94	1.23
27	1.44	61	1.67	95	1.94
28	2.00	62	0.94	96	1.40
29	2.53	63	1.90	97	1.13
30	1.94	64	1.80	98	1.88
31	2.38	65	1.20	99	1.24
32	2.49	66	1.28	100	1.73
33	1.61	67	1.56		
34	2.06	68	1.29		

Table E.8. Sample 9.

Sample 9 (in situ)					
Lat/Long					
N 37 42.697		W			
111 20.797					
#	Diam.(mm)	#	Diam.(mm)	#	Diam.(mm)
1	7.11	35	4.47	69	29.03
2	5.95	36	9.07	70	22.84
3	6.32	37	8.14	71	10.03
4	6.58	38	4.59	72	6.77
5	6.80	39	4.13	73	4.67
6	5.73	40	3.86	74	4.75
7	6.80	41	5.00	75	4.97
8	5.16	42	36.55	76	6.15
9	26.08	43	7.65	77	4.77
10	5.67	44	5.84	78	6.51
11	5.67	45	2.76	79	5.41
12	5.65	46	8.80	80	5.55
13	5.73	47	6.96	81	5.72
14	6.12	48	5.63	82	3.63
15	4.87	49	9.63	83	5.98
16	6.03	50	4.28	84	5.05
17	7.01	51	5.60	85	5.04
18	6.64	52	5.00	86	26.00
19	8.37	53	7.53	87	22.48
20	6.71	54	3.94	88	6.95
21	7.13	55	7.68	89	5.22
22	6.64	56	6.63	90	5.15
23	4.36	57	5.45	91	5.08
24	6.09	58	5.53	92	26.74
25	6.63	59	4.84	93	7.94
26	3.18	60	5.69	94	9.30
27	6.10	61	4.93	95	6.68
28	7.17	62	3.56	96	9.40
29	8.06	63	6.67	97	6.40
30	6.03	64	5.59	98	3.76
31	6.99	65	6.03	99	5.26
32	5.92	66	4.04	100	5.61
33	4.61	67	4.26		
34	5.26	68	6.55		

Table E.9. Sample 10.

Sample 10					
Lat/Long					
N 37 42.706'					
W 111 20.936'					
#	Diam.(mm)	#	Diam.(mm)	#	Diam.(mm)
1	26.91	35	20.71	69	16.95
2	24.77	36	26.17	70	24.98
3	26.60	37	23.70	71	24.41
4	25.67	38	25.35	72	28.32
5	16.75	39	22.85	73	26.40
6	19.83	40	16.67	74	20.22
7	24.61	41	26.23	75	33.65
8	27.33	42	32.36	76	23.54
9	15.59	43	18.38	77	24.38
10	25.77	44	19.98	78	25.19
11	21.93	45	27.01	79	19.21
12	27.14	46	24.95	80	23.20
13	20.72	47	25.82	81	26.24
14	21.56	48	24.91	82	29.12
15	27.59	49	18.43	83	23.36
16	18.64	50	21.52	84	17.78
17	18.70	51	23.09	85	18.68
18	21.61	52	24.17	86	27.06
19	25.92	53	22.94	87	16.72
20	29.61	54	21.75	88	19.51
21	23.46	55	25.89	89	20.91
22	19.90	56	23.15	90	27.26
23	29.16	57	28.16	91	26.41
24	25.40	58	27.01	92	19.98
25	21.86	59	22.41	93	24.00
26	25.78	60	25.78	94	19.45
27	33.72	61	30.52	95	21.62
28	25.88	62	22.83	96	21.16
29	22.54	63	33.03	97	20.51
30	17.20	64	21.49	98	25.12
31	27.54	65	21.65	99	28.20
32	23.25	66	25.05	100	18.24
33	25.77	67	27.92		
34	18.80	68	25.37		

APPENDIX F

NEAREST NEIGHBOR SPACING AND DIAMETER

Nearest neighbor concretion spacing was measured either in the field or from photographs (using Jmicrovision software) by measuring the diameter of the concretion and the distance to its nearest neighbor. Random measurements were made by generating random points in Jmicrovision software using the same number of points as concretions in a given area. Due to the difference in volumetric densities for each reaction front, locations were each analyzed separately. Locations of measurements, actual measurements and comparative random measurements are listed in Tables F.1 (macro concretions) and F.2 (micro concretions). Macro concretions measurements are all measured in field except for Sample 62107 1361. Micro concretions were all measured from photographs except for Sample WP016 6/21/07.

Table F.1. Macro concretions

MACROS (all measurements in cm)						
Sample	62107 1361			WP002 081407MA (measured)		
Latitude	N 37° 42.894'			N 37° 42.971'		
Longitude	W 111°			W 111° 23.598'		
	Measured	Random	Diameter	Measured	Random	Diameter
	1.3	24.9	0.41	56.7	199.7	1
	4.5	24.9	0.27	54.5	198.1	2.6
	9.6	1.1	2.01	29.5	200.2	2.9
	3.8	3.1	0.46	40	1.6	2.4
	7.1	1.2	0.38	40.2	11.9	2.6
	8.4	4.7	0.23	41	2.6	3
	14.3	1.4	0.40	48	7.4	2.9
	2.9	3.0	1.65	42.2	16.6	0.7
	3.0	1.4	0.32	56.5	33.5	2.3
	5.5	1.1	0.30	52	36.3	3.1
	6.9	4.5	0.38	79	34.0	2.4
		1.3	2.38	41	45.4	0.9
		3.0		40.2	57.3	1.2
		2.8		63	45.3	1.2
					69.7	
					38.1	
					36.0	

Table F.1. continued.

MACROS (all measurements in cm)						
Sample	WP020 52807 (measured in field)			WP012 52507 (measured in field)		
Latitude	N 37° 40.805'			N 37° 41.507'		
Longitude	W 111° 22.433'			W 111° 23.876'		
	Measured	Random	Diameter	Measured	Random	Diameter
	33	48.8	2.8	48	62.3	2
	36	19.3	2.3	31.5	64.9	1.5
	51	13.5	1.5	69	9.7	3.6
	10	12.4	1.5	122	11.6	3.5
	14	22.2	1.4	130.5	16.5	3
	20.1	15.0	3.3	160	106.7	3.5
	36.2	11.9	0.5	58	7.9	3
	12.5	19.1	3.3	136	51.9	4
	3	34.4	0.4	57.5	26.6	4.3
	17.7	30.9	0.7	137	15.9	4
	13.6	33.8	1.7			
	28.3	52.8	2.6			
	25.5	35.6	0.9			
	47.7	67.4	2.5			
		62.9				

Table F.2. Micro concretions.

MICROS (all measurements in mm)						
Sample	# WP016 6/21/07 (measured in field)			6192007 1345 (photograph)		
Latitude	N 37° 42.894'			N 37° 42.689'		
Longitude	W 111° 20.841'			W 111° 20.861'		
	Measured	Random	Diameter	Measured	Random	Diameter
	8.79	6.45	1	0.09	58.61	0.96
	5.16	7.39	1.5	4.37	58.41	1.84
	7.81	3.00	0.5	7.93	59.00	1.66
	8.62	14.81	0.5	6.49	2.75	0.96
	2.76	14.95	3	5.18	3.40	1.22
	11.17	2.43	2	2.68	6.29	0.70
	12.39	9.77	1	7.10	3.52	1.22
	6.94	10.51	2	10.31	2.79	1.14
	3.36	10.26	0.5	4.15	5.95	2.01
	11.48	12.63	0.5	6.91	3.94	1.05
	8.54	4.09	1	3.94	5.55	0.96
	6.19	5.64	0.5	9.80	4.58	0.96
	6.96	9.98	0.5	6.69	5.81	1.44
	3.99	1.45	0.5	4.39	7.34	0.79
	6.33	5.36	1	7.60	4.61	1.40
	9.48	4.31	0.5	3.27	3.23	1.83
	4.22	5.12	1	6.29	6.11	1.40
	5.63	4.81	1	9.19	7.57	1.14
	6.21	5.98	2	3.15	3.33	1.75
	5.15	4.23	2	5.16	4.37	0.87
	4.42	6.44	0.5	5.95	5.28	0.70
	8.51	8.18	1	3.88	7.16	0.88
	3.72	4.18	0.5	5.56	6.56	1.48
	7.86	8.96	0.5	4.05	9.04	0.55
	5.13	5.29		9.30	8.47	0.96
						0.81
						1.58

Table F.2. continued.

MICROS (all measurements in mm)						
Sample	6192007 1345 cont.			WP024 6/22/07 (photograph)		
Latitude				N 37° 40.823'		
Longitude				W 111° 22.594'		
	Measured	Random	Diameter	Measured	Random	Diameter
	2.96	4.19	0.79	5.29	1.27	0.84
	3.98	4.33	0.96	3.51	1.56	0.98
	9.44	5.37	0.61	4.83	1.24	1.20
	8.72	1.39	1.75	1.89	1.45	0.85
	4.00	6.05	1.66	6.42	3.66	0.66
	4.69	5.59	1.06	1.79	1.53	0.72
	3.90	2.62	3.81	7.44	2.22	0.90
	3.94	3.92	1.31	4.04	5.78	0.88
	5.94	1.11	0.96	1.91	2.52	1.46
	5.47	3.16	1.05	5.42	5.64	0.80
	3.74	1.27	2.53	2.32	7.07	0.56
	3.71	4.02	3.20	2.67	6.50	0.95
	7.72	2.33	1.23	2.67	6.52	0.92
	7.27	5.23	0.96	4.66	6.91	0.69
	4.34	1.27	1.41	2.61	6.36	1.00
	4.10	2.87	0.87	3.81	6.29	0.74
	2.44	3.27	1.05	3.89	6.04	0.81
	3.32	1.09	0.62	3.67	2.66	0.54
	5.36	1.92	0.61	2.40	1.03	0.64
	5.77	3.86	0.96	4.83	3.14	0.65
	3.23	6.02	0.96	2.48	1.30	0.92
	4.17	2.06	0.52	3.86	2.49	0.81
	7.18	4.60	0.66	3.70	3.47	1.09
	3.93	3.22	0.87	5.44	2.55	1.11
	4.93	4.50	0.89	3.28	3.63	0.57
	8.48	5.17	1.05			0.75
	6.27		0.45			0.52
	5.12		0.35			
	11.11		0.47			
	10.54					
	2.15					
MICROS (all measurements in mm)						
Sample	WP 002 08/14/07 (photograph)			7/18/2007 (photograph)		
Latitude	N 37° 42.971'			N 37° 40.816'		
Longitude	W 111° 23.598'			W 111° 22.566'		
	Measured	Random	Diameter	Measured	Random	Diameter
	4.20	4.12	2.59	2.47	0.61	1.01
	4.17	5.16	6.08	2.48	5.09	1.09
	4.08	4.21	4.15	2.42	0.85	0.78
	5.85	3.53	1.33	4.44	4.05	0.45
	5.17	3.58	5.33	4.22	1.44	1.00
	2.76	3.70	1.10	5.29	3.71	1.76
	5.24	3.56	1.95	4.83	1.65	1.22
	2.84	1.46	1.56	4.35	4.12	1.04
	4.75	2.35	1.68	5.05	4.31	1.24
	2.39	4.39	1.86	5.18	4.25	0.91
	5.48	1.30	1.04	4.58	2.58	0.93
	2.63	2.19	1.64	2.98	5.36	1.28
	3.46	4.46	2.14	2.78	1.82	1.43
	4.72	7.84	1.44	3.00	3.57	1.43
	8.30	2.33	5.95	2.78	1.48	1.12
	3.57	5.06	1.00	2.55	3.14	0.77
	7.15	2.42	1.73	3.04	2.25	0.85
	2.59	2.88	1.29	3.47	1.96	1.02
	5.96	3.91	1.16	8.69	3.00	1.24
	2.55	2.92	2.57	2.07	3.16	0.38
	3.36			1.61	2.98	0.69
				1.94	9.30	0.94
				2.04	6.63	0.85
				6.74	3.49	0.83
				5.64	3.59	1.13

Table F.2. coninued

MICROS (all measurements in mm)						
Sample	8150037 (photograph)			WP 004 08/17/07 (photograph)		
Latitude	N 37° 42.064'			N 37° 41.728'		
Longitude	W 111° 23.863'			W 111° 22.630'		
	Measured	Random	Diameter	Measured	Random	Diameter
	11.58	3.33	1.38	3.54	8.21	0.99
	10.16	11.60	1.85	6.98	0.88	1.06
	9.81	3.07	1.25	3.79	4.80	1.89
	3.62	5.57	1.67	8.55	0.92	1.77
	14.36	6.72	1.33	4.19	3.79	2.01
	5.25	5.40	2.01	4.16	3.78	2.10
	6.53	7.90	1.77	4.44	3.89	2.56
	5.74	8.70	2.06	7.70	4.58	1.77
	6.59	8.09	1.95	8.24	2.92	2.19
	11.23	5.04	1.61	7.12	2.94	1.59
	6.35	4.46	1.45	1.28	12.28	1.83
	13.83	4.91	1.69	1.11	12.44	1.70
	6.49	5.02	1.27			
	13.62	10.94	0.99			
	6.52	11.26	1.14			
	12.46	10.65	1.47			
	6.98	9.10	1.04			
	6.54	9.73	1.38			
	9.29	5.47	1.54			
	13.23	5.67	1.41			
	9.11	5.86	1.67			
	13.59	5.87	2.23			
	10.45	7.50	1.74			
	10.76	22.07	1.02			
		6.37	0.71			
		6.20	2.05			
MICROS (all measurements in mm)						
Sample	52507_181 (photograph)			805_95 (photograph)		
Latitude	N 37° 41.718'			N 37° 42.213'		
Longitude	W 111° 22.336'			W 111° 23.981'		
	Measured	Random	Diameter	Measured	Random	Diameter
	5.00	37.30	0.60	2.56	4.56	0.71
	7.15	38.00	0.73	1.12	2.06	0.78
	13.27	37.57	0.78	3.14	1.01	0.18
	4.87	2.59	0.97	2.66	1.93	0.31
	9.71	2.56	0.92	2.16	0.65	0.65
	7.40	2.51	0.82	3.55	1.37	0.51
	11.10	2.53	0.97	1.28	0.71	0.82
	1.85	3.06	0.82	1.02	3.33	0.62
	4.62	2.78	0.82	3.77	2.93	0.31
	3.57	3.12	0.51	2.70	1.45	0.24
	2.42	2.69	1.03	2.06	1.47	0.41
	1.64	4.15	0.92	0.97	1.34	0.22
	6.00	5.94	0.72	1.27	0.78	0.17
	9.94	3.00	1.23	0.92	1.71	0.34
		2.23	0.72	2.95	1.61	0.34
		2.72		2.10	1.66	0.78
		2.23				
		5.67				

Table F.2. continued

MICROS (all measurements in mm)						
Sample	805_95 cont.			6_19_20_07_1349 (photograph)		
Latitude				N 37° 42.689'		
Longitude				W 111° 20.861'		
	Measured	Random	Diameter	Measured	Random	Diameter
	6.00	3.81	0.44	52.33	15.60	8.36
	6.55	1.04	0.58	69.87	22.53	2.14
	3.46	3.63	0.46	17.70	15.63	6.41
	1.49	0.89	0.40	8.45	38.13	3.19
	1.28	3.05	0.51	23.81	34.87	3.18
	3.32	3.04	0.61	33.57	2.86	2.14
	4.68	3.18	0.52	24.32	31.21	3.81
	2.29	2.95	0.71	48.29	2.44	1.67
	3.52	4.29	0.51	43.05	33.46	4.91
	4.98	1.19	0.48	16.46	31.33	7.86
	4.36	1.94	0.51	17.85	21.54	9.52
	4.04	1.24	0.34	47.73	25.90	4.05
	2.43	2.20	0.68	33.03	21.34	8.42
	4.45	0.97	0.31	13.64	21.91	9.30
	1.36	7.70	0.22	58.80	22.81	9.33
	5.49	0.91	0.36	17.54	20.85	4.53
					35.30	2.87

APPENDIX G

WHOLE ROCK ANALYSIS OF OXIDES AND TRACE ELEMENTS

Whole rock analysis was performed by ALS Chemex in Sparks, NV. Oxides are listed first, then trace elements. Trace elements are organized by metals/transition metals, metalloids and rare earth elements and tables list rinds normalized to interiors followed by concretions normalized to host rock. Elements that were not present or present in undetectable amounts are not listed. Locations of samples are listed in Appendix A.

Table G.1. Oxides: rind normalized to interior

SAMPLE	Recvd Wt.	SiO ₂	Al ₂ O ₃	Fe ₂ O ₃	CaO	MgO	Na ₂ O	K ₂ O	TiO ₂	MnO	P ₂ O ₅
	kg	%	%	%	%	%	%	%	%	%	%
UT07-RB-1JN.001rind	<0.02	64.00	2.02	25.20	0.10	0.17	0.04	0.94	0.05	0.70	0.11
UT07-RB-1JN.002rind	<0.02	66.40	2.06	23.60	0.07	0.15	0.04	1.04	0.07	0.28	0.08
UT07-RB-1JN.003rind	<0.02	63.20	1.74	28.70	0.11	0.13	0.04	0.91	0.04	0.46	0.10
UT07-SF-20JN.001rind	0.06	66.40	2.01	23.20	0.06	0.13	0.04	1.05	0.06	0.36	0.10
UT07-SF-20JN.002rind	0.02	64.30	1.50	27.20	0.09	0.12	0.04	0.84	0.03	0.30	0.03
UT07-SF-20JN.003rind	<0.02	66.80	1.56	26.10	0.07	0.11	0.04	0.82	0.03	0.46	0.08
average rind		65.18	1.82	25.67	0.08	0.14	0.04	0.93	0.05	0.43	0.08
UT07-RB-1JN.001int	<0.02	92.20	2.43	3.05	0.04	0.08	0.05	1.29	0.04	0.05	0.03
UT07-RB-1JN.002int	<0.02	94.20	2.54	0.80	0.03	0.08	0.06	1.50	0.06	0.01	0.03
UT07-RB-1JN.003int	<0.02	92.20	2.12	1.62	0.03	0.07	0.05	1.33	0.04	0.02	0.02
UT07-SF-20JN.001int	<0.02	94.40	2.85	0.70	0.03	0.10	0.06	1.59	0.09	0.01	0.01
UT07-SF-20JN.002int	<0.02	94.30	1.90	1.44	0.04	0.07	0.05	1.13	0.03	0.02	0.01
UT07-SF-20JN.003int	<0.02	95.50	1.88	0.79	0.02	0.07	0.05	1.16	0.03	0.01	0.01
average interior		93.80	2.29	1.40	0.03	0.08	0.05	1.33	0.05	0.02	0.02
normalized rind/ interior		0.69	0.79	18.33	2.63	1.72	0.75	0.70	0.97	21.33	4.55

Table G.1. continued.

SAMPLE	BaO	C	S	SAMPLE	BaO	C	S
	%	%	%		%	%	%
UT07-RB-1JN.001rind	0.08	0.08	0.04	UT07-RB-1JN.001int	0.03	0.08	0.02
UT07-RB-1JN.002rind	0.03	0.09	0.02	UT07-RB-1JN.002int	0.03	0.02	0.01
UT07-RB-1JN.003rind	0.03	0.10	0.03	UT07-RB-1JN.003int	0.03	0.06	0.01
UT07-SF-20JN.001rind	0.05	0.07	0.01	UT07-SF-20JN.001int	0.03	0.01	0.01
UT07-SF-20JN.002rind	0.02	0.08	0.02	UT07-SF-20JN.002int	0.03	0.04	0.01
UT07-SF-20JN.003rind	0.04	0.08	0.02	UT07-SF-20JN.003int	0.03	0.03	0.01
average rind	0.04	0.08	0.02	average interior	0.03	0.04	0.01
				normalized rind/ interior	1.39	2.08	2.00

Table G.2. Metals/ Transition Metals: rind normalized to interior

SAMPLE	Rb	Cs	Sr	Ba	V	Cr	Co	Ni	Cu
	ppm	ppm	ppm	ppm	ppm	ppm	ppm	ppm	ppm
UT07-RB-1JN.001rind	27.70	1.01	59.80	789.00	108.00	10.00	178.50	253.00	27.00
UT07-RB-1JN.002rind	27.90	1.01	37.70	279.00	95.00	10.00	124.00	191.00	14.00
UT07-RB-1JN.003rind	23.00	0.77	40.00	280.00	100.00	10.00	129.00	192.00	24.00
UT07-SF-20JN.001rind	28.00	0.96	41.80	420.00	122.00	20.00	127.00	175.00	17.00
UT07-SF-20JN.002rind	19.60	0.68	32.60	197.50	108.00	10.00	151.50	109.00	11.00
UT07-SF-20JN.003rind	21.70	0.78	31.70	356.00	100.00	10.00	99.40	135.00	15.00
average rind	24.65	0.87	40.60	386.92	105.50	11.67	134.90	175.83	18.00
UT07-RB-1JN.001int	33.70	0.95	38.60	292.00	13.00	60.00	12.40	21.00	15.00
UT07-RB-1JN.002int	38.20	1.10	37.90	272.00	5.00	70.00	0.80	5.00	13.00
UT07-RB-1JN.003int	33.80	0.93	40.00	255.00	8.00	60.00	3.30	8.00	19.00
UT07-SF-20JN.001int	42.40	1.31	48.40	292.00	9.00	70.00	1.90	6.00	12.00
UT07-SF-20JN.002int	29.00	0.89	38.30	230.00	10.00	50.00	4.00	9.00	24.00
UT07-SF-20JN.003int	30.50	1.02	40.10	231.00	6.00	40.00	1.30	6.00	19.00
average interior	34.60	1.03	40.55	262.00	8.50	58.33	3.95	9.17	17.00
normalized rind/ interior	0.71	0.84	1.00	1.48	12.41	0.20	34.15	19.18	1.06
SAMPLE	Zn	Y	Zr	Nb	La	Hf	Ta	W	Hg
	ppm	ppm	ppm	ppm	ppm	ppm	ppm	ppm	ppm
UT07-RB-1JN.001rind	793.00	10.30	65.00	1.10	8.40	1.90	0.10	8.00	0.03
UT07-RB-1JN.002rind	564.00	10.00	91.00	1.50	5.50	2.50	0.10	4.00	0.04
UT07-RB-1JN.003rind	630.00	9.90	39.00	0.90	4.90	1.00	0.10	6.00	0.05
UT07-SF-20JN.001rind	687.00	8.50	91.00	1.20	5.80	2.60	0.10	5.00	0.06
UT07-SF-20JN.002rind	783.00	15.40	37.00	0.60	5.40	1.00	<0.1	10.00	0.02
UT07-SF-20JN.003rind	562.00	16.70	29.00	0.70	5.00	0.80	0.10	5.00	0.18
average rind	669.83	11.80	58.67	1.00	5.83	1.63	0.10	6.33	0.06
UT07-RB-1JN.001int	61.00	2.60	47.00	1.00	3.20	1.30	0.10	1.00	0.06
UT07-RB-1JN.002int	17.00	2.80	84.00	1.20	3.40	2.30	0.10	1.00	0.02
UT07-RB-1JN.003int	50.00	2.30	63.00	1.10	3.20	1.70	0.10	1.00	0.03
UT07-SF-20JN.001int	20.00	3.30	150.00	1.60	3.90	4.10	0.10	1.00	0.01
UT07-SF-20JN.002int	52.00	2.20	32.00	0.70	2.60	0.90	0.10	2.00	0.03
UT07-SF-20JN.003int	26.00	2.30	36.00	0.80	3.60	1.00	0.10	1.00	0.02
average interior	37.67	2.58	68.67	1.07	3.32	1.88	0.10	1.17	0.03
normalized rind/ interior	17.78	4.57	0.85	0.94	1.76	0.87	1.00	5.43	2.42

Table G.3. Metalloids: rind normalized to interior

SAMPLE	Ga	As	Se	Sn	Sb	Te	Pb	Bi
	ppm	ppm	ppm	ppm	ppm	ppm	ppm	ppm
UT07-RB-1JN.001rind	4.20	27.10	0.60	1.00	0.37	0.05	30.00	0.28
UT07-RB-1JN.002rind	3.30	48.20	3.10	1.00	0.39	0.03	31.00	0.51
UT07-RB-1JN.003rind	3.00	59.90	5.00	1.00	0.51	0.06	39.00	0.32
UT07-SF-20JN.001rind	3.20	85.80	3.60	1.00	0.37	0.06	20.00	0.13
UT07-SF-20JN.002rind	2.40	111.00	3.10	1.00	0.40	0.04	64.00	0.18
UT07-SF-20JN.003rind	2.70	65.80	2.80	1.00	0.33	0.02	32.00	0.11
average rind	3.13	66.30	3.03	1.00	0.40	0.04	36.00	0.26
UT07-RB-1JN.001int	2.50	6.00	0.40	1.00	0.22	0.01	11.00	0.08
UT07-RB-1JN.002int	2.50	4.60	<0.2	1.00	0.21	0.01	15.00	0.07
UT07-RB-1JN.003int	2.30	2.20	<0.2	1.00	0.22	<0.01	9.00	0.04
UT07-SF-20JN.001int	2.90	3.80	<0.2	<1	0.16	<0.01	14.00	0.06
UT07-SF-20JN.002int	2.20	3.20	<0.2	1.00	0.14	<0.01	10.00	0.03
UT07-SF-20JN.003int	2.20	4.90	<0.2	<1	0.21	<0.01	16.00	0.07
average interior	2.43	4.12	0.40	1.00	0.19	0.01	12.50	0.06
normalized rind/ interior	1.29	16.11	7.58	1.00	2.04	4.33	2.88	4.37

Table G.4. Rare Earth Elements: rind normalized to interior

SAMPLE	Ce	Pr	Nd	Sm	Eu	Gd	Tb	Dy	Ho	Er	Tm	Yb	Lu	Th	U
	ppm	ppm	ppm	ppm	ppm	ppm	ppm	ppm	ppm	ppm	ppm	ppm	ppm	ppm	ppm
UT07-RB-1JN.001rind	15.20	2.68	10.00	2.23	0.53	1.90	0.37	1.97	0.41	1.03	0.15	0.86	0.13	1.31	2.24
UT07-RB-1JN.002rind	9.50	1.78	6.90	1.61	0.62	1.59	0.30	1.71	0.35	0.89	0.12	0.71	0.12	1.28	1.80
UT07-RB-1JN.003rind	9.30	1.62	6.10	1.43	0.45	1.48	0.28	1.61	0.35	0.91	0.12	0.72	0.11	1.20	1.19
UT07-SF-20JN.001rind	9.10	1.76	7.10	1.56	0.48	1.55	0.26	1.52	0.32	0.83	0.11	0.69	0.10	1.48	0.89
UT07-SF-20JN.002rind	9.50	1.73	6.80	1.44	0.31	1.67	0.35	2.17	0.46	1.20	0.15	0.75	0.12	0.81	2.49
UT07-SF-20JN.003rind	14.10	2.09	8.20	2.02	0.64	2.12	0.43	2.50	0.53	1.39	0.18	0.98	0.15	0.86	1.12
average rind	11.12	1.94	7.52	1.72	0.51	1.72	0.33	1.91	0.40	1.04	0.14	0.79	0.12	1.16	1.62
UT07-RB-1JN.001int	6.00	0.70	2.40	0.43	0.20	0.41	0.07	0.42	0.09	0.27	0.05	0.31	0.05	0.74	0.37
UT07-RB-1JN.002int	6.00	0.66	2.10	0.38	0.16	0.37	0.07	0.43	0.09	0.32	0.05	0.38	0.06	0.83	0.35
UT07-RB-1JN.003int	5.80	0.64	2.10	0.32	0.12	0.37	0.05	0.36	0.08	0.25	0.04	0.29	0.05	0.71	0.31
UT07-SF-20JN.001int	6.80	0.73	2.40	0.41	0.21	0.42	0.07	0.45	0.12	0.37	0.06	0.44	0.08	0.87	0.46
UT07-SF-20JN.002int	4.60	0.53	1.80	0.31	0.17	0.33	0.06	0.31	0.07	0.23	0.04	0.26	0.03	0.58	0.28
UT07-SF-20JN.003int	5.90	0.66	2.30	0.33	0.15	0.37	0.06	0.32	0.08	0.22	0.03	0.23	0.04	0.59	0.27
average interior	5.85	0.65	2.18	0.36	0.17	0.38	0.06	0.38	0.09	0.28	0.05	0.32	0.05	0.72	0.34
normalized rind/ interior	1.90	2.97	3.44	4.72	3.00	4.54	5.24	5.01	4.57	3.77	3.07	2.47	2.35	1.61	4.77

Table G.5. Oxides: concretions normalized to host rock

ELEMENT	Recvd Wt.	SiO ₂	Al ₂ O ₃	Fe ₂ O ₃	CaOMgO		Na ₂ O	K ₂ O	Cr ₂ O ₃	TiO ₂	MnO	P ₂ O ₅	BaO	C
HOST ROCK	kg	%	%	%	%	%	%	%	%	%	%	%	%	%
UT07-HW-1Jn.002	0.05	94.2	2.43	1.2	0.02	0.07	0.05	1.26	0.1	0.06	0.01	<0.01	0.03	0.3
UT07-HW-1Jn.003	0.07	92.5	2.36	0.73	0.02	0.07	0.05	1.26	0.07	0.05	<0.01	<0.01	0.03	0.18
UT07-HW-1Jn.004	0.02	92.9	2.61	0.74	0.01	0.08	0.05	1.42	0.06	0.07	0.01	<0.01	0.03	0.25
UT07-HW-1Jn.005	0.04	93.8	2.48	0.89	0.02	0.07	0.05	1.3	0.09	0.06	0.01	<0.01	0.03	0.22
UT07-HW-1Jn.006	0.04	92.7	2.52	0.82	0.02	0.07	0.05	1.29	0.08	0.07	0.01	<0.01	0.03	0.24
UT07-HW-2Jn.002	0.1	92.8	2.77	1.72	0.07	0.09	0.06	1.4	<0.01	0.06	0.01	0.03	0.03	0.06
UT07-HW-2Jn.003	0.06	92.6	2.61	0.79	0.03	0.08	0.05	1.32	0.08	0.05	<0.01	0.01	0.03	0.06
UT07-HW-2Jn.004	0.05	92.4	2.79	0.82	0.03	0.09	0.05	1.38	0.08	0.05	<0.01	0.02	0.03	0.11
UT07-HW-2Jn.005	0.02	92.5	2.66	0.85	0.03	0.08	0.05	1.26	0.09	0.06	<0.01	0.01	0.02	0.05
UT07-HW-2Jn.007	0.08	92.5	2.61	0.64	0.03	0.08	0.05	1.35	0.06	0.05	<0.01	0.02	0.03	0.01
UT07-SF17Jn.002	0.02	92.9	2.15	1.03	0.02	0.06	0.04	1.12	0.12	0.05	0.01	0.01	0.02	0.11
UT07-SF17Jn.003	0.05	95	2.25	0.57	0.01	0.06	0.05	1.18	0.06	0.06	<0.01	<0.01	0.02	0.05
UT07-SF17Jn.004	0.04	93.8	2.22	0.64	0.01	0.06	0.04	1.16	0.07	0.06	0.01	0.02	0.02	0.06
UT07-SF17Jn.005	0.03	95.6	2.1	0.59	0.02	0.06	0.03	1.14	0.06	0.05	<0.01	<0.01	0.02	0.12
UT07-SF17Jn.006	0.04	94.3	2.16	0.65	0.01	0.06	0.04	1.14	0.07	0.06	<0.01	<0.01	0.02	0.09
UT07-SF17Jn.007	0.03	94.5	2.45	0.78	0.02	0.07	0.05	1.31	0.07	0.05	0.01	0.01	0.03	0.17
UT07-SF18Jn.002	0.02	93	2.9	0.83	0.03	0.09	0.05	1.37	0.09	0.08	0.01	0.03	0.03	0.06
UT07-SF18Jn.003	0.05	92.3	2.8	0.62	0.03	0.08	0.05	1.34	0.06	0.08	0.01	<0.01	0.03	0.13
UT07-SF18Jn.004	0.02	92.7	2.83	0.48	0.03	0.08	0.05	1.37	0.04	0.08	0.01	0.02	0.03	0.03
UT07-SF18Jn.005	0.02	92.9	2.83	0.46	0.03	0.08	0.05	1.38	0.03	0.08	0.01	0.02	0.03	0.03
UT07-SF18Jn.006	0.02	92.9	2.84	0.47	0.03	0.09	0.05	1.36	0.04	0.08	0.01	0.01	0.03	0.05
UT07-SF18Jn.007	0.03	92.3	2.83	0.51	0.03	0.09	0.05	1.37	0.04	0.08	0.01	0.02	0.03	0.09
UT07-SF11Jn.002	0.05	92	2.68	0.89	0.02	0.1	0.05	1.46	0.08	0.04	<0.01	0.01	0.03	0.19
UT07-SF11Jn.003	0.05	91.6	3	0.65	0.03	0.11	0.06	1.63	0.05	0.05	<0.01	<0.01	0.03	0.15
UT07-SF11Jn.004	0.02	91.9	3.06	0.52	0.03	0.11	0.06	1.69	0.03	0.07	<0.01	0.03	0.03	0.06
UT07-SF11Jn.005	0.05	95.1	2.37	0.59	0.03	0.09	0.05	1.31	0.05	0.03	<0.01	0.04	0.02	0.1
UT07-SF11Jn.006	0.1	91.9	2.91	0.61	0.03	0.11	0.05	1.55	0.05	0.05	<0.01	0.02	0.03	0.13
UT07-SF-13Jn.003	0.03	93.6	1.94	0.71	0.01	0.07	0.04	1	0.05	0.03	0.01	0.01	0.02	0.04
UT07-SF-13Jn.004	0.02	93.5	1.98	1.23	0.01	0.07	0.04	1.1	0.13	0.03	0.01	0.02	0.02	0.31
UT07-SF-13Jn.005	0.03	94.2	1.59	0.6	0.02	0.06	0.03	0.86	0.04	0.03	0.05	<0.01	0.02	0.16
UT07-SF-13Jn.006	0.02	94.5	1.74	0.68	0.02	0.07	0.03	0.84	0.07	0.03	0.01	0.02	0.02	0.12
UT07-Sf-13Jn.007	0.02	95.8	1.68	0.65	0.01	0.06	0.03	0.81	0.07	0.03	0.01	<0.01	0.02	0.03
average host rock	0.0403125	93.3	2.47	0.75	0.02	0.08	0.05	1.27	0.07	0.06	0.01	0.02	0.03	0.12
	Recvd Wt.	SiO ₂	Al ₂ O ₃	Fe ₂ O ₃	CaOMgO		Na ₂ O	K ₂ O	Cr ₂ O ₃	TiO ₂	MnO	P ₂ O ₅	BaO	C
CONCRETIONS	kg	%	%	%	%	%	%	%	%	%	%	%	%	%
UT07-HW-1Jn.001	0.04	82	2.22	11.7	0.05	0.1	0.06	1.14	0.05	0.07	0.17	0.06	0.03	0.15
UT07-HW-2Jn.001	0.46	84.5	2.65	8.17	0.05	0.12	0.05	1.36	<0.01	0.05	0.13	0.07	0.03	0.1
UT07-HW-2Jn.006	0.13	85.6	2.45	7.97	0.04	0.13	0.05	1.22	0.02	0.05	0.09	0.07	0.02	0.06
UT07-SF17Jn.001	0.03	80.9	2.18	10.6	0.02	0.08	0.05	1.2	0.06	0.04	0.37	0.08	0.05	0.1
UT07-SF18Jn.001	0.02	89.4	2.59	3.37	0.04	0.09	0.05	1.3	0.05	0.08	0.14	0.05	0.03	0.15
UT07-SF11Jn.001	0.02	85	2.2	9.03	0.04	0.1	0.05	1.24	0.06	0.03	0.08	<0.01	0.02	0.18
UT07-SF-13Jn.001	0.07	79.1	1.8	13.2	0.02	0.08	0.03	0.92	0.03	0.05	0.36	0.04	0.05	0.1
average concretion	0.11	83.8	2.3	9.14	0.04	0.1	0.05	1.2	0.05	0.05	0.19	0.06	0.03	0.12
concretion/host rock	2.7286822	0.9	0.93	12.2	1.56	1.27	1.04	0.94	0.67	0.95	15.8	3.25	1.25	1.02

Table G.6. Metals/Transition Metals: Concretions normalized to host rock

ELEMENT	Rb	Cs	Sr	Ba	V	Cr	Co	Ni	Cu	Zn	Y	Zr	Nb	La	Hf	W	Hg
HOST ROCK	ppm	ppm	ppm	ppm	ppm	ppm	ppm	ppm	ppm	ppm	ppm	ppm	ppm	ppm	ppm	ppm	ppm
UT07-HW-1Jn.002	33.5	1.05	27.6	233	<5	690	2.8	12	6	17	2.5	82	1.1	3	1.9	2	0.02
UT07-HW-1Jn.003	33.6	1.01	27.5	226	<5	470	1.2	8	5	12	2.2	68	1.1	2.9	1.6	2	0.01
UT07-HW-1Jn.004	37.5	1.12	29.2	251	<5	410	1.3	7	5	14	2.7	83	1.2	3	1.9	2	0.02
UT07-HW-1Jn.005	34.2	1.05	27	233	<5	600	1.4	9	6	12	2.3	82	1.1	2.7	1.9	2	0.01
UT07-HW-1Jn.006	34.6	1.14	29.4	238	12	540	1.2	9	6	5	2.5	94	1.3	2.9	2.3	2	0.01
UT07-HW-2Jn.002	34.5	1.22	29.7	242	12	10	1	6	9	6	3.2	65	1.4	3.5	1.6	2	0.01
UT07-HW-2Jn.003	33.4	1.14	28.5	230	12	450	1	7	5	<5	2.9	50	1	3.6	1.3	2	<0.
UT07-HW-2Jn.004	36.1	1.27	30.9	250	14	490	1.1	8	6	7	3.3	54	1.1	3.3	1.4	1	0.01
UT07-HW-2Jn.005	32.3	1.19	28.6	222	14	550	1.2	9	5	6	3.2	64	1.2	3.8	1.6	2	0.01
UT07-HW-2Jn.007	34.1	1.19	29.2	238	13	350	0.9	6	5	<5	3	45	0.9	2.9	1.1	2	0.01
UT07-SF17Jn.002	28.9	0.95	26.6	209	10	720	1.5	10	5	<5	2.5	79	1.1	2.8	2	2	0.01
UT07-SF17Jn.003	29.1	0.95	27.1	211	9	370	0.9	7	5	5	2.7	83	1.1	3.9	2	2	0.01
UT07-SF17Jn.004	30.1	0.97	27.5	209	10	420	1	7	5	<5	2.7	87	1.1	2.8	2.2	1	0.01
UT07-SF17Jn.005	28.3	0.91	26	205	7	370	0.8	5	<5	<5	2.4	84	1	2.5	2.1	1	0.01
UT07-SF17Jn.006	29.2	0.95	27	212	11	440	1	6	<5	<5	2.6	84	1.1	2.9	2.1	1	0.01
UT07-SF17Jn.007	33.2	1.08	29.5	233	11	430	1	7	5	<5	2.6	73	1.1	3	1.8	2	0.01
UT07-SF18Jn.002	35.2	1.29	32.5	247	23	550	1.4	10	12	8	3.9	122	1.6	3.7	3	4	0.02
UT07-SF18Jn.003	35.3	1.28	32.7	249	19	410	1.2	8	10	8	3.9	120	1.6	3.8	2.9	3	0.01
UT07-SF18Jn.004	34.2	1.22	31.6	245	16	260	1	5	10	6	3.8	123	1.4	4.3	3.1	3	0.01
UT07-SF18Jn.005	35.9	1.34	32.4	255	18	200	1.2	5	10	9	3.7	123	1.5	3.5	3.1	3	0.01
UT07-SF18Jn.006	35.7	1.28	32.6	251	16	250	0.9	6	12	8	4	121	1.5	8.2	3	2	0.02
UT07-SF18Jn.007	35.7	1.31	32.8	250	19	270	1	6	10	9	3.9	128	1.8	3.6	3.2	3	0.01
UT07-SF11Jn.002	37.5	1.26	35.6	261	9	570	1.5	8	6	6	2.8	30	0.9	5.5	0.8	1	0.01
UT07-SF11Jn.003	40.9	1.38	37.5	278	8	320	1.1	7	5	6	3.3	33	1	3.5	0.9	1	0.01
UT07-SF11Jn.004	42.8	1.48	40.2	288	6	180	1	5	5	5	3.7	57	1.3	4	1.5	1	0.01
UT07-SF11Jn.005	29.7	0.99	28.5	212	7	310	0.9	6	5	<5	2.2	24	0.7	2.5	0.7	1	0.01
UT07-SF11Jn.006	39.3	1.33	36.7	267	8	310	1	7	5	5	3	38	1	3.8	1	1	0.01
UT07-SF-13Jn.003	26.3	0.95	25.6	199	8	320	2.1	7	5	11	2.5	26	0.6	2.5	0.7	1	0.01
UT07-SF-13Jn.004	28.1	0.88	26.1	213	<5	790	2	13	6	8	2.5	25	0.7	3.6	0.7	1	0.02
UT07-SF-13Jn.005	21.6	0.64	21.6	182	<5	280	2.3	5	<5	12	1.9	30	0.6	2.1	0.7	4	0.01
UT07-SF-13Jn.006	21.7	0.78	21.8	163	<5	540	1.1	6	<5	6	2	31	0.6	2.2	0.8	2	0.01
UT07-Sf-13Jn.007	20.8	0.77	19.9	160	<5	520	1.5	6	5	6	2	28	0.6	5.7	0.7	10	0.01
average host rock	32.6	1.11	29.4	230	12.2	418	1.27	7.28	6.57	8.21	2.89	69.9	1.1	3.5	1.74	2.16	0.01
	Rb	Cs	Sr	Ba	V	Cr	Co	Ni	Cu	Zn	Y	Zr	Nb	La	Hf	W	Hg
CONCRETIONS	ppm	ppm	ppm	ppm	ppm	ppm	ppm	ppm	ppm	ppm	ppm	ppm	ppm	ppm	ppm	ppm	ppm
UT07-HW-1Jn.001	30.4	1.16	32.8	286	68	370	63.8	42	7	262	10.5	90	1.2	3.7	2.1	7	0.06
UT07-HW-2Jn.001	33.9	1.33	33.5	237	301	10	24.6	45	62	172	7.1	62	1.2	3.6	1.4	19	0.04
UT07-HW-2Jn.006	31	1.41	32.6	214	412	10	20.3	40	85	165	6.8	58	1	3.5	1.3	32	0.06
UT07-SF17Jn.001	31.4	1.05	43.5	432	130	360	45.8	63	11	227	7.4	48	0.9	5.2	1.2	27	0.06
UT07-SF18Jn.001	29.2	1.11	28.1	256	189	290	5.1	22	100	61	4.2	98	1.2	3.1	2.4	26	0.06
UT07-SF11Jn.001	31.4	1.05	52.3	226	42	380	23.3	46	9	207	6.2	27	0.7	3.5	0.7	2	0.02
UT07-SF-13Jn.001	22.8	0.92	35.1	405	48	220	84	87	8	408	8.9	54	1	5.3	1.5	4	0.11
average concretion	30	1.15	36.8	294	170	234	38.1	49.3	40.3	215	7.3	62.4	1.03	3.99	1.51	16.7	0.06
concretion/host rock	0.92	1.04	1.26	1.28	14	0.56	30.1	6.77	6.13	26.1	2.53	0.89	0.93	1.14	0.87	7.75	5.97

Table G.7. Metalloids: concretions normalized to host rock

ELEMENT	Ga	As	Se	Sb	Te	Pb	Bi
HOST ROCK	ppm	ppm	ppm	ppm	ppm	ppm	ppm
UT07-HW-1Jn.002	2.8	4.2	0.3	0.08	0.01	7	0.02
UT07-HW-1Jn.003	2.6	2.9	0.2	0.05	0.01	6	0.01
UT07-HW-1Jn.004	2.8	3	0.3	0.05	0.01	7	0.02
UT07-HW-1Jn.005	2.7	2.3	0.2	0.06	0.01	6	0.02
UT07-HW-1Jn.006	2.8	3.9	0.3	0.15	0.01	5	0.01
UT07-HW-2Jn.002	3.1	3.6	0.3	0.14	0.01	8	0.03
UT07-HW-2Jn.003	2.9	3.3	<0.2	0.1	0.01	6	0.02
UT07-HW-2Jn.004	3.1	1.9	<0.2	0.08	0.01	6	0.02
UT07-HW-2Jn.005	3	2.6	<0.2	0.09	<0.01	6	0.02
UT07-HW-2Jn.007	2.9	2.5	<0.2	0.06	0.01	6	0.02
UT07-SF17Jn.002	2.3	1.5	<0.2	0.09	0.01	5	0.02
UT07-SF17Jn.003	2.3	0.8	<0.2	0.05	0.01	5	0.02
UT07-SF17Jn.004	2.3	1.3	<0.2	0.06	0.01	5	0.01
UT07-SF17Jn.005	2.2	0.9	<0.2	0.05	<0.01	5	0.02
UT07-SF17Jn.006	2.2	0.9	<0.2	0.06	<0.01	5	0.02
UT07-SF17Jn.007	2.5	1.2	<0.2	0.08	0.01	6	0.03
UT07-SF18Jn.002	3.2	9.1	<0.2	0.11	0.04	6	0.03
UT07-SF18Jn.003	3	7.3	<0.2	0.09	0.01	6	0.02
UT07-SF18Jn.004	2.9	6.1	<0.2	0.06	0.02	6	0.01
UT07-SF18Jn.005	2.9	32.8	<0.2	0.28	0.02	6	0.01
UT07-SF18Jn.006	3	5.3	<0.2	0.05	0.02	6	0.01
UT07-SF18Jn.007	3.1	6.1	<0.2	0.1	0.01	6	0.02
UT07-SF11Jn.002	3	5.5	<0.2	0.06	<0.01	6	0.01
UT07-SF11Jn.003	3.1	6.1	<0.2	0.05	<0.01	6	0.03
UT07-SF11Jn.004	3.3	6.5	<0.2	<0.05	<0.01	6	0.01
UT07-SF11Jn.005	2.4	4.2	<0.2	<0.05	<0.01	5	0.01
UT07-SF11Jn.006	3.1	4.3	<0.2	0.06	<0.01	6	0.01
UT07-SF-13Jn.003	2.3	3.6	<0.2	0.05	<0.01	<5	0.02
UT07-SF-13Jn.004	2.3	2.9	<0.2	0.09	0.01	5	0.01
UT07-SF-13Jn.005	1.8	1.9	<0.2	<0.05	0.01	<5	0.01
UT07-SF-13Jn.006	2	2.3	<0.2	0.05	0.01	<5	0.02
UT07-Sf-13Jn.007	1.9	3.8	<0.2	0.05	<0.01	<5	0.01
average host rock	2.68125	4.52	0.27	0.08	0.01	5.86	0.02
	Ga	As	Se	Sb	Te	Pb	Bi
CONCRETIONS	ppm	ppm	ppm	ppm	ppm	ppm	ppm
UT07-HW-1Jn.001	2.8	59.6	1.9	0.41	0.01	35	0.02
UT07-HW-2Jn.001	4.6	100	42.9	0.51	0.02	12	0.03
UT07-HW-2Jn.006	5.1	140	34.7	0.58	0.02	12	0.04
UT07-SF17Jn.001	3.5	66.2	1.2	0.55	0.17	16	0.17
UT07-SF18Jn.001	3.7	111	0.7	0.48	0.05	6	0.02
UT07-SF11Jn.001	3	113	0.2	0.13	0.02	13	0.02
UT07-SF-13Jn.001	2.6	41.6	0.9	0.19	0.03	26	0.02
average concretion	3.6142857	90.1	11.8	0.41	0.05	17.1	0.05
normalized concretion/host	1.3479853	19.9	44.2	5.02	3.59	2.93	2.66

Table G.8. Rare Earth Elements: concretions normalized to host rock

ELEMENT	Ce	Pr	Nd	Sm	Eu	Gd	Tb	Dy	Ho	Er	Tm	Yb	Lu	Th	U
HOST ROCK	ppm	ppm	ppm	ppm	ppm	ppm	ppm	ppm	ppm	ppm	ppm	ppm	ppm	ppm	ppm
UT07-HW-1Jn.002	4.9	0.57	2.1	0.39	0.14	0.42	0.07	0.41	0.09	0.28	0.04	0.32	0.05	0.9	0.53
UT07-HW-1Jn.003	4.7	0.52	1.9	0.34	0.12	0.36	0.07	0.35	0.08	0.24	0.04	0.28	0.04	0.84	0.44
UT07-HW-1Jn.004	5.1	0.56	2.2	0.42	0.14	0.43	0.07	0.42	0.08	0.3	0.04	0.34	0.05	0.84	0.51
UT07-HW-1Jn.005	4.8	0.51	1.9	0.35	0.12	0.37	0.06	0.36	0.08	0.26	0.04	0.33	0.05	0.87	0.42
UT07-HW-1Jn.006	5	0.56	1.9	0.37	0.13	0.41	0.06	0.37	0.08	0.28	0.04	0.32	0.05	0.85	0.42
UT07-HW-2Jn.002	6.1	0.8	2.9	0.59	0.18	0.61	0.09	0.54	0.11	0.34	0.06	0.31	0.06	0.87	0.44
UT07-HW-2Jn.003	5.5	0.72	2.7	0.53	0.17	0.53	0.08	0.48	0.1	0.29	0.04	0.29	0.05	0.76	0.39
UT07-HW-2Jn.004	6.1	0.81	3	0.59	0.2	0.63	0.09	0.52	0.11	0.33	0.05	0.33	0.05	0.82	0.43
UT07-HW-2Jn.005	5.8	0.77	2.8	0.57	0.17	0.6	0.09	0.51	0.11	0.33	0.05	0.33	0.05	0.8	0.42
UT07-HW-2Jn.007	5.5	0.71	2.7	0.55	0.17	0.57	0.08	0.47	0.1	0.31	0.05	0.29	0.04	0.73	0.39
UT07-SF17Jn.002	5.2	0.65	2.4	0.48	0.14	0.45	0.07	0.41	0.08	0.27	0.04	0.3	0.05	0.78	0.35
UT07-SF17Jn.003	5.5	0.72	2.6	0.54	0.16	0.52	0.07	0.43	0.09	0.31	0.05	0.34	0.05	0.82	0.35
UT07-SF17Jn.004	5.3	0.68	2.5	0.49	0.17	0.54	0.08	0.44	0.09	0.3	0.04	0.34	0.05	0.77	0.34
UT07-SF17Jn.005	5	0.59	2.1	0.38	0.12	0.41	0.06	0.38	0.08	0.28	0.05	0.31	0.05	0.77	0.34
UT07-SF17Jn.006	5.3	0.66	2.4	0.46	0.14	0.47	0.07	0.42	0.09	0.3	0.04	0.32	0.05	0.78	0.36
UT07-SF17Jn.007	5.6	0.69	2.5	0.53	0.17	0.51	0.07	0.47	0.1	0.3	0.05	0.31	0.05	0.79	0.43
UT07-SF18Jn.002	6.8	0.92	3.5	0.68	0.21	0.71	0.11	0.64	0.13	0.41	0.06	0.4	0.07	0.96	0.43
UT07-SF18Jn.003	6.8	0.91	3.4	0.7	0.22	0.77	0.12	0.62	0.13	0.42	0.06	0.43	0.07	0.95	0.42
UT07-SF18Jn.004	6.6	0.89	3.3	0.66	0.19	0.67	0.1	0.6	0.13	0.4	0.06	0.43	0.07	0.89	0.42
UT07-SF18Jn.005	6.7	0.89	3.3	0.69	0.21	0.69	0.1	0.62	0.13	0.42	0.06	0.41	0.07	0.97	0.45
UT07-SF18Jn.006	6.9	0.92	3.5	0.69	0.2	0.7	0.11	0.62	0.13	0.4	0.07	0.42	0.07	0.95	0.43
UT07-SF18Jn.007	6.7	0.93	3.4	0.68	0.22	0.71	0.12	0.63	0.14	0.42	0.07	0.45	0.07	0.95	0.46
UT07-SF11Jn.002	5.9	0.77	2.9	0.59	0.19	0.57	0.08	0.47	0.1	0.29	0.04	0.27	0.04	0.79	0.29
UT07-SF11Jn.003	6.5	0.91	3.4	0.72	0.24	0.73	0.1	0.54	0.11	0.32	0.04	0.31	0.04	0.82	0.31
UT07-SF11Jn.004	7.5	1.03	3.8	0.78	0.25	0.75	0.12	0.63	0.12	0.37	0.06	0.37	0.06	0.89	0.34
UT07-SF11Jn.005	4.8	0.63	2.3	0.51	0.14	0.48	0.07	0.39	0.08	0.23	0.03	0.24	0.04	0.69	0.24
UT07-SF11Jn.006	6.6	0.85	3.2	0.65	0.21	0.61	0.09	0.51	0.1	0.32	0.05	0.31	0.05	0.84	0.32
UT07-SF-13Jn.003	4.8	0.64	2.4	0.5	0.15	0.51	0.08	0.41	0.09	0.25	0.04	0.23	0.03	0.72	0.24
UT07-SF-13Jn.004	4.6	0.62	2.4	0.48	0.15	0.49	0.08	0.39	0.08	0.25	0.03	0.24	0.04	0.69	0.23
UT07-SF-13Jn.005	3.9	0.47	1.8	0.36	0.1	0.33	0.05	0.31	0.07	0.21	0.03	0.21	0.03	0.65	0.23
UT07-SF-13Jn.006	4.4	0.54	2.1	0.42	0.12	0.41	0.06	0.35	0.07	0.22	0.03	0.22	0.03	0.72	0.24
UT07-Sf-13Jn.007	4.3	0.51	2	0.42	0.11	0.39	0.06	0.35	0.07	0.21	0.03	0.2	0.04	0.7	0.25
average host rock	5.6	0.72	2.67	0.53	0.17	0.54	0.08	0.47	0.1	0.31	0.05	0.32	0.05	0.82	0.37
	Ce	Pr	Nd	Sm	Eu	Gd	Tb	Dy	Ho	Er	Tm	Yb	Lu	Th	U
CONCRETIONS	ppm	ppm	ppm	ppm	ppm	ppm	ppm	ppm	ppm	ppm	ppm	ppm	ppm	ppm	ppm
UT07-HW-1Jn.001	7.4	1.19	5.6	1.41	0.46	1.61	0.27	1.63	0.33	0.87	0.11	0.67	0.1	0.87	1.31
UT07-HW-2Jn.001	6.9	0.86	3.1	0.66	0.23	0.77	0.15	1	0.24	0.72	0.11	0.65	0.1	0.82	1.06
UT07-HW-2Jn.006	6.8	0.86	3.1	0.63	0.23	0.72	0.14	0.98	0.24	0.72	0.11	0.67	0.1	0.75	1.08
UT07-SF17Jn.001	9.3	1.64	7	1.59	0.51	1.79	0.27	1.47	0.28	0.7	0.09	0.49	0.07	0.76	2.26
UT07-SF18Jn.001	5.6	0.76	2.9	0.59	0.19	0.69	0.1	0.65	0.14	0.42	0.07	0.42	0.06	0.87	1.31
UT07-SF11Jn.001	8.6	1.13	4.5	1.08	0.35	1.21	0.2	1.18	0.24	0.62	0.08	0.47	0.06	0.68	1.11
UT07-SF-13Jn.001	15.4	1.55	6.4	1.28	0.39	1.49	0.22	1.32	0.28	0.75	0.1	0.59	0.09	0.8	0.73
average concretion	8.57	1.14	4.66	1.03	0.34	1.18	0.19	1.18	0.25	0.69	0.1	0.57	0.08	0.79	1.27
concretion/host rock	1.53	1.59	1.75	1.93	2.02	2.18	2.35	2.5	2.54	2.23	2.07	1.77	1.65	0.97	3.42